Etching of CVD diamond surfaces

By:

Maria D. Stoikou MPhys (Hons.)

Submitted for the degree of Doctor of Philosophy,

Heriot-Watt University,

School of Engineering and Physical Sciences

August 2010

Abstract

This thesis presents a fundamental study on etching of diamond surfaces. Details of the growth by microwave plasma Chemical Vapour Deposition (CVD) and etching by microwave hydrogen plasma, oxygen reactive ion etching (RIE) and thermal oxidation are presented.

Prolonged exposure of {100} diamond surfaces to microwave hydrogen plasma was investigated by atomic force microscopy (AFM). Reduction of surface roughness has been observed while formation of etch pits has not been detected. X-ray photoelectron spectroscopy (XPS) detected the removal of graphitic carbon and reduction of oxygen under hydrogen plasma etching. Electrical sheet resistivity has been observed to be depended on the texture of the CVD diamond films as well as on the ambient exposure time. Both the surface and electronic properties are shown to agree with theoretical models.

Formation of columnar structures accompanied the oxygen RIE of CVD diamond films and cubo-octahedral crystallites. Using scanning electron microscopy (SEM) and AFM the preferential formation of columnar structures in the inter-granular area of the diamond films has been detected. Surface contamination by silicon oxide has been identified by EDAX on the diamond surface and specifically on the columnar structures. Analysis by XPS demonstrated that the RIE etched surfaces were oxygen terminated and also were partially graphitised. A discussion on the mechanism of columnar formation has been presented.

From the thermal oxidation of cubo-octahedral CVD diamond crystallites the activation energies and pre-exponential factors of the {100} and {111} diamond surfaces were measured, using optical profilometry, to be 221 ± 34 kJ mol^{-1}, 2.3×10^{9} nm s^{-1} Pa^{-1} and 286 ± 29 kJ mol^{-1}, 1.9×10^{14} nm s^{-1} Pa^{-1} over the temperature range $535^{o}C$ to $600^{o}C$ respectively. Thermal oxidation of {100} and {111} diamond surfaces was accompanied with the formation of etch pits, increase of surface roughness and the exposure of {113} diamond surfaces between the {100} and {111} surfaces. A mechanism for the thermal oxidation of the diamond surfaces has been proposed.

Acknowledgements

First and foremost, I would like to thank my supervisor Phil John for accepting me in his research group, for giving me the opportunity to learn and contribute in this fascinating research field. Next I would like to thank my second supervisor John. I.B. Wilson for all the guidance, encouragement, continuous support and advice he had provided me within the course of this research.

I would like also to express my gratitude to Ian Drummond for the innumerous technical help and advice, to Isaela Villalpando for the XPS measurements, to Marian Millar for the XRD measurements, to Neil Ross for all the guidance and technical support on the RIE experiments, to Mark Leonard for allowing me to use the MISEC cleanroom facilities and to Margaret Corrigan from University of the West of Scotland for the EDAX analysis. Also to Fraser Gray and to my fellow colleagues who I had the pleasure of working with in this research group.

Many thanks to my friends, who have been incredibly supportive, who had encouraged me when needed and celebrated when required. To my dearest Pierre-Antoine special thanks are needed, for all the encouragement, motivation, and love and for still putting up with me!

I gratefully thank my parents, Polixeni and Dimitris, for supporting me through all my academic endeavours. Without their love, understanding and financial support this would not had been possible. All I have to say is thanks for not giving up!

ACADEMIC REGISTRY
Research Thesis Submission

Name*:*	**Maria D. Stoikou**		
School/PGI:	**School of Engineering and Physical Sciences - Chemistry**		
Version: *(i.e. First, Resubmission, Final)*	**Final**	Degree Sought	**PhD**

Declaration

In accordance with the appropriate regulations I hereby submit my thesis and I declare that:

1) the thesis embodies the results of my own work and has been composed by myself
2) where appropriate, I have made acknowledgement of the work of others and have made reference to work carried out in collaboration with other persons
3) the thesis is the correct version of the thesis for submission and is the same version as any electronic versions submitted*.
4) my thesis for the award referred to, deposited in the Heriot-Watt University Library, should be made available for loan or photocopying and be available via the Institutional Repository, subject to such conditions as the Librarian may require
5) I understand that as a student of the University I am required to abide by the Regulations of the University and to conform to its discipline.

* *Please note that it is the responsibility of the candidate to ensure that the correct version of the thesis is submitted.*

Signature of Candidate*:*		Date:	

Submission

Submitted By *(name in capitals):*	
Signature of Individual Submitting:	
Date Submitted:	

For Completion in Academic Registry

Received in the Academic Registry by *(name in capitals):*			
Method of Submission *(Handed in to Academic Registry; posted through internal/external mail):*			
E-thesis Submitted			
Signature:		Date:	

Table of Contents

Table of Figures

List of Tables

List of Publications

Maria D. Stoikou, Philip John, John I.B. Wilson, *Unusual morphology of CVD diamond surfaces after RIE,* Diamond and Related Materials, 2008. **17**(7-10):p. 1164-1168

Poster sessions

Maria D. Stoikou. Phillip John, John I.B. Wilson, Unusual morphology of CVD diamond surfaces after RIE, DIAMOND 2007, Sept 2007, Berlin

Chapter 1. Introduction

The plethora of unique physical and chemical properties of diamond has fostered a substantial research effort in the past thirty years for the utilisation of the material for a wide range of technological applications [1]. Due to the limited availability of diamond substrates many of the applications have been restricted in the past. The enormous research effort in the last few decades into the chemical vapor deposition (CVD) of diamond has provided a rich source of research data and, significantly, the commercial availability of large polycrystalline and single crystal diamond substrates.

1.1 Diamond devices

Diamond films are amongst the most favorable materials for hard coatings that can be used for a variety of applications. One such application, which has been discussed in the literature [2], is the coating for plasma facing components of tokamak fusion reactors. Since diamond has demonstrated a higher erosion resistance to hydrogen plasma exposure [3] than the commonly used graphite it is considered the future material as protective coatings for the key divertor components.

Diamond has attracted enormous attention as a suitable material for the fabrication of electronic and optical devices. So far there are reports on the successful fabrication of diamond-based X-ray detectors [4, 5], diodes [6], ultraviolet (UV) photo-detectors [7-9], light emitting diodes [10] and electron emitting [11, 12] devices. Recently impurities within the diamond lattice have attracted lot of attention as some are active optical centers. More specifically, the nitrogen-vacancy (N-V) colour centre in diamond is an ideal candidate for hybrid solid state quantum devices [13].

Conducting diamond has attracted attention as a material for microelectrodes and as an ideal platform material for bio-interfaces. This is due to the superior electrochemical properties of diamond including a wide potential window [14], chemical stability, excellent bio-compatibility [15] and bio-inertness which has been demonstrated in a number of electrochemical [16, 17] and biological [18] applications.

1.2 Diamond surfaces

The intrinsic physical properties are a crucial factor for the potential applications of diamond although the surface properties and geometries are equally important for the prospective applications. The properties of any device would be affected by the nature of the termination and morphology of the diamond surface.

A crucial step in diamond device fabrication would be the processing and polishing of the surface down to atomic scale level. Working with a chemically inert substrate which is the hardest material known is very demanding. Reducing the surface roughness of diamond has been the subject of extensive research and different routes have been explored. Mechanical polishing of the diamond surface by abrading material is one of the most commonly applied post-growth techniques to attempt to produce an atomically smooth surface. Such techniques lead to a damaged diamond surface, with an intrinsic surface roughness depending on the direction of polishing with respect to the crystallographic axes, which could dramatically affect the performance of any potential diamond device.

In the past years there has been enormous experimental work focused on the optimisation of single diamond crystal growth with atomically smooth surfaces by examining the effect of deposition process parameters [19], such as temperature, gas composition, pressure and substrate orientation. Surface crystal defects on diamond surfaces, such as hillocks and etch pits [20, 21], have been investigated as their presence induces surface roughness and incorporation of impurities. Despite the work done so far on the CVD of homoepitaxial diamond growth surface defect formation is still not well understood.

1.3 Surface treatments

A wide range of surface treatments has been applied for the reduction of the surface roughness of single crystal and polycrystalline diamond films [22-30]. Plasma-based treatments have demonstrated that, under optimal process conditions, atomically smooth surfaces [27, 30, 31] are formed. Plasma-based treatments following growth is,

therefore, worthy of further exploration to understand the mechanism underlying the improved quality of the homo-epitaxial diamond [32-35] surface.

The termination, and thus chemistry of diamond surfaces, can be altered upon exposure to various plasmas [36-39] including that of hydrogen plasmas. Not only has a reduction of the surface roughness to atomic level been demonstrated but also a concomitant change in electronic properties, notably the formation of p-type surface conductivity [40-44], which is an intriguing property for future electronic applications.

Oxygen terminated diamond surfaces are hydrophilic and alter the chemical reactivity [45], electrical conductivity [46, 47], field emission [48] and Schottky barrier [49] of the crystal. The modification of the diamond surface to make it chemically reactive is very important for the functionalisation of the surface with biomolecules, such as proteins, DNA and enzymes. Oxidation of diamond surfaces can be achieved by different routes such as: photochemical reactions [50], plasma treatments [51, 52] thermal [53, 54], electrochemical [55, 56] and ozone treatments [57, 58]. The introduction of oxygen-carbon functional groups on the diamond surface, such as ether (C-O-C), carbonyl (C=O) and hydroxyl (OH), has shown to be strongly dependent on the process conditions and crystallographic orientation [228, 240].

The focus of the work reported in this thesis is the effect of microwave hydrogen plasma treatment on diamond films with (100) crystallites epitaxially aligned to the underlying single crystal silicon substrates. In addition the interaction of oxygen with diamond surfaces has been examined by means of reactive ion etching and thermal oxidation. As diamond oxidation has been found to be strongly depended on crystallographic orientation, the present studies have been conducted on CVD diamond films as well as on isolated individual CVD diamond cubo-octahedral crystallites with well-defined (100) and (111) diamond planes.

Chapter 2. CVD diamond films

2.1 Introduction

The element carbon forms the basic unit of organic chemistry, biological molecules and results in life on earth. Due to the catenation property of carbon to form chains or rings, not only with single bonds, but also with double and triple bonds, and with bonding variety to other chemical elements, carbon forms nearly ten million known chemical compounds [59].

As the sixth element of the Periodic Table, an isolated carbon atom has a ground-state electronic configuration of $1s^2 2s^2 2p^2$. There are two core electrons occupying the 1s orbital and four valence electrons equally distributed between the 2s and 2p orbitals. To accommodate the geometries of bonding in carbon the four valence electrons are promoted to the valence state of $1s^2 2s^1 2p_x 2p_y 2p_z$. Elemental carbon can exist in the three main allotropes, namely:

Graphite: The crystal structure of graphite is shown in Figure 2.1a). It comprises hexagonal symmetric basal planes. The valence electrons of each carbon atom form three equivalent sp^2 orbitals for bonding within the planes whereas the planes are held together by van der Waals forces. Each carbon atom in the hexagonal rings forms three σ covalent bonds, having a strength of 524 kJ/mol [60]. The distance between the basal planes is 0.335 nm whilst the distance between the adjacent atoms in the basal hexagons is only 0.142 nm. The anisotropic crystal structure of graphite results in large anisotropic properties of the material. Due to the delocalised π-cloud above and below the planes of carbon atoms the material is an electrical conductor. As the adjacent planes are held by weak van der Waals forces they can slip past each other therefore making graphite a soft material.

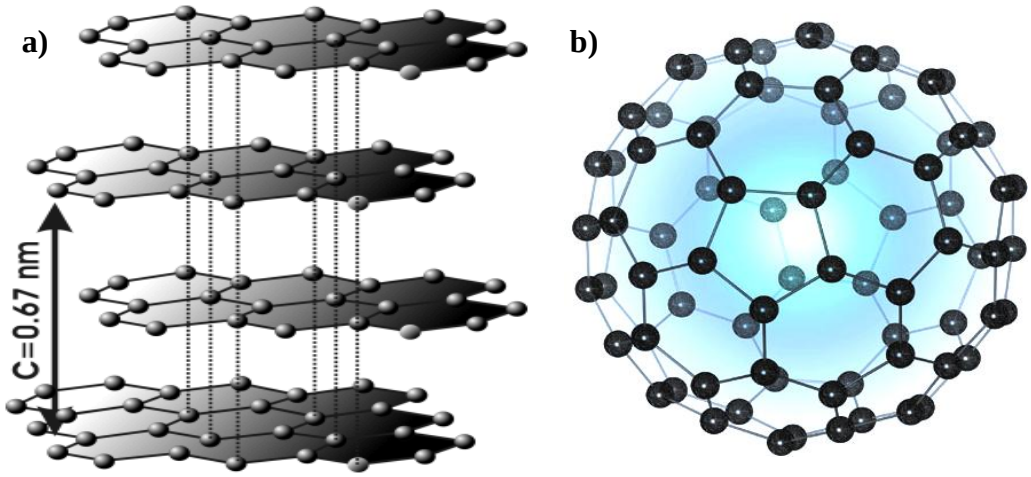

Figure 2.1 sp^2 carbon crystal structure: a) graphite and b) C_{60} molecule.

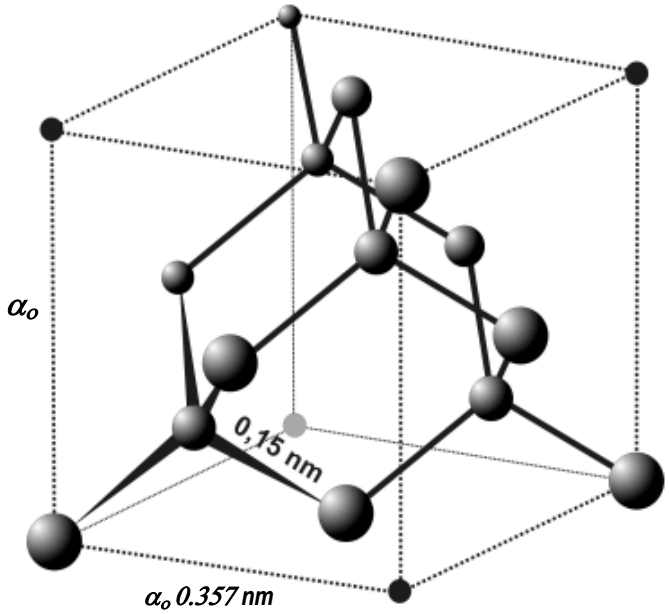

Figure 2.2 Diamond crystal structure.

Fullerenes: A schematic representation of a simple C_{60} molecule is shown in Figure 2.1b). The carbon atoms are arranged in five- and six- membered rings to form spherical shells that contain exactly 60 carbon atoms: the first fullerenes C_{60} [61]. From the discovery of a C_{60} other fullerenes have been reported in which a number of interesting shaped molecules are possible such as spheres, ellipses or cylinders. The fullerenes molecules are very stable structures and the four valence electrons are fully utilised in bonding [61].

Diamond: is a network of tetrahedrally coordinated carbon atoms, as shown in Figure 2.2, with a short bond length (0.154 nm) and high bond strength of 711 kJ/mol [60]. The carbon atom is hybridised forming four equivalent sp^3 orbitals. Each carbon atom forms four σ covalent bonds with the neighboring atoms with an angle of ca. 109^o directly toward the four corners of a tetrahedron [60].

The diamond crystal structure is a face-centered cubic (FCC) lattice, where the basis comprises two identical carbon atoms at each lattice point: one at (0, 0, 0) and the other at $(\frac{1}{4}, \frac{1}{4}, \frac{1}{4})$, where the coordinates are given as fractions along the cube sides. This is equivalent as two interpenetrating FCC lattices, offset from one another along a body diagonal by one-quarter of its length.

The unit cell of diamond, Figure 2.2, has a cube length (α_o) measured to be ~ 3.57 Å (0.357 nm) at room temperature [60] where the centre-to-centre C-C bond length is ≈ 1.54 Å equivalent to one quarter of the cubic body diagonal. There are eight carbon atoms within the unit cell and therefore the atomic number density corresponds to $8/ \alpha_o^3 \approx 1.76 \times 10^{23}$ cm^{-3}.

Diamond exhibits a range of remarkable properties due to its isotropic crystal structure. The mechanical and physical properties [62, 63] of single crystal diamond are presented in Table 2-1 whilst the optical and electrical properties are summarised in Table 2-2.

The three-dimensional stability of the tetrahedral bonding arrangement and the incompressibility of the C-C bonds are responsible for diamond's extreme hardness. Natural diamond is used for the calibration of the Mohs hardness scale, on which diamond has the maximum value of 10.

At the equilibrium position the C-C bonds are relatively short. Due to their small size the carbon atoms are able to come close to each other before they experience net repulsive forces. Overlap of the orbitals of the adjacent carbon atoms in a C-C bond, creates a large energy separation between the occupied bonding orbitals and the unoccupied antibonding orbitals. This creates the formation of a very large energy gap between the valence and conduction band states in the electronic structure of diamond.

Property	**Value**
Crystal Structure	Diamond (cubic)
Lattice constant	3.567 Å
Density	3.51 g cm^{-3} [69]
Atomic concentration	1.763 x 10^{23} cm^{-3}
Thermal conductivity (300 K)	2 x 10^{3} W m^{-1} K^{-1}
Thermal expansion coefficient (300 K)	0.8 x 10^{-6} K^{-1}
Mechanical hardness	90 GPa
Bulk modulus	1.2 x 10^{12} N m^{-2}
Melting point	4000^{o}C
Heat capacity	0.4715 J g^{-1} $^{o}C^{-1}$
Heat of formation	714.4 kJ mol^{-1}
Modulus of elasticity	700-1200 GPa
Poisson's Ratio	0.1-0.29

Table 2-1 Mechanical and physical properties of single crystal diamond [68].

Property	**Value**
Refractive index (10 μm)	2.40
Visible light spectrum	2.40 – 2.46
Dielectric constant (45 MHz – 20 GHz)	5.6
Dielectric strength	10^{6} V /cm
Electrical resistivity (single crystal)	10^{16} Ω cm
Electronic bandgap (indirect)	5.45 eV
Electron mobility (300 K)	2200 cm^{2} V^{-1} s^{-1}
Hole mobility (300 K)	1600 cm^{2} V^{-1} s^{-1}
Saturated drift velocity	2.7 x 10^{7} cm s^{-1}

Table 2-2 Optical and electrical properties of diamond.

Diamond is characterised as a large band-gap semiconductor, if not as an insulator at room temperature, with an indirect bandgap of ~ 5.45 eV at 300 K [62].

2.2 The synthesis of diamond

The discovery, in 1772, that diamond is a carbon allotrope by the French scientist Lavoisier triggered the early attempts to synthesise diamond using graphite as a starting material. These methods were proven to be extremely difficult because, at room temperature and pressure, graphite is the thermodynamically stable allotrope of carbon. The difference between the standard enthalpies of diamond and graphite is 2.9 kJ mol^{-1} [64]. The presence of a large activation barrier between the two phases prevents kinetic interconversion to take place under normal conditions i.e. 298 K and 1 atm pressure.

2.2.1 The high pressure high temperature synthesis

In contrast to the early work, diamond can be formed under conditions where is thermodynamically the most stable form of carbon. This principle is the basis of high-pressure high-temperature (HPHT) synthesis to convert graphite to diamond. This technique was announced by ASEA in 1955 [65] and General Electric in 1955 [66] and since then it has been extensively used to produce synthetic diamond. Usually the process involves the presence of a suitable metal catalyst which reduces the activation energy for the conversion. The HPHT technique originally produced single crystal diamonds of very small sizes and this limited the applications of the material. There are a number of factors which affect the quality of the grown crystal. An excellent review has been published for the growth of large single crystals of diamond by HPHT synthesis [67].

2.2.2 The chemical vapour deposition of diamond

The chemical vapour deposition process (CVD) is one of the most common techniques used in the fields of microelectronics and photonics for the growth and deposition of different materials. The principles of the CVD process involve the mixing of different gases in an environment that provides excitation of the gases in a manner to cause the deposition of a solid layer of material.

The use of the CVD process in the growth of diamond was initiated by using a carbon containing gas in a low pressure regime. First attempts using this concept were performed by Eversole [69] and Deryagin *et al* [70] under low pressure and on natural diamond crystals at 900^{o}C. For those early experiments the growth rate was very small because graphite was deposited at the same time, since both phases were able to grow. The addition of atomic hydrogen into the gas mixture during the deposition process led to preferential etching of any graphitic phases compared to diamond [71, 72]. Further improvement of the process by the Russian research group led to the growth of diamond on non-diamond surfaces [73].

In 1982 the Japanese research group in the National Institute for Research in Inorganic Materials (NIRIM) developed a hot filament reactor for the growth of diamond films. This technique showed that good quality diamond can grow on non-diamond substrates at a growth rate of ~1 μm h^{-1} [74]. It took only one further year to develop another method to grow diamond using a microwave plasma reactor [75].

2.2.3 Low pressure diamond synthesis

To date, there have been substantial technological advances in the growth of single crystal (homoepitaxial growth) diamond and polycrystalline diamond films which have been performed using different techniques. The different types of growth systems are categorised according to the type of activation mechanism used in the gas-phase for the deposition of diamond. They can involve thermal methods, such as hot filament and oxyacetylene torch, and plasma methods such as DC electric discharge and microwave plasmas. From the engineering point of view they may vary but they share common features as growth systems:

1. They use a large amount of electrical or chemical energy to achieve dissociation of molecular hydrogen and hydrocarbon molecule, as they need
   i) a carbon containing gaseous precursor such as CH_4 diluted in an excess of hydrogen (1% vol. CH_4) to form fragments which are reactive at the deposition surface.
   ii) to dissociate molecular hydrogen sustaining a super-equilibrium concentration of gas-phase hydrogen atoms.

2. They operate at moderately low pressures, usually a few Torr to 1 atm.
3. The gas temperature is high, typically 1700^{o}C around the activation zone. Cooling is applied to the substrate to ensure and maintain a substrate temperature in the range approximately 600 – 900^{o}C.

Hot Filament CVD

The development of the hot filament (HF) CVD process by Matsumoto [76] in 1982 initiated research which led to the industrial production of CVD synthetic diamond. In a typical HF reactor Figure 2.3, a metal coil is heated to around 2000^{o}C at a reduced pressure (~ 20 Torr) of the reactant gas mixture of H_2/CH_4. The substrate temperature depends on the filament temperature and the distance between the substrate and the filament. It is feasible to heat the substrate independently to 600 – 900^{o}C, as well as to apply a bias voltage either to the filament or the substrate.

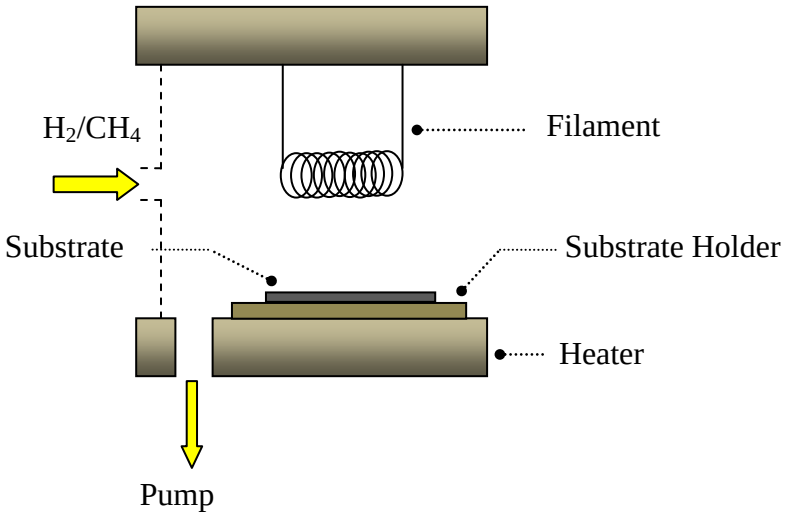

Figure 2.3 Schematic representation of a hot-filament CVD reactor.

The gas flow design of the HF reactor is very important as diffusion is the dominant transportation process of the active reagents to the substrate. A metal carbide layer forms around the residual filament under CVD conditions. Molecular hydrogen adsorbs on the carbide layer, where thermal energy causes dissociation to atomic hydrogen which diffuses back to the gas mixture. Atomic hydrogen production is limited by the surface area of the filament and the available surface sites for dissociation. For the extended growth of diamond the thermal and mechanical stability of the metal carbide

layer is crucial. For example tantalum is one of the preferable metals for filament as it remains rigid at high temperatures.

HFCVD technology is one of the most popular processes for the growth of synthetic diamond because of its basic simplicity, low cost, easy of scale up and it is feasible to coat different types of substrates with diamond films on various complex geometries. In summary large area of material can be coated with high growth rates [77]. Nevertheless the application of the HF technology is limited due to the quality of the diamond films produced, because of the possible contamination from the filament source material [78].

The DC arc-jet reactor

The DC arc-jet reactor is one of the most common plasma-jet systems used for diamond deposition. Extremely high flow rates of process gases are used in the plasma, which are ionised by high electrostatic potentials. There is a secondary chamber that is used to expand the jet which reaches the substrate surface at high velocities. The technology is categorised according to the pressure of the second chamber (which could be 100 Torr to 1 atm) and the method used to sustain the discharge.

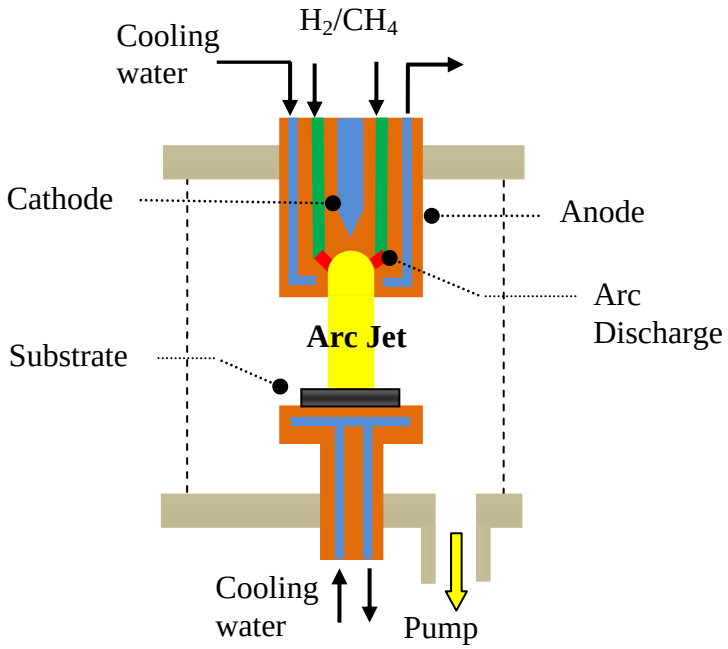

Figure 2.4 Schematic diagram of DC arc jet plasma reactor used for diamond deposition.

In the DC arc-jet, ionisation is caused by the high electric field that is used to drive high, steady currents through the flowing process gas. A schematic illustration of a typical plasma jet employed for diamond deposition is showed in Figure 2.4. Very high growth rates have been obtained using the DC arc-jet reactor [79], but the deposition of diamond is limited to a small area exposed to the jet. Since arc-jets generate high temperature the thermal shock at the surface of the substrate is large and could lead to delamination of the underlying deposited material. Sophisticated cooling systems have usually been employed in the plasma-jets to avoid this problem.

2.3 Microwave plasma enhanced chemical vapour deposition synthesis

Due to its simplicity, flexibility and early commercial availability the microwave plasma enhanced chemical vapour deposition (MPECVD) became the most widely technique used for the deposition of high quality synthetic diamond within a relatively low pressure gas regime.

In this type of CVD process the excitation energy is provided to the gas mixture by means of microwave power, with a frequency of 2.45 GHz as most commonly used. The MPECVD systems are also referred to in the scientific literature as microwave plasma assisted CVD (MPACVD). The substrate to be coated is contained within the same chamber as the process gases. Microwave power is then coupled into the chamber through a dielectric window via a waveguide and an antenna for the creation of a plasma discharge. A stub tuner is used to tune the microwave matching circuit, as shown in Figure 2.5. The substrate is usually immersed in, or adjacent to, the plasma in the chamber.

A schematic representation of the processes that take place during the MPECVD diamond growth is shown in Figure 2.6. Free electrons in the gas are accelerated by coupling with the electrical component of the microwave field. Electron energy is transferred to the system through gas-phase collisions leading to vibrational excitation, molecular dissociation and, ultimately, ionisation of molecular hydrogen. As a consequence this creates a non-equilibrium plasma and the atomic hydrogen, which may be also be in a energetically excited form, initiates the radical gas-phase chemistry [80].

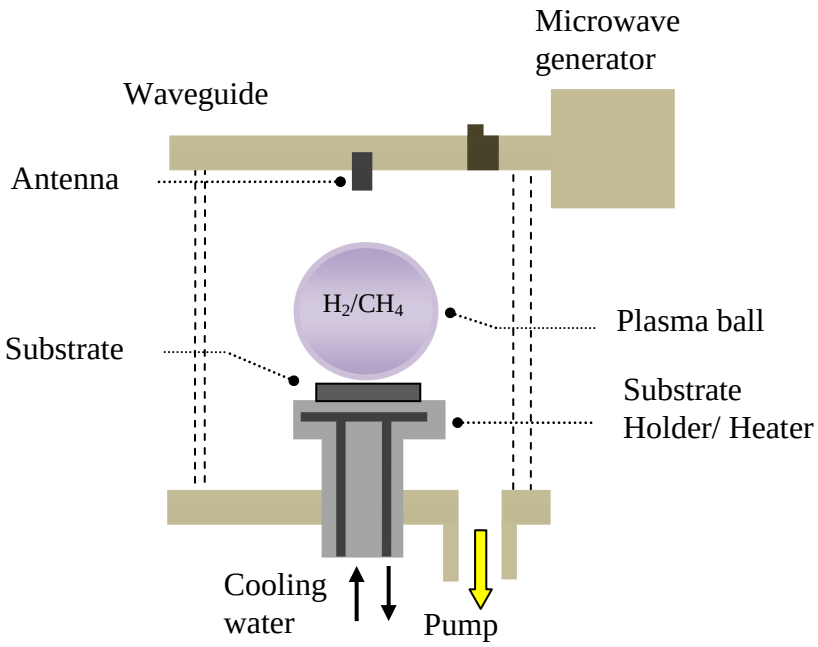

Figure 2.5 The schematic diagram of the microwave plasma CVD reactor.

A schematic representation of the processes that take place during the MPECVD diamond growth is shown in Figure 2.6. Free electrons in the gas are accelerated by coupling with the electrical component of the microwave field. Electron energy is transferred to the system through gas-phase collisions leading to vibrational excitation, molecular dissociation and, ultimately, ionisation of molecular hydrogen. As a consequence this creates a non-equilibrium plasma and the atomic hydrogen, which may be also be in a energetically excited form, initiates the radical gas-phase chemistry [80]. The diamond precursors impinge on the substrate and, under the right conditions, diamond growth takes place. The design of the MPECVD reactors is such to ensure that the local maximum in the microwave field intensity lies above the water-cooled substrate. The geometry and dimensions of the reactor provides stability of the plasma within the reactor [81].

There has been impressive progress on increasing the microwave power capabilities and technologies of MPECVD systems since the 1980's, which has led to a significant increase of the deposition rate and the quality of the material [82,83]. Microwave activation for diamond growth creates an electrode-free discharge which enables the use of high temperatures and/or higher pressures for process conditions avoiding equipment degradation and sample contamination. A drawback of using MPECVD technology is the high cost of the design and manufacture of the systems especially when high powers are used.

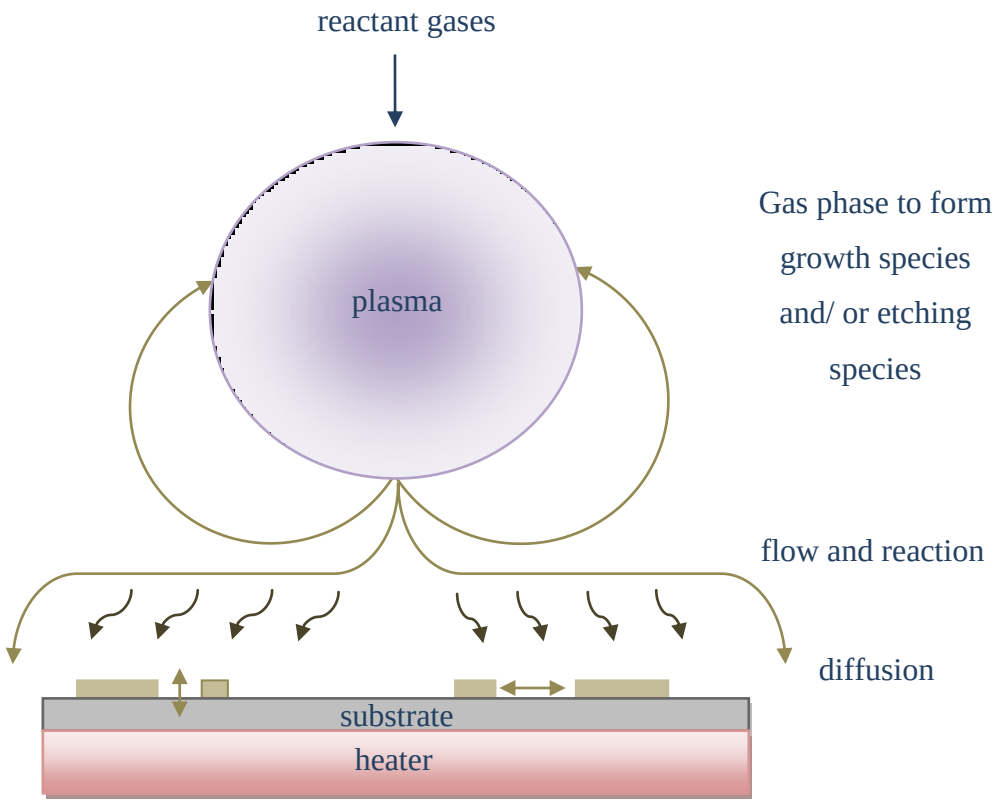

Figure 2.6 Schematic representation of the different processes taking place during diamond MPECVD.

A direct comparison between various MPECVD systems is impossible since the design of the reactors differs. As well as the way of providing heating to the substrate, gas pressures and the gas composition differ from one research group to another. Despite this a model has been developed for the MPECVD diamond growth process that agrees broadly with the experimental results. The detailed mechanism of diamond growth by MPECVD is not completely understood especially the surface processes [84]. Analytically we consider the different processes that take place during the MPECVD diamond growth as shown in Fig. 2.6.

2.4 Gas-phase processes in CVD diamond synthesis

In CVD diamond synthesis the gas chemistry involves reaction of hydrocarbon species and their dissociated fragments. Attempting to understand the gas phase chemical kinetics of C/H/O species and growth mechanism has seen an enormous effort in experimental, theoretical and modeling research in CVD diamond synthesis.

2.4.1 Formation of atomic hydrogen

The CVD diamond synthesis, at the low pressure regime, is carried out in the excess of molecular hydrogen in the gas mixture. Formation of atomic hydrogen is crucial for the gas chemistry during the CVD process.

The formation of atomic hydrogen achieved by the electronic dissociation of molecular hydrogen in a microwave plasma CVD system

$$H_2 + e^- \Rightarrow 2H + e^-$$

and by thermal decomposition of molecular hydrogen on the hot filament surface:

$$H_2 \Leftrightarrow 2H$$

Within an appropriate pressure regime, energy transfer from electrons to heavy third bodies (M) can occur, giving the third bodies energy enough to dissociate molecular hydrogen, thus:

$$H_2 + M \rightarrow 2H + M$$

The consumption of atomic hydrogen can be achieved by a number of reactions, but the rates of atomic hydrogen formation and consumption equalise resulting in a steady state of atomic hydrogen within the plasma. Plasma process parameters, mostly the pressure and the microwave power, influence the concentration of atomic hydrogen species. Consumption of atomic hydrogen can be achieved through formation of molecular hydrogen by third body reaction:

$$H + H + M(H_2) \rightarrow H_2 + M(H_2)$$

Such a reaction is strongly influenced by the pressure and the reaction rate may become very slow at low pressures. Diffusion of atomic hydrogen to the chamber walls or the substrate may occur before atomic hydrogen recombines in the gas phase.

2.4.2 Hydrocarbon chemistry

The presence of hydrocarbon species in the plasma mixture introduces new pathways for the consumption of atomic hydrogen. Therefore the dynamic hydrogen abstraction/hydrogen addition reactions with hydrocarbons are the dominant process within the CVD reactor.

The formation of hydrocarbon species: CH_3, CH_2, CH and C are feasible via a series of fast (H-shifting) reactions, in the hot plasma regions, involving the H abstraction reaction:

$$CH_y + H \Rightarrow CH_{y-1} + H_2 \qquad y = 4\text{-}1$$

$$C_2H_x + H \Leftrightarrow C_2H_{x-1} + H_2 \qquad x = 6\text{-}1$$

While in the cooler regions of the plasma, addition reactions can take place.

$$CH_y + H + M \Rightarrow CH_{y+1} + M \qquad y \geq 0$$

$$C_2H_x + H + M \Leftrightarrow C_2H_{x+1} + M \qquad x \geq 0$$

although the reverse reaction path is possible requiring a third body (M).
The various CH_y ($y \leq 4$) species exhibit a wide spatial distribution of relative densities in the CVD growth chamber, as their densities depend on the local H atom density and the gas temperature T_{gas}.

It would be expected that C_2H_x species would be present under typical CVD growth conditions. It has been observed experimentally that the same concentration of methane (CH_4), methyl (CH_3), acetylene (C_2H_2), H and ethylene (C_2H_4) were evident [85] in a MPECVD system when either acetylene/hydrogen gas mix or methane/hydrogen gas mix was deployed under the same process conditions.

The C_2H_x species are formed by CH_y radical recombination reaction path ways:

$$CH_x + CH_y \Leftrightarrow C_2H_{x+y}$$

$$CH_x + CH_y \Leftrightarrow C_2H_{x+y-1} + H$$

$$CH_x + CH_y \Leftrightarrow C_2H_{x+y-2} + H_2$$

For example the formation of acetylene, can achieved by the following reaction paths:

$$CH_3 + CH_3 \Leftrightarrow C_2H_6$$

$$C_2H_6 + H \Leftrightarrow C_2H_5 + H_2$$

$$C_2H_5 + M \Leftrightarrow C_2H_4 + H + M$$

$$C_2H_4 + H \Leftrightarrow C_2H_3 + H_2$$

$$C_2H_3 + H \Leftrightarrow C_2H_2 + H_2$$

or $$C_2H_6 + M \Leftrightarrow C_2H_2 + 4H + M$$

The formed C_2H_x species in the plasma undergo a series of gas-phase H-shifting (abstraction and /or addition) reactions. Acetylene C_2H_2 has been found to be the most thermodynamically favoured hydrocarbon at high T_{gas}. Through a series of recombination and H-shifting reactions the formation of C_nH_x species ($n > 2$) can be achieved and as the carbon mole fraction increased in the input gas mixture such species gain an increasing relative abundance.

The MPCVD reactors are characterised by a steep T_{gas} gradient. As a consequence the total gas phase number densities, the H atom densities and the inter-conversion reaction rates between these species are all sensitive functions of location within the reactor chamber. Advanced mass spectroscopic techniques [86-88] had been employed and the presence of stable hydrocarbon species like CH_4, C_2H_2 and C_2H_6, and CH_3 radicals have been reported under typical CVD diamond gas mixtures and process conditions.

Recent studies on the gas-chemistry of MPCVD reactors show that interconversion between $CH_4 \rightarrow C_2H_2$ takes place and it is sensitive to local T_{gas} and [H] which are influenced by the process conditions (pressure, input power, input gas mixing ratios, etc) and location inside the reactor. Transient species such as C_2 and CH radicals, and electronically excited H atoms, were found to be independent of the carbon source gas in the CVD reactor. Therefore any chosen hydrocarbon source gas will be converted into a mixture dominated by CH_4 and C_2H_2 through interconversion reactions [86].

2.4.3 Growth additives

Oxygen

The addition of oxygen in the gas growth mixture of diamond, either in the form of molecular oxygen or as an oxygen- containing compound e.g. CO, CO_2, alcohol or acetone, is very common [89-92]. The presence of oxygen in the gas mixture has been proposed to improve the film quality [92] since oxygen etches graphite rapidly or any other non-diamond components and removes these phases from the diamond film. The presence of oxygen in the gas mixture has been found to:

i) increase growth rates [84]
ii) alter the α parameter [89], which describes the shape of diamond cubo-octahedral crystals and is defined as the ratio between the growth rates of {100} and {111} diamond faces respectively.
iii) reduce impurity incorporation such as boron [93] and nitrogen [90].

Despite the type of carbon source used in the MPECVD system acetylene has been reported [84] to be the dominant stable hydrocarbon product arising from the plasma. It is believed that oxygen consumes acetylene through a complex multi-reaction process that can be summarised thus,

$$C_2H_2 + O_2 \rightarrow 2CO + H_2$$

Considerable research into MPECVD has established that it is feasible to grow diamond under very precise ratios of carbon, hydrogen and oxygen. This is exemplified by the ternary phase diagram developed by Bachmann and co-workers [94]], as shown in Figure 2.7. According to the collated observations the successful growth of diamond takes place under precise ratios of C-H-O which is independent of the type of carbon containing species and the growth method. Diamond growth is achieved on a narrow region of the Bachmann phase diagram defined as the diamond growth region in Figure 2.7, below this region no growth is achieved while above it no-diamond carbon is generally deposited.

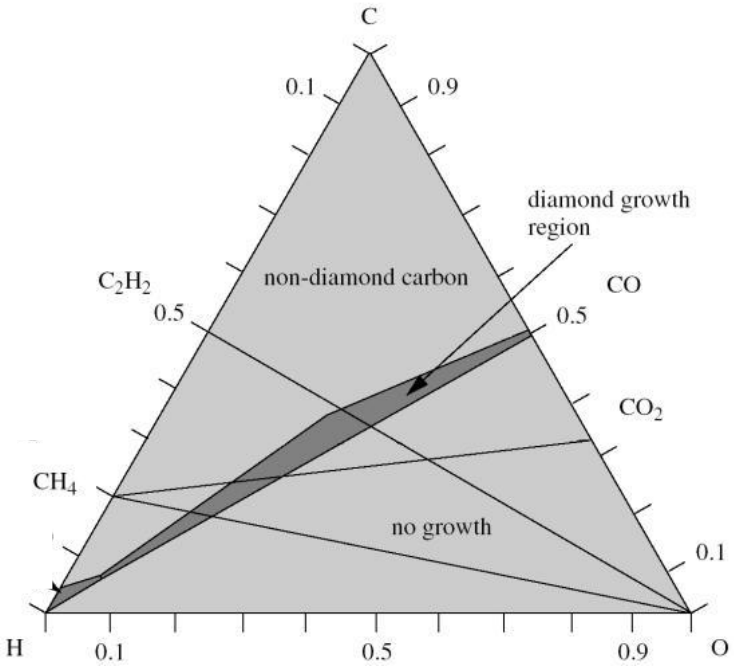

Figure 2.7 A simplified form of the Bachmann phase diagram for diamond growth in C–H-O containing CVD systems [94].

Halogens

Other types of gases that have been used in CVD growth gas mixtures are fluorine and chlorine, either as pure gas or as organic species containing fluoro- or chloro- groups [95-98]. The role of these species is not completely understood but, as with all those systems, it is believed that they contributed to improve the growth surface stabilisation, preferential etching of non-diamond carbon or to enhance the concentration of the growth species. When halogens are used for the growth of diamond it has been found to result in halogen terminated surfaces as well as to decrease the growth temperatures. The incompatibility of present CVD reactor materials and pumps to halogen species excluded their use in this work.

Nitrogen

Nitrogen is one of the most common impurities found in natural diamond. When added to the CVD growth gas mixtures it leads to a profound increase in the growth rate [99]. Addition of nitrogen at low concentrations in the gas mixture produces high quality highly oriented/textured films [100-102]. There is an ongoing debate about the

effect on the growth of diamond films. One of the mechanisms that has been proposed, as with oxygen, is the preferential etching of the non-diamond carbon by nitrogen species. The drawback of nitrogen addition to the growth mixture is that the resulting diamond films have altered electronic properties via the incorporation of nitrogen in the diamond lattice. Nitrogen is an interstitial donor with ionisation energy of 1.7 eV [102] and since this level is deep the presence of nitrogen produces a diamond insulator at room temperature.

Dopants

By adding dopants into the growth gas mixture during CVD growth the electronic properties of the diamond films can be altered. It is believed that a low concentration of dopants does not change the chemistry of the diamond growth. The mechanism of how the dopants influence the growth is still not understood. The incorporation of dopants into the crystal lattice alters the electronic properties of diamond creating both n-type and p-type semiconductor behaviour of the material. The successful incorporation of nitrogen [102], phosphorus [103-105] and boron [106-109] into the diamond lattice has been demonstrated.

Boron doped diamond exists in nature and is a p-type semiconductor, with an acceptor level of 0.37 eV above the valence band maximum. Growth of p-type diamond by CVD techniques can be achieved by addition of diborane (B_2H_6) or trimethylboron $B(CH_3)_3$ into the gas mixture. The incorporation of boron atoms has been found to depend on the growth facet of diamond. The incorporation ratio of boron is higher for the (111) plane rather for the (100) indexed planes [109]. As a consequence there is an spatially inhomogeneous boron distribution within the polycrystalline diamond films [106].

There are several impurities that introduce n-type doping in diamond. Nitrogen is an interstitial donor, with a very deep donor level of 1.7 eV. Phosphorus creates a donor level of 0.6 eV below the conduction band minimum

The addition of a dopant precursor gas into the growth chamber contaminates the chamber wall. Thus subsequent deposited materials will contain the dopant. One solution to overcome this problem is the use of different reactor chambers for doped and intrinsic diamond film growth.

An alternative route to diamond doping, commonly employed, is ion-implantation. This method allows the doping of selective areas on the film surface as well as the formation of areas with different conductivity. Ion implantation is always accompanied by lattice damage. The ion damaged areas are converted to graphite by annealing due to the metastability of the sp^3 diamond configuration with respect to the thermodynamically stable sp^2 bonding configuration of graphite [110-111].

2.5 Surface chemistry in CVD diamond synthesis

The current understanding of the macroscopic mechanism of CVD diamond synthesis originates from the extensive research work done experimentally and theoretically. The bonding and structures of diamond surfaces have been analysed extensively by the modern techniques of theoretical chemistry. The focus of the theoretical research is based on the relative stability of surface structures and their reaction barriers for different adsorbate species. While surface science methods have attempted to unravel the CVD growth mechanism of diamond it is acknowledged that further advances in surface chemistry may rationalise the growth rate and quality of diamond crystals.

The general model [84] for CVD diamond synthesis on hydrogen terminated diamond surfaces is a two step process as growth takes place under conditions of excess hydrogen. Growth is initiated by site activation via a surface hydrogen abstraction reaction:

$$H(g) + CH(s) \Leftrightarrow H_2(g) + C^{*}(s)$$

followed by addition of hydrocarbon radical where (s) represents surface species.

$$H\ (g) + C^{*}\ (s) \Leftrightarrow CH\ (s)$$

In this simple growth model the number of active sites is determined by the competition between formation of active sites and hydrogen atom recombination with the surface radicals [112].

2.5.1 Diamond surfaces

The surface processes during CVD diamond growth is dependent on the crystal planes exposed to the gas phase. In the case of polycrystalline CVD diamond films, the morphology of the deposited film strongly depends on the relative growth rates of {111} and {100} planes. Figure 2.8 shows the atomic geometries, in perspective views, of clean (100) and (111) diamond surfaces [113]. However, it should be recognised that steps may also exist on diamond surfaces.

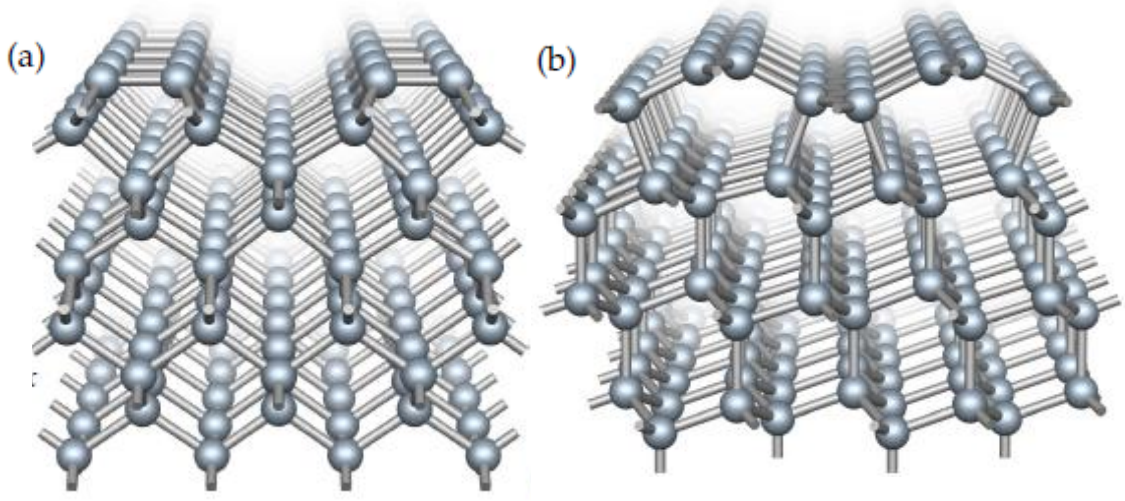

Figure 2.8 Atomic geometries for the clean a) (100) (2x1) surface and b) (111) (2x1) Pandey-chain surface [113].

The {100} diamond surface results from a network of vertically oriented zigzag chains of carbon atoms. As each new layer of atoms is added to the structure the chains rotate by 90^{o} due to lattice symmetry. The (100) diamond surface of polycrystalline diamond reveals square facets characteristic of (100)-highly oriented/textured CVD diamond thin films.

Clean (100) diamond surfaces are completely free from hydrogen and exhibit a 2x1 reconstruction symmetry with π-bonded dimer rows [114]. Hydrogen termination of (100) diamond surface has also been observed directly by scanning tunnelling microscopy (STM) to show the 2x1 reconstructed.[115-117] surface.

Several theoretical models have been developed to describe the stability of hydrogen terminated (100) diamond surfaces [118-120]. The monohydride termination has been found to be the most stable form of the (100) 2x1 surface [121] . Each carbon atom of the C-C dimer rows of the (100) 2x1:H surface has two back bonds to the diamond lattice and one bonded to hydrogen, as depicted in Figure 2.9.

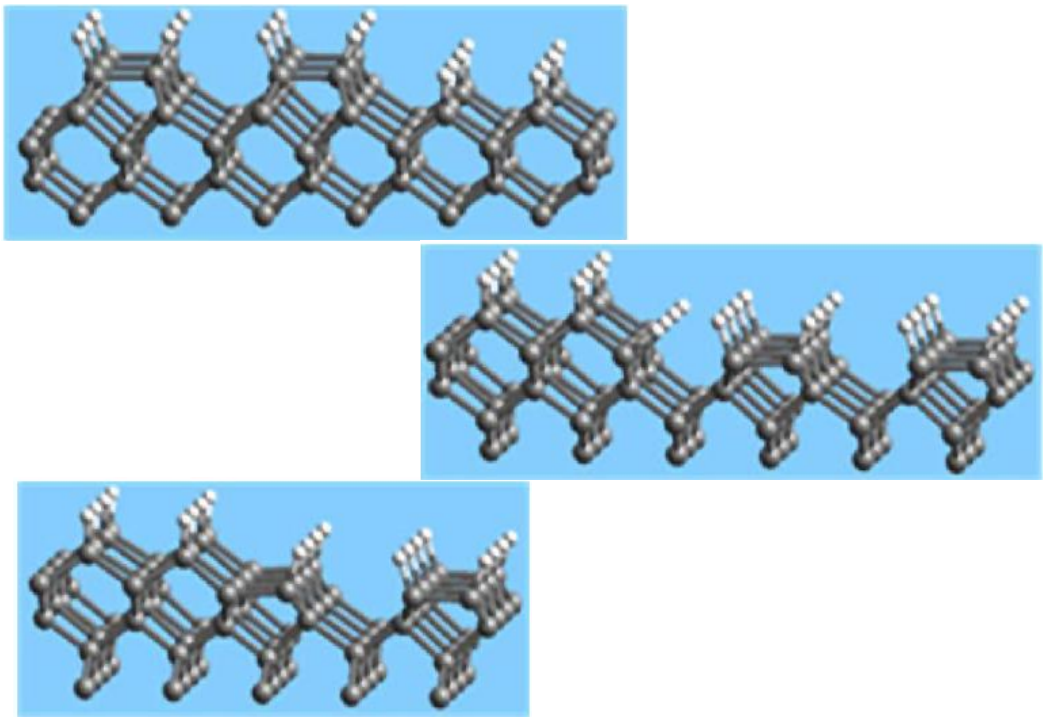

Figure 2.9 Schematic of (100) 2x1:H diamond surface and the different surface steps [122].

Theoretical models predict the monohydride-dimer bond length to be 1.60 Å [123,124] in agreement with measurements by dynamic low energy electron diffraction (LEED). Vibrational modes of C-H dimer rows have been observed by FTIR at 2919 cm^{-1} for the asymmetric mode and 2899 cm^{-1} for the symmetric stretch modes. The values are in agreement with theory.

On ideal {111} diamond surfaces each carbon atom is bonded to three other neighbouring carbon atoms to form a network of hexagons. The diamond (111) surface reconstructs to domains of (2 x 1) unit cells upon annealing to the hydrogen desorption temperature of ~ 900^{o}C [125-127]. According to Pandey's chain model [128] the clean hydrogen-free surface is reordered in π-bonded chains. To date, the accepted view [125-127] of the of (111) hydrogen terminated diamond surface, shows a 1x1 surface reconstruction, where the surface dangling bonds are saturated with hydrogen atoms. A

simple model of C(111) 1x1:H surface consists of each carbon surface atom bonded to each hydrogen atom, as shown in Figure 2.10, with different types of surface steps. The surface C-H bond produces a sharp vibrational mode at 2832 cm^{-1}, as observed by FTIR [129-130].

The dimer rows produce an angle of 120^{o} to each other on the (111) surface. Steps with a height of 0.2 nm have been observed on the (111) diamond surface [129] which is in agreement with the theoretical value of a single bilayer step of 0.206 nm [126]. Other diamond planes have been observed macroscopically [32, 33], however due to their scarcity {110} and {113} diamond surfaces are not well characterised.

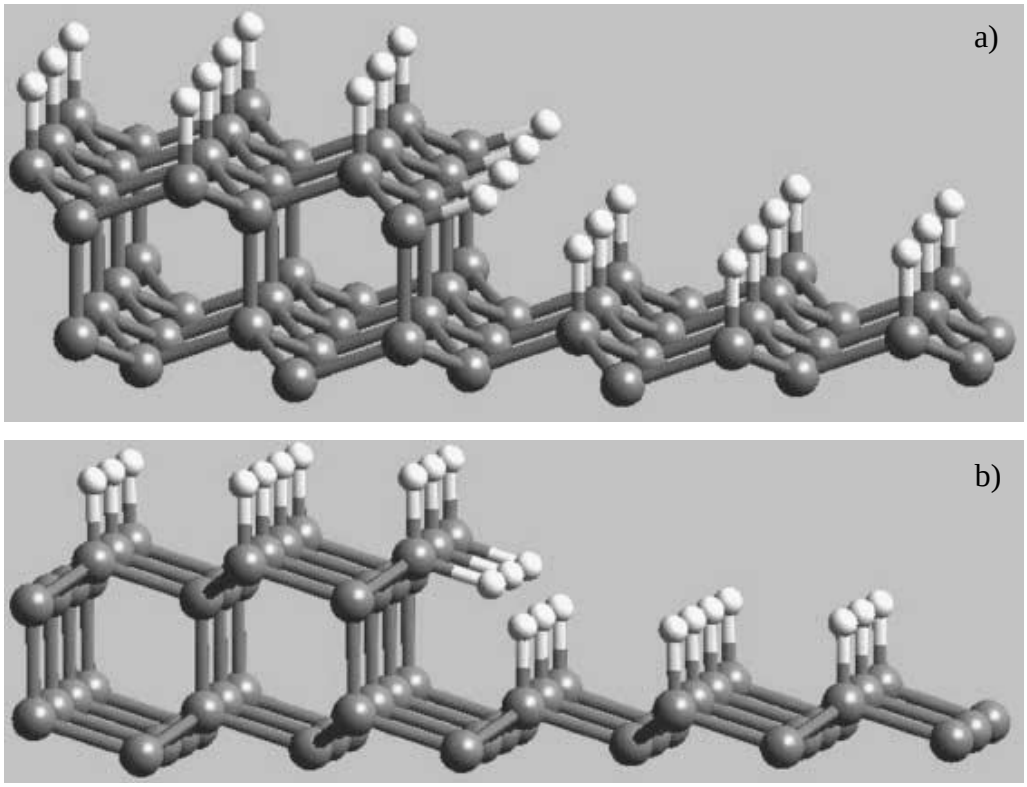

Figure 2.10 Schematic of the hydrogen terminated (111)(1x1) :H diamond surface, with representation of steps, a) a step edge with a local {110} like structure, and b) a step edge with a local {100} dihydride structure [131].

2.5.2 Diamond growth mechanism

The diamond growth mechanism, governed by surface chemical reactions, has been the subject of vast research, debate and controversy over the last 20 years. Plasma spectroscopic techniques of CVD diamond growth indicated the importance of the methyl radical and acetylene as the dominant precursor species. The presence of other

hydrocarbon radicals, C and C_2 show lesser concentration inside the plasma therefore their importance on CVD diamond growth was assumed to be negligible. Based on those experimental observations, different macroscopic mechanisms have been proposed for the CVD diamond growth. Methyl, CH_3, [112,132], acetylene (C_2H_2) [133-137] or both radicals have been considered as the dominant precursor species leading to diamond growth.

Growth on the {100} surface

Many growth models consider a (100):H 2x1 reconstructed diamond surface, and incorporation of CH_3 radical into the growing surface [137]. Growth is initiated by hydrogen abstraction from one of the C-H dimer bonds and the creation of a surface radical. The radical site on the (100) surface will undergo addition of methyl radicals following diffusion from the gas-phase towards the diamond surface, as shown in steps 1-3 of Figure 2.11 [138]. The incorporation of the adsorbed methyl radical into the surface dimer bond is accompanied by an additional H abstraction and bond rearrangement, as shown in steps 4-6 of Figure 2.11. The addition of an H atom to the surface radical completes the process, as shown in steps 6-7 in the Figure 2.11. At the growth temperatures used during diamond CVD growth the inserted CH_2 may be unstable and different reaction pathways have been discussed in the literature for the removal/etching of CH_2 or CH_3 [125, 138].

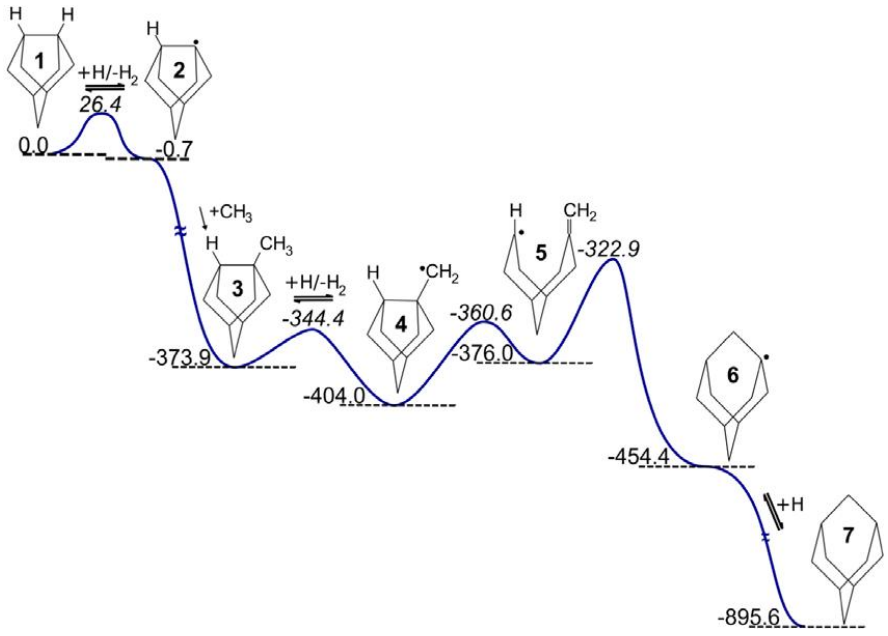

Figure 2.11 Reaction path for incorporating a CH_2 group into a C–C dimer bond, energies are quoted in units of kJ mol^{-1}. Reprinted from [140].

Incorporation of methyl radicals can also be feasible across the trough between two dimer rows. This mechanism has been proposed by Harris [132, 135] and further developed by Harris and Goodwin [140] including the Garrison *et al* [137] mechanism so-called GDSB. Two different reaction paths have been proposed for the incorporation of methylene across the trough between successive C-C dimers in a chain row. Figure 2.12 shows the two reaction paths; the steps 8 to 12 depicts the methyl addition to a surface radical followed by the formation of a surface radical by hydrogen abstraction. The reaction path is terminated by rearrangement to form the inserted methylene structure. Steps 8, 13 to 11 and 12, starts from a biradical site where methyl radical is incorporated into one radical site followed by hydrogen abstraction and the insertion of methylene between the two dimer rows. The analytical work by Cheesman *et al* [138], on bridging the trough in a dimer chain, concluded that the best site for CH_3 adsorption is adjacent to a dimer already bridged by CH_2.

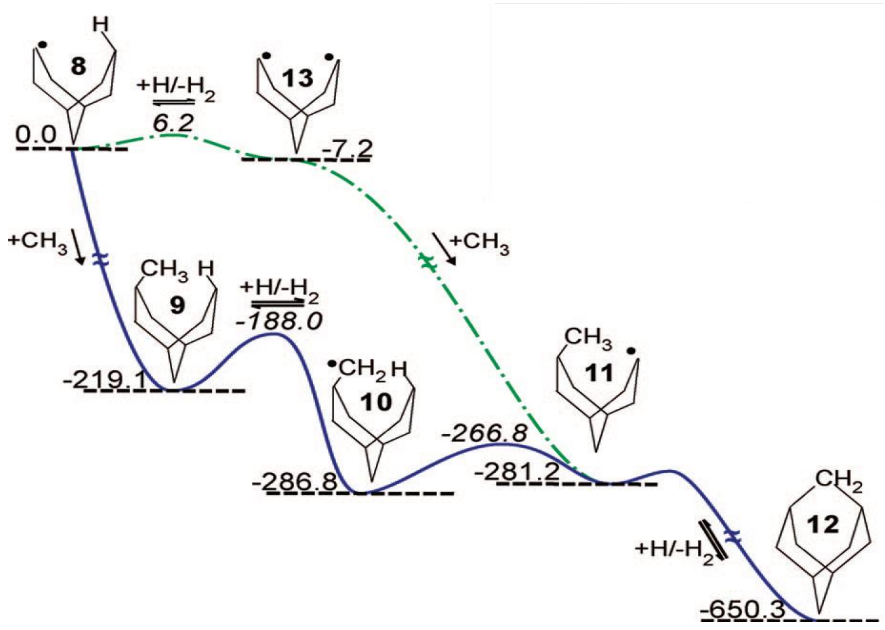

Figure 2.12 Reaction path(s) for incorporating a CH_2 group across the trough in a dimer chain that has one pre- and post-incorporated dimer as immediate neighbors [138]. Energies are quoted in units of kJ mol^{-1}

The reaction path from 10 to 11, shown in Figure 2.12, proposes feasible surface migration of radical sites between the surface dimer and an adjacent adsorbed CH_3 group. Frenklach *et al* [141, 142] suggested that surface migration is important for the growth of (100) diamond surfaces and assists in the growth of dimer rows and the ultimate formation of smooth surfaces. So far there is no direct experimental evidence on surface migration during CVD diamond growth. Empirical observations on single

crystal diamond growth under CVD growth conditions, support the diffusion (migration) of absorbed species to the edges of the surface steps, therefore promoting the formation of large crystal domains with very smooth surfaces [19,143]. But post growth treatment of (100) diamond surface in hydrogen plasmas also indicates that etching and migration processes take place simultaneously under CVD growth conditions. A very recent 1D Monte Carlo model of the CVD diamond growth mechanism developed by May and co-workers [144] managed to reproduced many surface structures observed empirical on (100) diamond surfaces. According to their model, adsorbed species on the surface can migrate along and across dimer rows, and their presence is essential for step growth and the formation of smooth surfaces. Growth rates would be predicted to reduce without surface migration, by the above mentioned model, and formation of rough and spiky diamond surfaces would be promoted.

A growth mechanism has been proposed by the addition of acetylene to the (100):H 2x1 diamond surface [133,145], as shown in Figure 2.13. Methyl and acetylene radical species have been proposed as dominant precursor species for few diamond growth models [125, 146].

Recent macroscopic growth models [147] on CVD diamond growth promote the view that hydrocarbons with 2 or more carbons, such as C_xH_y ($x \geq 2$) cannot contribute to the growth of the diamond surface. Due to the β-scission reactions the concentration of those carbon species is low both in the gas phase and in the growing diamond surface. The β-scission reaction process stops the formation of polymer chains on the growing diamond surface, as shown in Figure 2.14. Carbon groups such as C_2H_2 and C_2H_4 can be removed from surface-adsorbed hydrocarbon species containing two or more carbon by the abstraction of a terminal hydrogen atom followed by rearrangement to break the C-C bond to the terminal H and to release the gaseous C_2H_2 or C_2H_4 species.

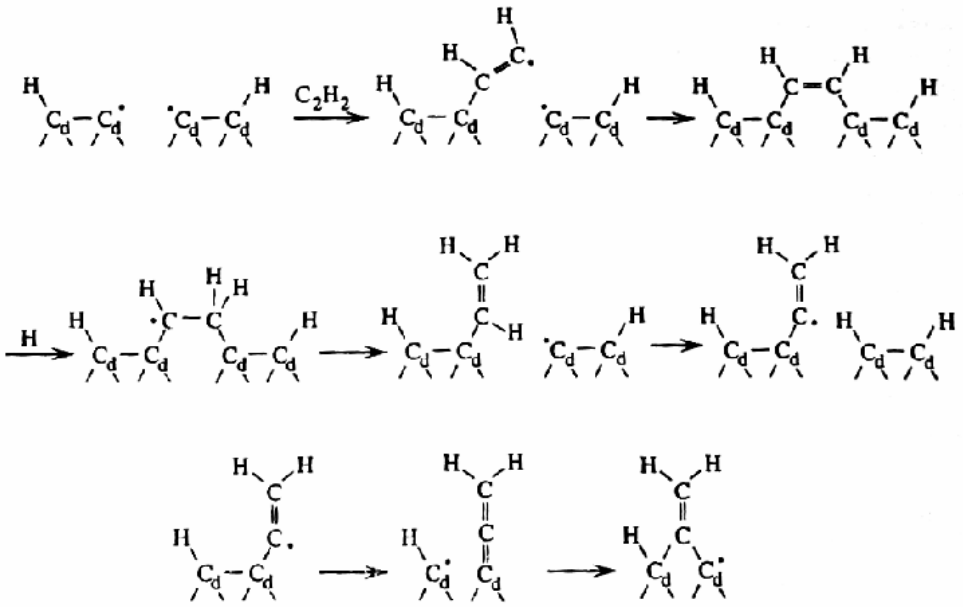

Figure 2.13 Diamond growth mechanism proposed by Skokov, Weimer and Frenklach for the addition of acetylene onto the (100):H 2x1 surface [145].

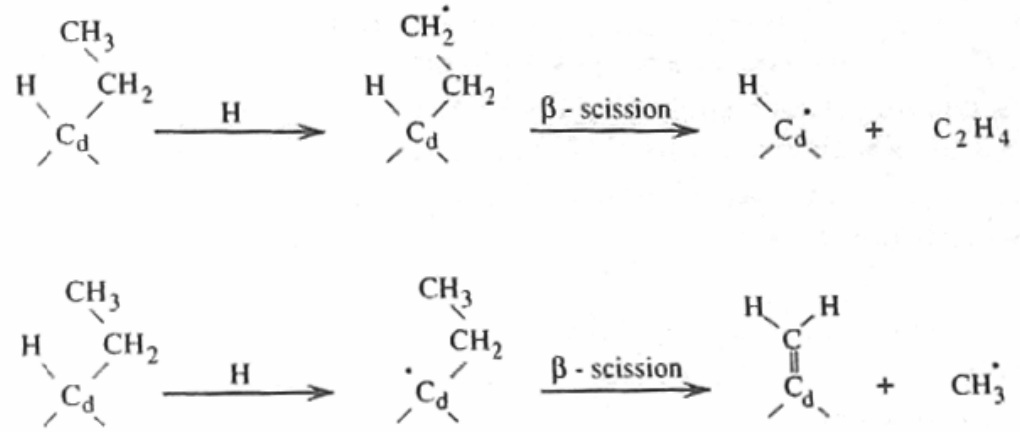

Figure 2.14 The removal of surface ethyl group by β-scission process [147].

The size of crystallites on polycrystalline CVD diamond films has been found to depend strongly on the ratio between CH_4 and H in the gas mixture. In this manner diamond films with crystallite sizes ranging from several microns have been grown as well as crystallites in the order of few nanometers. Contrary to the growth models which consider methyl as the dominant precursor for the growth process, work conducted by May *et al* [148-151] involved the competitive growth by all the C_1 radical species that could be present in the gas mixture in the vicinity of the growing (100) diamond surface.

Hydrogen abstraction on the (100) 2x1 reconstructed surface forms two types of surface radical sites, as is shown in Figure 2.15: monoradical sites which exhibit a single dangling bond on a surface carbon atom, and biradical sites, where two surface radical sites have been formed on adjacent carbons. The occurrence of radical sites strongly depends on the local surface geometry. According to the developed model, methyl radicals are still the major growth precursor, which can add to biradical sites, terminating and stabilising the surface dangling bonds.

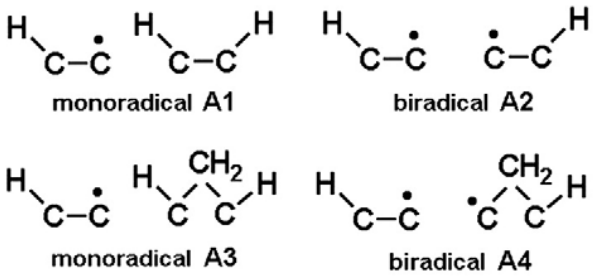

Figure 2.15 Radical sites on (100) diamond surface during CVD growth. The labelling of the sites is in accordance with the scheme of Skokov *et al* [145].

When radicals such CH and C are incorporated onto surface radical sites, they can be added to both biradical and monoradical sites, as they create less steric repulsion. After addition to surface radical sites they remain highly active, as they still contain dangling bonds. The fate of the added CH and C species have been investigated, as well as the importance of surface migration of CH_2 (induced by H abstraction) on the grown (100) diamond surface [150, 151].

In summary the proposed model suggest that the relative concentration of [H] and [CH_3] species at the growing surface, depends on the process conditions which, in turn, strongly affects the growth rate, morphology and crystal size of the diamond film.

Growth on the diamond {111} surface

The microscopic {111} diamond surface, as observed on many occasions, is rough and contains many steps, terraces and kinks. In comparison with the {100} diamond surface growth on the {111} plane is much faster and occurs via a more complicated process.
In contrast to (100):H 2x1 diamond surface, the (111):H 1x1 surface has not been investigated to the same level and, on the microscopic level, the growth mechanism is less well understood.

Microscopic growth models, starting with (111) 1x1:H surface, have proposed a mechanism in which CH_3 addition to the growing {111} surface occurs up to a monolayer coverage to which CH_3 is finally added to form a new layer [152]. Models adopting CH_3 radicals predict very slow growth rates for the (111) diamond surface via layer nucleation. Models incorporating CH_x radicals into the lateral growth of the (111) diamond surface have been successful by modelling step edges and kinks [153-155] producing a step-flow process for monolayer growth [156]. Recently Butler and Oleynik [131] investigated the plausible growth sequence for the nucleation of the next layer of growth on a diamond (111) surface and more specifically they examined the formation of commonly observed twins on those diamond surfaces. The models consider C_2H_y species as a way to avoid the complications of CH_y additions. Comparable growth rates have been produced by the addition of the species into the growth [125, 156]. So far no mechanism has predicted the high surface roughness of the as-grown {111} diamond surface.

2.5.3 Textured diamond growth

Textured diamond growth is characterised "*by the evolutionary selection of specific crystallite orientation*" [157]. Thus the resulted film surface is terminated predominantly by one type of facet. The plane with the direction of slowest growth perpendicular to the surface dominates the morphology as modelled by Van der Drift [158].

The crystal structure can be described in terms of the relative rates of growth orthogonal to {100} and {111} diamond surfaces. The α growth parameter introduced by Wild *et al*. [159, 160] describes the crystal by means of k_{100} and k_{111} the growth rates of {100} and {111} diamond faces respectively and can be measured by the relative sizes of the crystal facets. According to the α parameter various crystal shapes can be created, as shown in Figure 2.16.

$$\alpha = \frac{k_{100}}{k_{111}}\sqrt{3}$$

The α parameter, describes the relative growth rates and the resulting diamond crystallite shape.

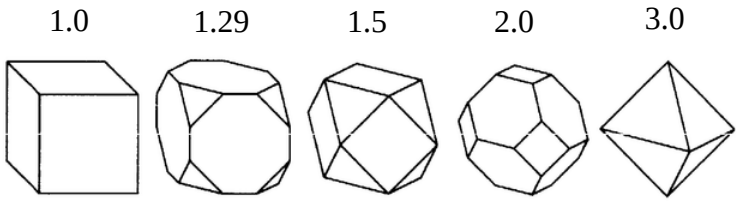

Figure 2.16 Idiomorphic crystal shapes for different values of the growth parameter α [161].

The reaction rate at each low index plane is different; therefore depending on experimental conditions the reaction rates for each plane can be enhanced or retarded. The relative growth rates determine the morphology of the growth diamond surface. The knowledge of the reaction mechanism on the low-index planes of diamond is vital for the understanding of the diamond nucleation and growth, since it is believed that the rate-limiting processes are generally thought to occur on sites associated with these particular surfaces.

2.6 Oriented {100} diamond growth

Diamond crystallites can be grown with defined crystallographic surfaces by controlling the growth parameters. Those crystallites can be randomly oriented about the azimuthal axis or aligned with the silicon crystallographic axes. Those films result in high angle grain boundaries which affect the mechanical, electrical and structural properties of the films.

Nucleation is the initial step for diamond heteroepitaxy. The nucleation density and rate are crucial issues for the deposition of diamond films. A common diamond nucleation method is to abrade the substrate material, producing high energy pits and scratches in the substrate that will act as diamond nucleation centers. Despite being the most common nucleation process it is not applicable to substrates with complex geometries or when attempting to grow heteroepitaxial smooth surfaces. Most commonly the substrate is abraded or scratched with fine (~ 1μm) industrial diamond paste or particles. Abrading substrates with diamond paste or particles produce high nucleation density, as the diamond particles scratch the substrate and are embedded in the near surface acting as seed crystals for the nucleation. A follow-up treatment for the scratched surface is the ultrasonic vibration with an abrasive paste in methanol or

acetone. It had been observed that such films exhibit better uniformity and higher nucleation densities ($10^7 – 10^{11}$ cm^{-2}) [161].

The nucleation route would create randomly oriented nucleation centers which will grow into randomly oriented diamond crystallites and be inimical to heteroepitaxy. Biasing pretreatment of the substrate has been introduced in order to increase the diamond nucleation density [162, 163]. This nucleation route is referred as bias enhanced nucleation (BEN) and is commonly applied to both microwave and thermal CVD systems.

By selecting the right gas phase growth mixture, substrate, BEN, suitable pre-treatment and the correct plasma conditions it is feasible to deposit diamond crystallites that are locally epitaxially aligned to the underlying substrate [164]

The mechanism of diamond nucleation enhancement by BEN has been controversial. It is widely accepted that the application of bias between the substrate and the plasma, causes the movement of the plasma closer to the substrate, allowing gaseous ions to be accelerated towards the substrate and subsequent implantation into the near surface. The plasma chemistry of the system may be altered during the BEN procedure by the removal of those positive ions (the substrate is normally negatively biased) or/and movement of them closer to the substrate. The changes caused by BEN on the growth process are not completely understood.

Early observations show the formation of a layer of β-SiC [165] on silicon substrates, which was confirmed by infrared spectroscopy [166] and TEM measurements [167]. The formation of a β-SiC layer between the silicon and the diamond may to be necessary to reduce the lattice mismatch between the two materials. Theoretical calculations and TEM observations support another model of diamond growth onto silicon without an intermediate β-SiC layer.

When bias is applied to MPCVD systems the plasma ball is shaped and deforms, as in the case for the MPECVD system at Heriot Watt University. On the application of the bias a planar ring appears around the base of the ball plasma and the whole plasma moves closer to the substrate. It seems that the area where the plasma deforms corresponds to the area of localised epitaxy. Using a DC voltage of -320 volts and

biasing for few minutes to the point where the bias current begins to increase is necessary to achieve the highest nucleation density.

Chapter 3. CVD diamond growth

3.1 The CVD growth system

All the chemical vapour deposition (CVD) diamond thin films that have been used in these studies have been grown using an ultra-high vacuum (UHV) microwave plasma chemical vapour deposition (MPCVD) system that has been designed and built-in house at Heriot-Watt University [168].

Heriot-Watt's MPCVD system has the following important design specifications:

- Free standing plasma in order to avoid sputtering of substrate or chamber materials.
- Low base pressure system ($< 10^{-8}$ mbar) for high purity growth.
- Operating pressure of 10-100 mbar.
- The system is controlled via a computer for continuous unattended running and prevents user errors.
- Substrate heating temperatures up to 1000^{o}C.
- The deposition parameters can be controlled independently.
- The substrate is electrically isolated and enables bias enhanced nucleation.
- Incorporation of mass spectrometer for *in-situ* gas and vacuum analysis.
- Separate load-lock facility that enable the load or removal of the sample without venting the main chamber to atmospheric pressure and avoiding any nitrogen ingress.
- Viewing windows for *in-situ* optical measurements of the plasma and the substrate conditions.
- Capability to accept substrates up to 100 mm in diameter.

The MPCVD system comprises two main sections: the actual growth chamber and a load-lock for sample entry/removal. The load-lock section of the system minimises any intrusion of nitrogen during the growth process and any atmospheric contamination of the growth chamber. Figure 3.1 shows the actual system whilst a schematic representation is shown in Figure 3.2.

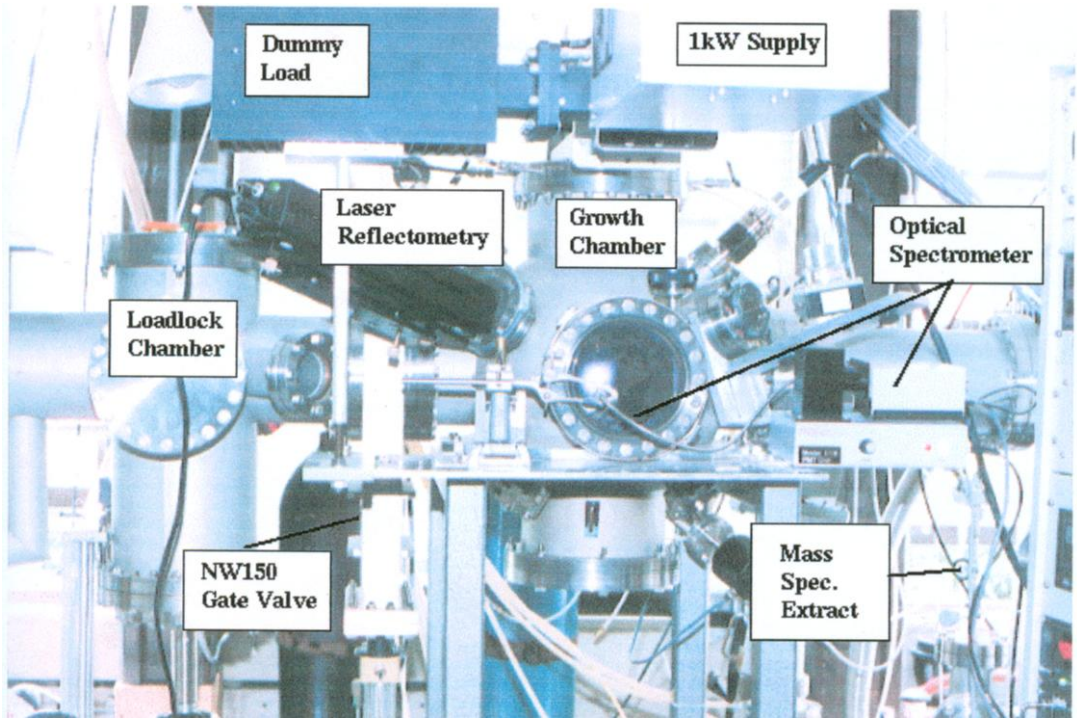

Figure 3.1 The 1kW MPCVD growth system at Heriot-Watt University.

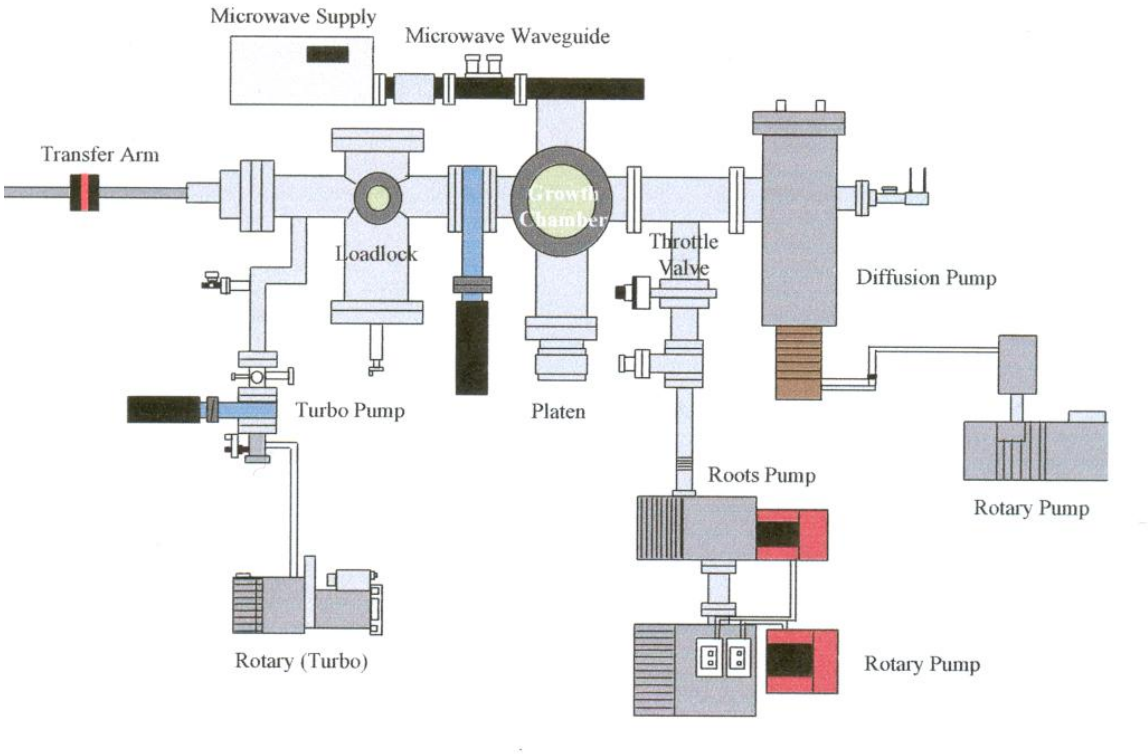

Figure 3.2 Schematic diagram of the 1kW MPCVD growth system.

The two stainless steel vacuum chambers of the system are connected through a gate valve, the growth and the load-lock chambers, which are sealed with UHV grade copper gaskets. The growth chamber is constructed from a 380 mm (15 in.) diameter stainless steel sphere (Leisk Engineering/VSW). It has 16 ports in total, for viewing, for *in-situ* monitoring, gas inlets, for the heater, for the microwave applicator, vacuum gauges, pumping port and the gate valve. The growth chamber volume is ~40 litres and behaves as a stirred flow reactor. There are two pressure regimes in which the chamber operates. During sample transfer and between experiments it operates at a base vacuum pressure of $< 10^{-8}$ mbar. During deposition experiments the pressure was varied up to 100 mbar by the introduction of reagent gases.

The entrance of the load-lock and the water cooled quartz window, through which the microwave radiation propagates into the chamber, are sealed with viton O-rings.

A liquid nitrogen trapped oil diffusion pump (Edwards EO4), with a pumping speed of 600 l s^{-1}, is used to pump the main growth chamber to base pressure of more than 10^{-8} mbar. The diffusion pump is backed by a rotary pump (Edwards EDM124), with a pumping speed of 14.6 m^3 hr^{-1}. The growth chamber can be isolated from the diffusion pump by a computer controlled gate valve. The system pumps are fitted with a nitrogen purge to their ballast valves and / or exhaust lines to dilute any potential explosive gases below their explosion limits before they come into contact with air. The growth chamber pressure, in the 10^{-4}-10^{-11} mbar range, is monitored using a UHV trigger Penning gauge (Leisk), while the diffusion pump backing pressure is monitored with a Pirani gauge (Edwards PRH10).

The operation and safety of the system is controlled from a Hewlett Packard computer using HP basic software developed in-house. Microlink units are used to connect the pc to the pressure gauges, the gas mass flow controllers, the vacuum valves, most of the pumps and the microwave power supply. For safe system operation the substrate transfer arm, water flows, chamber pressure and exhaust gas hood are all interlocked with the computer.

The samples were placed on a molybdenum holder on the top of the heater platen. The heating element is a serpentine graphite resistor powered by an 8 kW low voltage power supply. To provide vacuum integrity between the chamber and the heater, but also to ensure that neither the plasma nor the gases in the chamber are in contact with the heating element, the heater is fully encapsulated in a stainless steel and molybdenum platen. The heater element is fully purged with argon before heating to ensure that degradation or oxidation of the graphite elements does not occur. Water cooling is provided to the two electrodes, the bottom flange and to the stainless steel casing component of the platen.

The heater can be controlled by setting up the percentage of the transformer output power. This can be set to a specific value, ramped from one value to another or cycled between two values. For control purposes the temperature of the heater is measured by a thermocouple which is located within the body of the heater. It should be noted that this measured temperature is not the actual surface temperature of the substrate. The temperature of the sample and the heater could be measured during the experiments using a (Micron 3003) two–wavelength pyrometer operating in 1.17 and 1.25 μm range. The platen, where the sample placed, is electrically isolated from the chamber by a ceramic break allowing a bias-voltage to be applied between the chamber and the sample platen.

The microwave system comprises a 1 kW magnetron producing 2.45 GHz radiation from an RFA switch mode power supply, a circulator, a dummy load, motor driven tuning stubs and an antenna which feeds the microwaves from the rectangular waveguide into a circular microwave applicator. The design and the construction of the applicator was carried out at Heriot-Watt University. The applicator is fitted with a water-cooled quartz window which is sealed with Viton O-rings to maintain the vacuum integrity between the reaction chamber and the rest of the microwave system.

A perforated stainless steel extension is fitted below the window, extending down towards the substrate, allowing the cavity to extend into the chamber. This encourages a stable plasma ball to form at the end of the cavity extension just above the substrate surface, but still allows for optical monitoring of the plasma. It is also possible to obtain a stable plasma ball in the centre of the chamber even with the heater and platen completely removed and the lower port blocked off. For safety reasons, the microwave

waveguides are flushed with nitrogen so that, in the event of failure of the quartz window, nitrogen would flood into the hydrogen filled chamber rather than air. The windows are screened with fine metallic mesh to prevent microwave leakage into the laboratory.

The samples are introduced into the growth chamber via the load-lock. The main section of the load-lock is an extended six-way cross, which has four 150 mm internal diameter ports. One supports an x-y translation stage with a linear motion transfer arm and one providing access to the main chamber. The other two are blocked off to allow for future expansion. There are two 200 mm diameter flanges, the top to provide sample access and has a viton L-rubber seal, the bottom one is fitted with a bellows-sealed linear motion system for moving samples up and down. In addition the six-way cross is fitted with two viewports to ease the sample loading and transfer. The top flange is fitted with a Viton O-ring sealed fused quartz window. One pumping line leads from the load-lock to a smaller six-way cross. This cross is fitted with four ports, to which two pressure gauges and an inlet, where argon is used to vent the system, are connected. The load-lock chamber is pumped using a turbo-molecular pump (Balzers TPU050) to a pressure of around 10^{-7} mbar backed by an Edwards E2M2 rotary pump (with pumping speeds of 50 L s^{-1} and 2.8 m^3 hr^{-1} respectively) via a computer controlled gate valve. The pumps are fitted with a nitrogen purge to the exhaust lines, so that if the main chamber valves or pumps fail, the reactant gases can be pumped away safely through the load-lock. The pressure is monitored in the load-lock by a combination of an Edwards (PRH10) Pirani and a Penning (CP25K) gauge. The two gauges monitor the 10^{3}-10^{-3} mbar and 10^{-2}-10^{-7} mbar ranges, respectively. Argon is used to vent the system in order to minimise the amount of oxygen, nitrogen and water vapour entering the system. A cassette mechanism is incorporated within the load-lock which has four positions for circular molybdenum 4" diameter sample holders, minimising the number of times the system has to be opened to the atmosphere. The samples are transferred to the growth chamber by a magnetically coupled transfer arm fitted with a fork which locates slots in the molybdenum holders. The system is controlled through a pc that allows the automated venting and pump-down sequences.

The pc controller is a 20 MHz Hewlett Packard series 9000, model 340, which is connected to several input/output units which allow controls and monitoring of most of the system's components. The pc program is written in HP Basic. To summarize the program performs the following main functions:

- Remote operation of all the valves and most pumping groups
- Control of gas flows via a mass flow controllers
- Remote control of the heater platen
- Elaborate checks to prevent operator error
- Pressure monitoring for leaks
- Mass spectrometer operation and data collection
- On screen display of the system status
- Automatic shutdown in case of system failure

Relatively high pressures and flow rates are used during deposition and this is achieved using mechanical/Roots pump (Edwards) combined with an automated throttle valve (MKS). The process gases are admitted into the growth chamber via mass flow controllers and computer-controlled pneumatic valves. Two types of mass flow controllers are used:

a) MKS (model 2259B) for CO (0-10 sccm), CH_4 (0-10 sccm) and H_2 (0-1000 sccm)
b) Brooks (model 5850TR) flow- meter for Ar (0-100 sccm) and O_2 (0-10 sccm).

In each case there is an absolute on/off valve fitted immediately downstream of the flow controller. These flow controllers are connected to two corresponding units which act as power supplies, readout and control units.

a) An MKS 247C 4-Channel readout unit and
b) A Brooks 5876 dual channel unit.

As has been mentioned previously, the important design specifications of the MPCVD system allowed control of the flow rates of the process gases and the growth chamber pressure. To achieve this, the output from a Baratron gauge is used to control a throttle valve controller (MKS 5252A) connected to an (MKS type 253-A) sealing butterfly

throttling valve on the chamber pump line. The Edwards gauges are powered by and read via a Leisk (VC50 UHV) Penning controller and the Baratrons by an MKS PDR-C2C readout unit. Chamber pressures were measured using Penning gauges (MKS and Edwards) and capacitance manometers (MKS).

Safety features have been incorporated into the hardware and into the pc software in order to avoid user error and equipment failures. For example, in the event of a main power failure, the pc is reset and the power is lost from all the electrically operated valves which are arranged so as to shut off all gas flows and close all the gate valves. Power is also lost from the heater, so the sample is cools down safely and at the same time the plasma is extinguished. When the power returns the pc software does not automatically restart, so there is no gas flow, no valves opens and the heater element remains off. At the same time an interlock ensures that the microwave power supply remains off. As described above there are also safety features in the case of cooling water failure and fume cupboard failure.

3.2 CVD diamond films growth details

3.2.1 Substrate preparation

The CVD diamond thin films have been grown on single crystal silicon wafer substrates (Compart) during these studies. Prior to any growth experiment the silicon substrates were subjected to a cleaning procedure in order to remove both organic and inorganic contamination. The properties of the silicon substrates are summarised in Table.3-1 as provided by the manufacturer.

Diameter / mm	100
Crystallographic Orientation	(100)
Thickness / μm	525
Surface finish	Mirror polished in one side
Dopant	Boron (p-type)
Resistivity / Ω cm	1 - 20

Table 3-1 Properties of silicon wafers used in CVD diamond thin film growth.

The cleaning procedure of the silicon wafers prior to any CVD diamond thin film growth consisted of the following steps:

- Ultrasonic agitation of the wafer, in a glass beaker with 400 ml of acetone (Fisher, reagent grade) for 5 min,
- followed by ultrasonic agitation of the wafer, in a glass beaker with 400 ml of methanol (Fisher, reagent grade) for 5 min.
- Ultrasonic agitation of the wafer, in a glass beaker with 1 L of deionised water (>15 Ω cm) and three drops of a proprietary cleaning agent, (Decon 90), for 10 min.
- Further 10 min of ultrasonic agitation of the wafer, in a glass beaker with fresh 1 L of deionised water without the Decon solution.
- Finally 10 min of ultrasonic agitation of the wafer, placed in a glass beaker with 1 L of deionised water.
- The wafer was removed from the baker with clean stainless steel tweezers and drying it under a stream of filtered oxygen free nitrogen (BOC, 99.9 %) at 5 bar.
- The complete dried wafer was stored in a clean fluoroware box.

The effectiveness of the above mentioned cleaning sequence has been verified using laser ionisation microprobe analysis (LIMA), prior to and after the procedure.

3.2.2 The diamond growth procedure

For a CVD diamond thin film growth experiment, the silicon wafer was transferred to a molybdenum boat in the load-lock of the 1 kW CVD kit. The load-lock was evacuated to a vacuum of around 10^{-6} to 10^{-7} mbar using a turbomolecular and rotary pump. At that stage the diffusion pump valve was closed, isolating the main chamber and the load-lock gate valve was opened. The molybdenum boat and the wafer were transferred to the platen using the magnetically driven transfer arm. After placing the molybdenum boat and wafer on the platen (substrate heater), the transfer arm was withdrawn from the main chamber and the load-lock gate valve was closed.

The main chamber was pumped, by opening the diffusion pump gate, to a stable pressure value of 10^{-7} to 10^{-8} mbar. Then the main chamber was isolated again by closing the diffusion pump gate valve. Hydrogen gas (Linde, 99.999%) was used to fill

the main chamber to a pressure of ~ 20 Torr. The platen (substrate heater) was then set to ramp up to the desired power setting, typically ramping at 0.5 % full power per minute.

The growth/deposition of the (100) highly oriented CVD diamond thin films on silicon substrates consists of the following stages:

- Hydrogen plasma etching.
- Pre-carburisation.
- Bias enhanced nucleation.
- (100) textured growth.
- Hydrogen plasma termination.

For each of the above stages the process conditions are summarised in Table 3-2. After the desired substrate temperature was achieved and stabilised, the main chamber pressure was reduced to 20 Torr using the by-pass line and hydrogen gas flow was introduced into the chamber, usually using a gas flow of 500 sccm.

Stage	Bias/ V	Gas Flow Rate / sccm			Temperature/ °C	Power/ W	Pressure/ Torr	Time/ hr
		H_2	CH_4	CO				
H_2 - Clean	0	500	0	0	840	500	35	0.5
Pre-Carburisation	0	300	6	0	840	500	35	3
Bias Enhanced Nucleation	-320	300	6	0	800	220	20.7	0.3
Textured Growth	0	85	2	70	730	800	36	20-70
H-Termination	0	500	0	0	730	800	36	1

Table 3-2 Process conditions for CVD (100) highly oriented CVD diamond thin films growth.

As the main chamber pressure was stabilised the microwave power was then increased gradually until the plasma was ignited, usually below 300 W. When the plasma was not initiated at >220 W of applied microwave power, a change of the electrical field caused by the movement of the mechanical shutter protecting the front window of the chamber, enabled the plasma to be ignited.

Gas	Purity / %	Impurities / ppm				
		H_2O	C_xH_n	N_2	O_2	Ar
H_2	**99.999**	**2**	**0.3**	**3**	**1**	**-**
CH_4	**99.995**	**3**	**12**	**5**	**1**	**-**
CO	**99.997**	**8**	**1**	**8**	**2**	**2**
Growth mixture	**---**	**<5**	**<1**	**<6**	**<2**	**<1**

Table 3-3 Gas purity and composition.

For each of the growth stages shown in Table 3-2, the desired pressure and microwave power were then gradually obtained at a rate of 2 Torr and 50 W per minute to minimise any thermal shock on the main chamber windows and substrate, thus avoiding any cracking of the chamber windows.

The platen (substrate heater) was grounded for all the growth stages except in the case of the bias enhanced nucleation (BEN) stage. The platen was electrical isolated from the main chamber during the BEN growth stage and a negative bias of -320 V D.C. was applied relative to the grounded chamber, while the current flow through the platen was recorded as a function of time. The diamond nucleation considered to occur at the point was the current flow through the platen rises sharply [164]. At that point the negative bias is turned off and the platen was again earthed.

The purity and composition of the gases that are used during the CVD diamond thin film growth experiments are shown in Table 3-3 as provided by the manufacturer.

The temperatures at each of the growth stages shown in Table 3-2, were recorded using a two-wavelength (1.17 μm and 1.25 μm) pyrometer (Micron 3003) focussed at the centre of the substrate through the main chamber quartz window at an angle of 70 degrees to the substrate normal.

3.3 Diamond sample cleaning procedure

The as-grown (100) CVD diamond thin films, before any further treatment or examination, were sliced into square samples of around 1cm x 1cm dimensions with the use of diamond pen or by laser machining. Due to the potential contamination that might arise from the cleaving method, a cleaning procedure was adopted to ensure the sliced surfaces were clean before any further analysis or experiment.

3.3.1 Solvent cleaning procedure

This cleaning procedure is similar to the procedure used for the cleaning of the silicon wafer before the diamond CVD growth synthesis and consisted of the following steps:

- Ultrasonic agitation of the diamond sample, in a glass beaker with 100 ml of acetone (Fisher, reagent grade) for 10 min,
- followed by ultrasonic agitation of the diamond sample, in a glass beaker with 100 ml of methanol (Fisher, reagent grade) for 10 min.
- Deionised water with three drops of Decon 90, has been used for further 10 min of ultrasonic agitation of the diamond sample in a glass beaker.
- Further 10 min of ultrasonic agitation of the diamond sample, in a glass beaker, in 100 mL deionised water without Decon solution.
- The diamond sample was removed from the beaker using clean stainless steel tweezers, while a stream of filtered oxygen free nitrogen (BOC, 99.9%) at 5 bar was use to dry the sample, before it was placed and stored into clean fluoroware box.

3.3.2 Acid cleaning procedure

This cleaning procedure was used in cases where the contamination of the diamond samples was not removed by the adaptation of the solvent cleaning procedure. The procedure consisted of the following steps:

- The diamond sample was placed into a glass beaker using stainless steel tweezers.
- A solution of 9:1 H_2SO_4 : HNO_3 was added to the samples in a glass beaker.
- The fluorinated polypropylene beaker was connected with a glass condenser.
- The heater element was set to the desired temperature.
- The acid solution was allowed to reach boiling point and boiled for 15 min.

- After the elapsed time of 15 min the heater element was turned off and the acid solution was allowed to cool down.
- The cooled acid solution was removed from the beaker before the diamond sample was removed using stainless steel tweezers.
- The diamond sample was subject to ultrasonic agitation for 10 min in 100 mL of deionised water.
- The diamond sample was removed from the beaker using clean stainless steel tweezers, while a stream of filtered oxygen free nitrogen (BOC, 99.9%) was use to dry the sample, before it was placed and stored into clean fluoroware box.

3.4 In situ analysis

The 1 kW MPCVD system, is equipped with an optical emission spectrometer and a quadrupole mass spectrometer to characterize the plasma as well as the chamber vacuum integrity respectively.

3.4.1 Optical Emission Spectroscopy

Optical emission spectroscopy (OES) is one of simplest and oldest methods to monitor plasma processes. A typical OES system comprises a monochromator, which generally is a diffraction grating, and a detector to monitor the light emitted from the plasma source. The emission of radiation from plasma was collected through a fibre-optic cable to the monochromator. The light was dispersed and recorded as a function of wavelength. The resolution of the system is determined largely by the resolution of the dispersing element of the monochromator. The OES system has limited spatial resolution and is typically a line of sight technique, although the collection of light could be further improved by the use of collection lenses. Optical emission spectroscopy (OES) measures the emission of light from the excited states of species within the plasma. The technique is useful due to its easy implementation and applicability for certain species.

The optical emission from the microwave plasma was monitored by a computer-controlled, grating-based, optical spectrum analyzer (Monolite 6800). The emission of the plasma was collected through a 50 mm diameter quartz lens to a fibre-optic cable which was connected to the input slit of the spectrometer. The analyser consists of a scanning grating monochromator, a PMT detector and a system controller interfaced to

a computer. The grating and the PMT are optimized to a bandwidth of 200-900 nm and system resolution of 0.7 nm. These parameters were used for monitoring the plasma composition while each spectrum collected from an average of 4000 scans to reduce the spectral noise level. The analyzer wavelength was calibrated using a HeNe laser before any measurement was taken.

3.4.2 Mass spectrometry

The 1kW growth system was equipped with a mass spectrometer placed downstream from the plasma region; the distance between the plasma and the sampling region is long and thus enables the analysis of residual gas or stable gas species in the growth chamber. Because of the relatively high chamber pressures of 10-100 mbar, the pressure is reduced by pumping the gas through a needle valve by a Balzers TPU050 turbomolecular pump backed by a Balzers Duo 1.5A rotary pump, with pumping speeds of 50 L s^{-1} and 1.8 m^3 hr^{-1} respectively. The mass spectrometer comprises a 1-100 amu quadrupole head with a corresponding VSW vacuum analysis controller. The system control is interfaced with the computer system software which provides data acquisition and analysis. The program has designed accordingly so the user can select the specific mass range or a series of masses with time or both.

3.4.3 Optical dual-wavelength pyrometry

As it was stated earlier the sample temperature was measured using an optical dual-wavelength pyrometrometer. This technique provides the ability to measure the surface temperature of any material of unknown emissivity. The temperature is determined by measuring the ratio of thermal energies at two infrared wavelength bands. The Micron model 3003 system used in these studies consists of a dual infrared detector head assembly equipped with a radiation chopper, electronic driver and preamplifier. The pyrometer operates at 1170 nm and 1250 nm, having a spot size of 0.38 cm diameter at a working distance of 30 cm and had a temperature resolution of $\geq$ 1%. The response time of the equipment is around 100 milliseconds. The calibration of the pyrometer was performed using a black body radiation source such as a stainless steel sample which has been heated in a tube furnace whose temperature is measured with a K type thermocouple. The pyrometer can then operate effectively within the temperature range

of 400^{o}C to 1000^{o}C, taking in consideration the absorption and the reflectivity of the chamber window.

3.5 Post growth analysis

The quality of the (100) CVD diamond films after successful growth were subject to the following characterisation techniques.

3.5.1 Optical microscopy

Diamond thin films have been examined using an optical microscope (Leica DMRM) at a 1000x magnification using white light in reflectance mode. The microscope was equipped with a three-color CCD camera which enabled the image to be captured on either a computer or on video printer. This enabled the examination the samples prior to further analysis, and to provide with information about the sample morphology and crystallographic habit.

3.5.2 Scanning electron microscopy (SEM)

The operation of SEM is based on scanning the surface of the material with electrons under high vacuum. The electron bombardment of the material will cause the emission of secondary electrons which consequently forms an image. A simple schematic diagram of the working principles of a SEM is given in Figure 3.3.

During these studies a Hitachi S-2700 SEM with a Princeton Gammatech detector and software has been used when high magnification images were required. Whilst diamond thin films are insulating materials; very good images can be obtained at 8 and 10 keV without the need for gold-coating the samples since diamond is an excellent secondary electron emitter.

A Philips XL30 Enviromental Scanning Electron Microscope (ESEM) located in the Institute of Petroleum Engineering at Heriot-Watt University has also been used. Occasionally a Hitachi S-4100 field emission SEM with an Oxford instruments ISIS EDX system with germanium detector located at the University of the West of Scotland,

Paisley, was employed when images of high magnification and additional features of the SEM were needed.

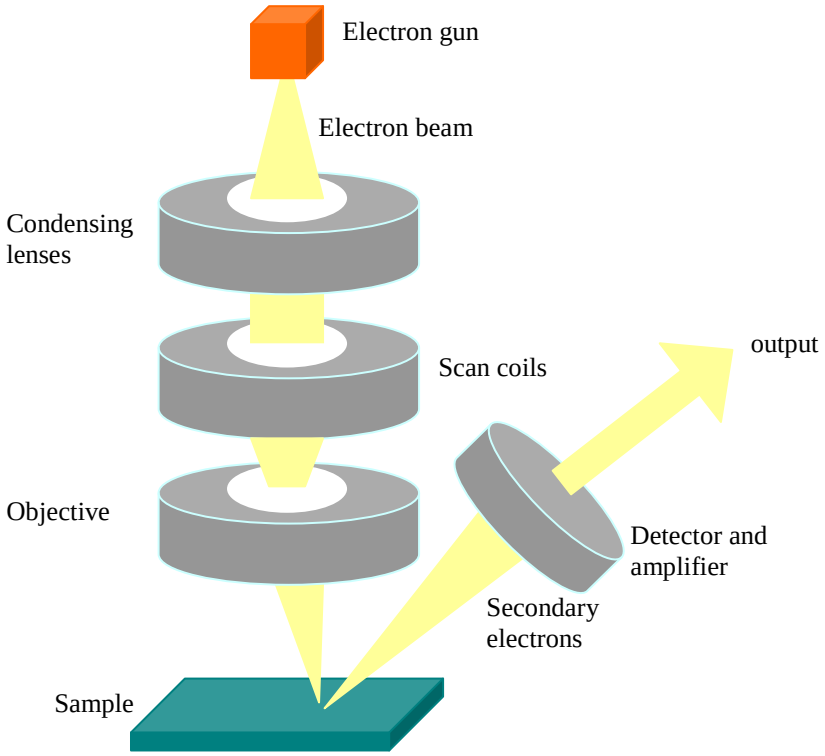

Figure 3.3 A simple schematic diagram of the SEM operation components. All the components were under high vacuum. The electron beam travels through the condensing lenses, scan coils and the objective lens before focusing on the sample surface. Emitted secondary electrons were collected by the detector and amplified before the output signal was generated.

These features include back scattering and energy dispersive X-Ray analysis (EDAX). The back scattering analysis uses another detector to measure the electron flux, while the output signal - the electrons that are back-scattered from the surface - is a measure of the different atomic masses within the materials being examined. The back-scattered images are composed of areas where relative high atomic masses produce an intense signal whereas areas with lower relative atomic masses produce signals which are less intense. The EDAX analysis is used for qualitative and quantitative chemical analysis of the chemical materials. The germanium detector of the ISIS EDX system is fitted with a window capable of transmitting low energy X-rays and able to detect all elements from boron to uranium.

3.5.3 *Atomic force microscopy*

Atomic force microscopy was used to examine the surfaces of diamond films when higher resolution images were required. Investigation of the surface roughness was also employed using the instruments software. A Topometrix Accurex scanning probe microscope was used in contact mode. A Dimension TM 3100 AFM has been used in tapping (non-contact) mode. Commonly used scanning probe microscopes contain the components illustrated in Figure. 3.4.

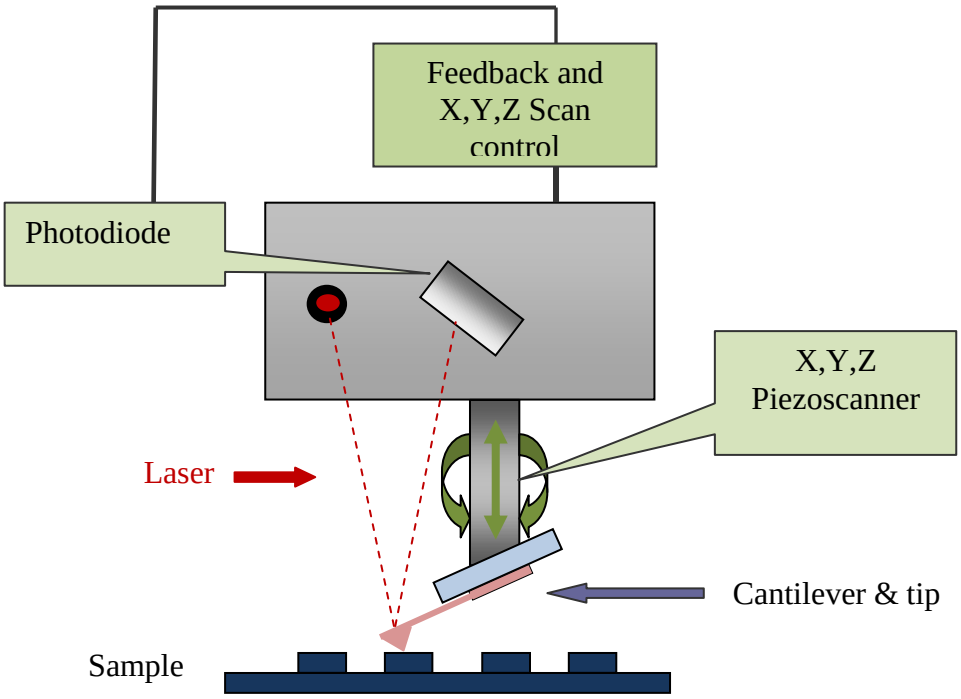

Figure 3.4 Schematic of a generalised AFM system. A cantilever is scanned over the sample surface either keeping a constant average distance between the tip and the sample or a constant resonant frequency. A photo-detector monitors any change on the laser beam reflected from the back of the cantilever.

An atomic force microscope probes the surface of a material with a sharp tip, which is located at the free end of a cantilever. As the tip approaches the sample surface, the forces between the tip and the sample surface cause the cantilever to bend or deflect. As the tip is scanned over the sample surface an optical detector measures the cantilever deflection. The measurements allow a computer to produce an image of the surface topography. The deflection of the cantilever from the sample surface is a result of several forces that act between the cantilever and the sample surface. There are two regimes where the AFM operates, contact mode and tapping (non-contact) mode.

When the AFM operates in contact mode the cantilever tip is in physical contact with the sample. Usually the spacing between the cantilever and the surface is few Å. As the scanner traces the tip across the samples surface the contact force causes the cantilever to bend to accommodate changes in surface topography. Optical techniques are often employed on AFM to detect the position of cantilever. A position-sensitive photodetector (PSPD) is used to measure the laser beam reflected off the back of the cantilever. Topographic data of the samples surface can be produced by the detection of the cantilever deflection.

During the tapping (non-contact) mode the cantilever vibrates near the surface of the sample. The distance between the cantilever and the surface is ten to hundred Å. A stiff cantilever vibrates near its resonant frequency (100 – 400 kHz) with an amplitude of a few tens to hundreds of Å. The system monitors changes in the resonant frequency or vibrational amplitude as the tip scan near the sample surface and keeps it constant with the aid of a feedback system that moves the scanner up and down. By keeping the resonant frequency or amplitude constant, the system also keeps the average tip to sample surface distant constant. Using the same principle as in contact mode, the motion of the scanner is used to generate a data set.

3.5.4 Optical metrology

Optical surface metrology is a non-contact, non-destructive technique that enables surface texture and topography measurements of solid surfaces. The technique utilises a high resolution optical microscope for the projection of interference pattern on the selected area of the material/surface. A NewView series optical profilometer (Zygo) has been used for the 3D inteferometric metrology of the diamond thin films and diamond cubo-octahedral crystallites. The Zygo optical profilometer system provides wide lateral area measurement as well as subnanometer z image resolution. Its offers a fast, high accuracy, non-destructive, 3D metrology of surface features and it uses MetroPro^{TM} software for advanced data analysis.

3.5.5 Fourier transform infrared (FTIR) spectroscopy

Fourier transform infrared (FTIR) spectroscopy is a commonly used technique to analyse materials by measuring absorption in the infrared region of the spectrum. The optical set-up of the FTIR spectrometer is shown schematically in Figure 3.5, and the principle is based on a Michelson interferometer. A broadband beam of infrared frequencies is passed through a beam splitter, where it is divided into two optical beams. One beam reflects off a flat mirror which is fixed in place, while the other beam reflects off a flat movable mirror which moves very short distances (typically few millimeters) away from the beam splitter. The two beams recombine back at the beam splitter after they reflected off of their respective mirrors. Constructive or destructive interference will occur depending on the path length difference of the two beams. The resulting signal is called an interferogram and has the property that every single data point that comprises the signal has information about every infrared frequency which originates from the source. The analysis of the produced interferogram is accomplished by Fourier transformation. A computer is used for this transformation and the intensity versus frequency spectrum is then produced.

FTIR spectroscopy is an excellent tool for both qualitatative and quantitative analysis of a material. Since all frequencies are measured simultaneously an FTIR spectrum can be collected in few seconds. The high optical throughput of the equipment along with the use of sensitive sensors reduces of the noise level of the collected signal. The fast collection of data enables signal averaging which reduces the random measurement noise. It is a non-destructive technique, which provides very accurate measurements without the need for external calibration, since an internal HeNe laser is used as a wavelength calibration standard. From a mechanical point of view it is simple equipment, with only one moving part (movable mirror) therefore limiting the possibility of mechanical breakdown.

Infrared studies of diamond films were performed on a computer-controlled Nicolet 510P FTIR spectrometer. The equipment allows the collection of spectra in the region of 4000-400 cm^{-1} with minimum spectral resolution of 4 cm^{-1}. The sample chamber was purged with dry nitrogen prior to any measurement to eliminate absorption from water vapour and carbon dioxide. Before any measurement a background spectrum was collected from a piece of silicon substrate and background correction was applied to the spectrum of the sample.

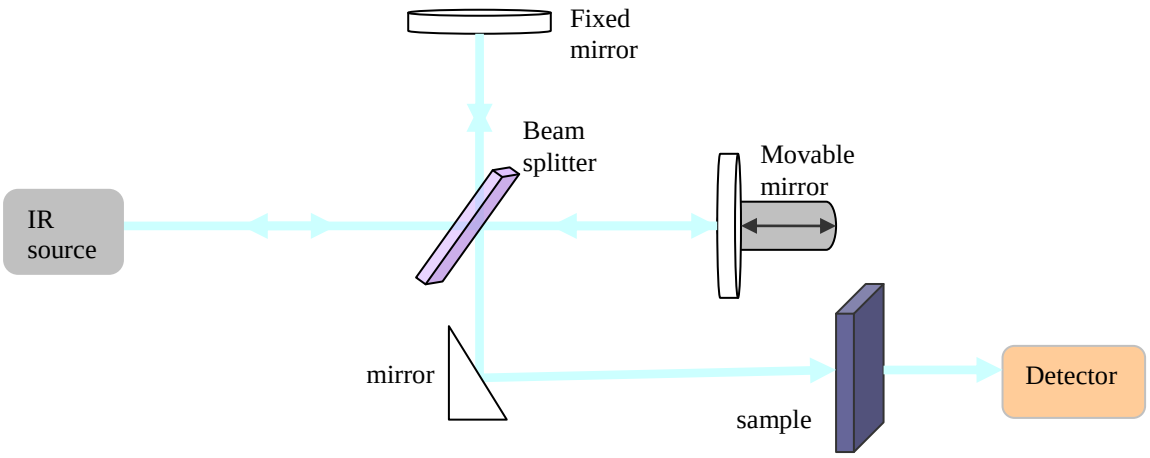

Figure 3.5 Schematic of the optical arrangement of the FTIR spectrometer. An infrared beam with a range of frequencies is directed at the beam splitter. The produced two beams recombine and produce an interferogram before passing through the specimen.

A Bruker 66v infrared spectrometer was also used for infrared studies of the diamond thin films. The spectrometer is equipped with a IRScopell microscope, used in the visible mode, to locate either the highly oriented region or the azimuthally disordered region on the diamond thin films samples or any other treated area of the sample. The IR spectra collected were averaged 32 times with a resolution of 4 cm^{-1}, using either the reflection and transmission mode. The background spectrum was collected for each mode using a piece of silicon wafer. Interference fringes caused by the overlap of the waves reflected from the air-diamond and substrate-diamond interfaces dominated the IR spectra. Since those fringes were out of phase in the reflectance and the transmittance mode, addition of the two spectra led to the removal of those features.

3.5.6 Laser Ionisation Microprobe Analysis

Laser ionisation microprobe analysis, (LIMA), was used to establish the elemental composition of the deposited diamond thin films. All analyses were performed using a Kratos Analytical 401L LIMA system that had been modified to incorporate a post-ionisation facility. In this technique a focused Nd:YAG laser (λ = 266 nm) pulse of 3 to 5 ns duration is used to ablate and ionise a portion of the sample surface with a spatial resolution of ca. 1 μm. The composition of the ionised plasma plume is then analysed by time-of-flight (ToF) mass spectrometry. All measurements were performed by

Edinburgh Surface Analysis Technology (ESAT) at Heriot-Watt University. The system has the capability of micron lateral resolution measurements with ppm sensitivity. LIMA analysis of diamond thin films had been performed to examine the contamination of the samples surface, after the cleaning procedure and growth.

3.5.7 X-Ray Diffraction

X-Ray diffraction (XRD) relies on the scattering of X-rays from a crystalline lattice. The electrons within the atoms in a solid will scatter a small proportion of the X-ray beam. A detector measures the angle at which the rays are diffracted. Using Bragg's law, Equation.3-1, it is possible to determine the atomic plane spacing (and thus unit cell dimension) and the crystallographic phases of the material.

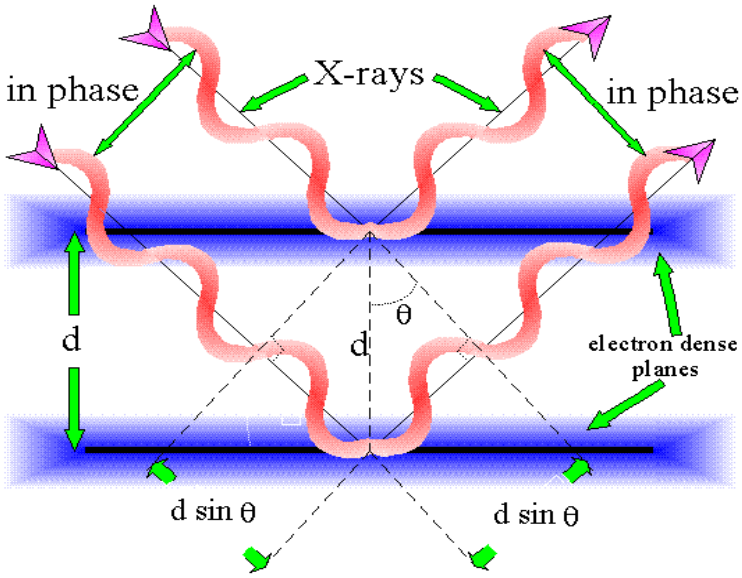

Figure 3.6 Schematic diagram of the general case of Bragg's law.

In theory, we assume that a parallel, monochromatic beam of X-Rays (of wavelength, λ) strikes a set of lattice planes with spacing of d_{hkl} and making a glancing angle θ with them. Bragg's law describes the diffraction of X-rays from a set of lattice planes with Miller indices, hkl, as:

$$\lambda = 2\, d_{hkl}\, \sin\theta \qquad \textbf{Equation 3-1}$$

where θ is the diffraction angle of the X-rays. In general the condition for a diffraction to occur shown schematically in Figure 3.6.

XRD was used to identify the presence of the diamond phase on silicon substrates. XRD also provided a way of checking whether the diamond surface has been graphitised or it has been affected by any applied treatments. It should be worth mentioned here that extended studies on the texture of CVD diamond films on silicon and other materials have been based on the evaluation of x-ray diffraction (XRD) pole figure measurements [169]. Due to the limitation of the X-ray diffractometer used, pole figure measurements have not been employed in these studies. Diffraction patterns of the diamond thin films were collected on a computer controlled Phillips PW 1730 powder X-Ray diffractometer using CuKa (1.541 nm) radiation thought the range of $30 < 2\theta / ^{o} < 100$. A Siemens/Bruker D500 incident X-Ray, power diffractometer, was equipped with a scintillation detector was able to record the 2θ angles and the corresponding d-spacing map, with each step of the detector. For this work, in the XRD analysis, each step size corresponded to a 2θ angle of 0.02^{o}. The computer data base then can be used to identify the matching peaks of the XRD analysis.

3.5.8 X-Ray Photoelectron Spectroscopy

X-ray photoelectron spectroscopy (XPS) utilises X-ray electromagnetic radiation to induce photoionisation of the core electrons of the samples atoms and analysis of the kinetic energy distribution of the emitted photoelectrons to study the composition of the near surface region of the sample. This technique is based on the principle of the photoelectric effect, where the photon is absorbed by an atom in a solid, leading to ionisation and the emission of a core (inner shell) electron with kinetic energy given as:

$$BE = h\nu - (E_{KE} - \Phi) \qquad \textbf{Equation 3-2}$$

where BE is the binding energy of the photoelectron referenced to the Fermi level of the solid, hν is the X-ray photon energy, E_{KE} is the kinetic energy of the photoelectron and Φ is the work function of the spectrometer. An electron energy analyser is used to measure the kinetic energy distribution of the emitted photo electrons and a photo electron spectrum can thus be recorded.

A Scienta ESCA300 spectrometer of the Central Laboratory of the Research Councils in Daresbury has been used for the XPS analysis of the diamond thin films. An overview of the instruments operation and important features is given below. All the spectra collected have been recorded using Al K_α (1486.7 eV) radiation that has been generated by electron bombardment of a water-cooled aluminum-covered titanium alloy disk rotating at 4000 rpm. Seven toroidally bent α-quartz (1010) crystals were used to monochromate the X-rays with a FWHM = 0.26 eV and focus the X-ray beam in a rectangular spot, (approximately 6 x 0.5 mm, at 45^o to the sample). A multi-element lens is used to collect the ejected electrons by the sample and focus them to a slit aperture (either 1.9 or 0.8 mm) at the entrance of a hemispherical electron analyser. Usually 5-element lens were used to collect spectra with high electron transmission but with poor spatial resolution. The addition of a 3 element lens between the sample and the main lens reduced the area under investigation and yielded a spatial resolution up to 25 μm. However the insertion of the lens decreased the electron through-put and the signal-to-noise ratio.

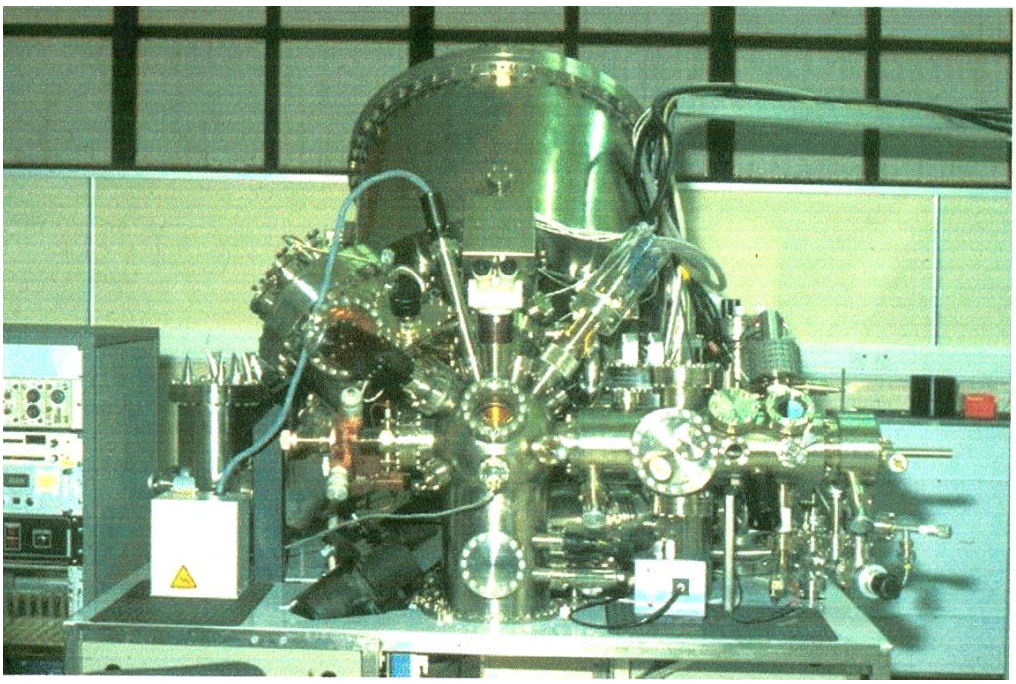

Figure 3.7 The Scienta ESCA300 X-ray photoelectron spectrometer. The sample analysis chamber is at the centre and the hemispherical analyser is located at the top of the photograph.

The energy of the electrons can be controlled by passing them through two hemispheres (600 mm diameter and 100 nm apart) at fixed potential. The setting of the potential allows the passing of specific energy electrons. The default potential of 150 eV has been

used and increased to 300 eV for spatially resolved spectra measurements. Also, the observation of electrons with a wide range of kinetic energies is feasible with the application of a retardation voltage at the electron lens. The spectral resolution of the system was 0.4 eV. On the exit of the hemispherical analyser a multichannel detector was mounted consisting of two 40 mm diameter microchannel plates, a phosphorus screen and CCD camera. The real-time monitoring of the signal is achieved through the display of the data from the CCD camera on a TV and recorded by a PC using XPS software supplied by the manufacturer.

Samples were placed on VG ESCALAB MkII stainless steel stubs using electrically conducting double-sided adhesive tape. Samples were transferred from the turbomolecular pumped load lock ($1x10^{-6}$ mbar) to the liquid nitrogen trapped diffusion pumped preparation chamber ($< 2x10^{-8}$ mbar) using wobble sticks. The samples were then transferred by the means of rack-and-pinion railway to the diffusion pumped analysis chamber ($< 4x10^{-9}$ mbar) that was trapped with liquid nitrogen. For the final stage the samples were transferred to a high precision XYZΘ manipulator. The chamber is equipped with a binocular microscope with a take-off angle set that allowed the positioning of the samples.

For compositional analysis the initial spectra were collected by a fast survey scan across the full range of measurable energies to identify the elements present in the sample. Taking this information as a basis, spectra were collected at higher energy resolution using longer collection times to produce an improved signal to noise ratio for quantitative analysis.

3.6 Diamond growth

3.6.1 Optical microscopy

Optical microscopy has been the first stage of sample characterisation, since it provides information about the texture, crystal size and the orientation of the films. Figure 3.8 shows optical microscope images of the as-grown (100) highly oriented and azimuthally disordered regions of the polycrystalline diamond thin film on silicon wafer.

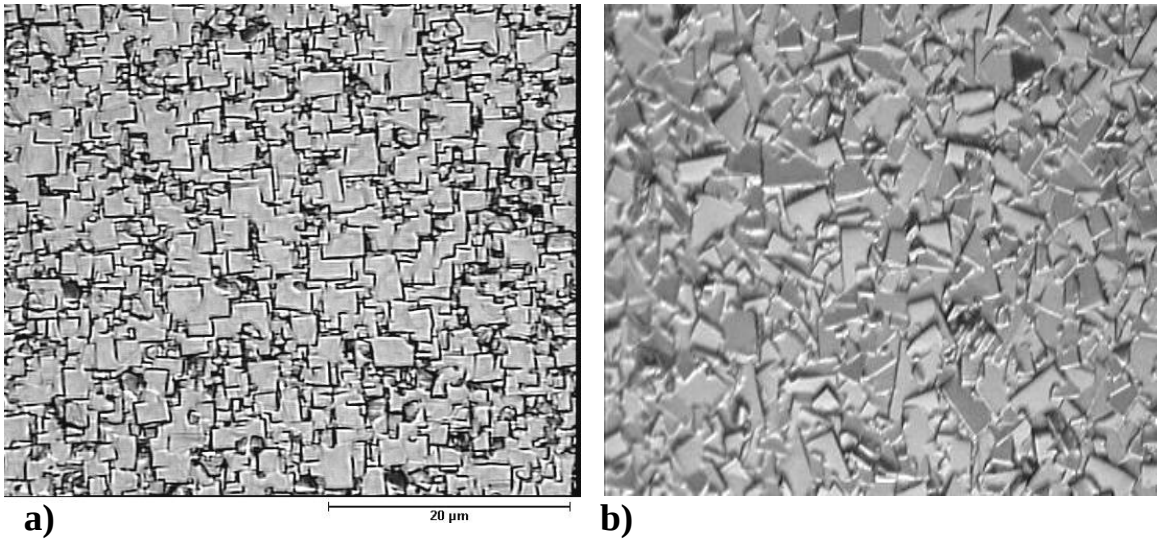

Figure 3.8 Optical microscope images of the as-grown (100) CVD diamond thin films on silicon, a) highly oriented region and b) azimuthally disordered area of the (100) diamond thin film.

3.6.2 Scanning electron microscopy

The analysis of the diamond thin films using scanning electron microscopy has been performed after the optical microscopy analysis, since SEM images provide better resolution and magnification of the area under investigation. Images were taken with accelerating voltages of 8 keV and 10 keV, with corresponding electron depth of 640 and 890 nm respectively. These depths were calculated from Equation 3-3. and the density of diamond [170].

$$X(\mu m) = 0.1 E_o exp^{(1.5/\rho)}$$ **Equation 3-3**

Where, x(µm) is the electron penetration depth, E_o is the acceleration voltage in keV and ρ is the density , for diamond the value of 3.52 g / cm^3 was taken.

SEM images of the as-grown (100) highly oriented and azimuthally disordered areas of a polycrystalline CVD diamond thin film are shown in Figure 3.9. The cross section of the as-grown diamond thin film grown on silicon is show in Figure 3.10 providing evidence of the columnar growth mechanism of the CVD diamond thin films.

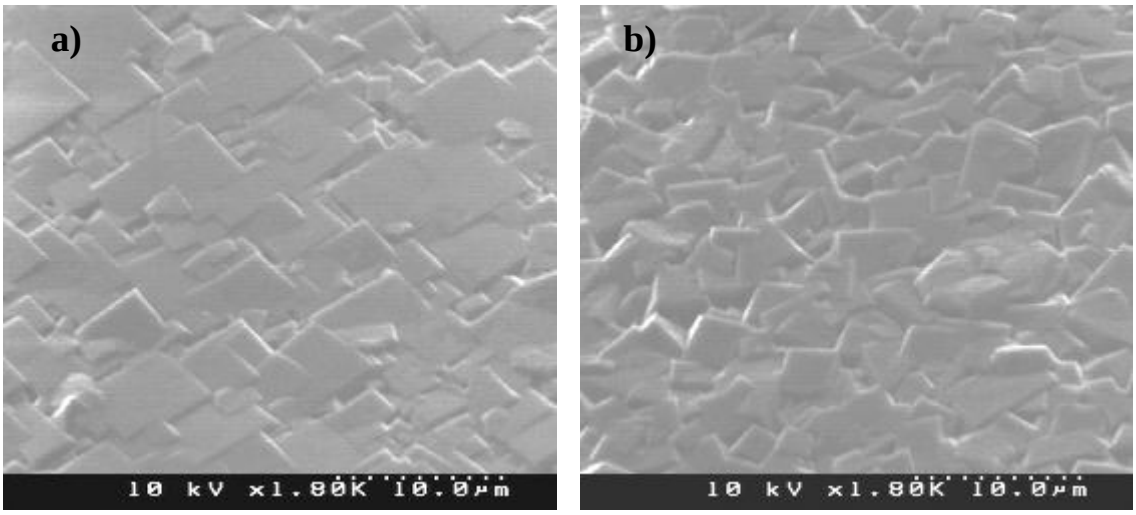

Figure 3.9 Images of scanning electron microscopy of as-grown a) highly oriented and b) azimuthally disordered (100) polycrystalline CVD diamond thin film.

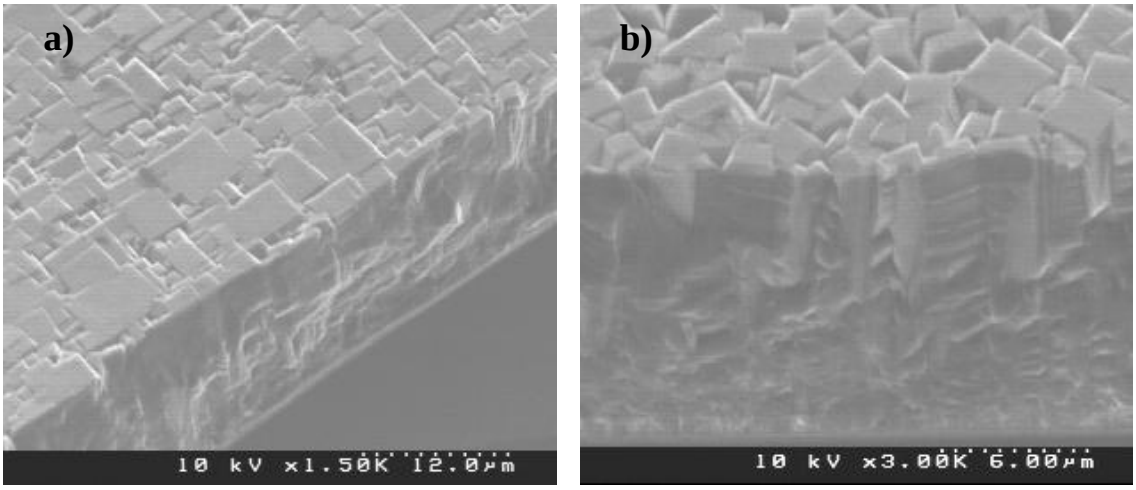

Figure 3.10 SEM images of the cross section of an as-grown a) highly oriented and b) azimuthally disordered (100) polycrystalline CVD diamond thin film, showing the columnar growth mechanism of the MPCVD diamond synthesis.

3.6.3 Atomic force microscopy

The surfaces of (100) polycrystalline CVD diamond thin films have been examined using the contact mode of AFM as shown in Figure 3.11. The Topometrix Accurex scanning probe microscope provides software that allows the surface characterisation of the area under examination. The surface roughness values, as R_a and R_{ms}, were measured for the AFM scan area as well as on any selected area of the scan.

The (100) diamond crystallites exhibit tilts in both orthogonal directions due to the growth mechanism. When the surface roughness values were to be measured on each individual crystallite the use of the 3-point leveling function of the software allowed the correction of the crystallite tilts by fitting a plane and leveling all the selected area. This method provides an accurate measurement of the surface roughness values of individual crystallites. Table 3-4, shows the surface roughness values, averaged over the surface of 10 different crystallites, following the above procedure. The average surface roughness values are within measured error range the same for both highly oriented and highly azimuthally disordered (100) polycrystalline CVD diamond thin film.

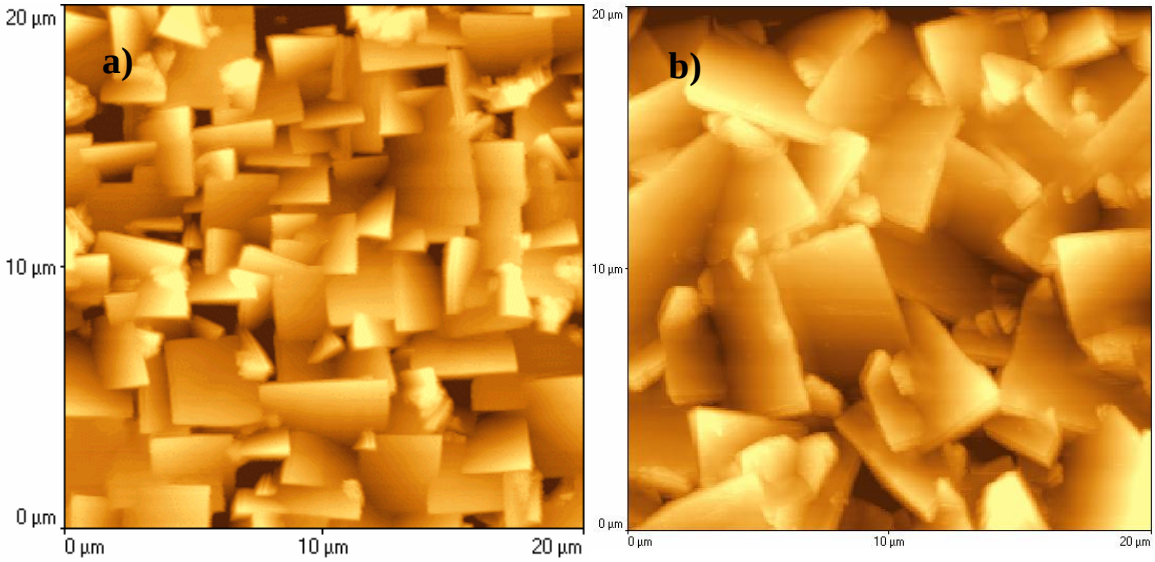

Figure 3.11 Atomic force microscope image of an as-grown a) highly oriented and b) azimuthally disordered (100) polycrystalline CVD diamond thin film.

Roughness Values on individual crystallites	R_a / nm	R_{ms} / nm
Azimuthally disordered (100) region	3.3 ± 0.3	4.1 ± 0.1
Highly oriented (100) region	3.1 ± 0.1	3.9 ± 0.2

Table 3-4 Average surface roughness values of as-grown (100) CVD diamond thin films.

3.6.4 Fourier Transform Infrared spectroscopy

When the CVD diamond thin films were subjected to infrared spectroscopy, oscillations resulted from interference between light rays that have undergone multiple internal reflections within the film were observed. The interference spectrum prohibited the collection of information regarding the infrared absorption bands. Figure 3.12, shows the interference fringes produced both on the transmittance T(v) and reflectance R(v) measured spectrum of the highly-ordered (100) CVD diamond thin film. Both T(v) and R(v) were out of phase for the corresponding wavenumber range. Information regarding chemical bonding in the material could not been obtained directly, although the film thickness could be measured.

Minimal transmission occurs when double the thickness of the film is equal to a half-integral number of wavelengths inside the film,

$$\nu_m = \left(\frac{1}{2}\right) nd\left(m + \frac{1}{2}\right) \qquad \textbf{Equation 3-4}$$

where ν_m is the frequency (in cm^{-1}) or wavenumber corresponding to the m_{th} interference minimum, n is the refractive index of the film (for diamond n ~ 2.41 [171]), d is the thickness of the film and m is an integer – the order of the interference pattern. For a particular interference minimum the value m can be obtained by dividing ν_m by the average spacing between minima. The thickness of the film can be obtained by plotting ν_m vs m.

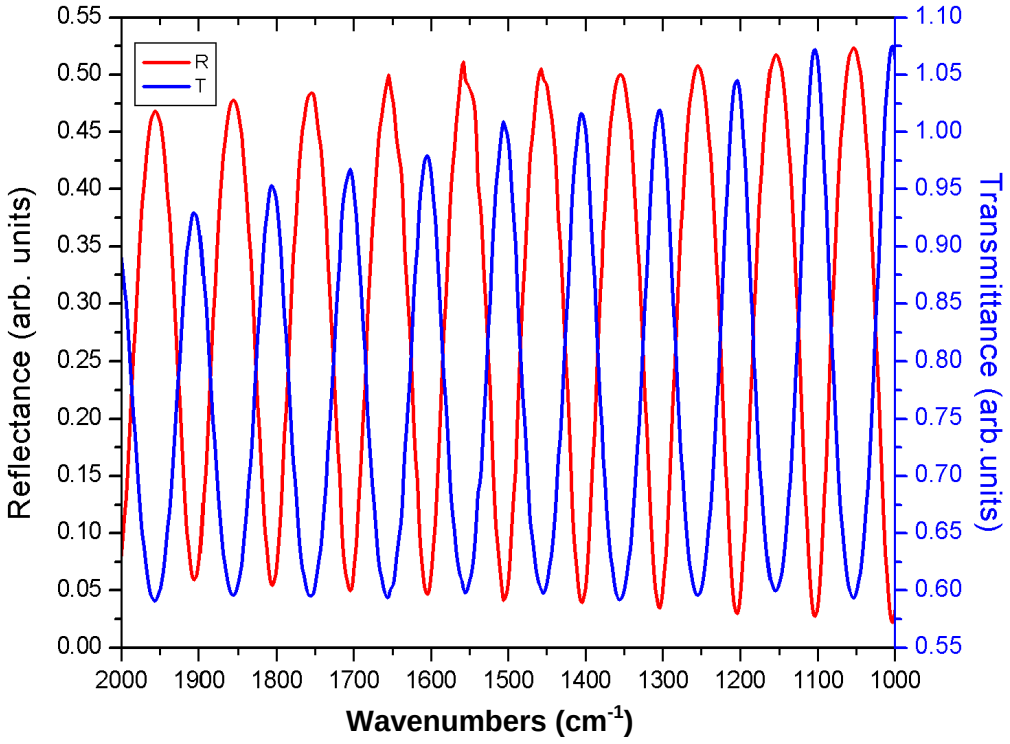

Figure 3.12 FITR spectra of free-standing CVD (100) highly ordered diamond thin film. Reflectance and transmittance spectra were collected at the same location of the sample.

The infrared spectrum A(v) of the (100) diamond thin film, was obtained by the addition of the R(v) and T(v). The region 2700 cm^{-1} to 3100 cm^{-1}, is shown in Figure 3.13, which corresponds to the CH stretching region and is of significance. In this spectral region absorption bands due to the stretching modes of sp^3- and sp^2- bonded CH_x, are commonly observed for CVD diamond thin films.

Deconvolution of the CH_x stretch region to different sp^2 and sp^3 peaks performed using peak positions and assignments accordingly to the published data, as shown in Figure 3.14. The deconvolution was carried out by fitting the minimum number of component peaks required to achieve a satisfactory fit. The initial positions of the peaks were obtained from published data [172-176] and all bands assumed a Gaussian peak shape. The peak positions are listed in Table 3-5.

Wavenumber [cm^{-1}]	Relative percentage area (%)	Mode of vibration
2815	5.2	CH on (111) / N – CH_3
2829	12.4	CH on (1x1)(111)
2852	13.8	Symmetric sp^3 CH_2,
2879	19.7	Symmetric sp^3 CH_3
2918	31.3	Asymmetric sp^3 CH_2
2961	14.4	Asymmetric sp^3 CH_3
3017	3.2	sp^2 CH

Table 3-5. Characteristic CH_x (x = 1- 3) stretching vibration frequencies of CVD diamond films.

The dominant absorption peak observed near 2918 cm^{-1}, as well as the absorption peak at 2852 $cm^{-1}$are attributed to the asymmetric and symmetric stretching bands of sp^3 – bonded CH_2 groups, respectively. The intensity of the asymmetric absorption band is usually greater compared to the symmetric absorption band in CVD diamond thin films [175]. The absorption bands at 2879 cm^{-1} and 2961 cm^{-1}, are due to the symmetric and asymmetric stretch bands of sp^3 – bonded CH_3 groups, respectively.

The two absorption peaks at 2815 cm^{-1} and 2829 cm^{-1} are most likely to originate from the CH stretch band on a (111) - like surface, since the absorption peaks around 2820 cm^{-1} and 2830 cm^{-1} relate to a hydrogen-terminated (111) diamond surfaces that were expected to be present at the grain boundaries of the (100) diamond film [174]. The absorption peak at 3017 cm^{-1} is related to sp^2-CH carbon bonds within the diamond film.

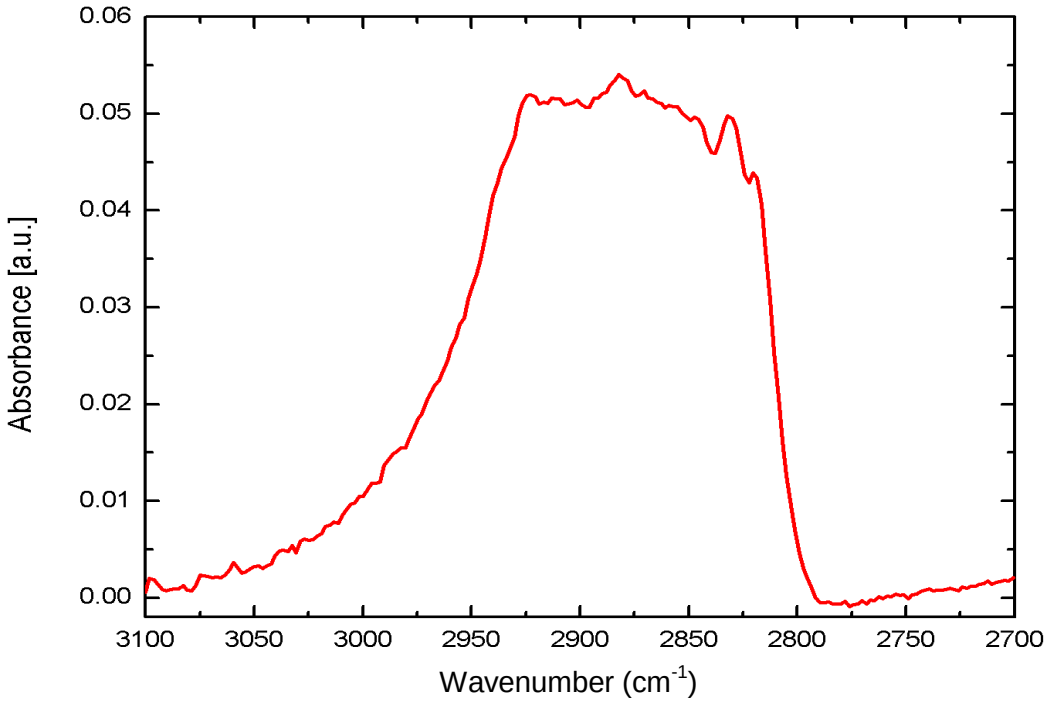

Figure 3.13 Absorption spectrum of polycrystalline diamond film, between 3100 – 2700 cm-1.

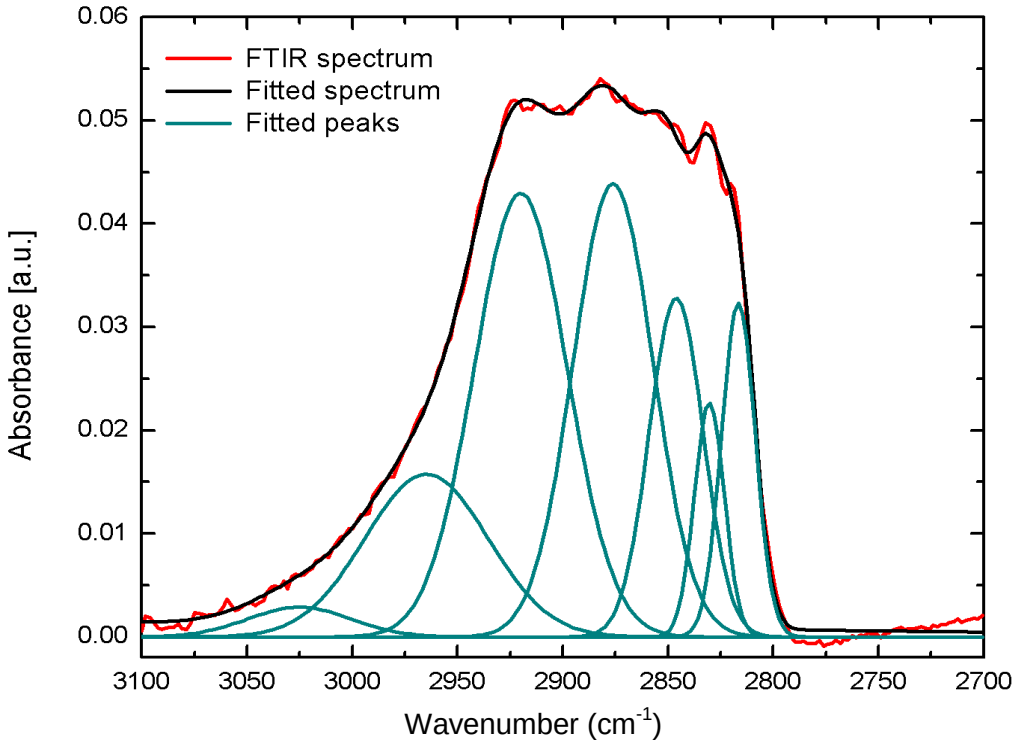

Figure 3.14 The CH stretch region of the as-grown (100) CVD diamond film, deconvoluted into a number of component peaks.

An FTIR spectrum from a CVD single crystal diamond plate were collected and shown in Figure 3.15, within the region of 7000 cm^{-1} to 400 cm^{-1} with a spectral resolution of 4 cm^{-1}. The spectrum shows the intrinsic absorption in the two-phonon range between 2666 cm^{-1} and 1333 cm^{-1}, while absorption in the three-phonon region at 3300 – 2750 cm^{-1} was also observed. As in the case of polycrystalline CVD diamond films, this region also contains information about hydrogen bonded to carbon in the diamond film.

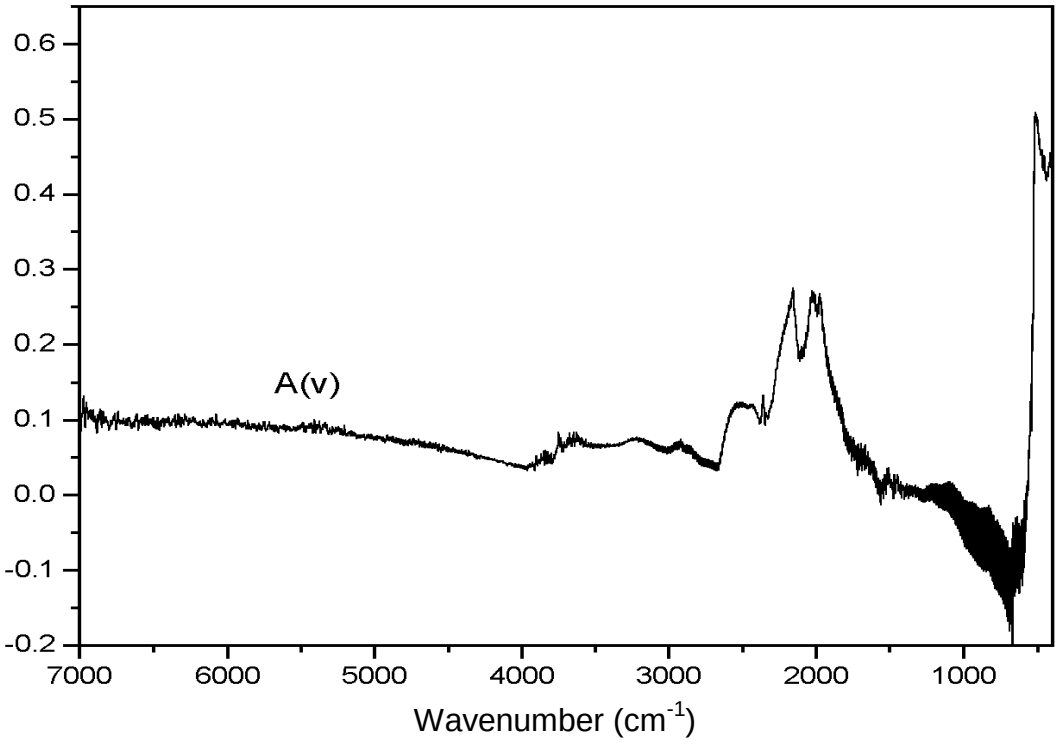

Figure 3.15 Absorption spectrum of single crystal CVD diamond film, showing the characteristic intrinsic two-phonon absorption region of diamond between 2666 and 1333 cm^{-1}.

3.6.5 Laser ionisation microprobe analysis

The chemical composition of the diamond thin film surface and near-surface regions has been examined using the LIMA technique. The solvent cleaning procedure was tested using the LIMA technique and verified to remove organic contamination from the diamond sample surface. Figure 3.16, shows the mass spectrum that has been collected from the surface of an as-grown (100) diamond thin film after the cleaning procedure. As it can been see from Figure 3.16. the chemical elements that were detected with the LIMA technique were carbon with a minor peak due to sodium, providing direct evidence for the effectiveness of the cleaning procedure that has been used for all the (100) diamond thin films. Using the LIMA technique it was feasible to make

measurements on different locations on the sample. Information could be provided on the entire diamond surface and not just from one location.

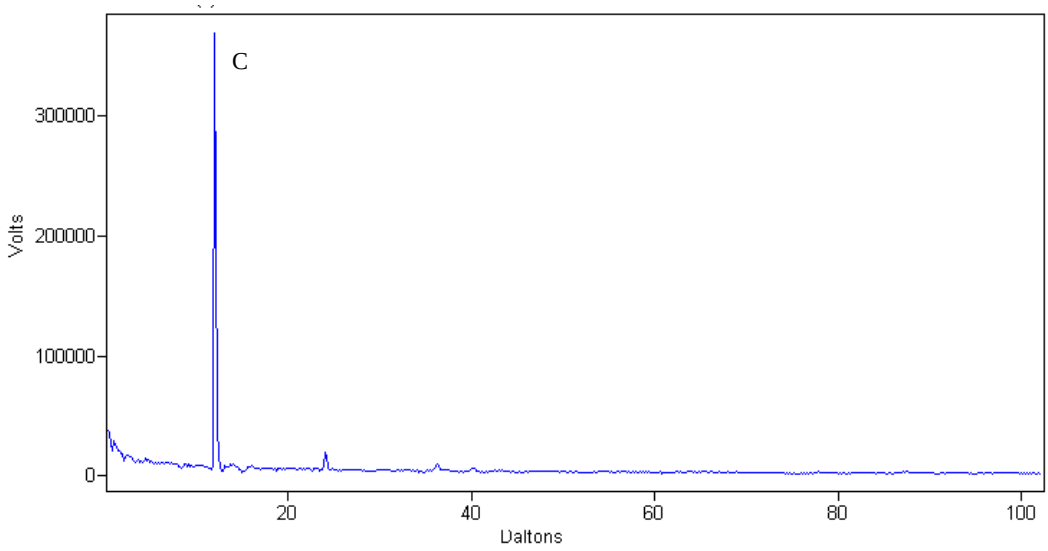

Figure 3.16 Surface chemical composition of an as-grown (100) diamond thin film, following cleaning procedure.

The effectiveness of the acid treatment to remove contamination from the diamond surfaces that was applied to some of the diamond thin films has also been verified by LIMA analysis. The same acid treatment has also been referenced in the literature [177] as a method for producing an oxygen-terminated diamond surface. The LIMA technique has been successfully applied to detect oxygen attachment on diamond powders [178]. The acid treatment was not intended to produce an oxidised diamond surface. No traces of oxygen were detected on the diamond surface. It was believed that the duration and the temperature of the acid treatment were insufficient to produce a significant oxidised diamond surface.

3.6.6 X-ray diffraction analysis

The X-ray diffraction patterns of a CVD (100) oriented diamond thin film is shown in Figure 3.17 while the most intense peaks obtained from the spectrum are presented in Table 3-6. For each peak, the 2θ value, corresponding d-spacing and the percentage intensity of the peak, with respect to the highest intensity peak, is listed.

2θ (°)	*d-spacing*	*% of largest peak*	*(hkl)*
43.9	2.0594	10.11	d(111)
69.0	1.3586	53.46	Si (400)
69.3	1.3540	100.0	Si(400)
75.2	1.2612	0.99	d(220)
91.4	1.0757	1.10	d(331)

Table 3-6 Significant XRD peaks in as-grown (100) CVD diamond thin film

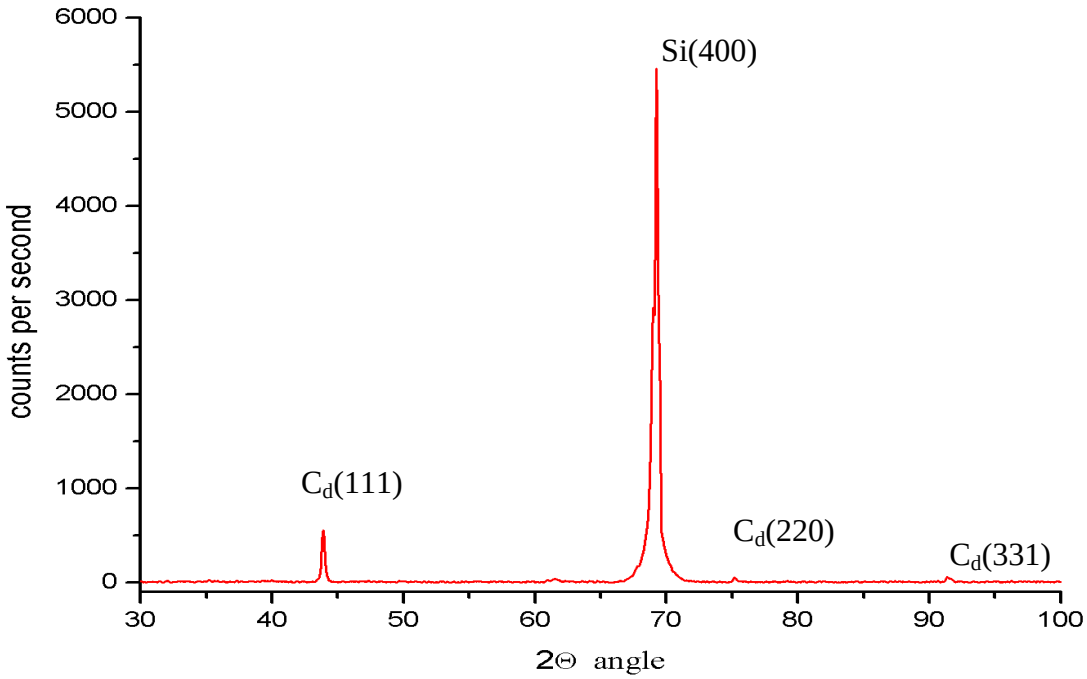

Figure 3.17 X-ray diffraction pattern within the range of 2θ values from 30° to 100° in XRD of a CVD (100) diamond thin film on silicon substrate.

The dominant peak observed at 69.3°, has been identified as the (400) crystallographic plane of the Si substrate of the CVD diamond film. The other peaks that have been observed correspond to the diamond crystal planes.

3.6.7 X-ray photoelectron spectroscopy

A survey scan of X-ray photoelectron spectra of a typical CVD (100) diamond thin film is shown in Figure 3.18. The carbon C1s peak can be seen at ~ 285 eV; the feature observed at ~ 310.6 eV it is attributed to plasmons created during the emission of the C1s electrons and the carbon Auger transition is observed at ~ 1223 eV. The presence of oxygen was been detected at oxygen O 1s ~ 532 eV and oxygen Auger transition at ~ 974 eV. Whilst the as-grown diamond thin films contain oxygen on the surface, the origin of the oxygen may arise from a number of sources.

High resolution C 1s and O 1s spectra of a typical diamond thin film are shown in Figure 3.19. Integration of the area under the electron core peak, using a linear base line, is proportional to the average concentration of the respective elements that are present within the analysis volume. Since the spectra were collected with charge compensation the C1s component peak position is measured relative to the main sp^3 carbon peak. The high resolution XPS spectra enables the number of different component peaks to be specified which could be convoluted to produce the total C1s peak shape. Analysis of the high resolution XPS data is discussed and presented in subsequent chapters. In these chapters the surfaces of the as-grown diamond thin films will be compared to surfaces subject to the different physical process.

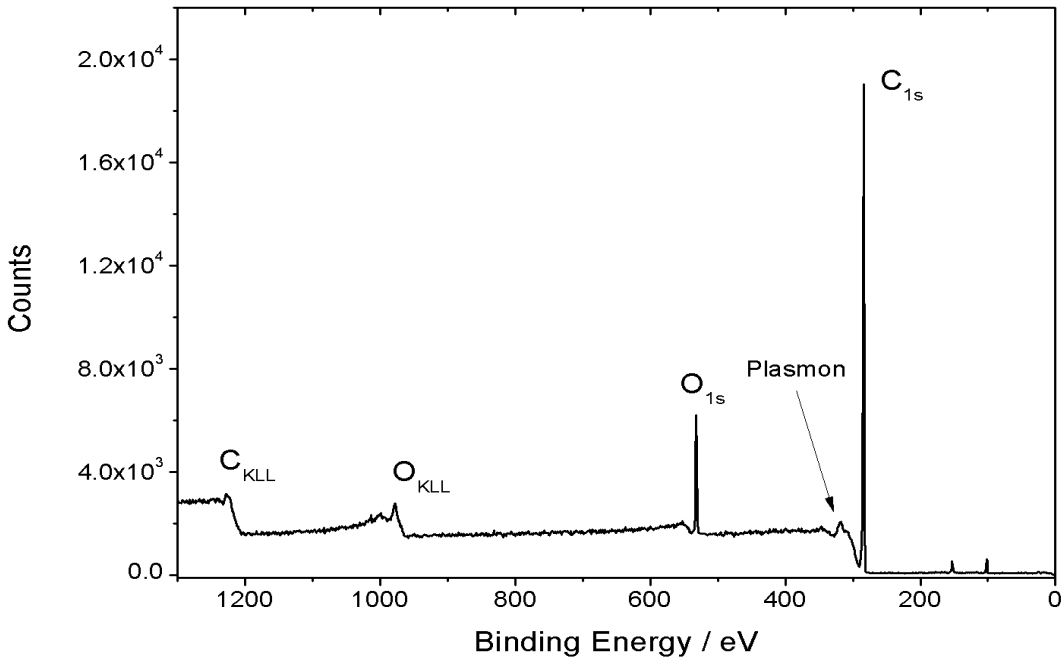

Figure 3.18 Wide scan XPS spectra from an as-grown CVD (100) highly oriented diamond thin film.

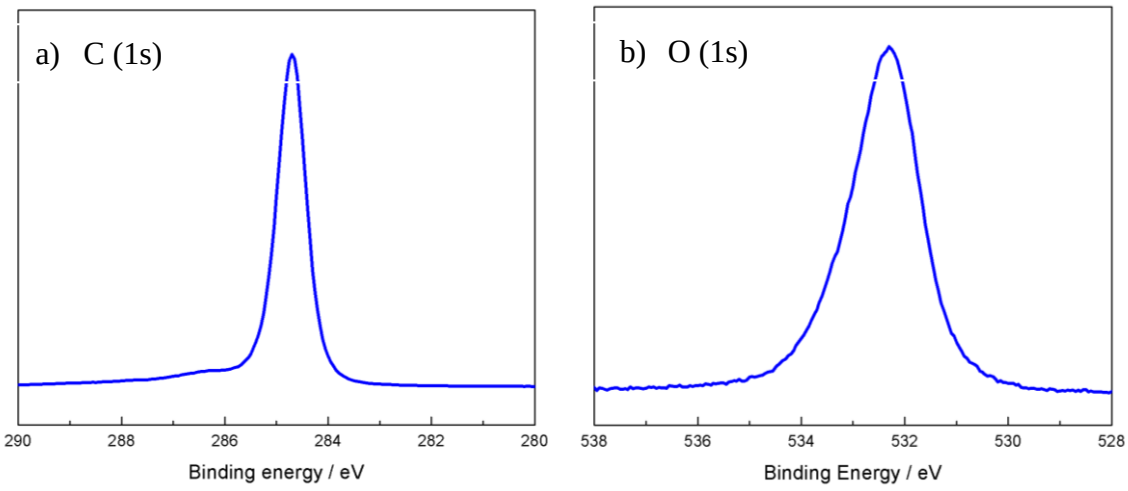

Figure 3.19 High resolution XPS spectra of the i) C 1s and ii) O 1s peaks of an as-grown diamond thin film.

3.7 Conclusions

Microwave plasma chemical vapour deposition has been used to produce high quality (100) faceted diamond thin films on (100) crystalline silicon substrates. Biased enhanced nucleation was used to achieve high azimuthal orientation of the diamond nuclei with the underlying substrate.

The emphasis of the work was to produce highly oriented (100) diamond films with defined surfaces. Films with highly ordered (100) diamond crystallites with an area of around 3 cm^2 per 4" diameter wafer were able to be produced.

Chapter 4. Hydrogenation of (100) CVD diamond surfaces

4.1 Introduction

In this chapter, the prolonged exposure of (100) highly oriented CVD diamond films to microwave hydrogen plasma treatment is presented. The interaction of atomic hydrogen with diamond surfaces has been an area of great interest, since hydrogen is used for the CVD growth process but also due to the unique physical and chemical properties that hydrogen terminated diamond surfaces exhibit. This chapter describes experiments on the effects of prolonged exposure to atomic hydrogen where atomic force microscopy has been employed to examine any change to the surface morphology. Infra-red and X-ray photoelectron spectroscopy have been used to examine the effects on the chemical composition of the hydrogenated diamond surfaces. The electrical analysis carried out on the hydrogenated diamond surfaces will also be presented on this chapter. The analysis consisted of I-V characteristics of the diamond surfaces after hydrogen plasma treatment.

4.2 Hydrogenated (100) diamond surfaces

Hydrogen plasma treatment is commonly employed to terminate the CVD diamond surface. This serves three reasons (i) to eliminate any non-diamond carbon material that may have deposited on the surface (ii) to remove oxygenated functional groups and (iii) to maintain a sp^3 electron configuration on the diamond surface. The successful homoepitaxial CVD growth of device-grade atomically smooth (100) diamond surfaces using low methane concentration using a CH_4/H_2 plasma, indicated the importance of H_2 plasma treatment on CVD diamond growth [179]. When hydrogen plasma treatment of substrates has been employed prior to CVD homo-epitaxial growth, atomically smooth diamond surfaces have been produced [34].

The unique physical and chemical properties of hydrogen terminated diamond surfaces have attracted a considerable amount of research. The p-type surface conductivity (SC) [44] and negative electron affinity [180-181] of hydrogenated diamond surfaces are very desirable properties for the development of diamond-based electronic devices. So far the fabrication of in-plane-gated FET's [182] and single- hole transistors (SHTs) [183] have been demonstrated using the nanoscale local anodic oxidation (AFM) technique [184] on a H-terminated diamond surface. The H-termination of diamond carbon bonds provide a template for organic molecules attachment and therefore for potential applications in biotechnology.

The hydrogen termination of diamond is most commonly achieved by microwave-assisted plasma treatment [27, 30, 143, 185-195] or by hot-filament-assisted treatment [117, 121, 196-199]. The interaction of atomic hydrogen with the (100) diamond surface has been the subject of many investigations using a variety of experimental and theoretical methods [27, 30, 117, 121, 123-124, 129, 141, 142, 145, 146, 185-201].

When atomic hydrogen interacts with the diamond surface the surface undergoes reconstruction and different hydrogen bonding configurations have been suggested in the literature. A simple schematic representation of the possible surface reconstructed structures of the hydrogenated diamond surface is depicted in Figure 4.1. A fully hydrogen-passivated (100) (1x1):2H diamond surface would contain two hydrogen atoms per unit cell and due to strong repulsion between the two hydrogen atoms such a surface reconstruction would be energetically unfavorable.

Theoretical models using empirical and semi-empirical techniques [118-120] have shown that the diamond (100) surface reconstructs via the formation of rows of symmetric dimers upon hydrogenation. The mono-hydrogenated C(100)–(2x1):H surface is considered to be the most stable hydrogenated {100} diamond surface [121]. Figure 4.1 (a) shows schematically the C(100)-(2x1):H reconstructed surface which consists of C-C dimers where each surface carbon atom is bonded to one hydrogen atom, and has two back bonds to the diamond lattice.

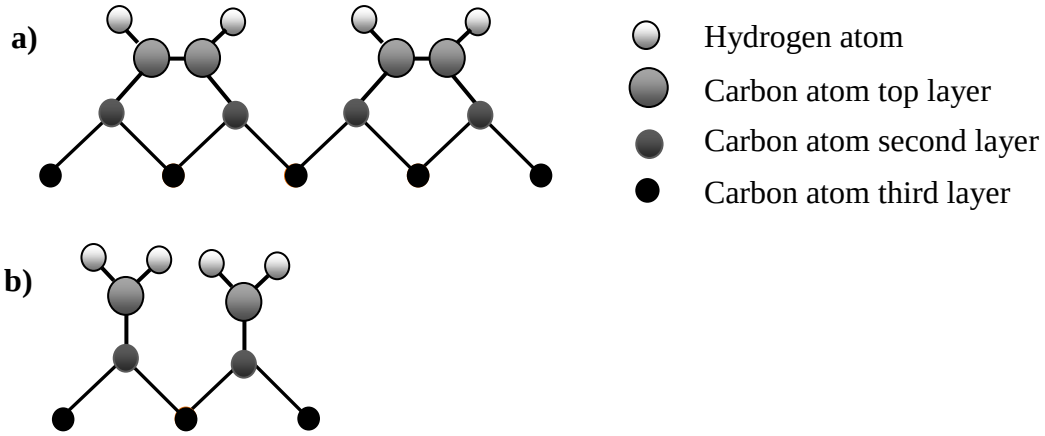

Figure 4.1 Schematic of the (100) diamond hydrogen terminated surface reconstructions. a) the C(100)-(2x1):H monohydride configuration and b) the C(100)-(1x1):2H dihydride configuration

STM studies [117, 194, 197] under UHV showed that such a surface has terraces consisting of atomic planes with dimer rows that are rotated by 90^{o} relative to the dimer rows of the adjacent atomic plane. A single domain (2x1) dimer reconstructed surface is revealed in the latter. Figure 4.2 shows STM topographies of the (100)-(2x1):H diamond surface of the a) unoccupied and b) occupied states respectively reproduced from reference [202]. In Figure 4.2 a) the bright lines highlight the CH-CH dimer rows of the (2x1) reconstructed surface; the 90^{o} rotation of the dimer rows on each adjacent atomic plane is apparent from the STM topography. The arrows in Figure 4.2 a) show the observed defect structures such as point defects and missing rows.

Two different types of steps have been observed on the (100)-(2x1):H diamond surface. Single atomic steps that contain dimer rows parallel to the step edges are marked as S_A steps and are highlighted in Figure 4.2 a) whilst single atomic step edges where the dimer rows are perpendicular to the step edges are referred as S_B steps [197]. The schematic representation of the atomic steps formed on the (100)-(2x1) :H diamond surface shown in Figure 4.3 is reproduced from reference [194]. As highlighted on Figure 4.2 b) the inter-row distance was measured to be 5.0 ± 0.2Å, whilst the bright features within the lines were measured to be separated by 2.5 ± 0.2Å and are attributed to the single geometry of CH-CH dimers [194, 202]. The length of the monohydride dimer bond has been measured by dynamical low energy electron diffraction (LEED) [186] to be 1.60Å which is in agreement with the theoretical models [123-124]. Infrared spectroscopy confirmed that the vibrational modes of the C-H dimer species are coupled

producing symmetric and antisymmetric stretching modes at 2919 cm^{-1} and 2899 cm^{-1} respectively [121].

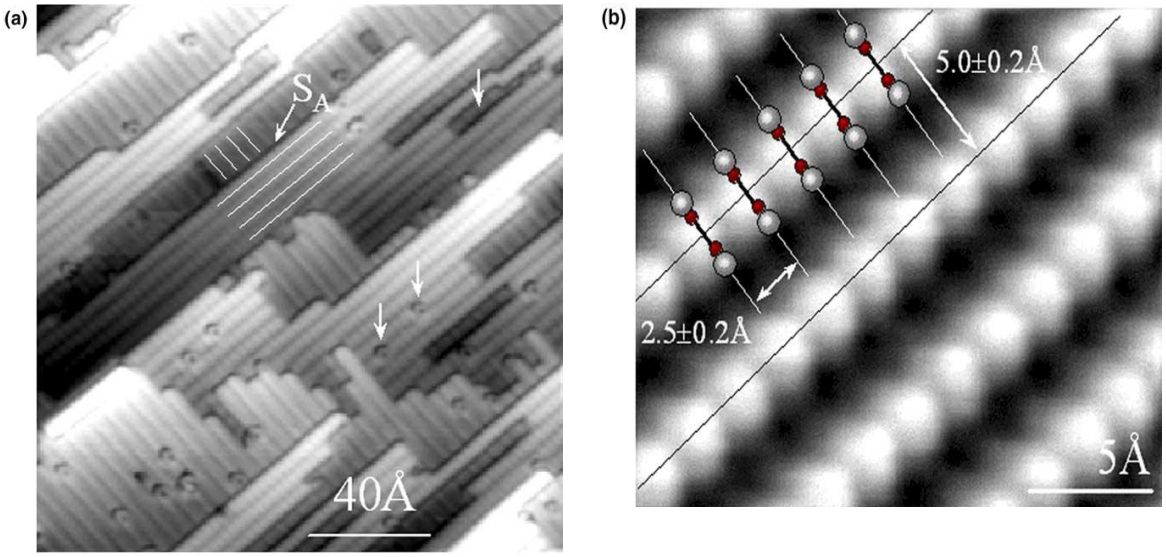

Figure 4.2 STM topographies of the hydrogenated diamond (100)-(2x1):H surface (a) unoccupied states and (b) occupied states. The bright lines on the top topography indicate the C-C dimer rows in the vicinity of the step (S_A) [202].

X-ray photoelectron spectroscopy measurements on the hydrogenated diamond surface show a shoulder shifted by 0.5-0.8 eV towards a higher binding energy compared with the C 1s bulk peak. The shoulder has been observed to be characteristic of partially covered diamond surfaces by hydrocarbon species, possibly methyl groups [202-203].

The reconstructed surface had been found to be stable to air exposure. Annealing the hydrogenated surface in UHV at the hydrogen desorption temperature region of 900-1200^{o}C produces a hydrogen-free surface. After annealing a new shoulder appears on the C 1s peak shifted by 0.9 eV towards lower binding energy for the diamond (100) surfaces. This feature has been attributed to the surface atoms that undergo relaxation to π-bonded dimer rows of the 2x1 reconstructed surfaces. The activation energy of 3.4 eV has been calculated for the transition from the mono-hydrogenated to hydrogen-free reconstructed surface [203].

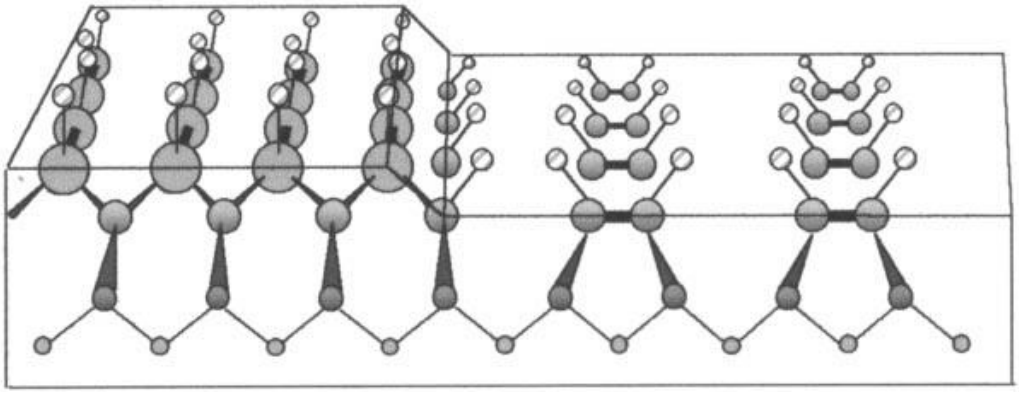

Figure 4.3 Schematic of the diamond C(100):H surface showing the steps and 90° domain rotation in successive C-atom layers [53].

4.3 Etching of diamond with hydrogen plasma

When activated hydrogen is used to etch diamond, either neutral or ionised mono-atomic hydrogen i.e. H or H^+ react with the surface and remove material. Experimental observations [199, 204] show that atomic hydrogen etches graphite faster than diamond. This data is in agreement with theoretical calculations [205]. Hydrogen plasma treatment removes the sp^2 carbon from the diamond film, which has been co-deposited on the diamond surface [117]. Amorphous carbon phases are generally located at the grain boundaries in polycrystalline CVD diamond films [206].

Etching experiments with a conventional CVD reactor using a hydrogen plasma under growth conditions (800 W, 780 ^oC, 30 torr, 200 sccm) show that hydrogen plasma will etch polycrystalline CVD diamond film with a rate of 0.15 μm/h [207]. Removal of the amorphous carbon forms was confirmed by Raman spectroscopy and resulted in improvement of the crystal quality. It has been found that negatively biasing the diamond samples during the hydrogen plasma results in faster etch rates [208]. Stoner *et al* [209] attributed the high etch rates for negatively biased-assisted plasma etching to the following mechanism. Diamond surfaces which are negatively biased in a hydrogen plasma will result in electron emission. The emitted electrons graphitise the exposed surface which can be etched faster by the plasma.

Studies show that H^+ ion bombardment of diamond films during growth/etching experiments occurs preferentially at the grain boundaries and causes redeposition of the material [207]. Depending on the process conditions of the negative biased plasma,

conical, island formation or tips-cones structures can been formed on polycrystalline diamond CVD films [210]. Zhang *et al* [211] attributed the formation of conical tips to the formation of an unevenly distributed electron emission caused by the defective sites and grain boundaries of the CVD diamond films. Therefore preferential etching by energetic hydrogen ions at the defective sites and column boundaries is caused by the local distribution of the plasma sheath.

Jiang *et al* [212] observed that crystallite grains grew laterally and their surface area increased on a (100)-oriented polycrystalline diamond film after a negative bias hydrogen treatment for the duration of 20 hours. The (100) facets were roughened after the treatment while an etch rate of 0.05μm/h was obtained. The cause of the lateral growth of the crystallites has been attributed to a preferential redeposition on the sides of the (100) facets where the H^+ ion damage is weak.

Creation of fibrous structure had been observed on polycrystalline CVD diamond film and diamond powders by changing the process parameters of the above etching mechanism [213]. Transmission electron microscopy confirmed that the fibrous structure consists of randomly oriented nanocrystals with a diameter smaller than 10 nm.

Ando *et al* [214] showed that etching of diamond whiskers by a microwave hydrogen plasma depends strongly on the pressure. Experimental observations show that homoepitaxial growth of diamond occurred at low pressures whilst the etching rate was low. It was notable that the growth rate depended on the crystal orientation of the diamond surface and the final shape of the whiskers depended on the duration of the plasma treatment.

There has been a controversy [30,187, 189] about the surface morphology of the (100) diamond surface after hydrogen plasma treatment. Atomically smooth diamond surfaces have been produced by microwave plasma treatment [27, 30,185, 187-189]. For a single crystal (100) diamond surface the roughness value has been reduced from 2 nm (rms) to 0.8 nm (rms) after exposure to hydrogen plasma treatment (1.2 kW, 870 ^oC, 40 mbarr) for 3 hours, while the surface roughness of (111) diamond surface had been reduced from the initial value of 7 nm to 0.8 nm after a plasma treatment of 17 hours [189]. In contrast there are references on the roughening of the (100) diamond surface after

hydrogen plasma treatment either by means of microwave or hot-filament treatment [190, 191, 196]. AFM analysis demonstrated the formation of macro-steps running parallel to [110] direction [185,190].

Pyramidal-type etch pits with square-symmetry have been observed to have been formed on the (100) diamond surface [30,143, 192, 197, 198] after hydrogen plasma exposure. The sides of the etch pits were found to comprise steps on the {111} facets [143, 192]. The etch pit density has been related to surface dislocation density [197] and misorientation angle of the diamond surface [30]. The roughening of the (100) diamond surface by hot-filament-assisted hydrogen treatment was examined by infrared absorption spectroscopy [196] and it was attributed to the formation of {111} oriented nanofacets on the (100) diamond surface. The same morphological changes have been observed on the (110) diamond surface [196, 200] whilst the (111) diamond surface remained intact [129].

The surface morphological changes due to exposure to atomic hydrogen produced by both microwave and hot-filament assisted etching have been examined by Cheng *et al* [199] and Küttel *et al* [189]. Smoothing of the (100) diamond surface has been observed by microwave hydrogen plasma treatment; whilst a roughening of the (100) diamond surface has been observed by hot-filament hydrogen exposure. The discrepancy between the two results has been suggested to be due to the higher energy ions present in a microwave-assisted plasma [196].

Smoothing of the (100) diamond surface has been attributed by many authors to etching [195, 197]. According to this mechanism atomic hydrogen etching occurs preferentially on the edges of the atomic steps of the (100) diamond surface. UHV STM studies [195] of the exposure of (100) diamond surface to atomic hydrogen produced by hot-filament treatment, showed that atomic-hydrogen etching is strongly temperature dependent.

For substrate temperatures of $\leq 500^{o}$C atomic hydrogen etching is highly isotropic and etching proceeds on both S_A and S_B atomic steps on the (100) diamond surface, leading to the formation of a very rough surface, with high density of square-etch pits. As the facets of the square-etch pits consist of (111) diamond surfaces enlargement of the etch-pits with plasma exposure time leads to (111) faceting of the (100) diamond surface [185, 196]. At elevated substrate temperatures of 1000^{o}C, the hydrogen etching

becomes anisotropic resulting in smooth surface with large domains while large etch pits have not been observed on the (100) diamond surface. Atomic steps S_B were found to be rough while atomic steps S_A were observed to be smooth. In addition double type A steps have been observed on the etched (100) diamond surfaces. These observations support the anisotropic etching mechanism of atomic hydrogen on the (100) diamond surface at elevated temperatures of 1000^oC [195].

Ri *et al* [30] observed a strong dependence on the misorientation angle of the surface morphological changes that occur on the (100) diamond surface after microwave hydrogen plasma treatment. Atomically smooth surfaces were produced after atomic hydrogen exposure for low misorientation angles $\theta_{off} < 1.5^o$. The surface roughness increased after hydrogen plasma etching with the increase of the misorientation angle. Based on these experimental observations a simple model has been proposed based on the anisotropic etching of hydrogen plasma treatment, where the active sites for etching are the step edges. A strong dependency on the etch pit density and the misorientation angle of diamond substrates was also discussed.

Lee and Badzian [143, 192] observed square-etch pits with fourfold symmetry on the (100) diamond surfaces after microwave hydrogen plasma exposure. The etch-pit density has been found to decrease with the increase of the misorientation angle of the diamond surface. The edges of the etch pits were found to be parallel to the <110> directions, while macrosteps along the [110] direction were observed which are in alignment with the orientation of the surface misorientation angle. Macrosteps parallel to [110] directions were also observed on the homoepitaxial diamond films grown on the plasma treated surfaces. Based on those experimental results the authors suggested that atomic hydrogen etching occurs by the migration of atomic steps along the <110> direction. The increase of the etch pit density with the decrease of the surface misorientation angle has been attributed to the creation and regression of new steps on a low angle misorientated surface.

Jiang and Rickers [215] employed AFM topography to examine the etch pit formation after hydrogen plasma treatment on (100) polycrystalline CVD diamond films. They correlated their experimental observations with the formation of the etch pits due to crystal defects present at the grain boundaries of the (100) polycrystalline CVD diamond films.

Based on STM observations under UHV conditions Stallcup *et al* [198] proposed that, at a substrate temperature of 500^{o}C, during hydrogen plasma treatment, the formation of dihydrides is favourable at the step edges. Such hydrocarbon species would exhibit stressed C-C bonds and they would be highly prone to etching. The stress is caused by the steric repulsion of the dihydride units. Etch pits formed due to etching perpendicular to the (100) diamond surface and lateral growth of the etch pits would occur due to preferential etching of steps at the edges of the pits.

Hydrogen atom-assisted surface diffusion has been proposed by Rawles *et al* [27] to be the dominant mechanism for the smoothing of the diamond surfaces during hydrogen plasma treatment. Observations made by SEM on diamond powders subjected to microwave-assisted hydrogen plasma treatment, for a substrate temperature range of 700-900^{o}C, showed that the size of diamond powders remained unchanged while faceting occurred. Hydrogen diffusion has been suggested to be responsible for those experimental observations.

Surface diffusion of the adsorbates has been proposed by many authors as a mechanism for the growth of smooth (100) diamond surfaces. Quantum mechanical calculations proposed that surface migration is significant during (100) diamond growth, at least on the 5-20 Å length scale, and assists the growth of dimer rows and smooth surfaces [145].

Frenklach and Skokow [141] modelled diffusion on the diamond surface during growth and according to their model diffusion is most favorable to occur along the surface sites where the hydrogen has been removed by abstraction. When the surface migration is included into the theoretical models, it predicts higher growth rates than those observed experimentally [146].

Other mechanisms that have been proposed for the growth of smooth (100) surfaces are i) anisotropic etching and ii) the preferential etching of under-coordinated atoms. The latter model, developed by Bettallie *et al* [146] based on quantum mechanical and kinetic Monte-Carlo calculations of the plasma CVD diamond growth, includes hydrogen etching. The model shows that etching plays a key role in the growth of smooth (100) diamond surface and it predicts that the probability of CH_2 removal from the (100) facets decreases for isolated, step-sited and surface CH_2 groups. Thus the

growth/etching of (100) diamond surface proceeds layer-by-layer involving steps. Further analysis and quantum mechanical modeling of the β-scission mechanism of the (100) diamond surface growth showed that preferential etching could explain the growth of atomically smooth 2x1 dimer reconstructed surfaces [201].

4.4 The surface conductivity of diamond

High surface conductivity was first observed on single crystal diamonds and CVD grown diamond films subjected to hydrogen plasma treatment [40]. Due to the nature of the treatment any possible modification induced will be restricted to the near surface region therefore the phenomenon was initially referred as hydrogen-induced surface conductivity. Surface conductivity of diamond films has been observed experimentally to be enhanced after exposure to a hydrogen plasma [216].

The typical surface conductivity, measured at room temperature, is observed in the range of 10^{-4} to 10^{-6} $\Omega^{-1}cm^{-1}$ created by p-type carriers with a lateral density in the range of the order of a few times 10^{13} cm^{-2} and a carrier mobility measured to be 10 to 100 $cm^2V^{-1}s^{-1}$ [217]. There is very little temperature dependence on the carrier concentration and mobility [217]. Empirical observations lead to the conclusion that hydrogen plasma is responsible for the formation of a p-conducting layer on the diamond surface. Such a unique surface property makes diamond a candidate material for electronic applications [182, 183].

Several models have been suggested to explain the distribution of acceptors responsible for the hole-accumulation layer. It was proposed that hydrogen forms point defects that act as shallow electron acceptors and provide the mobile holes [217]. The formation of such a distribution of acceptors was not clear. Some models suggested that they reside on the diamond surface [218], form layers 10 nm into the bulk of diamond [217] and even reside 30 nm below the diamond surface [219].

The surface conductivity of CVD diamond films and hydrogen plasma treated natural diamond crystals was found to depend strongly on the surface conditions. Upon hydrogen desorption, via thermal annealing *in vacuo* [220] and oxidation [217] the surface conductivity decreased and vanished. Based on those observations the relevance of hydrogen was suggested to be an indirect influence for the observed surface

conductivity. Maier *et al* [44] provided evidence to support the idea that chemisorbed hydrogen is necessary but not sufficient for the formation of surface conductivity. They postulated that for diamond surface conductivity electron acceptors are provided by atmospheric adsorbates. According to this model, Maier *et al* [44] suggested transfer doping via a redox reaction in an adsorbed water layer. The transfer doping model describes the exchange of electrons between an intrinsic semiconductor and surface material that acts as an electron acceptor. Therefore a thin wetting layer of molecules can be formed on the diamond surface upon exposure to ambient air which can accept electrons from the diamond via the reaction:

$$2H_3O^+ + 2e^- \rightarrow H_2 + 2H_2O$$

provided that the chemical potential of the absorbate layer is below the Fermi-level of diamond. This model has been supported by *ab initio* results and tight-binding molecular dynamics model calculations [221]. Experimental evidence provided by Hellner *et al* [220], Nebel *et al* [36, 42], Kulesza *et al* [222] and others [223, 224] support the transfer doping mechanism suggested by Maier *et al* [44]. Figure 4.4 summarises the p-type surface transfer doping of hydrogenated diamond surfaces.

In the general case of transfer doping the valence band maximum of the semiconductor must be at high energy, while there must be low-energy unoccupied states in the adsorbed material. Therefore, for the electron doping transfer mechanism to occur, a semiconductor with low ionisation energy is necessary as well as an adsorbed material with high electron affinity. The induced electron transfer between the surface acceptors and the diamond will be accompanied by electric fields that tend to equalise the Fermi levels and prevent any further electron transfer. The induced charge transfer creates band-bending towards the diamond surface and, since in the vicinity of the surface the Fermi level is below the maximum valence band, a hole accumulation layer is formed.

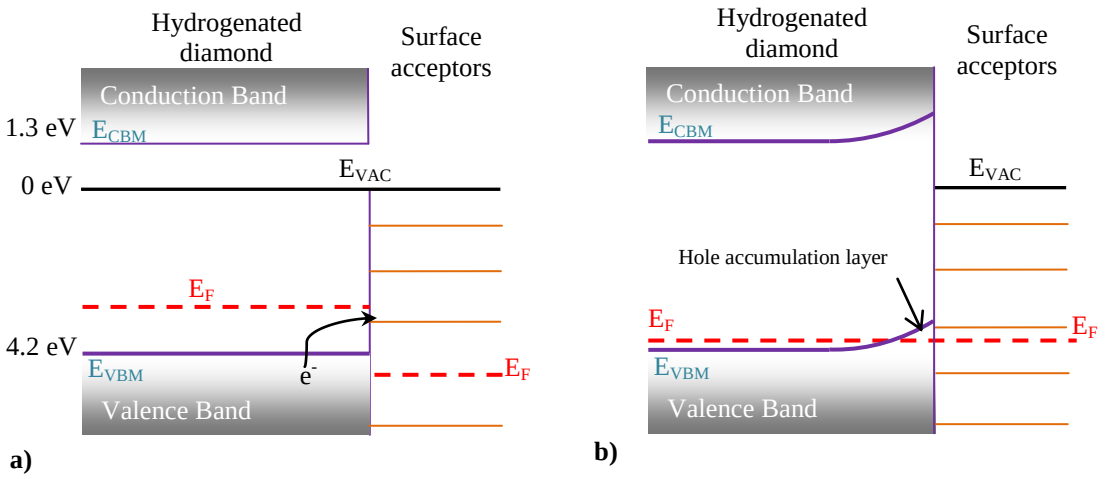

Figure 4.4 Schematic representation of the energy level of the diamond-surface acceptors material to illustrate the transfer doping of hydrogenated diamond. Scheme a) refers to the energy level before the electron transfer interface and b) displays the energy level in equilibrium after charge transfer.

As carbon has higher electronegativity[1] (χ = 2.5) than that of hydrogen (χ = 2.1), the polar carbon-hydrogen bonds on the diamond surface create surface dipoles $C^{\delta-}$- $H^{\delta+}$ with a positive component perpendicular to the surface. As a consequence the energy levels move upwards towards the vacuum energy. Therefore the electron affinity and ionisation energy are reduced in comparison with that of a clean diamond surface. The hydrogen terminated diamond surface exhibits a negative electron affinity of 1.3 eV and ionisation energy of 4.2 eV as labeled in the schematic diagram in Figure 4.4.

In contrast the termination of a diamond surface with oxygen atoms creates surface dipoles $C^{\delta+}$ - $O^{\delta-}$ since the electronegativity of oxygen (χ = 3.4) is much higher than that of carbon. Downward band-bending of the energy levels would be produced due to oxygen atom termination causing the increase of the ionisation energy and the electron affinity. Therefore it would be expected that oxygen termination of diamond surfaces would cause the depletion of holes in the sub-surface region of diamond and suppress the surface conductivity as observed experimentally [217].

[1]The eletronegativity values are referred to the Pauling scale.

The electrochemical transfer model of Maier *et al* [44], based on the electron transfer from the valence band of diamond to hydronium ions H_3O^+ can be considered as a possible microscopic mechanism for the surface transfer doping of diamond via atmospheric adsorbates. A number of different redox couples have been suggested in the literature as possible ways for the electrochemical surface transfer doping of diamond by an atmospheric adsorbate [58, 224]. Ristein *et al* [225] compared the band gap energy of clean and hydrogen terminated diamond with a number of common semiconductors. Only the valence band maximum of hydrogen terminated diamond overlaps with the atmospheric window. As a consequence, hydrogenated diamond surfaces are uniquely prone to an electrochemical surface transfer mechanism.

4.5 Experimental procedure

Microwave hydrogen plasma treatment has been applied to MPCVD (100) highly oriented polycrystalline diamond thin films. Highly oriented CVD diamond samples have been grown on p-type silicon (100) wafers following the procedure described in Chapter 3. The diamond thin films were cut into 1x1 cm square pieces and before any analysis and treatment were subjected to solvent cleaning.

The diamond thin films were analysed before and after they were returned to the 1 kW CVD system for additional exposure to hydrogen plasma. The same procedure described for the CVD diamond growth process, discussed in Chapter 3, was employed for the operation of the 1kW MPCVD system.

Details of the process conditions used for the microwave-assisted hydrogen plasma treatment applied to diamond samples are given in Table 4-1. The conditions were chosen to be approximately the same as the ones used for the growth of CVD diamond to ensure that the diamond surface was exposed to the similar amount of atomic hydrogen flux as during growth.The duration of each hydrogen plasma treatment was 4 hours. At the end of each treatment the sample was removed, via the transfer arm from the UHV CVD chamber, for analysis and loaded back again for further plasma treatment.

Parameters	Etching
H_2 gas flow (sccm)	500
Substrate Temperature (^oC)	800
Gas Pressure (Torr)	35
Microwave Power (W)	700
Total duration (h)	20

Table 4-1 Hydrogen plasma treatment process conditions.

4.6 Experimental results

The effect of the hydrogen plasma treatment on the surface morphology has been verified by the use of atomic force microscopy (AFM), the chemical structure of the near surface by X-ray photoelectron spectroscopy (XPS) and hydrogen incorporation by FTIR. Whilst all these post treatment techniques allow the investigation of the process effect on the diamond surface, mass spectroscopy and optical emission spectroscopy have been employed during the hydrogen plasma treatment in order to confirm the purity and consistency of the plasma.

4.6.1 Mass spectrometry

The quadrupole mass spectrometer response was calibrated with known concentrations of methane in hydrogen in an empty MPCVD chamber. Sufficient time was allowed to elapse before sampling since the system behaves as a perfectly stirred reactor.

Mass spectra collected during the calibration procedure are shown in Figure 4.5. Hydrogen was the only species identified by mass spectroscopy during the H-plasma stage. With 0.1 % of methane in the hydrogen mixture small quantities of methane related fragmentation peaks also became apparent. The methane signal (measured at m/z = 16) was proportional to the inlet CH_4 concentrations (of up to approximately 1.0 %) with a total flow rate of 1000 sccm. Methane decomposition is caused by plasma ignition. As shown in Figure 4.6, an increase in the yields of CH_4^+ and CH_3^+ is observed as a function of the initial CH_4 concentration.

Stable products of C_2H_2 and C_2H_4 arise from microwave plasma decomposition of diluted methane in hydrogen mixtures at microwave power less than 1kW [226]. Neither acetylene nor ethylene was detected for the plasma process parameters used. The relative proportions of those stable products are determined by the proportion of methane in the original mixture [227]. According to John *et al* [226] signals of C_2H_2 and C_2H_4 products increase as a function of the initial CH_4 concentration, while significant amounts were detected above 1.0 vol.% of CH_4 in a hydrogen gas mixture.

During each subsequent microwave hydrogen plasma treatment, the composition of the plasma was monitored by the collection of the mass spectra. Dynamic response of ions at (m/z = 15) and (m/z = 16), during the course of a H_2 plasma treatment are plotted in Figure 4.7.

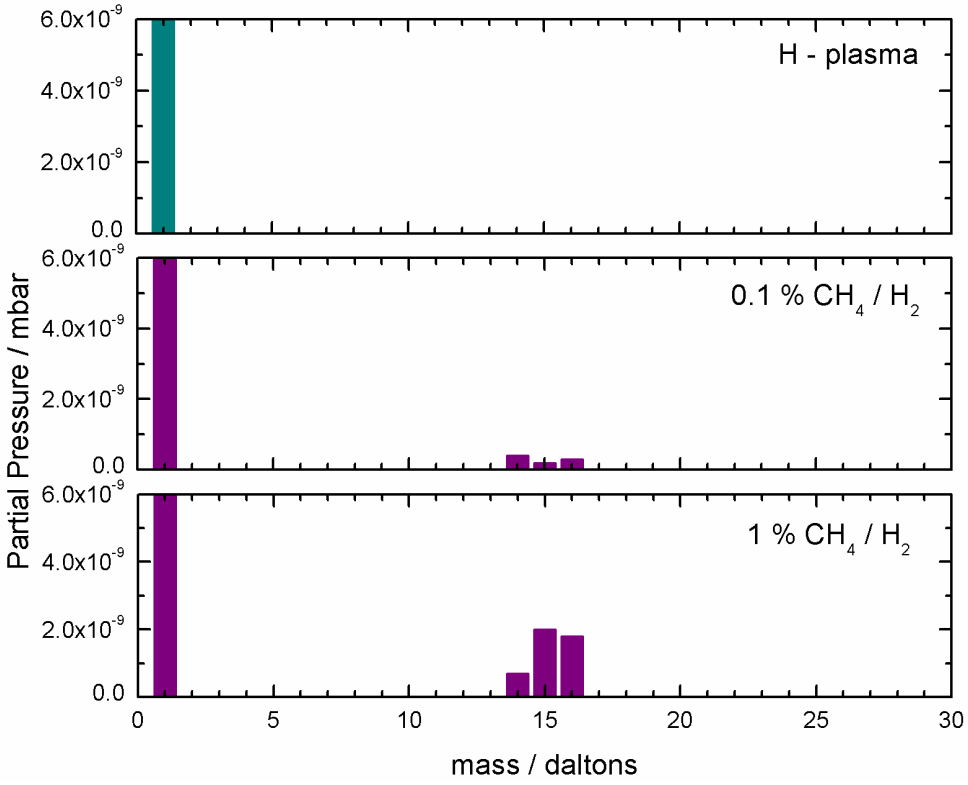

Figure 4.5 Mass spectra from hydrogen and different percentages of methane obtained from a hydrogen plasma with an empty CVD chamber (pressure, 35 torr; microwave power, 700 W and temperature, 800^{o}C).

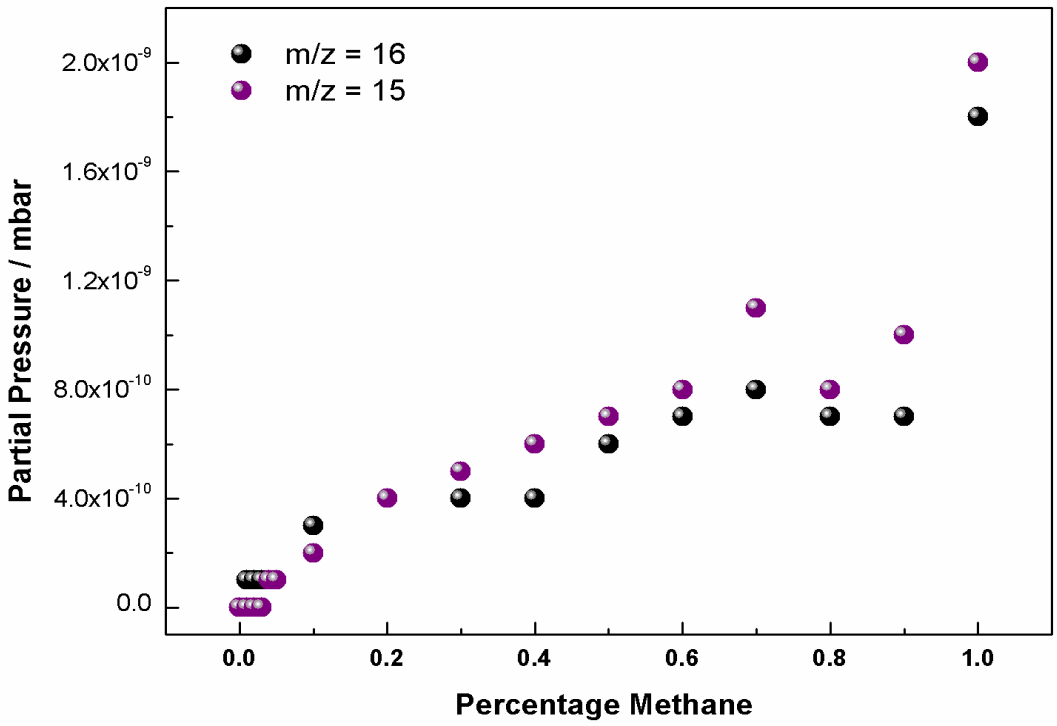

Figure 4.6 Dependency of the methyl ion yield (m/z = 15) and methane ion yield (m/z = 16) with the percentage of methane in hydrogen (pressure, 35 torr; microwave power, 700 W and temperature, 800^{o}C).

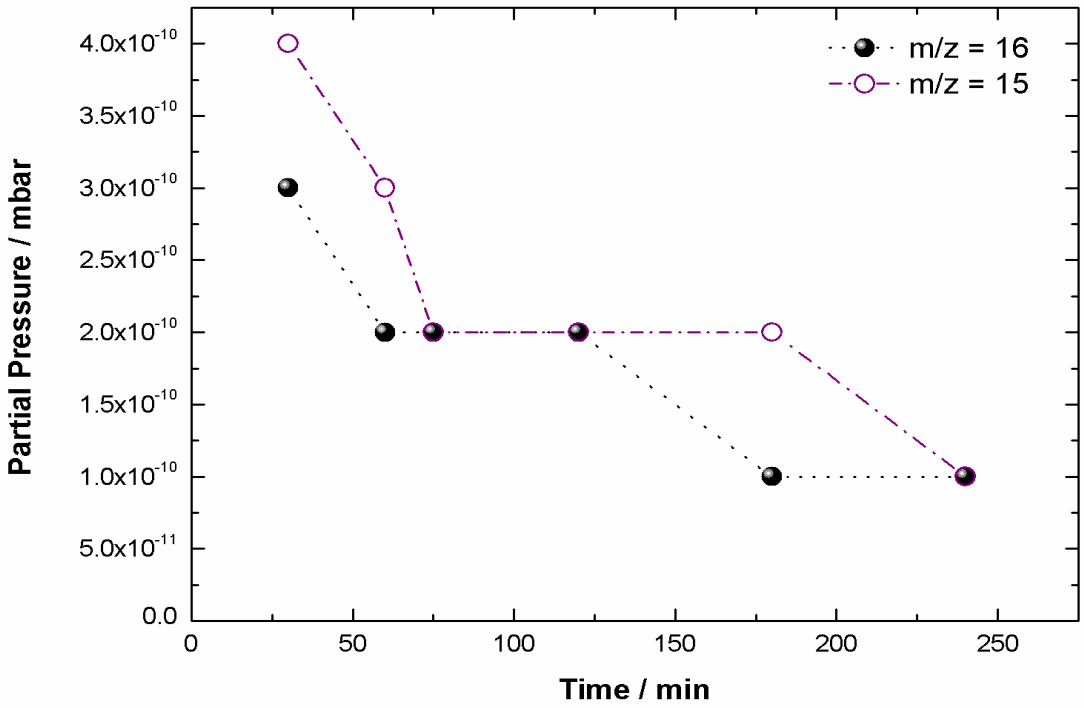

Figure 4.7 Average dependency of peak intensity at (m/z = 16) and (m/z = 15) with the duration of hydrogen plasma treatment, (35 torr, 700 W and 800 ^{o}C).

The average intensity of the peaks presented in Figure 4.7 was weak and decreased along with the treatment duration. This behaviour was observed for all five hydrogen plasma treatments. From comparison with the calibration mass spectra, the initial amount of methane inside the plasma chamber was ≤ 0.2% and approached a value below 0.1 % after 3 hrs of plasma treatment.

The measured yields of at the peaks at m/z = 15 and 16 decreased with the duration of the hydrogen plasma treatments. These results indicated that the presence of hydrocarbon in the CVD chamber was due to the etching of carbon deposited material on the chamber walls and it did not originate from the etching of the diamond surface. One might expect to that the level arising from the etching of the diamond film would be constant for the duration of the plasma treatment and do not decrease over the course of time.

4.6.2 Optical emission spectroscopy

Optical emission spectra were collected during the hydrogen plasma treatments. The characteristic Balmer emission lines, H_α (656.2 nm) and H_β (486.1 nm) of hydrogen were observed as shown in Figure 4.8. The emission lines from CH_x species were not observed at any time during the hydrogen plasma treatments.

4.6.3 Scanning electron microscopy

Scanning electron microscopy has been employed to examine the diamond thin films prior and after the hydrogen plasma treatments. No morphological changes have been observed to occur on the diamond surface on the magnification scale of SEM, as shown in Figure 4.9.

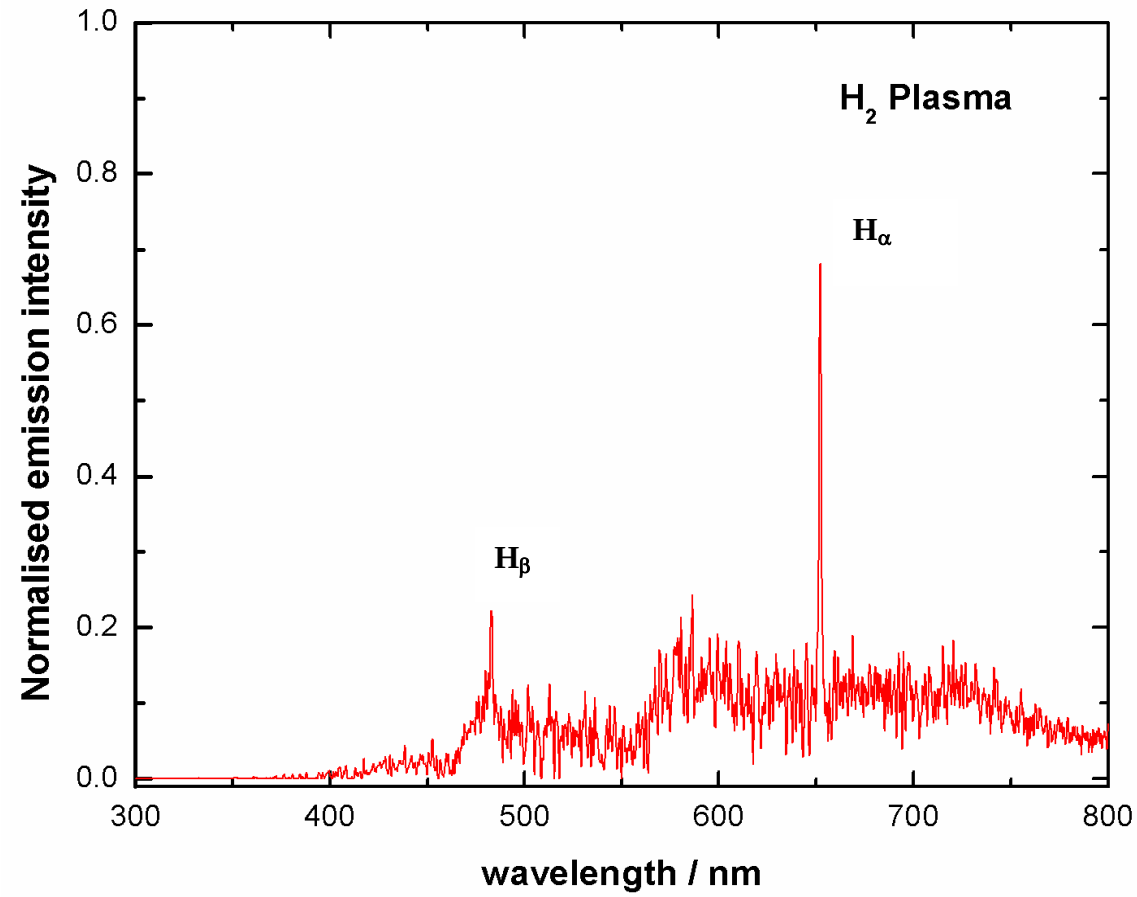

Figure 4.8 Optical emission spectra from the hydrogen plasma (35 torr, 700 W and 800°C).

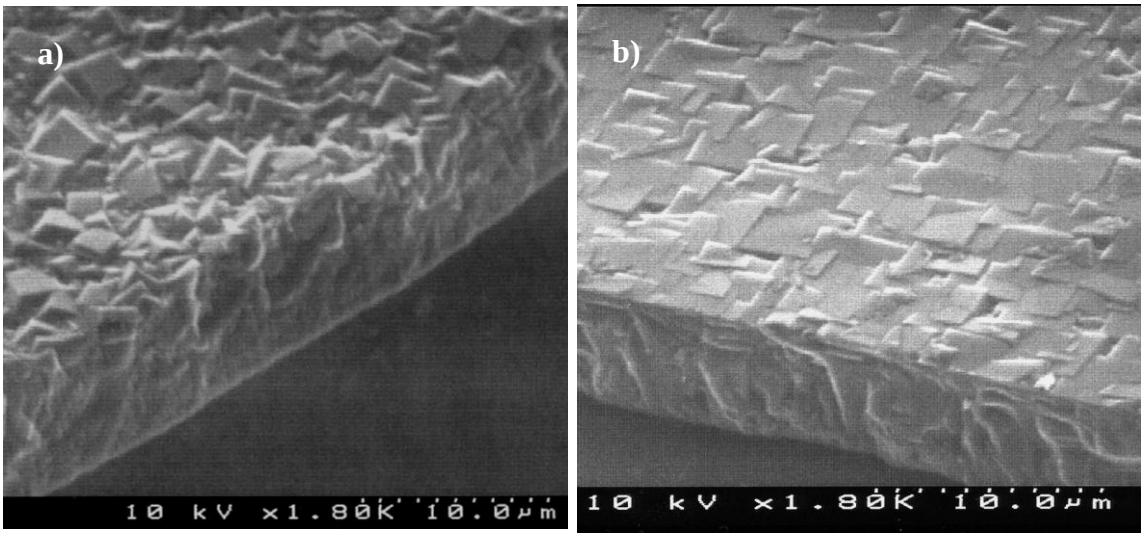

Figure 4.9 SEM image of a) azimuthally disordered and b) (100) highly oriented CVD diamond thin film after 20 hrs of microwave-hydrogen plasma treatment (pressure, 35 torr; microwave power, 700 W and temperature, 800°C).

4.6.4 Atomic force microscopy

Atomic force microscopy has been used to analyse the surface of a specific area on the diamond thin films prior and after each plasma treatment. AFM images of the same location of (100) highly oriented CVD diamond film treated in microwave hydrogen plasma at substrate temperature of 800^{o}C, pressure of 35 torr, gas flow rate of 500 sccm and applied microwave power of 700 W, are shown in Figure 4.10.

No appreciable morphological changes have been observed on the (100) highly oriented CVD diamond crystallites, including either pitting or roughening of the diamond surface. Some small raised features appeared on the diamond crystallites surface after the plasma treatment, and some raised features also remained. It is not clear if those features are due to diamond or contamination resulting from material handling and processing.

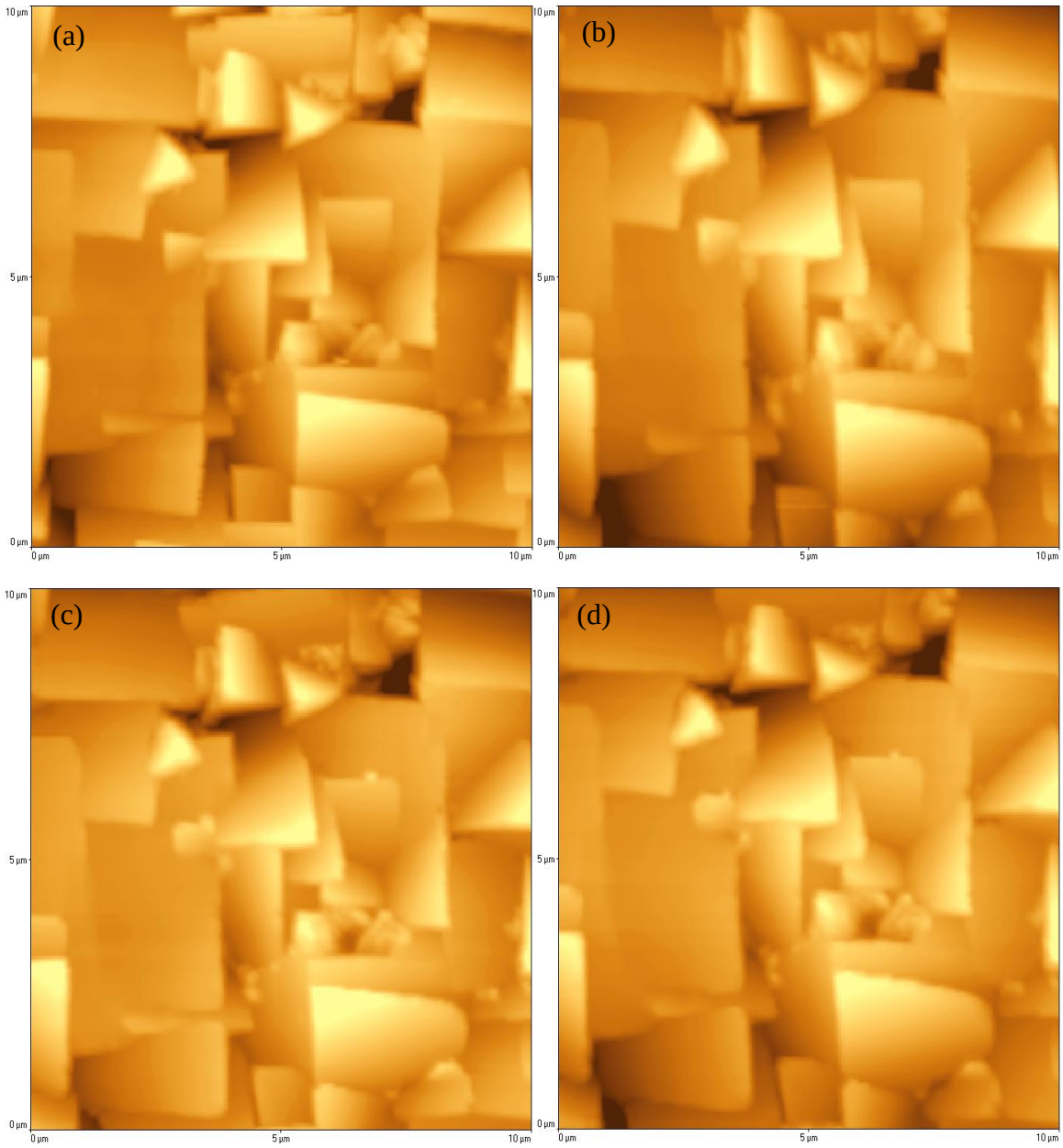

Figure 4.10 AFM images of the same (100) highly oriented CVD diamond crystallites after successive microwave-assisted hydrogen plasma treatments. (a) as-grown film, (b) 8 hours, (c) 16 hours and (d) 20 hours.

By selecting a specific (100) diamond crystallite from the (100) highly oriented CVD diamond film the surface morphology of the crystallite has been examined over the entire duration of the hydrogen plasma treatments. The SPMLab NT Vers.5 Analysis software supplied by Topometrix ThermoMicroscopes enabled the analysis of cross-sections on the AFM topographic images. Figure 4.11 shows the AFM topographic image and cross-section taken from the as-grown {100} highly oriented CVD diamond crystallites.

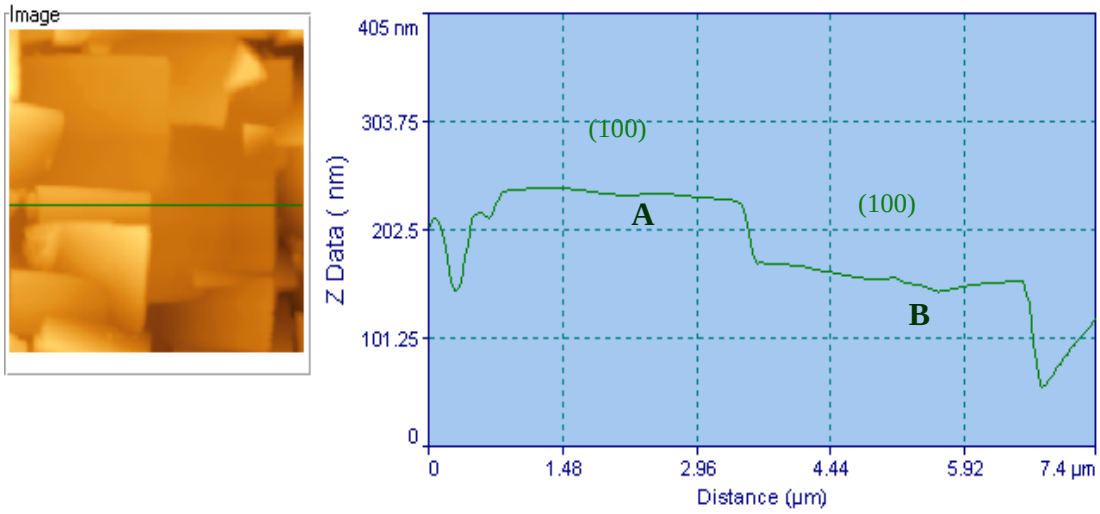

Figure 4.11 AFM topographic image and cross-section of as-grown {100} highly oriented CVD diamond crystallites.

On a specific location of the surface of the first crystallite (labelled as ***A***) was relative smooth whilst the surface of the second crystallite (labelled as ***B***) comprised a small crater of 325 ± 10 nm width and small triangular feature of 3 nm height.

Figure 4.12 (a-d) shows the surface cross-sections taken from the AFM topographic images from the ***B*** labelled crystallite of Figure 4.11, before and after each consecutive hydrogen plasma treatment.

The triangular feature vanished after the sample had been subjected to hydrogen plasma treatment for 4 hours. The lateral dimensions of the crater, towards the <110> diamond directions, have been increased (Figure 4.12 b). The crater width after 4 hours of hydrogen plasma treatment was 587 ± 10 nm.

As further hydrogen plasma treatment was applied to the (100) diamond surface the lateral dimensions of the crater feature increased further (Figure 4.12 c). The hillock highlighted in Figure 4.12 (a-d), reduced its lateral dimensions after 8 hours of hydrogen plasma treatment (4.12 c).

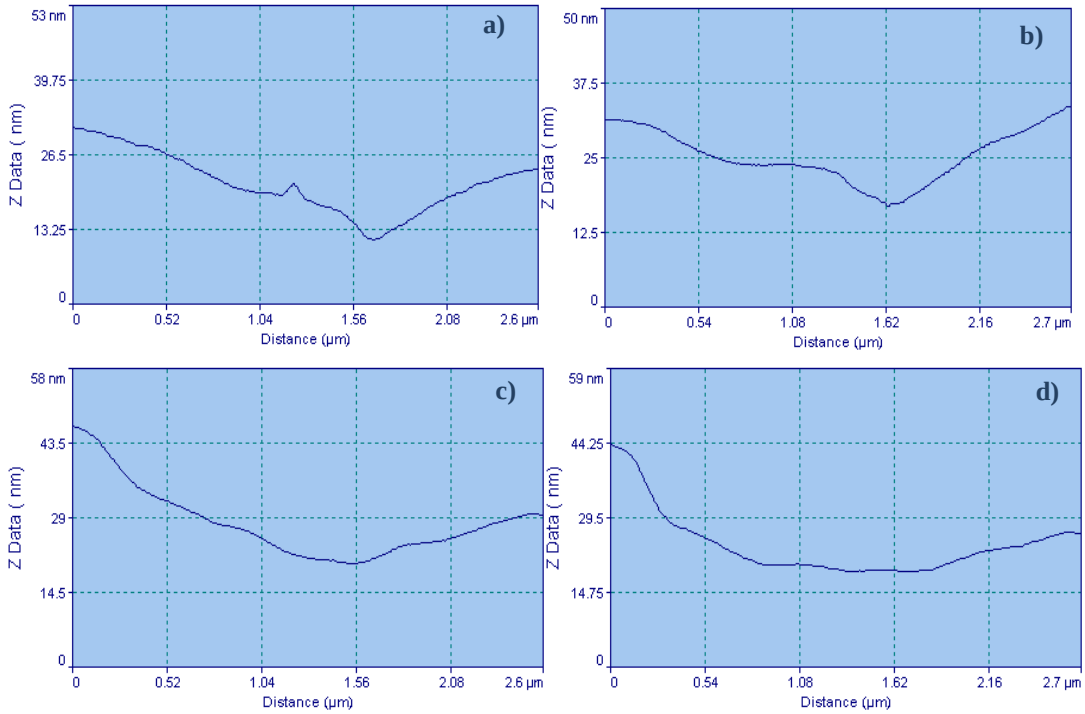

Figure 4.12 AFM topographic cross-sections of a) as-grown and subjected to b) 4 hours c) 8 hours and d) 12 hours of hydrogen plasma treatment of (100) diamond crystallite.

After 12 hours of subsequent hydrogen plasma treatments (Figure 4.12 d), the cross-section of the (100) diamond surface shows different surface morphology in comparison with the as-grown diamond (100) surface (Figure 4.12 a). Due to lateral etching along the <110> directions of the (100) diamond surfaces the crater dimensions have increased dramatically to 800 nm width and the hillock has reduced its height considerably.

On the left side of the cross-section a step feature appeared after 8 hours of hydrogen plasma treatment with a (110) diamond facet. As the (100) diamond surface was subjected to further hydrogen plasma treatment (16 hours in total) the surface hillock decreased in height and lateral dimensions (Figure 4.13 (a)). The crater has increased further its lateral dimensions and the diamond step on the left of the cross-section increased its height.

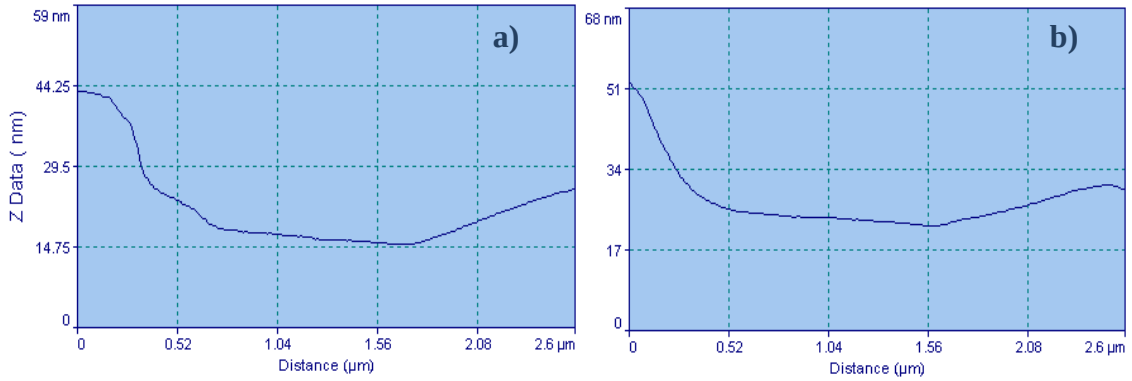

Figure 4.13 AFM topographic cross-sections of (100) CVD diamond crystallite subjected to a) 16 hours and b) 20 hours of hydrogen plasma treatment.

After the total 20 hours of hydrogen plasma treatment the (100) diamond surface, as it shown in Figure 4.13 (b), was flatter. The hillock was etched away while the crater lateral dimensions had increased. The (110) facet of the step on the left on the cross-section was smoother.

From the AFM topographic cross-sections it was feasible to deduce a value for the vertical and lateral etch rates of the (100) diamond surface induced by the hydrogen plasma treatments. The value of 14 ± 6 nm/hour for the vertical etch rate on the (100) diamond surface, as well as the value of 28 ± 4 nm/h for the lateral etch rate on the <110> directions were obtained from these studies. The measured etch rates values indicated anisotropic etching occurred on the (100) highly oriented CVD diamond by microwave hydrogen plasma treatment. Isotropic etching of (100) diamond surface cannot be supported by the present results, as equal vertical and horizontal etch rates on the diamond surface would have resulted in increased depth and width of the surface crater structure. According to STM investigations of hydrogen plasma etching of (100) diamond surface isotropic etching occurs at lower substrate temperatures (e.g. ~500^{o}C [200]) than 800^{o}C that has been used for the present hydrogen plasma treatments. In contrast the lateral increase of the crater dimensions on the (100) diamond surface supports the anisotropic etching model suggested by Ri *et al* [30] and verified experimentally by others [27, 30,185, 187-189, 197].

The AFM topographies of the 20 hours hydrogen plasma treated (100) highly oriented CVD diamond films revealed that the step feature on the left side of the cross-sections in Figure 4.13 (a-b) is the edge of (100) diamond crystallite (labelled as ***C*** in Figure 4.14). The C crystallite is shown on the AFM topographic cross-section on the hydrogen plasma treated (100) highly oriented CVD diamond film in Figure 4.14. It has been discussed in Chapter 2 that the growth of polycrystalline CVD diamond films proceeds by competitive growth between individual crystallites. The present results suggested that as the two neighbour (100) highly oriented diamond crystallites intersected, in this case crystallites ***B & C***, lateral growth of (100) diamond ***C*** crystallite surface occurred on the surface of ***B*** (100) diamond crystallite surface. The crater structure observed on the surface of the as-grown (100) diamond surface, Figure 4.12 (a), was a structural feature due to the lateral growth of ***C*** (100) diamond crystallite on the surface of ***B*** (100) diamond crystallite and due to the vertical growth of the ***B*** (100) diamond surface.

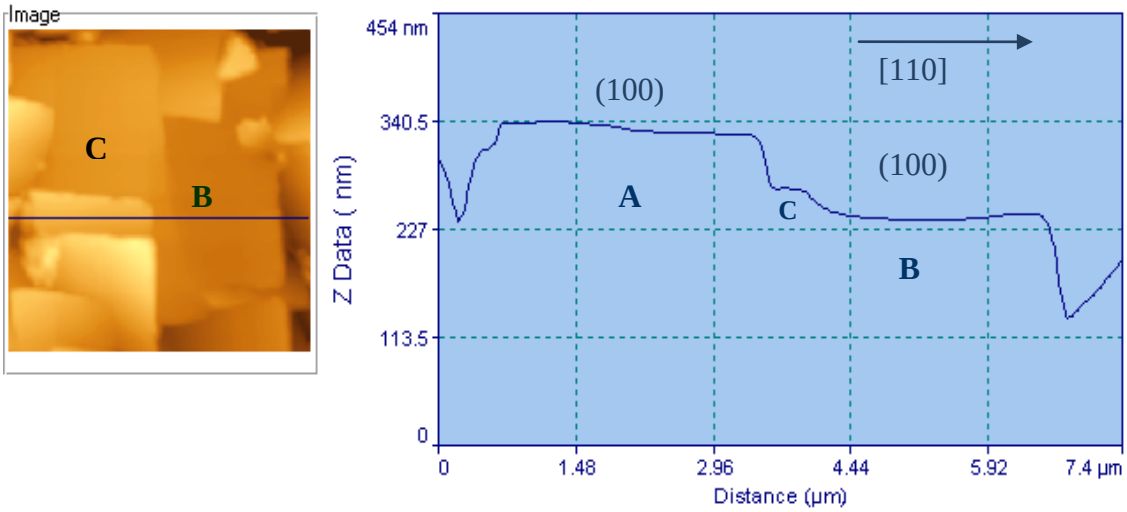

Figure 4.14 AFM topographic image and cross-section of (100) highly oriented CVD diamond crystallites that have been subject to 20 hours of hydrogen plasma treatment (35 torr, 700 W and 800^{o}C).

Figure.4.15 shows the variation of the surface roughness after 0, 4, 8, 12, 16 and 20 hours of microwave hydrogen plasma treatment. The SPMLab NT Ver.5 Analysis software enables the measurement of the surface roughness on any selected area of the AFM topographic images. The data plotted on Figure 4.15 are the average values of measurements taken from ten different {100} CVD diamond crystallites from the highly oriented diamond film. The crystallite tilts in orthogonal directions have been removed before the surface roughness data were collected using the levelling function of the AFM software.

The surface roughness of (100) highly oriented diamond crystallites decreases after each treatment. After prolonged exposure of the (100) diamond surface to microwave hydrogen plasma an average surface roughness value of ~ 1 nm has been attained.

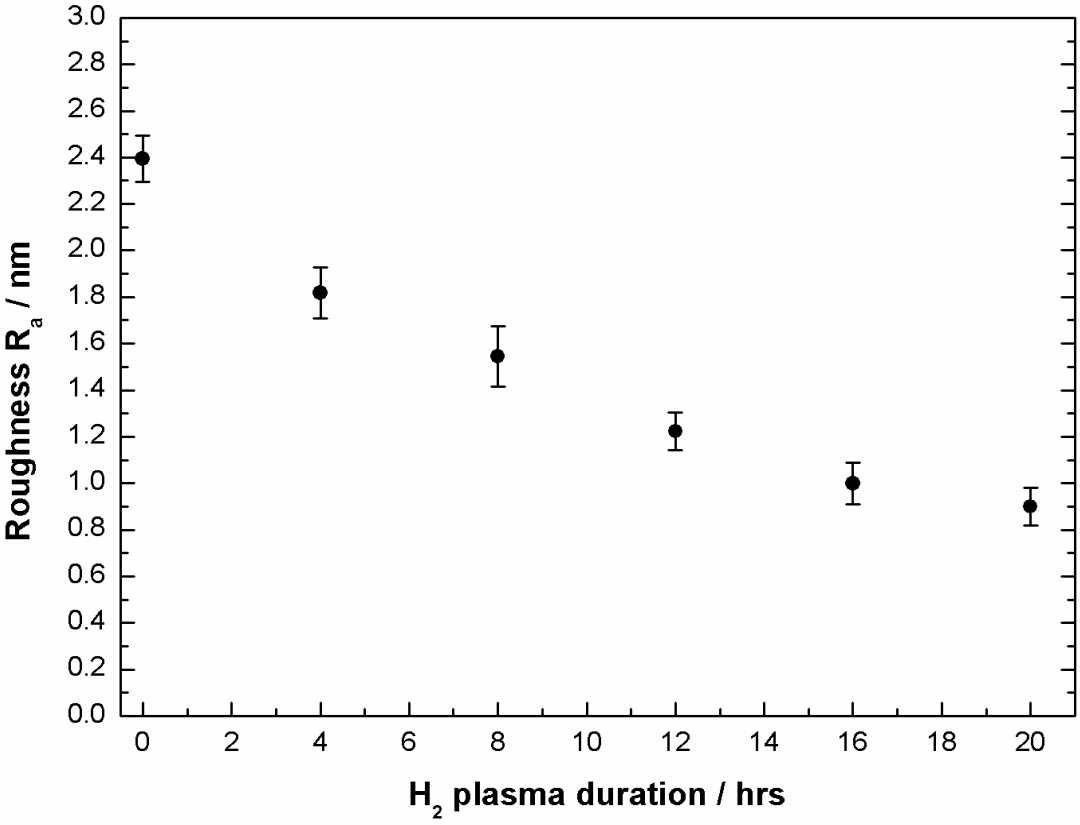

Figure 4.15 Variation of mean roughness (R_a) measured from AFM analysis, over the surface of ten {100} CVD diamond crystallites as a function of the duration of the *ex situ* microwave-assisted hydrogen plasma treatment. Error bars are the standard deviation of the mean.

The present AFM topographic results show the smoothing of the (100) diamond surface after exposure to atomic hydrogen produced by microwave- CVD plasma. The average measured value of the surface roughness reduced from 2.4 nm for the as-grown surface to 1 nm after 20 hours of hydrogen plasma.

The use of AFM topographic cross-section analysis enabled the measure of the vertical and lateral etch rates of (100) diamond at the present hydrogen plasma conditions used. The measured vertical etch rate of 14 ± 6 nm/h for the (100) diamond surface is much lower than the already reported etch rates of 150 nm/h [207] and 50 nm/h [212]. A direct comparison between the present results work and the previous published data

cannot be made as diamond samples have been growth under different conditions and gas mixtures, as well as due to the different type of CVD reactors and hydrogen plasma process conditions have been used. It has already been demonstrated experimentally and theoretically that sp^2 carbon would be etched faster in comparison with sp^3 carbon by hydrogen plasma treatment. High quality (100) highly oriented CVD diamond films are likely to be etched at a lower etch rate in comparison with other polycrystalline CVD diamond films. (100) diamond surfaces have been etched preferentially along the <110> diamond direction in comparison with the vertical etch rate on the (100) diamond surface.

We have observed the etching and removal of hillocks from the diamond surface. Previously published STM analysis of hydrogen plasma treatment of (100) CVD diamond crystallites shows that hydrogen etches away the hillocks formed during growth on the diamond surface and microscopic steps have been observed on the etched surface [195]. The resolution of the AFM topographic images was not adequate to examine formation of atomic steps on the <110> directions on the (100) diamond surface. Therefore it is not possible from the present data to deduce a detailed microscopic model for the hydrogen plasma etching of (100) diamond surface.

Ri *et al* [30] observed the smoothing of the (100) diamond surface after exposure to hydrogen plasma treatment and attributed the smoothening effect of hydrogen plasma treatment to anisotropic etching of step edges. Whilst the smoothing effect of hydrogen plasma treatment is identical to that reported by Ri *et al* [30] for natural diamond, the appearance of square-etch pits on the (100) surface following etching reveals significant differences. For natural diamond Stallcup *et al* [197] observed that square etched pits are formed due to dislocations and etching proceeds isotropically on the S_A and S_B steps. Lee and Badzian [143, 192] also observed the formation of square etch pits on the surface of natural (100) diamond after hydrogen plasma exposure to be correlated with the surface misorientation angle. The nature of nuclei responsible for the formation of etch pits in natural diamond is uncertain. Surface defects, such as crystal dislocations and impurities can be more reactive under microwave hydrogen plasma, as they often include amorphous carbon or graphite. Etching would be preferential on those surface features and it may lead to the formation of surface etch pits.

For polycrystalline (100) CVD diamond films the dislocation density has been found to be in the order of $2x10^{10}$ /cm^2 localised near the grain boundaries of the crystallites [215]. Such dislocations have induced square etch pits after hydrogen plasma treatment on the surface of polycrystalline diamond films [215]. Square-etch pits have not been observed by the AFM topographic results presented here for the 20 hours duration of hydrogen plasma treatment. In the model presented here, hydrogen atoms saturate the dangling bonds on the (100) diamond surface. The step edges would be more reactive and removal of the step edges would occur faster than etching at the intervening terraces. As the density of the atomic steps on the terraces approaches a fundamentally small value, a true layer-by-layer mechanism will be attained leading to the formation of atomically smooth (100) diamond surfaces.

4.6.5 Fourier Transform Infra-Red Spectroscopy

Transmission FTIR spectra of an as-grown (100) highly oriented CVD diamond film on silicon and after it has been exposed to microwave hydrogen plasma treatment are shown in Figure 4.16. The diamond sample was ≈ 1 cm^2 and an aperture was used to ensure that the IR beam collected data from the film. The spectra were not corrected for the presence of the silicon reference.

The principal components of the as-grown diamond film present on the IR spectrum are: CH_x peak (3000-2800 cm^{-1}), SiO_2 asymmetric stretch (1100 cm^{-1}), SiC peak (800 cm^{-1}) and the substrate Si peak (600 cm^{-1}).

The CH_x and Si peaks can be clearly be identified in the spectrum. However the peaks due to SiO_2 and SiC are relatively minor in the untreated film.

After the diamond film on silicon had been subjected to H_2-plasma treatment for 4 hours a very strong and broad SiC peak appears in the spectrum. There are no changes observed to the other silicon related absorption bands.

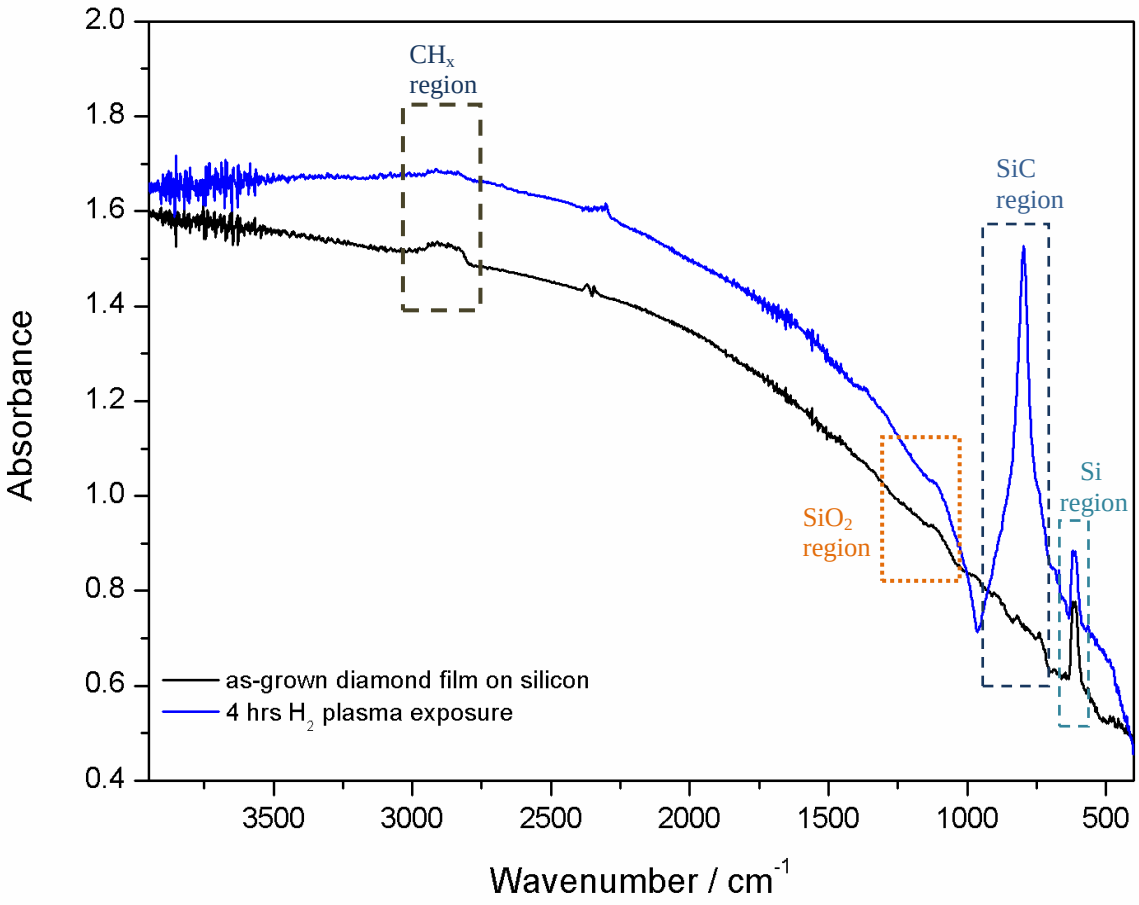

Figure 4.16 FTIR spectra of an as-grown (100) highly oriented CVD diamond film deposited on silicon treated with a hydrogen plasma at 800°C and 35 Torr.

The intensity of the stretching vibrational band of CH_x decreased after exposure to hydrogen plasma treatment. Despite purging the sample chamber with dry nitrogen it was not feasible to eliminate the presence of water vapour absorption at 4000-3600 cm^{-1} and 2100-1200 cm^{-1}, and CO_2 at 2400-2300 cm^{-1}.

A very strong IR absorption of the SiC band has been observed for the hydrogen plasma treated diamond film. The SiC band usually is observed on the IR absorption spectrum of CVD diamond films grown heteroepitaxially on silicon substrates with the pre-treatment (carburization) and bias enhanced nucleation steps. Experimental evidence shows that the intensity of the SiC absorption band decreases as the diamond film thickness increases [228].

For the further analysis of the broad SiC absorption peak observed at 900-700 cm^{-1}, the absorption due to silicon reference has been removed and the data have been normalized. Figure 4.17 shows the variation of the SiC band with the duration of the plasma treatment. The intensity of the band increased with the prolonged exposure to plasma and the band shape became sharper.

The SiC band has been deconvoluted with three Gaussian and Lorentzian mixture peaks bands, as this was the minimum number of the bands which enabled a good fit to the spectrum. The three bands were: one sharp band at 797 cm^{-1} and two low broad bands centered at ~ 750 cm^{-1} and ~837 cm^{-1}. The absorption peak at 797 cm^{-1} has been assigned to the transverse optical TO phonon vibration of cubic silicon carbide (β-SiC) [165]. The peak observed at 750 cm^{-1} has been assigned to the SiC stretching mode [229] that is usually observed at 760 cm^{-1}. The absorption band at 832 cm^{-1} could be assigned to amorphous silicon carbine [228], as shown in Table 3-2.

The peak wavenumber, FWHM and percentage of the Gaussian-Lorentzian components derived from the peak fitting of the broad SiC peak are shown in Figure 4.18. The data are presented as a function of the duration of the hydrogen plasma treatment.

The sharp peak at 797 cm^{-1} dominates the broad SiC envelope for all the measured spectra. The peak percentage area increases slightly with the exposure to the hydrogen plasma. The FWHM increases up to 12 hrs of treatment while further exposure to hydrogen plasma reduces the FWHM, indicating a very sharp band.

The band percentage area observed at 750 cm^{-1} remained constant (± 3%) up to 16 hrs of treatment, while a reduction of ~ 10 % observed after 20 hrs of hydrogen plasma exposure. The same trend was observed for the FWHM, the broad peak reduces in width after the 20 hrs of hydrogen treatment. A small reduction has been observed in the FWHM and percentage area of the peak at 832 cm^{-1}, after 12 hrs H_2-plasma treatment. Subsequent exposure to hydrogen plasma increased and restored the initial shape of the peak

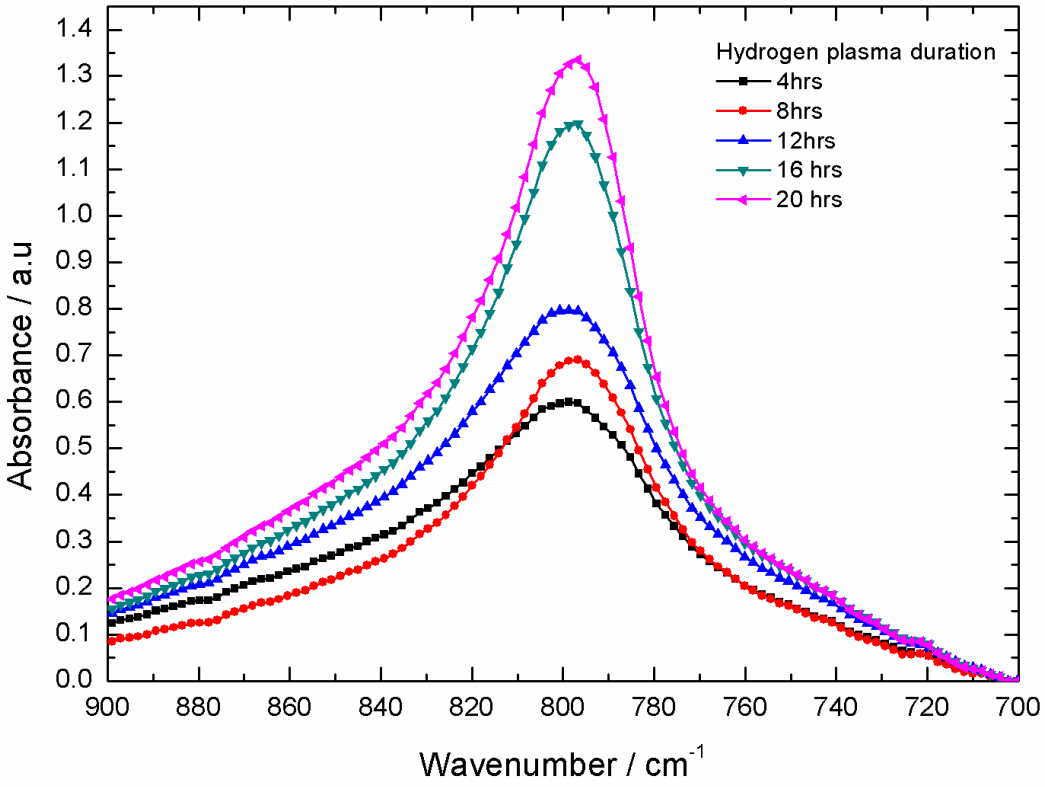

Figure 4.17 FTIR spectra of the SiC band dependence on the exposure to hydrogen plasma treatment.

Wavenumber/ cm^{-1}	FWHM /cm^{-1}	Area / %	Assignment	Ref
750	72	24.5	SiC stretching mode	**[229]**
797	39	57.1	cubic β-SiC	**[165]**
837	62	18.4	a:SiC	**[228]**

Table 4-2 Peak components of the deconvoluted SiC infrared absorption band.

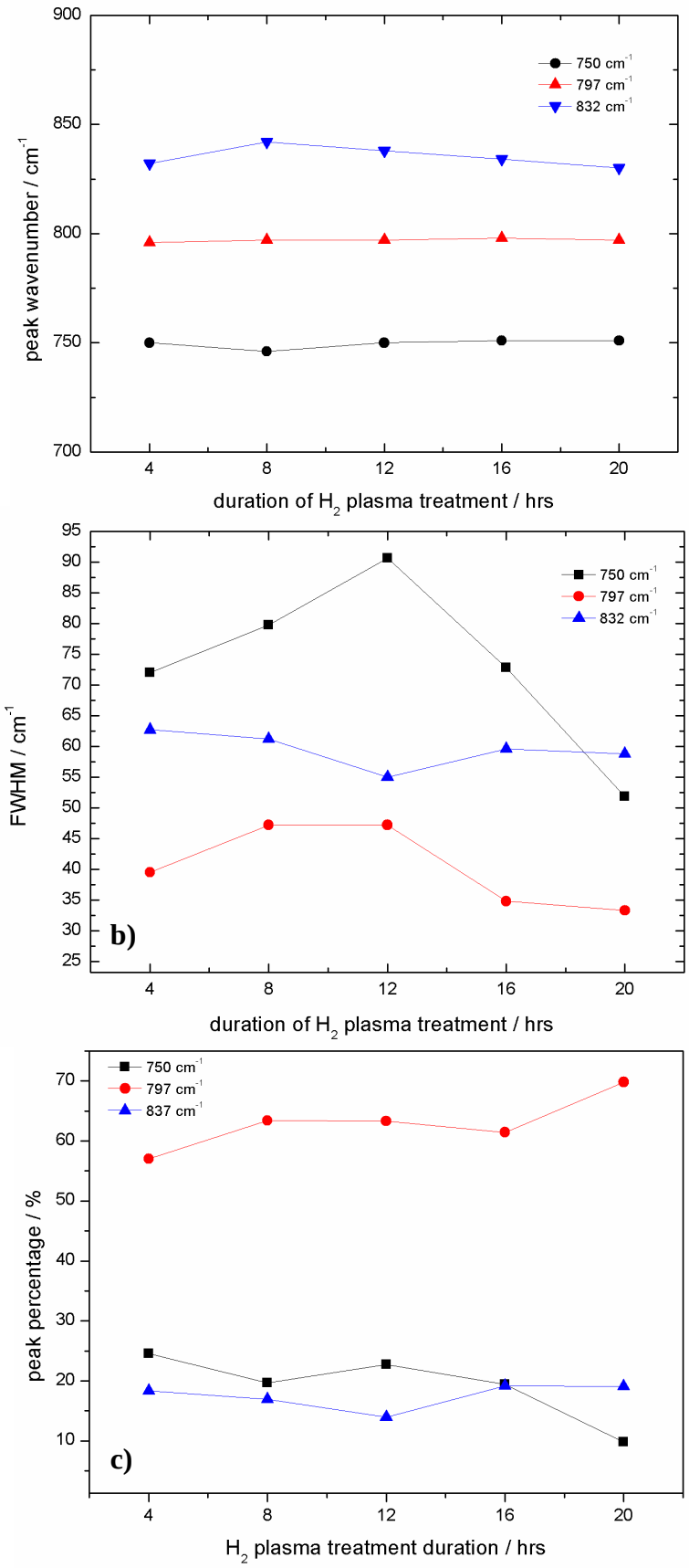

Figure 4.18 a) wavenumber, b) FWHM and c) percentage area of the SiC band peak components.

Whilst a very weak signal of SiC has been observed for the as-grown diamond film, the FTIR data indicated the presence of silicon carbide on the material after exposure to the hydrogen plasma.

The formation of silicon carbide as an interfacial layer between the silicon substrate and the diamond film during the growth process has been confirmed experimentally [167, 233]. Silicon carbide is formed by diffusion of carbon atoms into the silicon substrate during CVD diamond growth. It is clear that the silicon carbide layer is formed during either the carburisation and/or the bias step, as both CVD diamond growth stages provide hydrocarbon species to the silicon substrate. Typically the thickness of the SiC would be few atomic layers, since its thickness would depend on the availability of Si atoms which originate from the silicon substrate. The growth of SiC has been achieved by using gas mixtures of CH_4 and H_2 with or without SiH_4 over silicon substrate [231] by HFCVD and conditions similar to those used for diamond CVD deposition.

The present data showed only a thin layer of interfacial silicon carbide for the as-grown diamond film on silicon, its major detection was made following hydrogen plasma treatment.

The formation of silicon carbide without the presence of silicon precursor gas can be achieved through the following reaction paths; atomic hydrogen would react with the silicon substrate either by etching or diffuse into the silicon substrate. The etching of silicon would occur through the reaction:

$$Si + H \rightarrow SiH^{*} \qquad \text{(reaction 1)}$$

and SiH^{*} radicals would be formed. In the presence of CH radicals the formation of silicon carbide can achieved through:

$$SiH + CH - SiC + H_2 \qquad \text{(reaction 2)}$$

Following the subsequent microwave hydrogen plasma treatments, it was observed that the (uncoated with diamond) silicon substrate had changed color and it looked darker. According to the present data the formation of silicon carbide has been on the silicon substrate area that surrounds the CVD diamond film.

It is not completely understood how the formation of silicon carbide was enhanced on the silicon substrate from a hydrogen plasma treatment without a hydrocarbon source. Optical emission spectroscopy has not observed any hydrocarbon species during the course of the plasma treatments. The small hydrocarbon peaks measured by mass spectroscopy decreased with the duration of the plasma treatments. If the measured hydrocarbon peaks originated from the diamond surface then they would have been expected to display constant values for the duration of the treatments. As their intensity decreases it can be postulated that they originate from carbon deposited on the chamber walls, which can be etched away by the hydrogen plasma. Although atomic force microscopy data show that redeposition of diamond did not take place during the course of the plasma treatments, instead AFM analysis showed etching of the diamond surfaces with reduction of the surface roughness. Simultaneously non-sp^3 carbon etched from the diamond surfaces could be a possible source of hydrocarbons for the enhancement of silicon carbide.

The intensity of the CH_x stretching band at 3000 – 2800 cm^{-1}, was apparently reduced after the diamond film was subjected to hydrogen plasma treatment. Infrared absorption signals collected after subsequent hydrogen plasma treatment were very weak and unreliable for ensuring deconvolution analysis. For that reason data only from the as-grown and samples subjected to 4 hrs and 6 hrs of hydrogen plasma treatment (800^{o}C and 35 Torr) were deconvoluted. The deconvolution of the CH_x stretching band was performed by fitting the minimum number of component peaks required to achieve a satisfactory and repeatable fit, as shown in Figure 4.19.

The best fit deconvolution of the CH_x vibrational band was performed using five Gaussian-Lorentzian bands. Only for the sample treated for 16 hrs was necessary to use a sixth band. Details of the peak components of the as-grown diamond film are listed in Table 4-3 along with their FWHM and relative percentage area.

Wavenumber / cm^{-1}	FWHM / cm^{-1}	Area /%	Assignment
2822	25.9	11.9	sp^3 CH on (111)
2846	34.4	15.4	sp^3 CH_2 symmetric
2879	34.8	42.3	sp^3 CH_3 symmetric
2918	39.1	21.5	sp^3 CH_2 asymmetric
2944	34.4	8.9	sp^3 CH_3 asymmetric

Table 4-3 Peak components of the CH_x infrared absorption bands [172-176].

On polycrystalline diamond films most of the hydrogen is expected to be located at the grain boundaries, and it would occur in different hydrocarbon groups including CH, CH_2 and CH_3.

From the present data it is possible to identify that there is no discernible CH sp^2 or sp like carbon groups in the film, which are assigned to absorption peaks above 3000 cm^{-1}, as would be expected for a high quality diamond film. The band component observed at 2822 cm^{-1} can be assigned to stretching vibration of sp^3 CH groups on (111)-like diamond surface. The peaks components observed at 2846 cm^{-1} and 2918 cm^{-1} are likely to be the symmetric and asymmetric C-H stretching vibration modes of sp^3 CH_2 groups that usually appear at 2850 cm^{-1} and 2920 cm^{-1} respectively as indicated in previous studies. While the peak at 2879 cm^{-1} corresponds to the symmetric stretching vibration mode of sp^3 CH_3 groups normally observed at 2880 cm^{-1}, and the corresponding asymmetric vibration mode of sp^3 CH_3 group is typically observed around 2960 cm^{-1}, in those spectra an sp^3 CH_3 component peak was observed at 2944 cm^{-1}.

The sixth peak component necessary for the satisfactory fit of the deconvolution process of the 16 hrs plasma treated diamond sample, observed at 2984 cm^{-1} was assigned to the absorption peak of sp^3 CH groups on the reconstructed (100)-(2x1) diamond surface.

Details of the peak components, (wavenumber, FWHM and percentage area) produced by the deconvolution process of the CH_x band envelope are presented in Figure 4.20. From the present data, it was observed that there no change in peak wavenumber within the measured experimental error, for the duration of the plasma treatments. A remarkable decrease in the FWHM and percentage area of the peak at 2879 cm^{-1} has been observed after the plasma treatment.

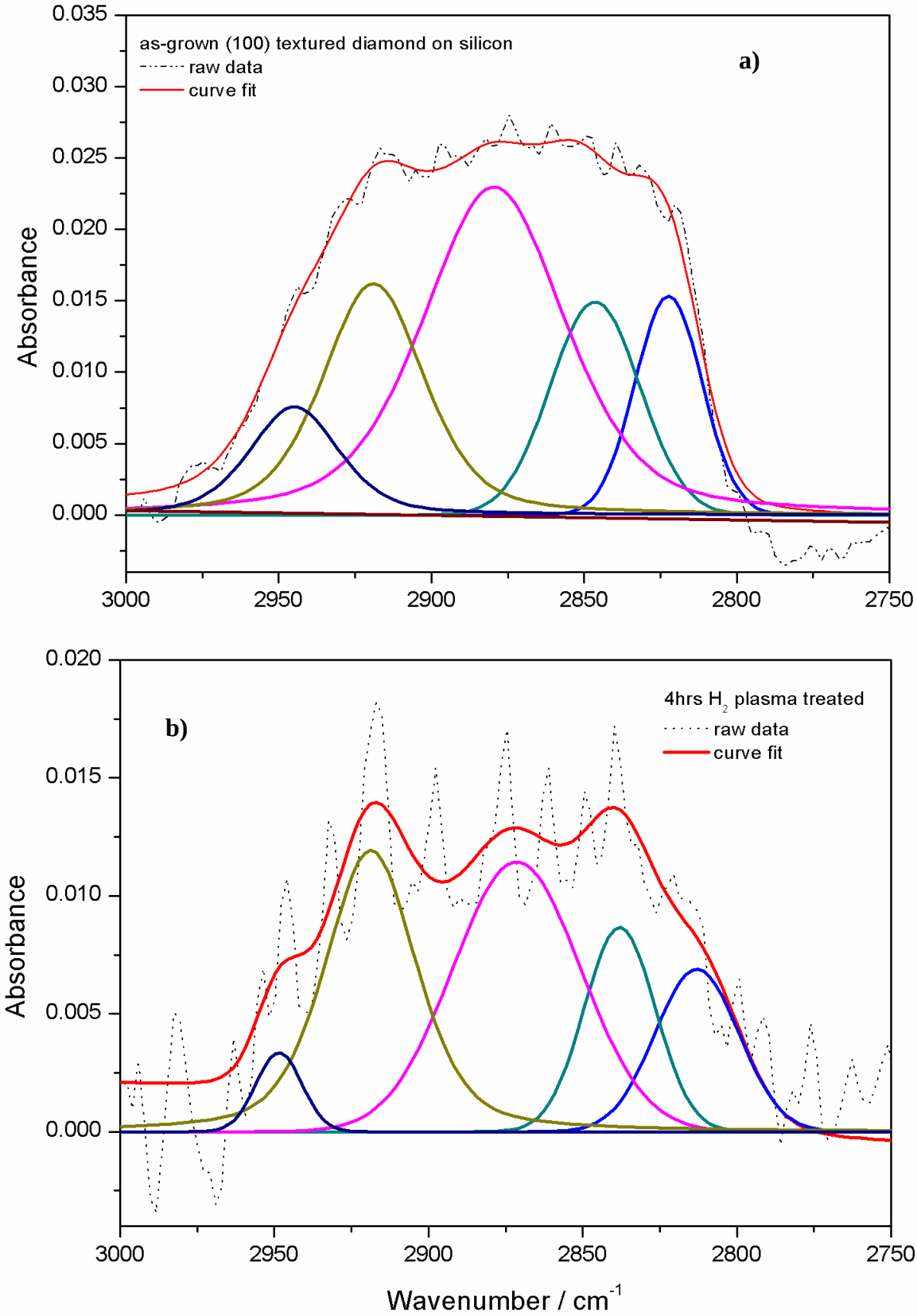

Figure 4.19 Deconvoluted CH_x stretching band of an a) as-grown (100) highly oriented CVD diamond on silicon and b) after subject to a microwave hydrogen plasma for 4 hrs at 800°C and 35 Torr. The deconvolution resulted into five Gaussian-Lorenzian peaks (colored line).

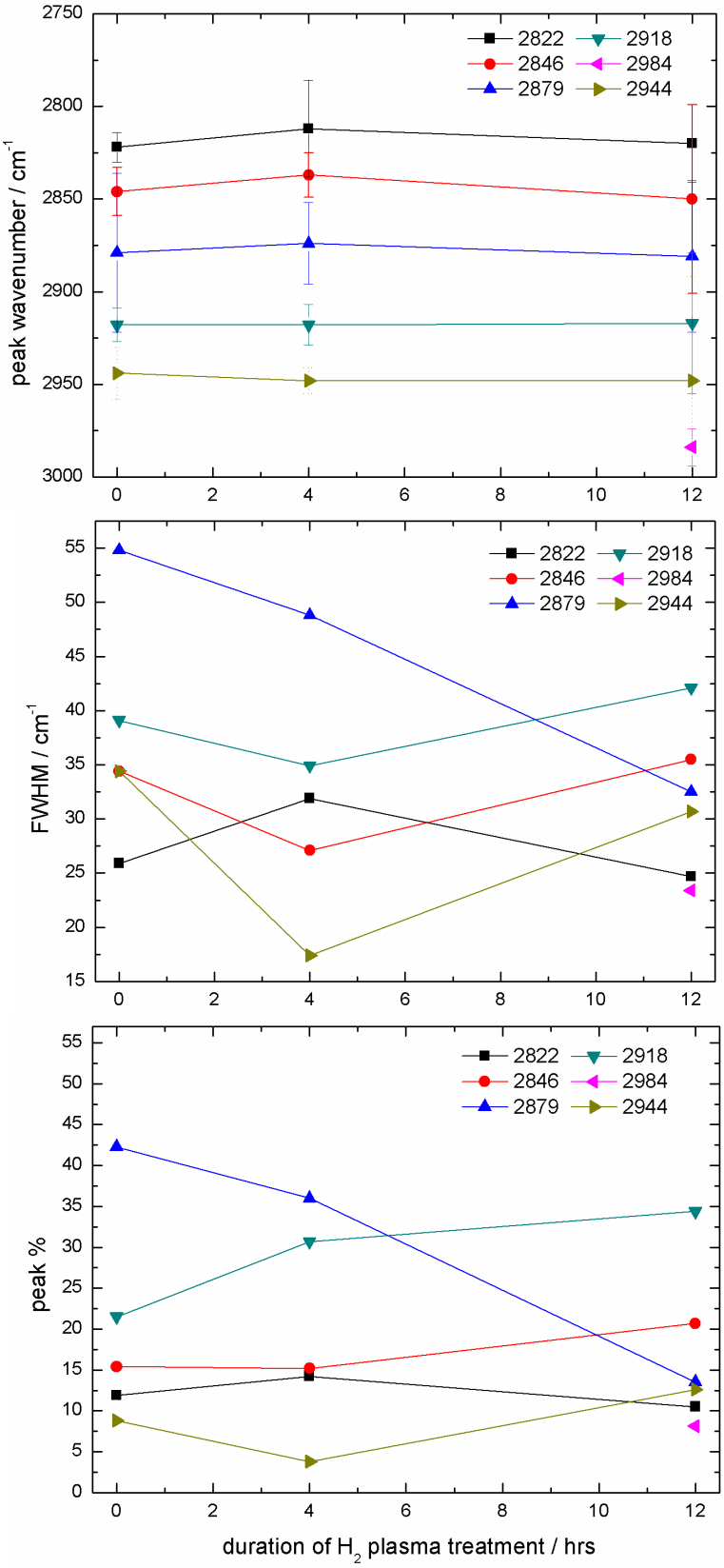

Figure 4.20 Measured a) peak frequency, b) FWHM and c) percentage area of the peak components of the CH_x stretching band resulted from the deconvolution of the band envelope. Data were collected with the duration of the H_2 plasma treatment.

The symmetric stretching vibrational band of sp^3 CH_2 at 2846 cm^{-1}, remained unaltered after the first 4 hrs of hydrogen plasma treatment. But a change of 5% has been observed to occur for the peak percentage area after 16 hrs of treatment. The FWHM and peak percentage area of the asymmetric stretching vibrational band of sp^3 CH_2 observed at 2918 cm^{-1} increased linearly with the duration of the hydrogen plasma treatment. Between the as-grown and the 16 hrs hydrogen treated diamond sample there was an increase of 12.9% on the peak percentage area. Both stretching vibrational bands have been associated with CH_2 on (100) 2x1 reconstructed surface, an increase of the peak components contribution to the CH_x stretching envelope can be associated to the increase of the hydrogen coverage of the (100) 2x1 diamond surface.

For the symmetric stretching vibration band of sp^3 CH_3 at 2879 cm^{-1} both its FWHM and peak percentage area decreased with the duration of the hydrogen plasma. The FWHM was reduced by 22.3 cm^{-1} and the peak percentage are by 28.8 % after 16 hrs of hydrogen plasma treatment. Those were the most dramatic changes that have been observed on the bands components of the deconvolution process as a function on the hydrogen plasma treatment duration.

On the contrary the asymmetric stretching vibrational band of sp^3 CH_3 observed at 2944 cm^{-1} did not produced any changes on measured values of FWHM, while the peak percentage area decreased by 5% after 4 hrs and increased by 3.8 % after 16 hrs of hydrogen plasma treatment. Percentage changes were measured from the initial value of the as-grown diamond film.

According to the results of the deconvolution process of the CHx absorption band, we observed the increase of the CH_2 groups to the absorption data with the increase of the hydrogen plasma exposure. Such observation can be assigned to the monohydride coverage of the (100)-(2x1) diamond surface. The decrease of the symmetric CH_3 group absorption with the duration of the plasma exposure, can be suggested to be due change of the surface coverage from CH_3 to CH_2. While the absorption related to CH on (111) diamond surface remained unchanged indicating no change occurred by the hydrogen plasma treatment.

4.6.6 X – Ray photoelectron spectroscopy

Figure 4.21 compares the wide survey XP spectra of typical as-grown and microwave plasma treated (100) highly oriented CVD diamond films. The peaks identified on the spectrum are denoted on the figure. The C 1s peak can be seen at 284.7 eV with its plasmons at the high energy side of the peak. The O 1s peak is observed at 532 eV. Clearly both samples contained oxygen within the region analysed by XPS. The two peaks located at 1220 eV and 970 eV are the Auger electrons for carbon and oxygen respectively. For the as-grown diamond film the Si 2s and Si 2p peaks were observed at 152 eV and 102 eV respectively. Silicon peaks were not observed for the microwave-assisted hydrogen plasma treated diamond film.

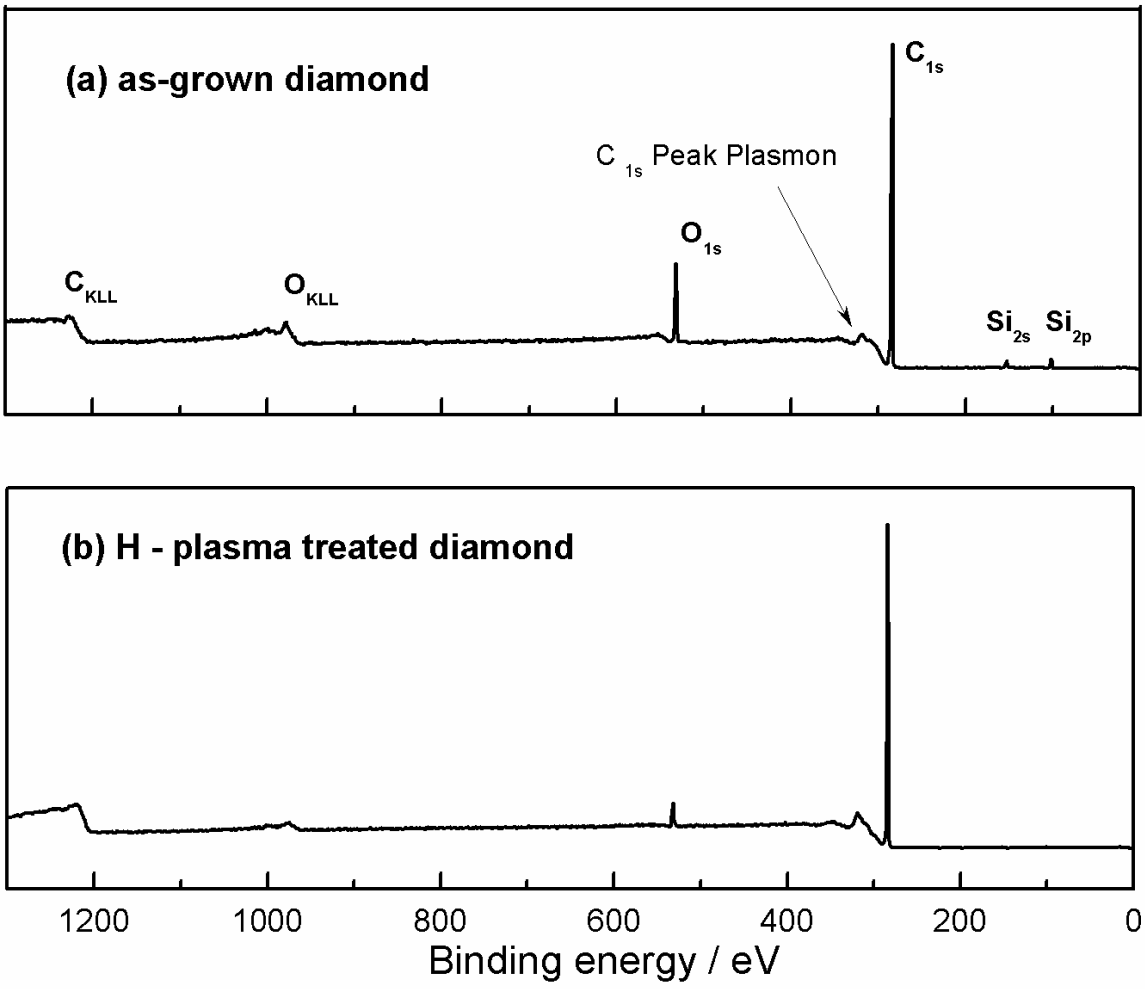

Figure 4.21 Wide scan XP spectra from (a) as-grown diamond sample and (b) a hydrogen plasma treated (100) highly oriented CVD diamond sample.

The XPS data presented here were collected from diamond samples (≈ 1 cm^2) on silicon and data were acquired from the epitaxial aligned region of the film. It has been described in chapter 3 that this region is grown on the periphery of the diamond film and it is in the vicinity of the uncoated silicon substrate. It may be possible that the collection of XP spectra, from the as-grown diamond sample, included area of the uncoated silicon substrate.

For the as-grown diamond film the presence of oxygen may possibly originate from CO that has been used during the diamond deposition process. Therefore a small amount may be incorporated into the diamond film. Another possible origin of oxygen on diamond surfaces could be due to contamination by exposure to ambient conditions [232]. Microwave hydrogen plasma treatment reduces the amount of oxygen present on the film surface.

Specifically the elemental composition of the two diamond samples is presented in Table 4-4. All the values have been determined using the ESCA software.

Sample	Atomic species	Area %
As – grown	C 1s	87.4
	O 1s	9.0
	Si 2p	3.6
Hydrogenated	C 1s	96.7
	O 1s	3.3

Table 4-4 XPS determined elemental composition for as-grown and hydrogen plasma treated (20 hrs) (100) diamond films.

The change in the peak shape depending upon surface termination can be seen when high resolution spectra of C 1s and O 1s peaks of as–grown and hydrogen plasma treated diamond films are compared in Figure 4.22.

The C 1s spectrum of the as–grown diamond film displays an asymmetric peak with a tail on the high binding energy region. For the hydrogenated diamond the C 1s spectrum has a symmetric shape.

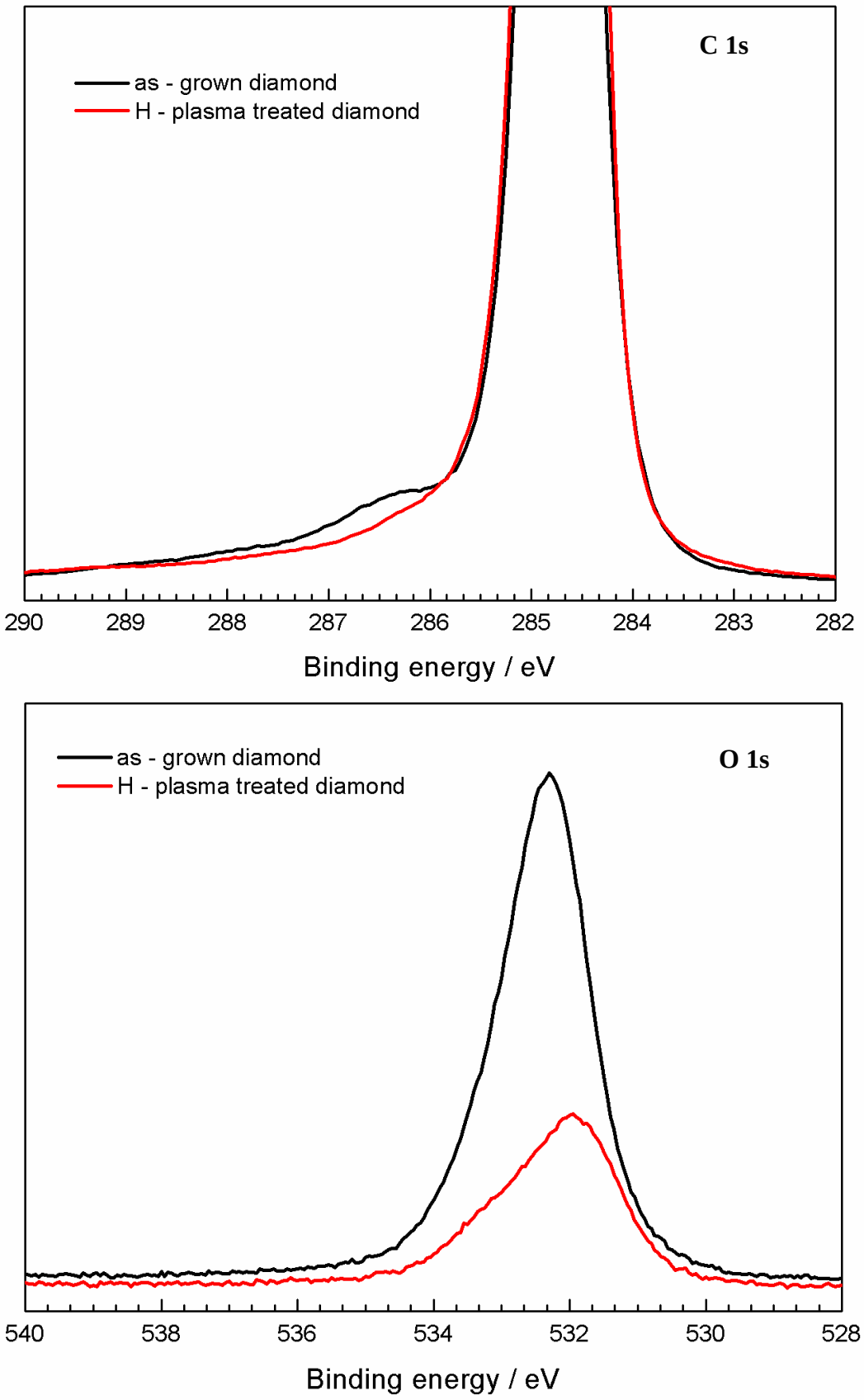

Figure 4.22 High resolution C 1s and O 1s XP spectra of as-grown and hydrogen plasma treated (20 hrs) (100) highly oriented CVD diamond films.

The shape of the O 1s spectrum of the two samples is identical and only the area differs, indicating the reduced levels of bonded oxygen, as has been observed on the survey scan data.

The peak areas of the high resolution C 1s and O 1s peaks are proportional to the concentrations of the respective species in the sample region under analysis. As the XP spectra were collected without charge compensation the C 1s components peak positions are measured relative to the main sp^3 carbon peak.

Deconvolution of the high resolution spectra was carried out by fitting the minimum number of peak components which provided accurate and repeatable fitting. The position of the peak components was determined by previously published data [228, 333-335]. A Gaussian-Lorentzian mix function has been used to describe the shape of the peak components and a linear background has been used for the analysis.

Interesting trends were observed for the as-grown and microwave hydrogen plasma treated (100) diamond films. The deconvoluted C 1s peaks are shown in Figure 4.23 while their average binding energies and FWHM of the component peaks are listed in Table.4-5.

Sample	**Peak assignment**	**BE shift (relative to sp^3 carbon peak) / eV**	**Peak FWHM / eV**	**Area / %**
As - grown	Diamond (sp^3)	0 (by definition)	0.6	78.9
	Graphitic (sp^2)	- 0.6 ± 0.2	0.7	3.7
	Hydrocarbon (CH_x)	+ 0.5 ± 0.1	0.8	12.3
	Ether (C-O)	+ 1.6 ± 0.1	0.8	3.2
	Carbonyl (C=O)	+ 2.0 ± 0.4	1.3	1.9
Hydrogenated	Diamond (sp^3)	0 (by definition)	0.60	78.1
	Hydrocarbon (CH_x)	+ 0.4 ± 0.1	0.86	21.9

Table 4-5 XPS C 1s components position, FWHM and integral area. The BE of the main peak occurs at 284.7 eV.

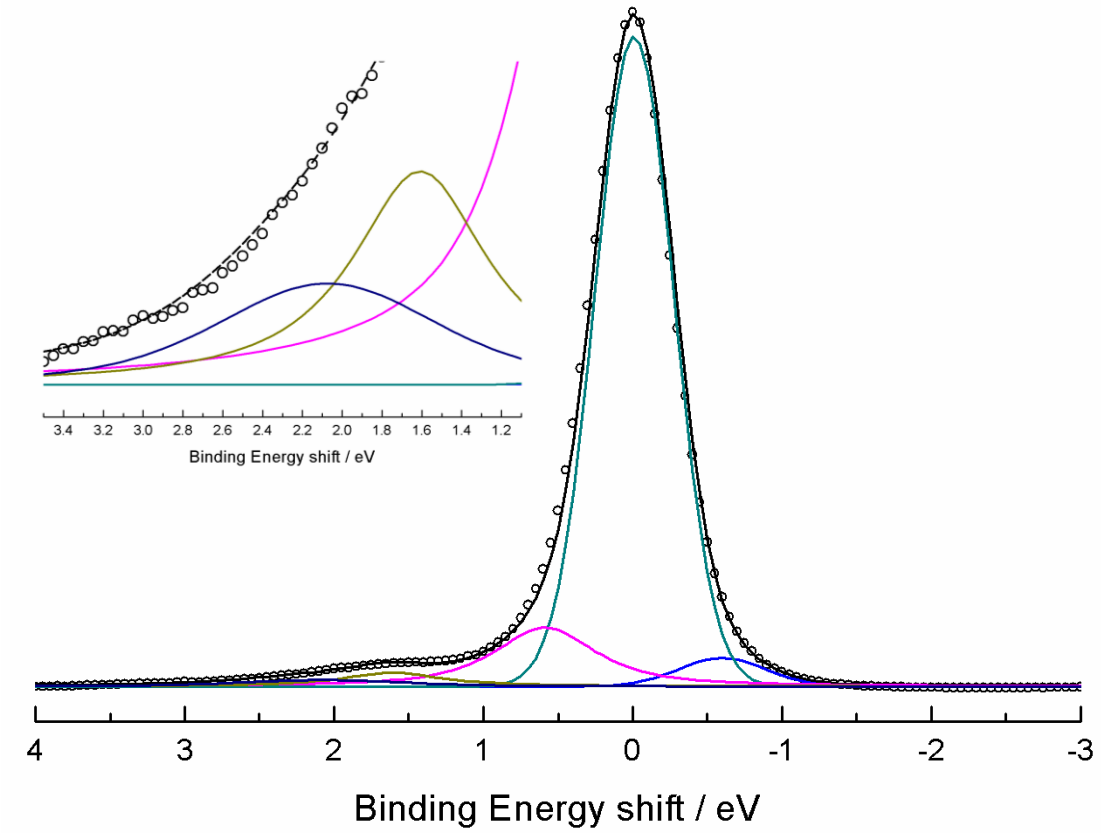

Figure 4.23 Deconvoluted high-resolution XP spectrum from the C 1s binding energy of an as-grown CVD diamond film, showing raw data (black circles) components peaks (coloured lines) and the sum of the peaks (black line). Binding energies are referenced to the main (sp^3) carbon peak. The high energy region has been magnified and presented in the insert.

The high resolution spectrum of the C 1s binding energy region of a (100) highly oriented CVD polycrystalline as-grown diamond thin film has been deconvoluted into five components, as listed in Table 4-5. The most intense peak centred at 284.7 eV can be attributed to the bulk diamond sp^3 component [233, 235]. The binding energies of all the other peak components are given relative to this peak.

The peak shifted by - 0.6 eV (blue line) towards the lower binding energy region this peaks can be assigned to graphitic carbon species sp^2 [228]. Three components were fitted to the high energy side of the C 1s spectrum. The peak shifted by + 0.5 eV with respect to the main sp^3 peak can be ascribed to carbon atoms bonded in polyhydride configurations CH_x ($x \geq 3$), located at the grain boundaries of the film [202, 203].

The remaining two components are shown in more detailed on the inset graph of Figure 4.23. The peak shifted by + 1.6 eV can be attributed to ether functional groups [233, 235], whilst the peak shifted by + 2.0 eV is attributed to carbonyl functional groups [235]**.** Therefore the small amount of oxygen present on the diamond surface appears to be either singly or doubly bonded to carbon atoms.

The C 1s peak of the hydrogen plasma treated diamond has been deconvoluted into two components, Figure 4.24. The main component was centred at 284.7 eV is attributed to the bulk diamond peak (sp^3) and the second component peak positioned at + 0.42 eV can be attributed to polyhydride carbon species, CH_x ($x \geq 3$).

It is possible to identify that there were no peaks at the low binding energy side attributed to sp^2 carbon forms. Atomic hydrogen attacks and removes any graphitic and amorphous carbon phase in comparison with diamond. Thus hydrogen plasma treated diamond resulted in a surface free of graphitic carbon.

The peaks observed at the high binding energy side attributed to oxygen bonded species on the diamond surface were absent. The removal of oxygen groups from the surfaces of diamond powders upon hydrogenation had been examined by means of FTIR spectroscopy [236]. Results shown the hydrogenation did not proceed at temperatures below 500 ^oC and that desorption of C=O is the dominant process. But since diamond powders comprise random crystallographic facets, those results [236] cannot be interpreted in terms of any specific diamond crystallographic surface.

There are two possible reaction mechanisms for the removal of oxygen species from the diamond surface by hydrogen plasma. One way is the stepwise reduction of carbonyl or ether by hydrogen molecules and/or hydrogen atoms to produce C-H surface groups. Alternatively here the simple thermal desorption of the carbonyl or ether groups to form either CO or CO_2, with subsequent hydrogen adsorption on the surface carbon atoms.

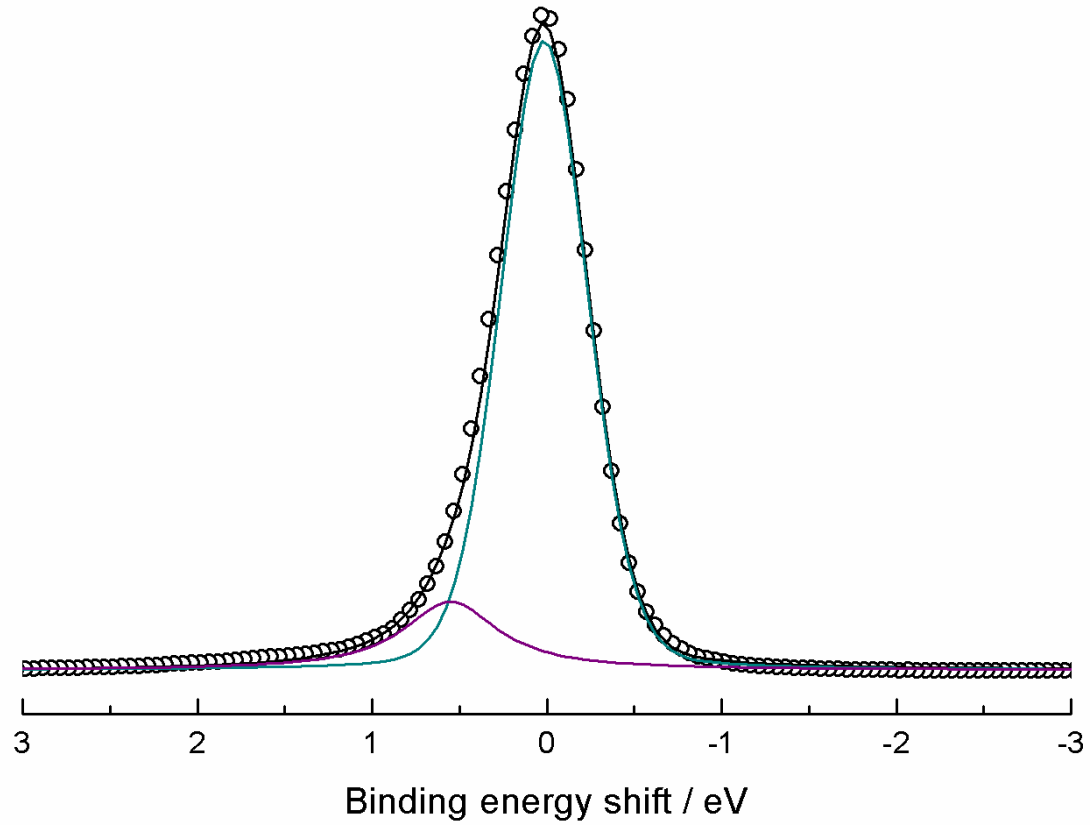

Figure 4.24 Deconvoluted high-resolution XP spectrum from the C 1s binding energy of a hydrogen plasma (800^{o}C, 20 hrs) treated CVD diamond film, showing raw data (black circles) components peaks (coloured lines) and the sum of the peaks (black line). Binding energies are referenced to the main (sp^3) carbon peak. The peak components of the C 1s binding energy spectra are summarised in Table 4-5.

The O 1s peaks were deconvoluted into two peak components, as that was the minimum number of peaks which produced an accurate and repeatable fitting procedure. The deconvoluted O 1s peaks of the as-grown and plasma treated diamond samples are shown in Figure 4.25.

For the as-grown diamond film the main peak component was located at 532.2 eV (FWHM = 1.31 eV) and it was assigned to carbonyl groups, whilst the second peak component at 533.0 eV (FWHM = 1.50 eV) was attributed to ether groups. For the O 1s peak of the hydrogen plasma treated diamond sample two similar components emerged. The main peak component was observed at 531.8 eV attributed to carbonyl group, whilst the second peak component was located at 533.0 eV, and was assigned to ether groups, details of the peak components characteristic are listed in Table.4-6.

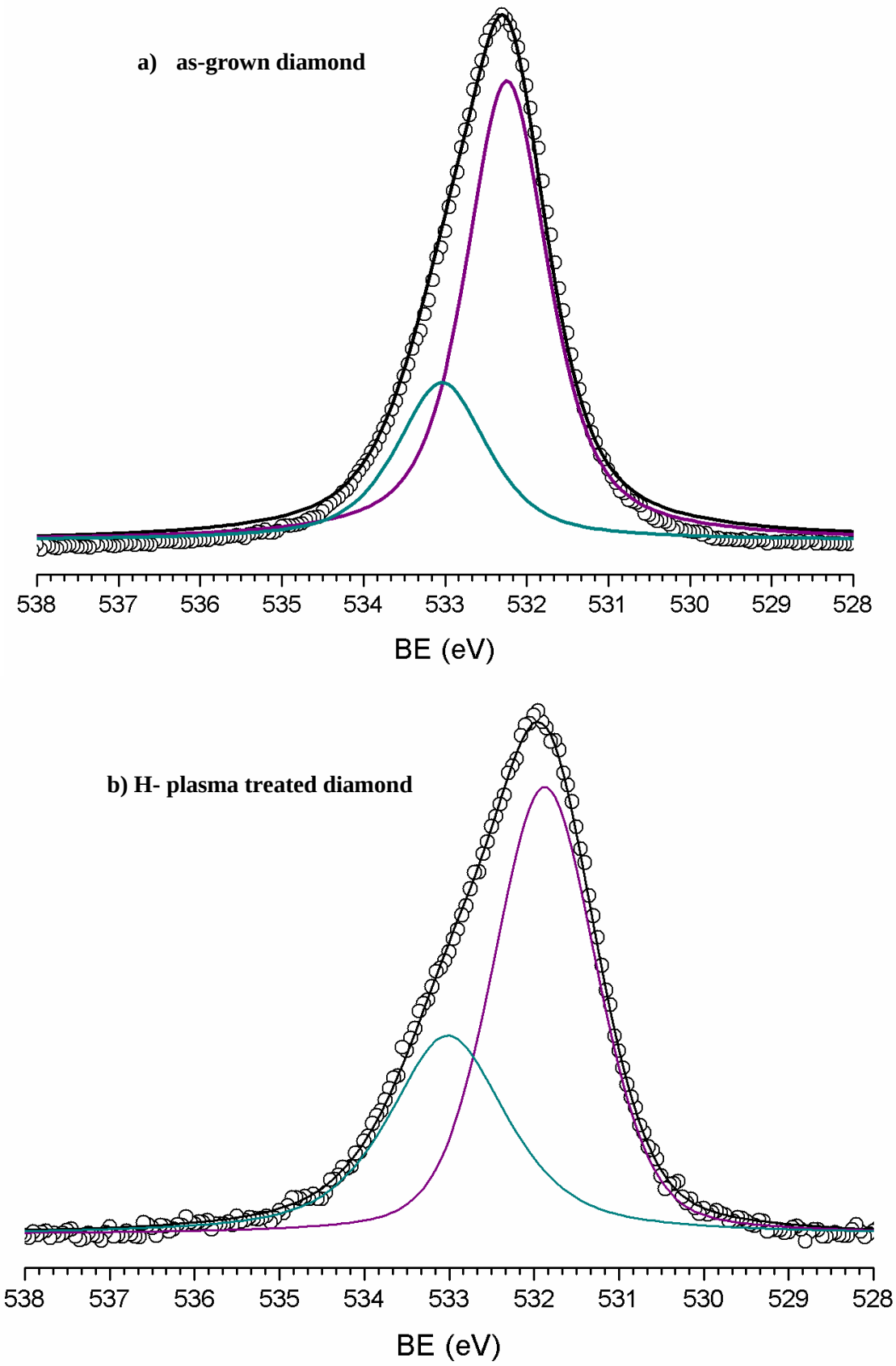

Figure 4.25 Deconvoluted high-resolution XP spectrum from the O 1s binding energy of a) as-grown and b) hydrogen plasma treated CVD diamond film, showing raw data (black circles), component peaks (coloured lines) and the sum of the peaks (black lines).

Sample	**Peak assignment**	**BE shift (relative to sp^3 carbon peak) / eV**	**Peak FWHM / eV**	**Area / %**
As - grown	Carbonyl (-C=O)	532.2	1.3	83.0
	Ether (-C-O-C-)	533.0	1.5	17.0
Hydrogenated	Carbonyl (-C=O)	531.8	1.4	63.5
	Ether (-C-O-C-)	533.0	1.6	36.5

Table 4-6 XPS O 1s peak components position, FWHM and percentage area.

The assignment of the peaks from the O 1s region is less well established than that from the C 1s region. Both diamond samples presented the same oxygen-carbon functional groups. The peak components of O 1s binding energy region should display binding energy shifts related to the formal oxidation states of the oxygen atoms. We would also expect the curve fitting of C 1s peak to produce results that would correlate with those of the O 1s peak fitting procedure.

The Si 2p peak of the as-grown diamond film was deconvoluted into two peak components, Figure 4.26. The main peak component was located at 102 eV while the second one was shifted by +0.8 eV. Details of the components peak arising from the deconvolution process of Si 2p are presented in Table 4-7.

Both peak components exhibits binding energies which are between that of the Si 2p of SiO_2 (104 eV) and that of SiC (100 eV). The peak at 102 eV could be assigned to silicon oxycarbide and the latter peak at 102.8 eV to non-stoichiometric silicon oxide SiO_x ($x < 2$) [237]. It is very unlikely that silicon would be present on the surface of the as-grown diamond film. Possibly the contribution of the silicon peaks on the XP spectra originate from the actual silicon substrate, as the uncoated silicon substrate could have been included in the area of XPS analysis.

The formation of silicon oxide and silicon oxycarbide phases, has been observed by XP spectroscopy when oxygen has been added to the CVD diamond growth mixture [237] as interfacial layers between silicon substrate and diamond layer. Although it is not clear if the formation of the interfacial layer is caused by the presence of oxygen during the growth process and/or oxidation by exposure to air.

Sample	Peak assignment	BE eV	Peak FWHM / eV	Area / %
As - grown	SiO_2	102.0	1.1	69.2
	SiO_x (x<2)	102.8	1.0	30.8

Table 4-7 XPS Si 2p peak components position, full width at half maximum and integral area.

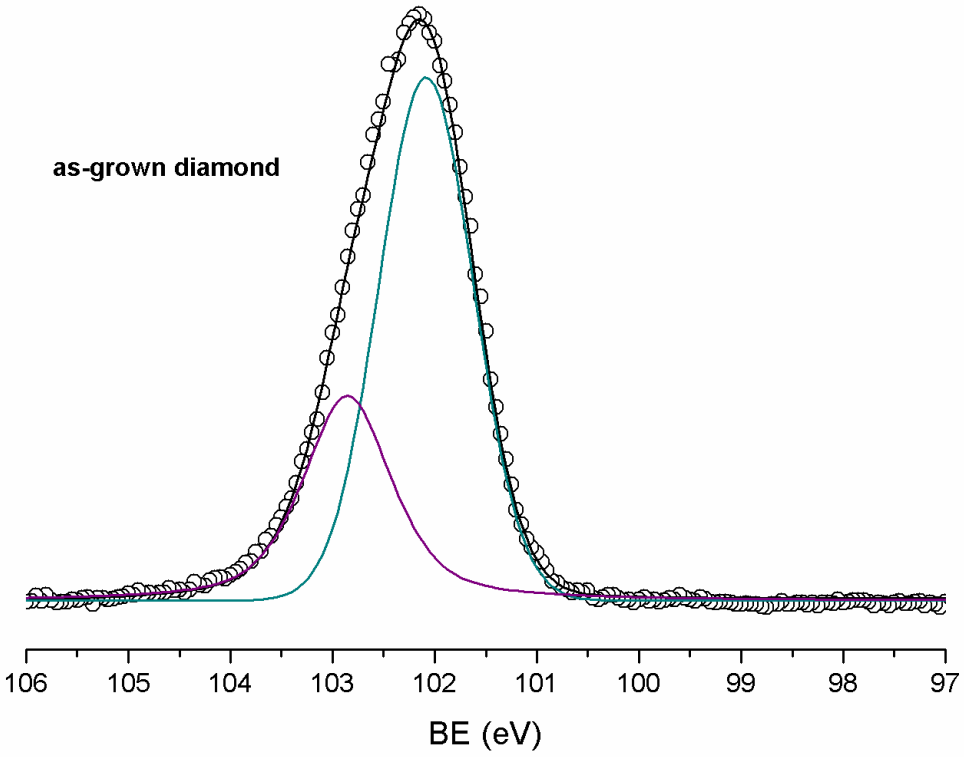

Figure 4.26 Deconvoluted high-resolution XP spectrum from the Si 2p binding energy region of an as-grown (100) highly oriented CVD diamond film on silicon. Raw data presented here as black circles, component peaks with coloured lines and the sum of the peaks with black line.

The presence of silicon species could be due to the formation of silicon carbide during the diamond growth. As it has been discussed previously it could also be induced by migration of silicon to the surface by the growth process from the silicon substrate.

The results presented here show that microwave hydrogen plasma treatment of CVD diamond removes graphitic carbon and oxygen phases from the surface layers. The amount of oxygenated carbon groups on the surface or near surface is reduced after the treatment but not entirely removed for the durations of treatments performed.

Table 4-8 summarises the previously reported positions of peaks on diamond surfaces and compares them to the results obtained from the present XPS results. A comparison of this work and the reported peak shifts shows a good agreement. The present peak fitting is consistent with previously reported data [228, 233].

Diamond sp^3 **C-C**	**Graphitic** sp^2 **C-C**	**CH_x** **(x ≥ 2)**	**Ether** **-C-O-Cc**	**Carbonyl** **-C=O**	**Carboxyl** **-C-OOH**	**Surface State**	**Ref**
284.7	- 0.6	+ 0.5	+ 1.6	+ 2.0		As-grown	This work
		+ 0.4				Hydrogenated	
	-0.7	+ 0.5	+ 1.2	+ 2.0	+ 2.9	Thermally oxidised	[233]
	-0.5		+ 1.0	+ 2.25	+ 3.3	Thermally oxidised	[228]
	-0.5	+ 0.6	+ 0.9		+ 4.5	Electrochemically oxidised	[234]
	-1.3	+ 0.5	+ 1.2 – 1.9	+ 3.6	+ 4.5	Electrochemically oxidised	[55]

Table 4-8 Comparison of this work and literature XPS binding energies of diamond surfaces containing carbon and oxygen groups.

4.6.7 Electrical characterisation

The methods and results of the electrical analysis carried out on as-grown and hydrogen plasma treated (100) polycrystalline CVD diamond films will be presented in this sub-section. The analysis consisted of investigating the current/voltage (I-V) characteristics of the (100) CVD diamond films.

It is well documented that hydrogen plasma treatment on diamond surfaces induces the surface conductivity phenomena, as discussed in section 4.4. With this knowledge it was felt that the I-V measurements will be an important characterisation technique for investigating the hydrogenation of the (100) polycrystalline CVD diamond films by hydrogen plasma.

The I-V characteristics were obtained from as-grown and hydrogen plasma treated (100) CVD diamond. Sheet conductivity measurements on azimuthally and highly-oriented (100) CVD diamond films were examined to study the effect of surface morphology. Finally the effect on sheet conductivity of prolonged exposure of a hydrogenated (100) diamond surface to ambient conditions was examined.

I-V Probe station

The I-V characteristics were measured on a probe station shown schematically in Figure 4.27. The Wentworth Labs station used consisted of a sample holder with vertical movement, a microscope and two electrical probes on magnetic bases for stability. The probes were connected to a 4140B HP pA meter/DC voltage source and their movements were micrometer-controlled in the x, y and z directions. The current and voltage readings were collected using an in-house built HPVee program. All measurements were taken in ambient light and at room temperature. Evaporation of metallic contacts has been omitted and thereby both electrical probes were pressed directly into the sample surface. The distance between the probes was kept approximately 3 mm for all the measurements taken.

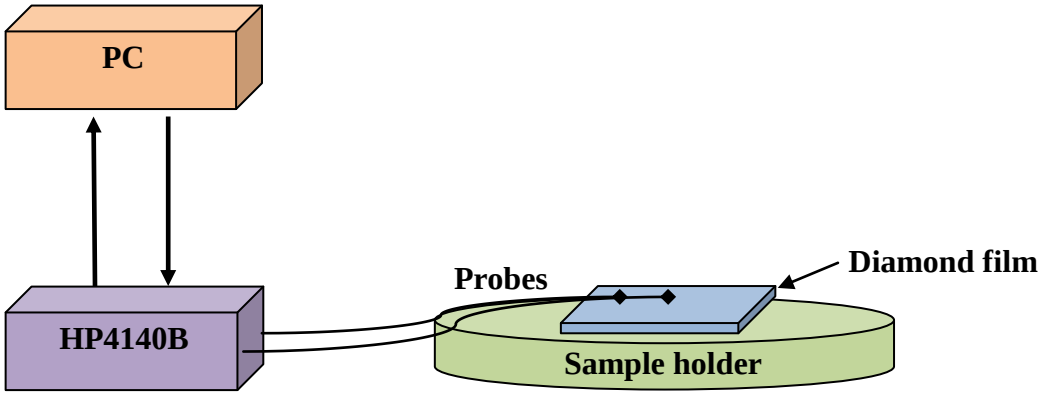

Figure 4.27 Schematic diagram of the probe station used for current/voltage characteristics.

The potential difference was supplied in a stepped formation: settings used for the I-V measurements are listed in Table.4-9.

Start voltage	0 V
Plateau Voltage	100 V
Step Voltage	0.5 V
Step Delay Time	1 sec

Table 4-9 Experimental parameters for the I-V measurements.

Current-voltage characteristics of an as-grown and a hydrogenated (100) highly oriented CVD diamond film deposited on silicon are plotted in Figure 4.28. The hydrogenation of the (100) diamond surface was achieved by exposure to a hydrogen plasma for 4 hours (800^{o}C, 700 W and 35 torr). For both I-V measurements the diamond samples were exposed to atmospheric air following hydrogen plasma treatment.

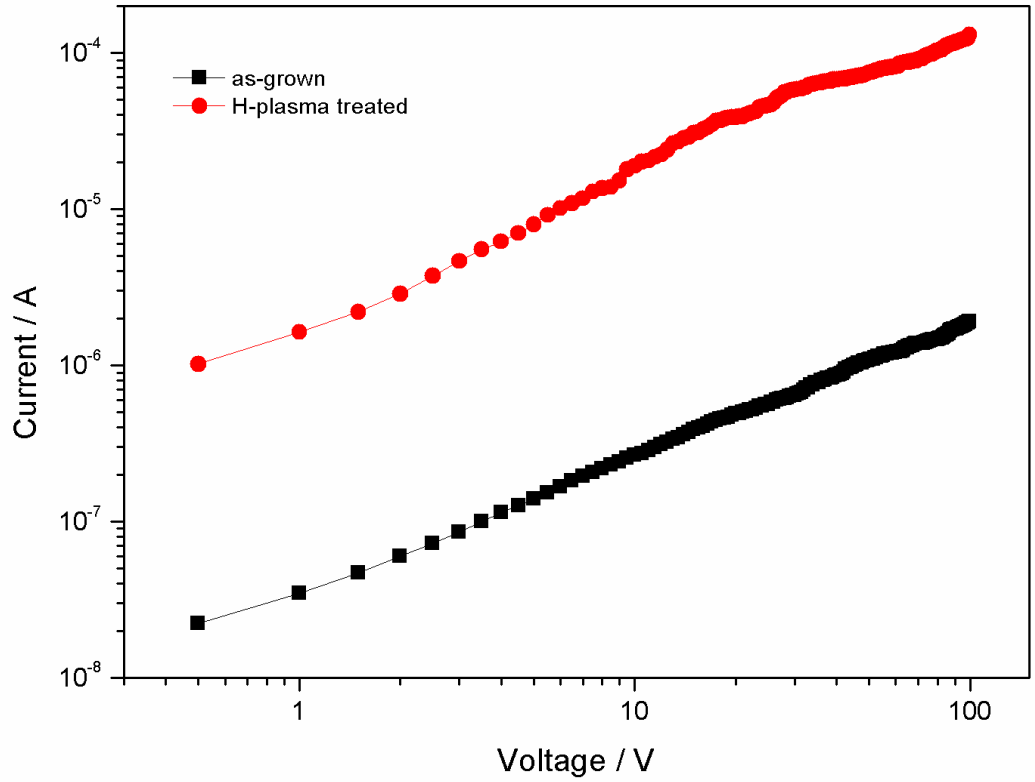

Figure 4.28 Current–voltage characteristics measured on as-grown (100) highly oriented CVD diamond film under room temperature and pressure (black squares), and subjected for 4 hours to hydrogen plasma treatment at substrate temperature 800^{o}C and hydrogen pressure of 35 torr (red circles).

As seen in Figure 4.28, the current-voltage characteristics for both, as-grown and hydrogen plasma treatment (100) diamond samples, exhibit the same trend. For low applied voltages the characteristics show a linear relationship, while for high applied voltages the current-voltage relation was found to be;

$$I \propto V^{1/2}$$

for both samples. The resistance, R, of the diamond samples has been determined from the I-V plots of Figure 4.28, for low applied voltage range, from:

$$R = V/I \qquad \textbf{Equation 4-1}$$

For the as-grown {100} diamond sample the value of R= 134 kΩ has been determined, while for the hydrogen plasma treated diamond sample the resistance value of R= 1.68 kΩ.

Although the as-grown diamond film was terminated in a hydrogen plasma, the measured resistance decreased by 132.4 kW, by further 4 hrs of hydrogenation. Similarly, upon hydrogenation of single crystal and polycrystalline diamond the conductivity was found to decrease by several orders of magnitude [216].

Four-point probe method

The resistivity of a given specimen is commonly measured using an array of collinear four-point probes; this technique can provide reliable measurements when the following aspects are considered [238]:

- The area of contact between each of the pin-like probes and specimen should be small compared with the distance **s** between the probes, as depicted in Figure 4.29.
- A significant parameter to determine the resistivity is the specimen thickness δ, and there are different solutions for thicknesses being larger, comparable and smaller than ***s***.

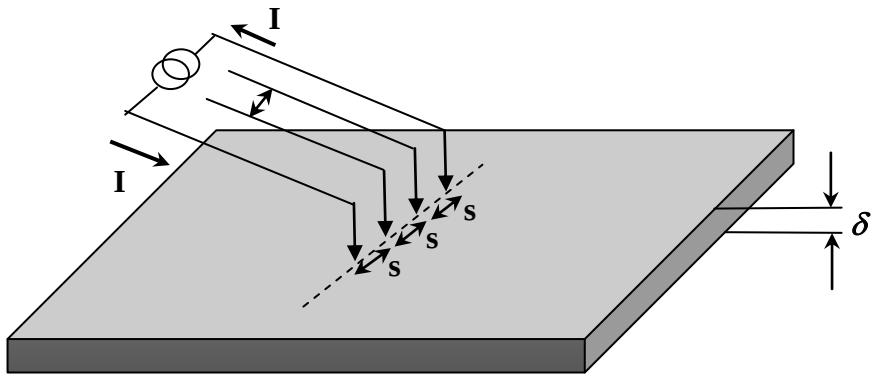

Figure 4.29 A collinear four-probe array on a sample of thickness δ.

For various values of constant current, the voltage is measured across the inner two probes to determine the resistance, R, according to:

$$\frac{dI}{dV} = \frac{1}{R}$$ **Equation 4-2**

The resistivity of the specimen ρ, is expressed as:

$$\rho = R * \frac{\pi \delta}{ln2} = 4.5324\, \delta\, R \qquad \textbf{Equation 4-3}$$

For the case where the interprobe spacing is larger than the specimen thickness, $s >> \delta$, , then sheet resistivity ρ_s can be expressed as:

$$\rho_s = \frac{\rho}{\delta}$$

$$\Rightarrow \rho_s = 4.5324R\ (\Omega\ \square^{-1}) \qquad \textbf{Equation 4-4}$$

The experimental apparatus used to measure the sheet resistivity of the diamond films, is depicted in Figure 4.30. A digital multimeter (Keithly 160 B) has been used to measure the potential difference between the two inner probes, while the two outer probes were connected to a programmable current source (Keithley 224). For this specific arrangement the probe diameter was ~ 0.08 mm and the probe interspacing was ~ 0.625 mm. This technique has been used to measure the sheet resistivity of the hydrogen plasma treated diamond films on silicon. Before any plasma treatment the diamond thin film thickness was measured, using SEM images, from the cross-section of the {100} diamond thin films to be of the order of ~ 5 μm.

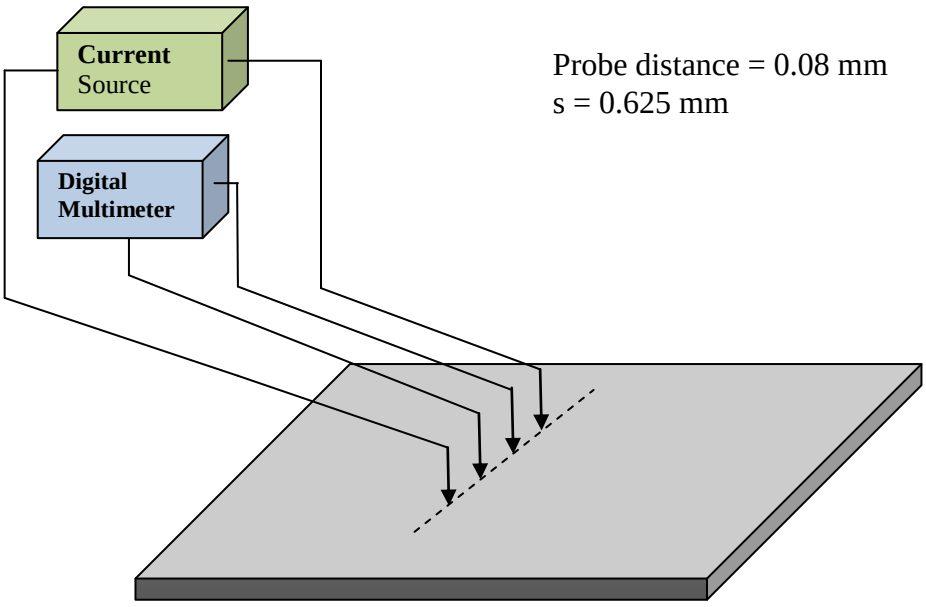

Figure 4.30 A schematic diagram of the 4 probe station used to measure the sheet resistance of hydrogen plasma treated diamond films.

The high resistivities of the as-grown CVD diamond films on silicon did not allow the collection of I-V data because the maximum compliance voltage of the current source was 100V and this was insufficient to derive the minimum current through the diamond.

Exposure to hydrogen plasma for 4 hrs at 800^{o}C and 35 Torr resulted in the decrease of the sheet resistivity and the successful collection of I-V data. Four-probe measurements were taken of the azimuthally disordered and highly oriented areas of the CVD diamond film after 4 hrs of microwave-assisted H_2 plasma treatment (800^{o}C and 35 Torr), to determine the sheet resistivities. In Figure 4.31, the I-V characteristics were plotted for both areas of the diamond sample and linear fitting procedure was applied to the data. The linear equations for the I-V of the azimuthally aligned diamond and highly oriented regions were found to be $I(A) = 1.25x10^{-4}\,V(Volts) - 4.06x10^{-9}$ and $I(A) = 2.57 \times 10^{-4}V(Volts) - 1.09x10^{-9}$ respectively.

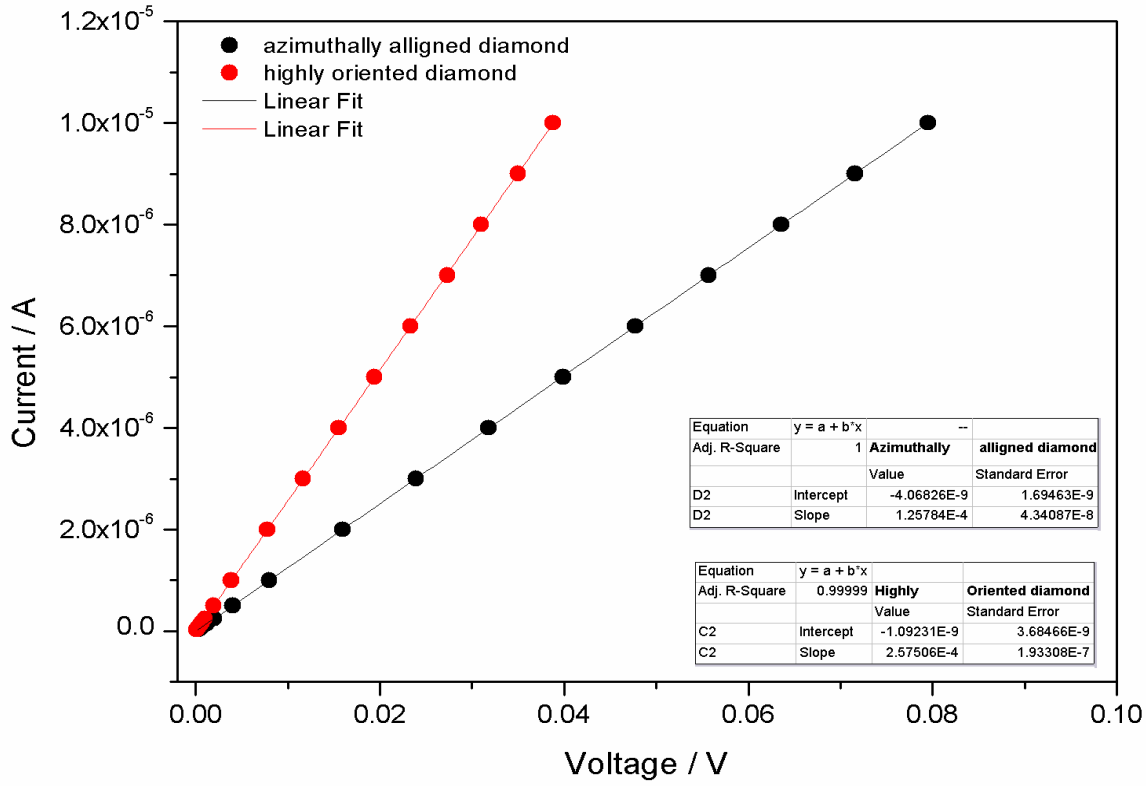

Figure 4.31 Current–voltage data plot for the azimuthally disordered (black circles) and highly oriented (red circles) (100) CVD diamond films. Details of the linear fitting procedure are listed in the inset tables.

From Figure 4.31, **R** = 8 kΩ, therefore, ρ_s = 36.26 kΩ □$^{-1}$ for the azimuthally disordered (100) diamond region and **R** = 3.9 kΩ, and then ρ_s = 17.63 kΩ □$^{-1}$ for the highly oriented (100) diamond region. The thickness of the conducting layer is uncertain therefore ρ cannot be calculated.

The surface resistivity values measured for the highly oriented and azimuthally disordered (100) CVD diamond films provide evidence for the effect of surface morphology and grain boundaries on the surface electrical properties of the diamond films. The crystallites in the azimuthally disordered diamond films exhibit large tilt angles in both x and y directions. As a consequence those surfaces can act as electron traps and disrupt the current flow in the lateral direction. However the grain boundaries can include sp^2 carbon which enhances the diamond conductivity [239]. XPS analysis presented in sub-chapter 4.6.6 shows that hydrogen plasma treatment removes graphitic forms of sp^2 from the CVD diamond surfaces and possibly in the intergranular regions. From the data presented here the large tilts and grain boundaries of azimuthally disordered (100) CVD diamond crystallites have a strong effect in decreasing the diamond film surface conductivity.

Figure 4.32 shows measured values of sheet resistivity from both azimuthally disordered and highly oriented (100) CVD diamond films as a function of the exposure time to atmospheric air after hydrogen plasma treatment. For both areas of the diamond films the sheet resistivity exhibits the same trend.

The surface resistivity has been decreased by exposure to ambient conditions (room temperature and pressure) by 31 kΩ/sq for the highly oriented (100) diamond film. While for the azimuthally disordered (100) diamond films the surface resistivity only a small and possibly insignificant decrease of 18.6 kΩ/sq has been observed.

Saturation of the surface resistivity has been observed for both highly disordered and highly oriented (100) CVD diamond films by exposure to ambient conditions for 20 hours. A small variation in the surface resistivity has been observed on the azimuthally disordered CVD diamond as a function of the exposure time to ambient atmospheric conditions. These small variations are more likely to have been caused due to the positioning of the tips on the surface of the azimuthally disordered diamond surface.

The present results are in accordance with the transfer doping model [44] presented in 4.4. The surface resistivity of {100} CVD diamond films has been decreased upon exposure to ambient atmosphere and reduction of the surface resistivity has been achieved by further exposure to air.

It was not feasible to measure the surface resistivity *in vacuo* directly after the hydrogen plasma treatment due to the limitations of the MPCVD system. Experimental observations support the view that chemisorbed hydrogen on the diamond surface is not directly responsible for the decreased surface resistivity of diamond crystals. Exposure to atmospheric condition is necessary for the reduction of the surface resistivity.

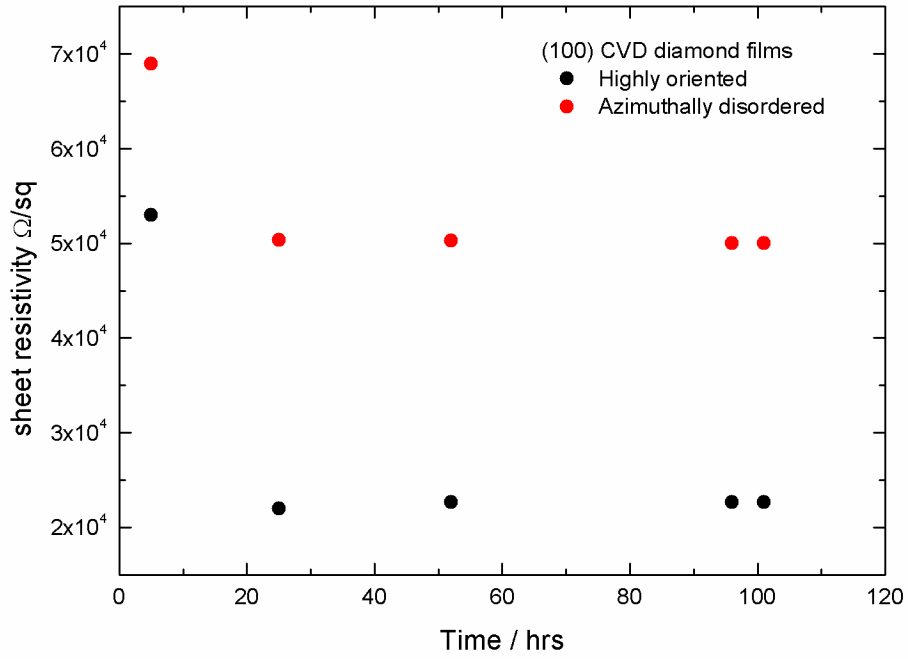

Figure 4.32 Sheet resistivity for the highly oriented and azimuthally disordered diamond films as a function of exposure to ambient air after microwave-assisted hydrogen plasma treatment.

According to the transfer doping model of Maier *et al* [44] when the hydrogenated diamond surface is exposed to ambient conditions a thin layer of water is formed on the diamond surface. Electron transfer from the diamond valence band maximum to the conduction band of the absorbates via a redox reaction will cause the formation of a hole accumulation layer in the diamond subsurface. The experimental evidence provided by Nebel *et al* [42] showed that the discrete electronic states created by the transfer doping on the hydrogenated diamond surface will be affected by: a) the arrangement of the H-termination, b) by the arrangement of the adsorbates on the

diamond surface and c) by the diamond surface roughness. Taking into account the models of Maier *et al* [44] and Nebel *et al* [42], the observed saturation of the measured surface conductivity of (100) CVD diamond films can be attributed to the full coverage of the diamond surface with absorbates by prolonged exposure to atmosphere. After full coverage of the diamond surface with adsorbates the surface resistivity cannot be reduced any further. Increase of the surface resistivity has not been observed by extended exposure of microwave-assisted hydrogen plasma treated polycrystalline CVD diamond films to air, as reported by Kulesza *et al* [222].

4.7 Conclusions

Surface morphological studies of the (100) highly oriented CVD diamond show the surface smoothing effect of prolonged microwave-assisted hydrogen plasma treatment. The vertical etch rates of high quality CVD diamond have been determined by AFM measurements. Faceting and square etch pits that are widely reported [30,143, 192, 197, 198] to form on natural diamond surfaces by hydrogen plasma treatment were not observed in this study. The data are consistent with the mechanism of anisotropic etching on dimer row edges on the (100) diamond surface as proposed by Ri *et al* [30].

Infra-red absorption spectroscopy demonstrated that exposure to hydrogen plasma treatment resulted in a relative enhancement of the CH_2 groups on the (100) diamond surface and grain boundaries and the decrease of the symmetric CH_3 groups. This is consistent with the coverage of (100) diamond dangling bonds with monohydrides in the 2x1 surface reconstruction.

Analysis of the high resolution XPS data was consistent with the fact that the (100) diamond surface is terminated by hydrogen. Hydrogen plasma treatments resulted in removal of graphitic and oxygen functional groups from the diamond surface.

Exposure of (100) CVD diamond films to hydrogen plasma treatment reduced the surface resistivity of the diamond film. Exposure to ambient conditions produced a further decrease of the surface resistivity of the diamond film in support of the transfer doping model [44]. Saturation of the measured surface resistivity for both azimuthally disordered and highly oriented (100) diamond films has been observed after long

exposure to ambient conditions. These results are in accordance with the model proposed by Maier *et a*l [44] .

Chapter 5: Reactive ion etching of CVD diamond

5.1 Introduction

Patterning of diamond surfaces has been successfully achieved by reactive ion etching (RIE). Despite the limitation of the RIE process, namely low etch rates and resulting texture of the etched diamond surface, the fabrication of diamond devices has been realised by the use of reactive ion etching under different gas chemistries. One of the most intriguing phenomena associated with oxygen reactive ion etching on diamond CVD films is the formation of columnar structures. Many authors have attributed the phenomenon to the deposition of electrode material onto the diamond surface during RIE.

Formation of columnar structures on diamond films has attracted attention for potential application as field effect emitters [243, 244], as well as micro-probes for biological applications [278]. The formation of columnar structures has been utilised in many publications with the use of a coating or resist layer and a subsequent RIE process [271, 272, 275, 278, 280]. To date there are no reports on the dependence of columnar structures on the different crystallographic planes of diamond films.

The present study presents the results of reactive ion etching carried out on (100) highly oriented and azimuthally disordered CVD diamond films on silicon using oxygen RIE. The effects of reactive ion etching process parameters, such applied pressure, RF power and gas flow rate have been investigated with respect to the formation of columnar structures. The use of both types of diamond films enabled the effect of grain boundaries areas on columnar structure formation to be examined. Finally isolated cubo-octahedral CVD diamond crystallites have been etched under different RIE oxygen conditions and the results have been correlated with those of the CVD diamond films.

5.2 Patterning of diamond

A crucial processing step in the fabrication and realisation of micro- and nano-electronic devices is a reproducible and controllable etching procedure. As diamond offers remarkable chemical inertness and hardness properties, the removal of surface layers in a smooth and damage free manner is difficult by conventional wet etching techniques. At normal temperatures diamond is chemically inert against acids and solvents, although it reacts with oxygen at temperatures above ~ 600^{o}C [240]. Under such high temperatures and chemically aggressive environments finding a material appropriate for masking purposes to control the etching/patterning process is a problem.

Selective deposition [241-244] and replication [245] has also been applied to CVD diamond film technology for the realisation of diamond devices. Several simple diamond MEMS microstructures have been realised using these techniques such as microlever beams, bridges [242], laser to fibre alignment [245], micro-motors [246] and microtips for field emission [243, 244]. Despite the promising published results both selective deposition and replication techniques present some disadvantages, as low growth nucleation density of the selective deposited film. Etching and patterning of diamond has also been demonstrated using laser processing [247, 248].

The limitations of the above mentioned techniques have encouraged the investigation of several dry etching processes for patterning of diamond surfaces. Plasma etching, ion beam etching, reactive ion etching and reaction ion beam etching fall into the family of dry etching processes. These techniques have been developed and applied for fine patterning in ULSI and photonic devices. The fabrication of micro-electromechanical parts (MEMs) has also been demonstrated by these techniques. Processes such as ion beam etching, reactive ion etching and electron cyclotron resonance etching have all been explored and produce uniformly etched structures in diamond. Several prototype diamond devices have been fabricated by dry etching. To date there are published reports on the development of diamond cold cathodes [249], field effect transistors [250, 251], MEMs [252], optical diffractive elements [253], piezoresistive pressure sensors [254], in-plane-gated field effect transistors [255], diamond microlenses structures [256] and X-ray lenses [257].

5.3 Dry etching patterning

The directionality of an etching process is defined by three typical etching profiles: isotropic, partially anisotropic and completely anisotropic, as shown in Figure 5.1. In case of isotropic etching the horizontal and vertical etch rates of the material are comparable and lead to the under-etching of the mask material as depicted in Figure 5.1 a). Anisotropic etching is characterised by high vertical etch rate in comparison with the horizontal etch rate of the material, leading to high aspect ratio etch patterns as shown in case of completely anisotropic etching in Figure 5.1 c).

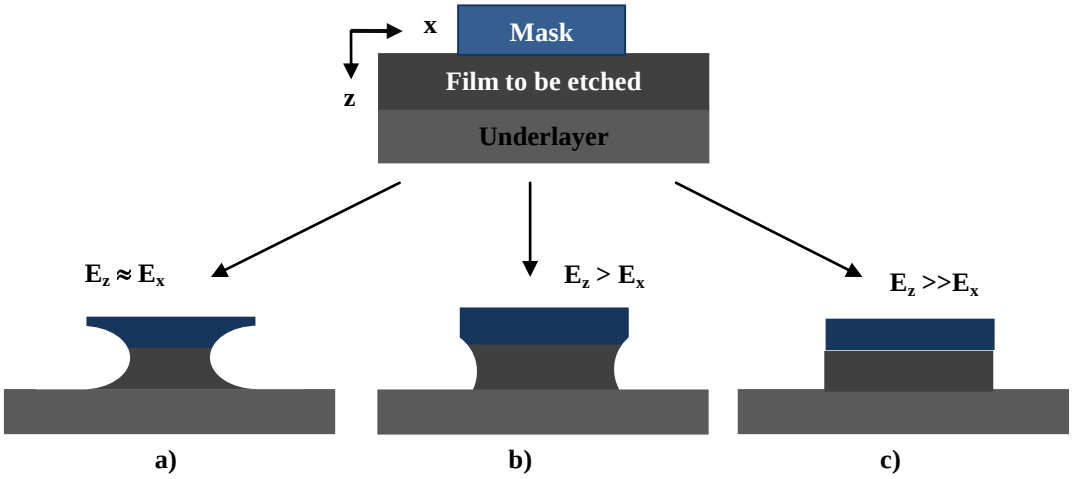

Figure 5.1 Schematic representation of the different etch profiles define the dry etching process technology, a) isotropic, b) anisotropic and c) completely anisotropic etching.

Dry or plasma etching technology generally provides highly anisotropic etching, through two general mechanisms associated with the process a) physical sputtering and b) chemical reactions. Figure 5.2 shows schematically that dry etching can be categorised as a) physical sputtering, b) chemical etching and c) ion-enhanced etching [258].

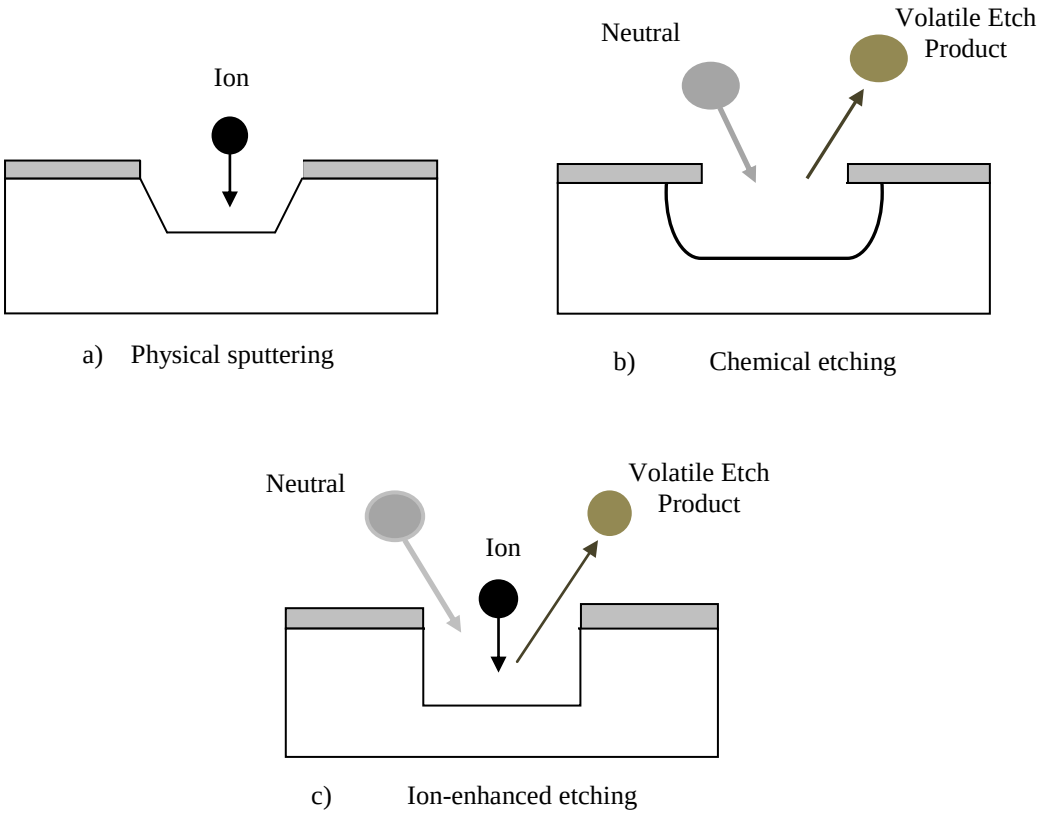

a) Physical sputtering

b) Chemical etching

c) Ion-enhanced etching

Figure 5.2 Schematic representation of the mechanisms occurring during plasma etching.

During physical sputtering; ions are accelerated as they cross the plasma sheath above the substrate electrode and they transfer large amounts of energy and momentum as they bombard on the substrate surface. This causes the removal of the substrate material. The high energies of the ions involved in sputtering can significantly damage the substrate material, produce a rough and uneven surface, and yield low etch rates and selectivity.

Chemical etching during dry etching proceeds in the following steps i) the production of reactants in the plasma ii) the transport of the reactants to the substrate surface and iii) the adsorption of the reactants on the substrate surface. The necessary chemical reactions take place on the substrate surface which results in the desorption of volatile etch products from the substrate surface. The removal rate of the substrate material is associated with little or no physical sputtering. Therefore the removal rate tends to be equal in the vertical and lateral direction on the substrate material. This causes the significant undercut of the masking material and therefore limits the transfer of fine features on the substrate material. As there is no ion bombardment, the plasma induced

damage is low and, depending on the volatile etch products formation, it can produce high selectivity.

During ion-enhanced etching both physical sputtering and chemical etching are present. The ions accelerated across the plasma sheath perpendicular to the surface of the substrate, produce a higher vertical material removal. As ion bombardment provides energy/momentum transfer to the substrate surface it improves the desorption rate of volatile etch products formed via chemical etching of the substrate surface.

A sidewall etching inhibiting mechanisms involve the addition of polymer forming gas precursor in the plasma chemistry in order to initiate the formation of a thin film on the sidewalls of the etched pattern. Highly anisotropic etch profiles can be achieved with polymer formation on the sidewalls of the etch patterns, as it acts as an etch barrier preventing lateral etching [258].

5.4 Reactive ion etching of diamond

Reactive ion etching uses low pressures > 10 mTorr, where the mean free path of ions is small and therefore generates low density plasmas.

The first report of reactive ion etching of diamond dates back to 1989 by Sandhu, et al. [204], where a low etch rate of 350 A/min was measured for natural single crystal diamond using 0.4 keV oxygen ions (200 W, 80sccm, 65mTorr) in a parallel plate RIE system. Etch rates of amorphous carbon films were twice as large compared to diamond.

Reactive ion etching of diamond has been demonstrated using hydrogen, oxygen, argon, fluorine and their compounds [31, 204, 207, 214, 260-268, 270-273]. Most of the published experiments have been conducted using pure oxygen plasmas with etching rate ranges of 10 – 100 nm/min for single crystals and polycrystalline CVD diamond films. It would be expected that oxygen would preferentially attack non-diamond carbon phases on the diamond films, and references to preferential etching along grain boundaries, crystal imperfections and sp^2 carbon phases have been reported [23, 263].

Etching of diamond with a pure oxygen plasma is attributed to the formation of excited O* and O_2* radicals by energetic electrons accelerated by the RF field of RIE system.

Upon interaction of radicals with the carbon atoms of the diamond surface etching proceeds by the formation of volatile products such as CO and CO_2. Mass spectroscopic studies during the RIE of diamond films show the presence of proportionally more CO_2^+ in comparison with CO^+ species [266]. This phenomenon has been attributed to the formation of CO_2 by the products of the etching process rather than due to etching of the diamond surface. The etching/oxidation mechanism of amorphous carbon and hydrogen terminated diamond films proceeds by hydrogen abstraction and oxygen addition [266]:

$$C + O \rightarrow C^* + OH\ (g)$$
$$C^* + O \rightarrow CO(s), CO(g), CO_2(g)$$

During the reactive ion etching process chemical etching cannot be treated in isolation, as despite the low concentration of ions in the plasma, a contribution via physical sputtering is vital for the removal of carbon atoms from the diamond surface. The addition of argon and fluorine containing precursors in the oxygen plasma has shown a dramatic increase of the etch rate of diamond films and crystals [31, 214]. Fluorine containing gases when added to an oxygen plasma increase the formation of atomic oxygen and therefore the increase of diamond etch rate. The same observations have also been verified for ion beam etching, where enhancement of the etch rate is achieved using oxygen as a carrier gas [29].

The use of oxygen plasma for the RIE of diamond limits the use of photoresist as a masking material for surface fine patterning. Photoresist is the most common masking material used for the fabrication of ICs. Since the selectivity[2] between the two materials is very low the application of organic resists is limited. The choice of masking material for diamond RIE etching is not straightforward. The criteria for the selection of masking material is based on selectivity ratios between the two materials, good adhesion of the masking material with the diamond surface and the suitability of the masking material to be patterned by conventional fabrication techniques (e.g. photolithography).

[2] Selectivity or selectivity ratio in IC technology is defined as the ratio of the etch rate of the material to be etched to the etch rate of the masking material. The selectivity ratio controls the masking layers thickness and the resolution of the transferred etched pattern.

Several metals such as aluminium (Al) [272], tungsten (W), titanium (Ti) [260,261] nickel (Ni) and nickel-titanium (Ni-T) [262, 263] have been utilised as masking layers for the reactive ion etching of diamond. In addition, there are several studies of SiO_2 as a masking material for planarization processes [270]. All of the above mentioned materials provide good selectivity ratios for the RIE of diamond.

Diamond surfaces etched by RIE show a dramatic increase of surface roughness. Oxygen reactive ion etching of polycrystalline CVD diamond films occurs via preferential etching along grain boundaries. Oxygen will attack non-diamond forms of carbon such as sp^2 graphitic phases faster than the diamond phase. Since grain boundaries have a high areal density of sp^2 carbon porous diamond surfaces with rounded nodules and columnar structures have been observed under specific oxygen RIE process conditions [265]. Formation of columnar structures[3] has been observed along the polycrystalline facets of CVD films with no preferential orientation along the grain boundaries.

The formation of columnar structures on diamond surfaces upon oxygen RIE has been attributed to sputtered material from the electrode of the system, which has subsequently been deposited on the diamond surface. The presence of aluminium and silicon on the diamond etch surface [31, 264, 271, 272, 274, 275] has been reported after the oxygen RIE process. The etch rate of those materials is much lower than that of diamond and upon interaction with oxygen would form their corresponding oxides. Metallic containing impurities, possibly as oxides, deposited on diamond surface would act as micromasks during the etching process and, consequently, cause the formation of columnar structures. Also the formation of microchannels has been reported during oxygen RIE on diamond surface, which causes the darker coloured appearance of the films after RIE [23]. The formation of columnar structures on diamond CVD films has been extensively studied in hydrogen plasmas under a negative bias on the substrate holder [273, 274].

[3] Columnar structures formed on diamond surfaces due to RIE process have been referred in some published work as whiskers and spikes or nano-rods. In these studies only the term columnar structures will be used in order to avoid confusion.

Smooth diamond surfaces have been obtained by adding fluorine containing precursors such as CF_4 and SF_6, to an oxygen plasma [31, 263]. The addition of fluorine to the plasma mixture suppresses the formation of columnar structures on diamond surfaces [31, 275]. As fluorine containing precursors are commonly applied to etch silicon, aluminium and their oxides the micromasking effect is diminished under those etching conditions.

The published reports on the RIE of diamond films and crystals have been carried out using commercially available parallel plate RF systems as well as on MPCVD systems [22, 214, 207, 265] capable of isolated application of negative or positive bias of the sample substrate.

Ion damage of diamond needs to be addressed as it is known that the bombardment of diamond with inert ions leads to a surface rich in sp^2 bonding. This is due to the metastable nature of diamond; if adequate energy is supplied to the diamond, a sp^3 to sp^2 transition can occur with bond fission and displacement of carbon atoms. In addition, one must be concerned with a significant build up of etchant atoms in a reactive ion process, as this may have adverse effects on the surface properties of the material.

5.5 Reactive ion etching process

RIE systems can be considered as an electrical circuit and as a chemical reactor operating interactively. Typically the plasma used for the reactive ion etching process is produced and sustained between two electrodes, where one electrode is capacitively coupled to a high frequency (e.g. radio frequency RF of 13.56 MHz) power supply via an impedance matching network while the other electrode is grounded. The samples are placed on the powered electrode. Figure 5.3 shows the schematic diagram of a typical reactive ion etching system.

The cathode, the powered electrode, is considerably smaller in surface area than the anode, the grounded electrode. Since the chamber walls are also grounded the ratio between the anode and cathode surface areas in this system is quite high. During operation of the plasma a negative dc bias voltage develops between the cathode and the plasma. The negative dc bias voltage is typically equal to one half of the RF voltage peak. This will cause the acceleration of the positive ions, whose energies depend on the

magnitude of the bias voltage, across the plasma sheath in a direction perpendicular to the cathode. The induced bias will lead to the preferential positive ion bombardment of the cathode with minimal sputtering of the anode [344]. The typical pressure regime of reactive ion etching ranges from few mTorr to ca. 200 mTorr [258].

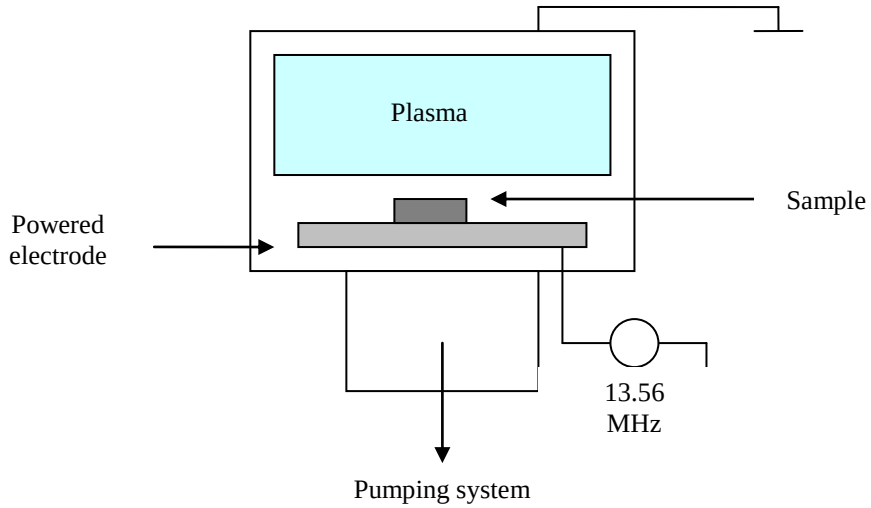

Figure 5.3 Schematic representation of reactive ion etching system.

5.6 Experimental

5.6.1 Diamond Samples

Etching studies presented in the work were conducted on (100) highly oriented and azimuthally disordered diamond films deposited on silicon substrate by MPCVD. The growth conditions of the films were presented in Chapter 3. The thickness of the diamond films were ~ 10 μm.

For comparison boron-doped (100) highly oriented and azimuthally disordered MPCVD diamond films have also been used. Doping was performed by ion-implantation (EMF, University of Edinburgh). The diamond film was subject to a flux of 5 x 10^{15} atoms cm^{-2} and an implantation energy of 50 keV. After ion-implantation the sample was subjected to annealing at 980^{o}C (sample temperature) in Ar (BOC 99.998 %) and 80 torr pressure for 2 hours.

The two types of (100) polycrystalline diamond films, intrinsic and boron-doped, were cut into square(~ 10 x 10 mm^2) samples and subject to solvent cleaning procedure prior to any analysis and etching treatments.

5.6.2 Reactive ion etching system

The RIE studies of CVD diamond films have been carried out in a capacitively coupled 13.56 MHz plasma reactor (PlasmaLab 80, Oxford Instruments Ltd). The plasma system comprises a vacuum chamber, shown in Figure 5.4, with a base pressure maintained by a Roots pump (Edwards Ltd) at a pressure of < 3mTorr. The desired process parameters such as: RF power, gas flow rate, chamber pressure, gas selection channel and process time can be set up prior any treatment and altered during the course of the experiment. The system automatically evacuates the plasma chamber twice at the end of any treatment, prior to reaching atmospheric pressure for access to the samples.

The diamond samples have been placed on the self-biased 20 cm diameter water-cooled electrode, located on the bottom of the vacuum chamber. The range of etching conditions used for this study is presented in Table 5-1. Most of the RIE treatments were applied for 60 min, otherwise the time duration is stated.

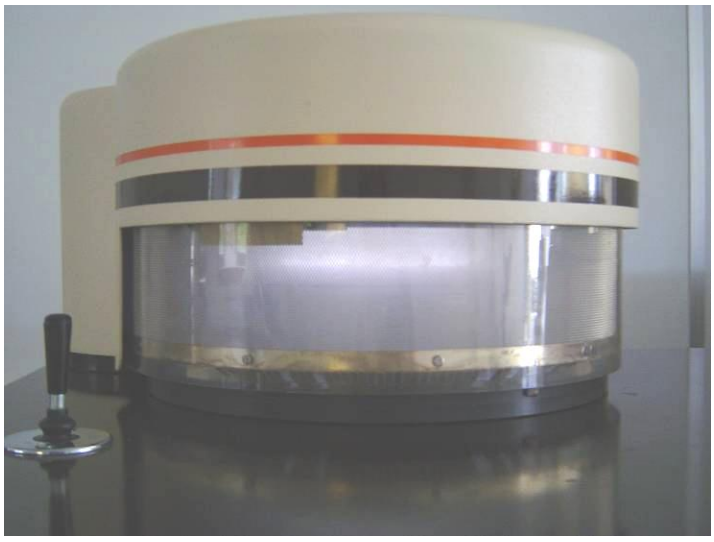

Figure 5.4 Parallel plate capacitively coupled plasma system used for the reactive ion etching of CVD diamond films.

Prior to any etching experiments oxygen plasma treatment was applied to an empty chamber in order to eliminate possible contamination from previous experiments.

Process parameters	
Sample	(100) polycrystalline CVD diamond
Gas	O_2 (99.999%)
Gas flow rate	20 – 80 sccm
Gas pressure	20 – 100 mTorr
RF power	50 – 250 W
Time duration	60 min or otherwise stated
Electrode temperature	14^{o}C

Table 5-1 Experimental conditions used for RIE studies of CVD diamond films.

5.6.3 Optical profilometry

Half of the surface area of the diamond films was covered with a silica mask prior to the RIE treatment. The etch steps formed on the diamond films' surface allowed the evaluation of the etch rates under different process conditions. The depth of the etched steps on the diamond films surface was measured by employing a 3-D optical profiler (Zygo. Ltd) and Dektak stylus profiler. Several optical topographies were acquired from the surface of the RIE treated diamond films in order to examine the uniformity of the etching process over the entire surface areas of the films. The etch rates presented in these studies are the average value of twenty individual measurements taken from the whole etched film surface. Error bars are one standard deviation of the mean value.

The etch rates of (100) highly oriented CVD diamond films have been determined as a function of O_2 applied pressure, O_2 gas flow rate and RF power at a constant power and substrate temperature.

Effect of O_2 applied pressure

The effect of applied O_2 pressure on the etch rate of diamond films has been examined for both the intrinsic and boron-doped CVD films. The oxygen pressure range examined was from 20 mTorr to 100 mTorr, and for all the experiments the RF power was kept constant at 200 W and the oxygen gas flow rate at 20 sccm. The RIE process was applied for the duration of 60 min for each experiment. Figure 5.5 Shows the effect of

the applied O_2 pressure on the etch rate of intrinsic and boron-doped (100) highly oriented CVD diamond films.

Increasing the O_2 pressure decreased the etch rate for both intrinsic and boron-doped (100) highly oriented CVD diamond films. As can be seen from Figure 5.5, the measured etch rates for both types of CVD diamond films decreased linearly with the increase of the pressure. The presence of boron dopants within the diamond films did not affect the etch rates under the present RIE conditions.

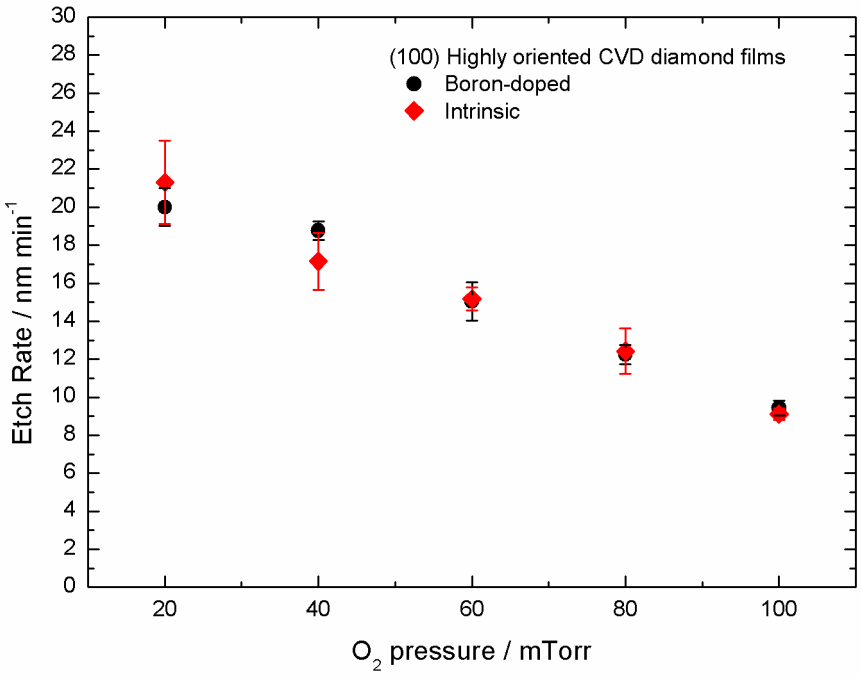

Figure 5.5 Measured etch rates of intrinsic and boron-doped (100) highly oriented CVD diamond films with O_2 applied pressure at constant RF power of 200W and oxygen gas flow rate of 20 sccm.

The present results are in agreement with the previous work on etching of diamond crystals and films [25, 28, 267], where diamond films, etch rate decreases with the increase of the applied pressure.

When the pressure applied to a reactive ion etching process is reduced, the ionisation of the gas increases and there is a concomitant increase in the ion density of the plasma. Taking account of the present results we can assume that ionic species in the oxygen plasma, such as O^+ and O_2^+, have a very important role in the etching of the diamond films.

The negative bias on the powered electrode is increased at low pressures and likewise the ion flux bombarding the diamonds film surface. The recombination rate in the plasma is low at low pressures therefore the energetic ions which accelerate towards the diamond film surface undergo very few collisions and impinge the diamonds surface nearly perpendicular leading to high etch rates.

As the pressure increases the ionisation of the gas source decreases. As a consequence the concentration of ions is reduced in the plasma. The collision rate in the plasma increases at higher pressures and therefore the number of accelerated ions which bombard the diamond surface with sufficient energy for material removal is reduced.

Effect of O_2 gas flow rate

In order to investigate the effect of oxygen gas flow rate on the etch rate of diamond films, the reactive ion etching process took place under constant RF power of 200 W and applied pressure of 60 mTorr. The range of gas flow rates examined was from 20 to 80 sccm. Studies were conducted only on intrinsic (100) highly oriented CVD diamond films.The measured etch rates as a function of the oxygen gas flow rate are shown in Figure 5.6.

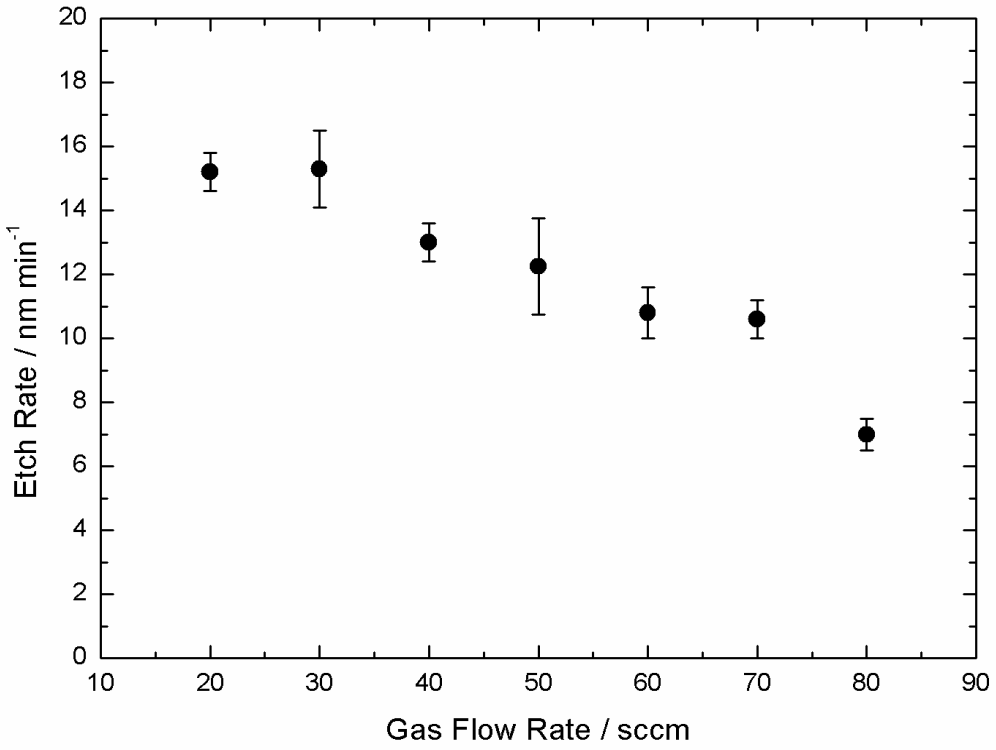

Figure 5.6 Etch rate of intrinsic (100) highly oriented CVD diamond films with O_2 gas flow rate at constant RF power of 200 W and a pressure of 60 mTorr.

The etch rate of CVD diamond films remained constant up to 30 sccm of oxygen gas flow rate. It can be seen from Figure 5.6 that the further increase of the oxygen gas flow rate decreases the etch rate, in an approximately linear manner. A plateau of the measured etch rate has been observed between 60 and 70 sccm of oxygen gas flow rates. Increasing the gas flow rate beyond 80 sccm resulted in a further decrease of the diamond etch rates.

The diamond etch rate is dependent on the oxygen gas flow rate as can be seen from the present results. The gas flow rate affects, via the residence time[4] , the amount of reactant species present in the plasma. As the oxygen gas flow rate increases, the residence time of oxygen species in the plasma decreases. Hence the induced decline of the measured etch rates with the increase of the oxygen gas flow rates shows that the residence time is insufficient to provide the necessary amount of reactant species for the effective removal of material.

Similar results have been obtained by Sirineni *et al* [23] on CVD diamond films. The etch rate of diamond films was enhanced up to 30 sccm of oxygen gas flow rate while at 40 sccm and beyond of oxygen gas flow rate the etch rates decreased. However there are few reports [23] on the effect of oxygen gas flow rate on the etch rate and morphology of diamond films and crystals after RIE, Leech *et al* [265] observed the increase of measured etch rate on diamond films with an increase of the oxygen gas flow rate.. The discrepancy between the present results and previous studies [23, 263, 277], has not been reconciled. It is reasonable to rationalise the effect of residence time, of oxygen reactant species in the plasma, on the etch rates of diamond CVD films.

Effect of RF power

The effect of applied RF power on the etch rate of intrinsic (100) highly oriented CVD diamond films was examined for a constant O_2 applied pressure of 20 mTorr and O_2 gas flow rate of 20 sccm. The duration of each RIE treatment was 60 min and the RF power range investigated was from 50 to 250 W.

[4] Residence time τ, is a characteristic parameter of the plasma system and is related to the volume and the pumping rate of the system as : $\tau = V / S$

Figure 5.7 shows the measured etch rates values as a function of applied RF power. As the applied RF power increased between 50 and 150 W the etch rates of the CVD diamond films increased monotonically. A further increase of the RF power between 150 and 250 W did not produce the same enhancement on the diamond etch rates. Above approximately 250 W the etch rates appear to saturate. The etch rate increased from 8nm/min to 23nm/min in average from 50W to 250W applied RF power.

Previously published results reported an increase of etch rate with the applied RF power [23, 25, 28, 260, 263, 265, 277, 278]. As the applied oxygen gas pressure has been kept constant for the above mentioned experiments the enhancement of the RF power, induced the increase of dissociation and ionisation in the plasma. Under optimum conditions the etching process is accompanied by an enhancement of the oxygen radical (O*, O_2*) concentration and more energetic ions therefore induce the increase of the diamond films etch rate.

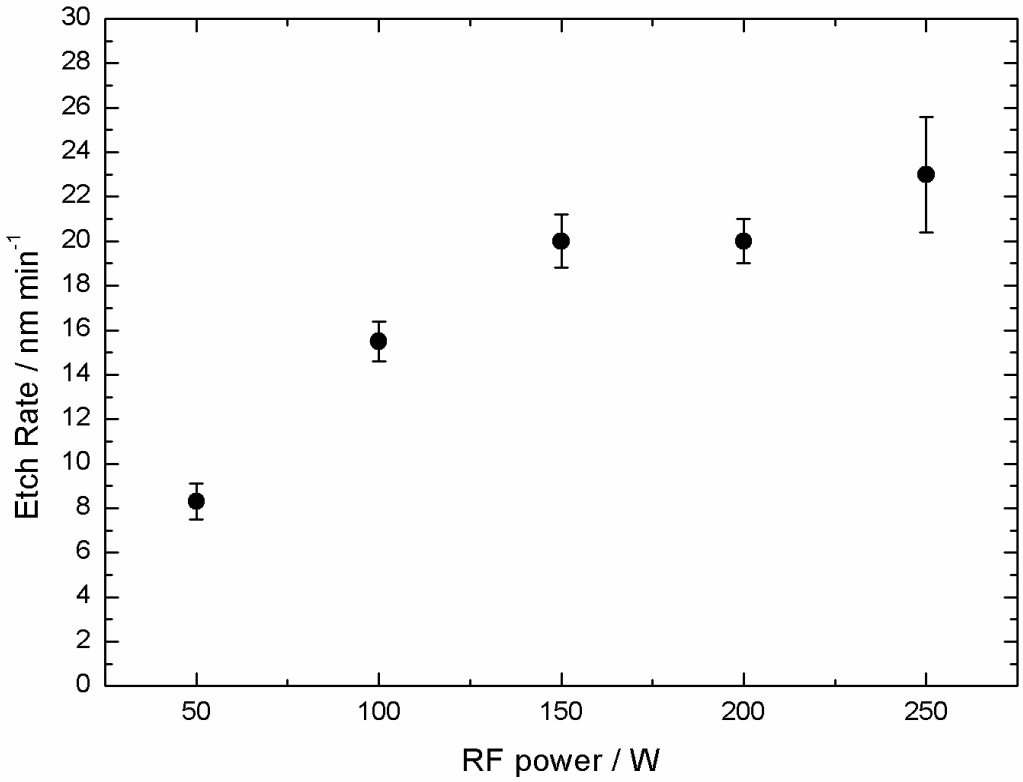

Figure 5.7 Etch rate of intrinsic (100) highly oriented CVD diamond films with applied RF power at constant oxygen pressure of 20 mTorr and 20 sccm gas flow rate.

5.6.4 Scanning electron microscopy

The surface texture of the etched CVD diamond films have been evaluated by scanning electron microscopy. The surface of an intrinsic as-grown (100) highly oriented CVD diamond film is shown in Figure 5.8 a). The diamond film was then subjected to RIE process for 60 min at 200 W RF power, 20 mTorr applied oxygen pressure and 20 sccm gas flow rate. The etched diamond surface is shown in Figure 5.8 b). The RIE treated surface of the (100) highly oriented CVD diamond film has been etched preferentially compared to the grain boundaries. The different etch rates were sufficient to delineate the crystalline grains. Columnar structures, which have been reported previously [23, 31, 214, 263, 271, 272, 278], were present on the etched surface of the CVD diamond film.

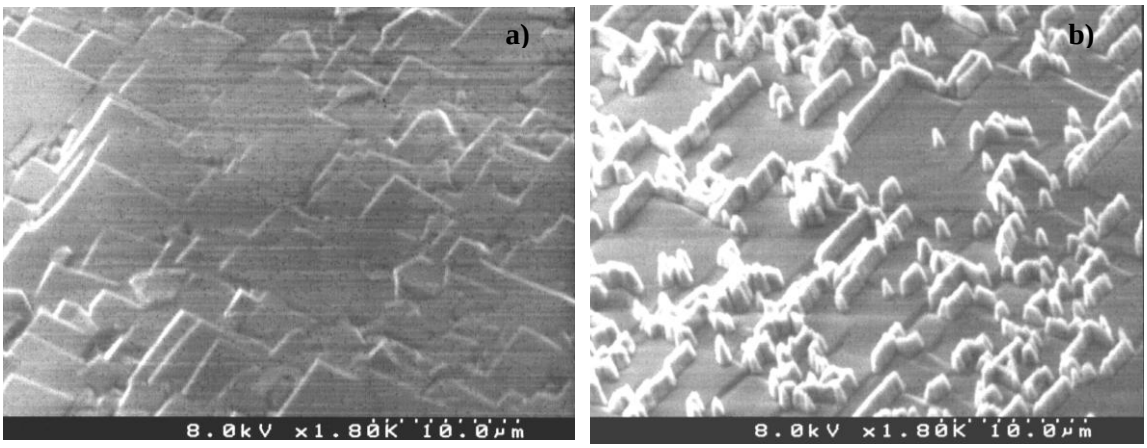

Figure 5.8 SEM images from (100) highly oriented CVD diamond films a) prior to treatment and b) after 60 min of oxygen RIE at 200 W, 20 mTorr and 20 sccm. The SEM images show a perspective view of the diamond surface.

Figure 5.9 shows that oxygen RIE treatment produce square 'corrals' of columns surrounding the (100) crystallites. The columns produced by the oxygen RIE treatment, had a diameter of ~390 nm and a height of ~1.2 μm under the specified conditions.

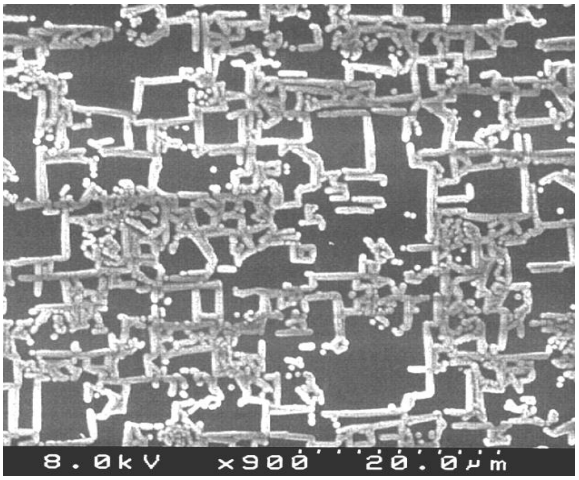

Figure 5.9 Top view of oxygen RIE treated (100) highly oriented CVD diamond film.

The surface of azimuthally disordered (100) intrinsic CVD diamond film, treated under the same RIE process conditions, such 200 W of RF power, 20 mTorr applied oxygen pressure and 20 sccm gas flow rate, was found to exhibit higher density of columnar regions. Figure 5.10 a) shown the surface of as-grown azimuthally disordered (100) CVD diamond film, whilst Figure 5.10 b) shows the same diamond surface after oxygen RIE process for 60 min.

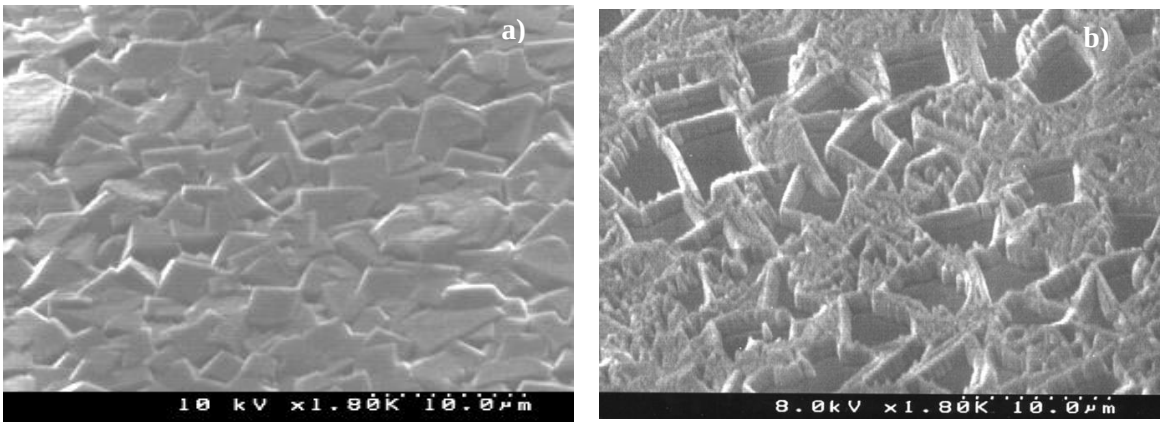

Figure 5.10 SEM images of azimuthally disordered (100) CVD diamond film a) prior and b) after oxygen RIE treatment at 200W, 20mTorr and 20sccm for 60min.

The higher density of columnar structures observed on azimuthally disordered (100) CVD diamond films have been correlated with the higher density of inter-granular area of those CVD diamond films, while the highly oriented (100) CVD diamond films exhibit a low inter-granular area, in comparison with the azimuthally disordered (100) CVD diamond films.

Similarly, preferential formation of columnar structures on the inter-granular area of boron-doped (100) polycrystalline diamond films has been observed after oxygen RIE at 200W, 20mTorr and 20sccm for 60min. Figure 5.11 shows the a) highly oriented and b) azimuthally disordered boron-doped (100) diamond films after RIE treatment. Based on these observations, the presence of boron-dopants on the (100) CVD diamond film, did not affect the etching process or the resulted surface morphology.

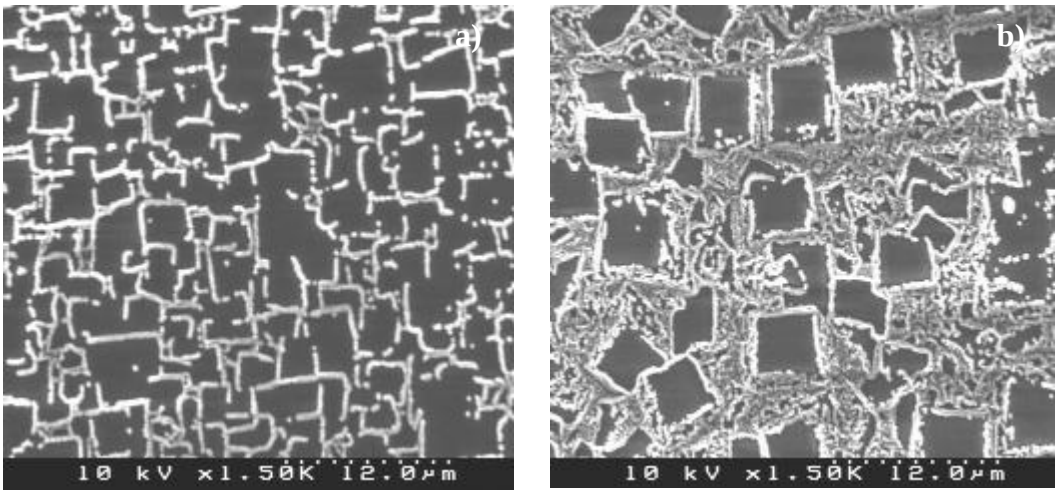

Figure 5.11 SEM images of boron-doped a) highly oriented and b) azimuthally disordered (100) CVD diamond film after oxygen RIE, at 20mTorr, 200W and 20sccm for 60 min.

For higher oxygen pressures the columnar structures were present on the (100) diamond surfaces after 60 min of RIE treatment. Figure 5.12 shows the top and perspective view of (100) highly oriented CVD diamond films after oxygen RIE treatment for 60 min at constant RF power of 200W, 20 sccm gas flow rate and two applied oxygen pressures of 40 and 60 mTorr.

As it can be seen from Figure 5.12 a-d) the columnar structures were not restricted only to the grain boundaries but they were present on the (100) diamond surfaces after the etching process.

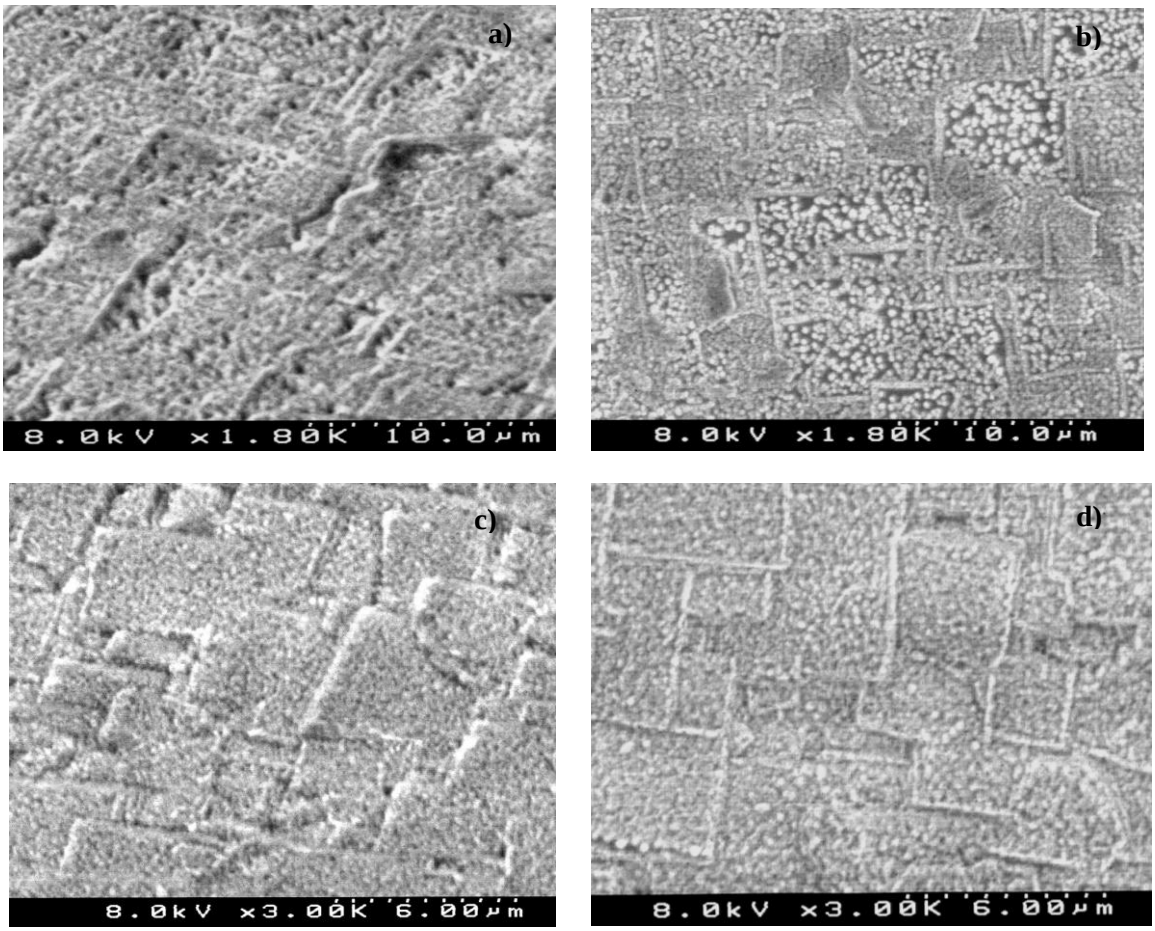

Figure 5.12 SEM images of (100) highly oriented CVD diamond films after they have been subjected to oxygen RIE treatment for 60 min at 200W, 20sccm at a-b) 40mTorr and c-d) 60mTorr.

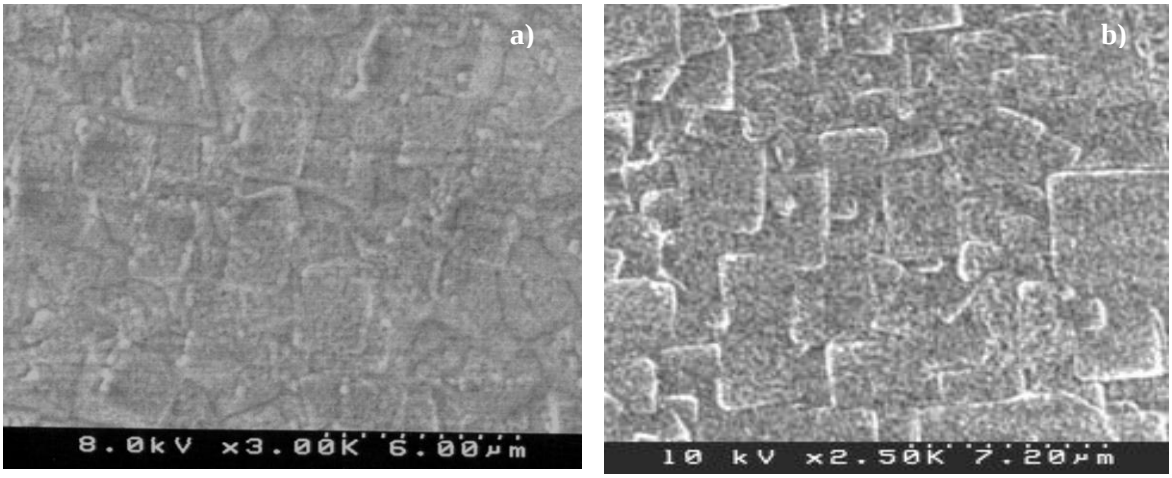

Figure 5.13 SEM images of the (100) highly oriented CVD diamond films subjected to oxygen RIE for 60min at 200W, 20sccm a) 80mTorr and b) 100mTorr.

For applied oxygen pressures above 80 mTorr to 100 mTorr the columnar structure formation has been suppressed and the formation of very fine structures have been observed on the (100) diamond surfaces. Figure 5.13 (a & b) shows the surface of (100) highly oriented CVD diamond films after 60 min of oxygen RIE treatment at 200W, 20sccm 80mTorr and 100mTorr.

Boron-doped (100) CVD diamond films have been subjected to oxygen RIE for the pressure range from 40mTorr to 100mTorr, for constant 200W and 20sccm for 60min. SEM analysis, on the boron-doped (100) diamond films, revealed exactly the same etching mechanism and columnar formation as on the intrinsic (100) diamond films. Results indicate that the presence of boron-doping on the CVD diamond films do not influence the etching process and does not affect the columnar structures formation.

The effect of the applied RF power has been examined at a constant applied oxygen pressure of 20 mTorr and gas flow rate of 20 sccm. Figure 5.14 (a – d) shows the surface morphology of the (100) highly oriented CVD diamond films after etching within the applied RF power range from 50 to 150 W.

The distribution of the columnar structures was unaffected by the applied RF power with only a sparse presence on the (100) planes. The measured etch rate of the diamond films as well as the column height have been found to increase with applied RF power.

At a low RF power of 50W the structures adopt a pyramidal shape with sharp tips (~71 nm) protruding from a ~275 nm structure. While at higher RF power, e.g. 150 W the structures adopt a symmetrical geometry as show in Figure 5.14 d). At higher RF powers ≥150W, the anisotropy of the oxygen RIE process increases and causes the formation of symmetrical column structures.

Formation of columnar structures on diamond surface, induced by reactive ion etching process, has been reported in previously [23, 31, 214, 263, 271, 272, 278]. The distribution of columnar structures has been found to be independent of the type of diamond plane, as a random distribution has been reported for single crystal [31, 214] and uncoated polycrystalline CVD diamond films [23, 262, 276].

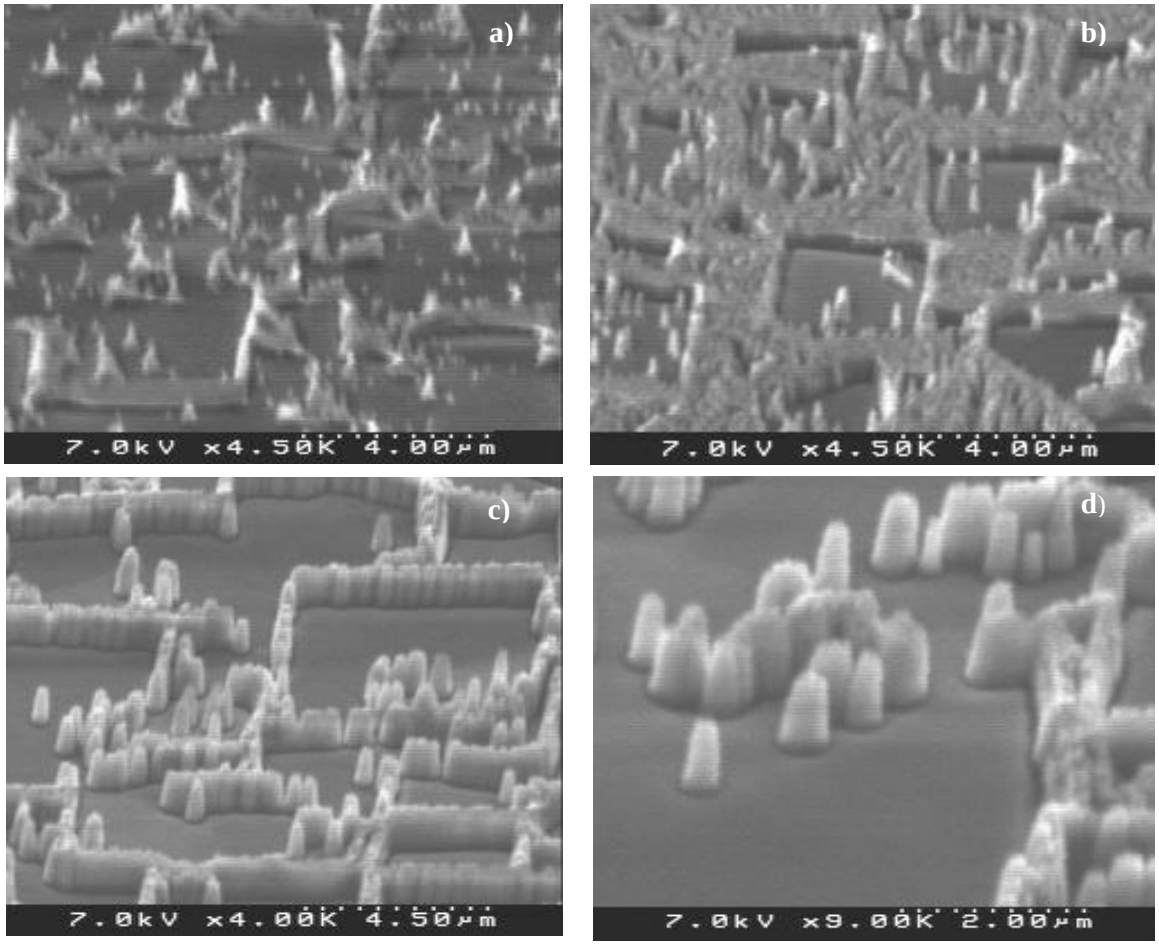

Figure 5.14 SEM images of oxygen RIE treated (100) highly oriented CVD diamond films for 60min at 20mTorr, 20sccm a) 50W, b) 100W c) & d) 150W applied RF power.

The studies of Dorch *et al* [275] show the change of columnar structures on applied oxygen pressure or RF power, while, Sirineni *et al* [23], found that columnar formation could be suppressed by using optimised RIE process conditions but Li *et al* [271], observed a random distribution of columnar structures.

In the present studies the distribution of columnar structure formation was found to be dependent on the oxygen pressure. At low pressures, of 20 mTorr, the formation of diamond columns was not uniform across the whole diamond surface. The distribution of columnar structures was restricted on the inter-granular area between the (100) diamond crystallites. The surface area of the etched (100) diamond crystallites appeared to be smooth after the RIE process.

As the applied oxygen pressure increased the columnar structures were distributed along the surface of the diamond films, with preferential formation along the grain boundaries. The height of the columnar structures was found to depend on the applied oxygen pressure and follow exactly the same trend as the etch rate of the diamond films. Etching has been found to be more resistant at the grain boundaries of the CVD diamond crystallites.

In order to examine the influence of the crystallographic plane on the formation of diamond columns, isolated cubo-octahedral CVD crystallites bounded by {100} and {111} diamond have been subjected to oxygen RIE treatment at low applied oxygen pressure regime.

One of the as-grown single and isolated CVD cubo-octahedral diamond crystallites is shown in Figure 5.15 a). It had been subjected to oxygen RIE treatment for 60 min, at 200 W, 40 mTorr and 20 sccm and Figure 5.15 b) shows the etched diamond crystallite.

As seen from Figure 5.15 a) & b) the {100} planes of the cubo-octahedral diamond crystallite have been etched and formed smooth surfaces, while the {111} planes sho surface roughening and the formation of columnar structures.

Figure 5.16 shows azimuthally disordered cubo-octahedral CVD diamond crystallites at the periphery of the diamond film that have been subjected to oxygen RIE at 100 W, 20 mTorr and 20 sccm for 60 min. It can be seen from the SEM image that, despite the different orientation of the {100} diamond planes with respect to the underlying silicon substrate, all the {100} planes have been etched uniformly and smooth surfaces have been produced.

In contrast, the {111} planes of the cubo-octahedral CVD diamond crystallites were covered with fine columnar structures. The present observation of the cubo-octahedral CVD diamond crystallites correlated with the observations made on the (100) highly oriented and azimuthally disordered CVD diamond films. During oxygen RIE the (100) diamond planes etched smoothly while the formation of columnar structures is favourable at the grain boundaries where {111} diamond surfaces exist.

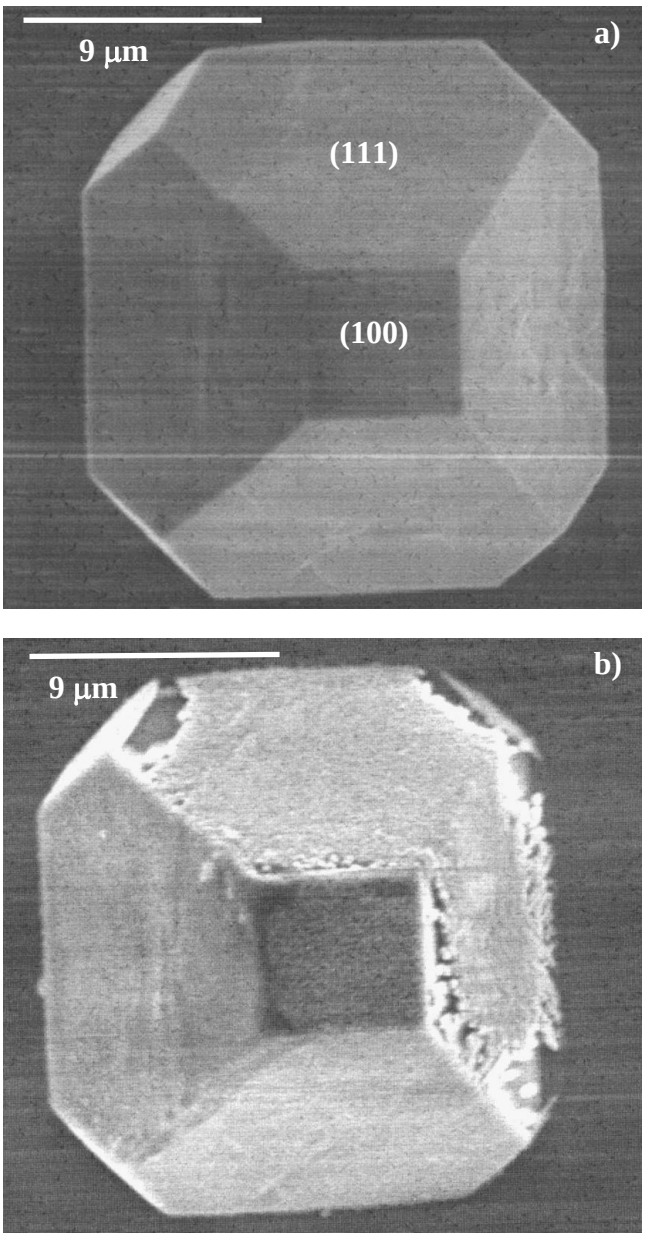

Figure 5.15 SEM images of a) an as-grown cubo-octahedral CVD diamond crystallite and b) after it has been subjected to oxygen RIE for 60min at 200W, 40mTorr and 20sccm.

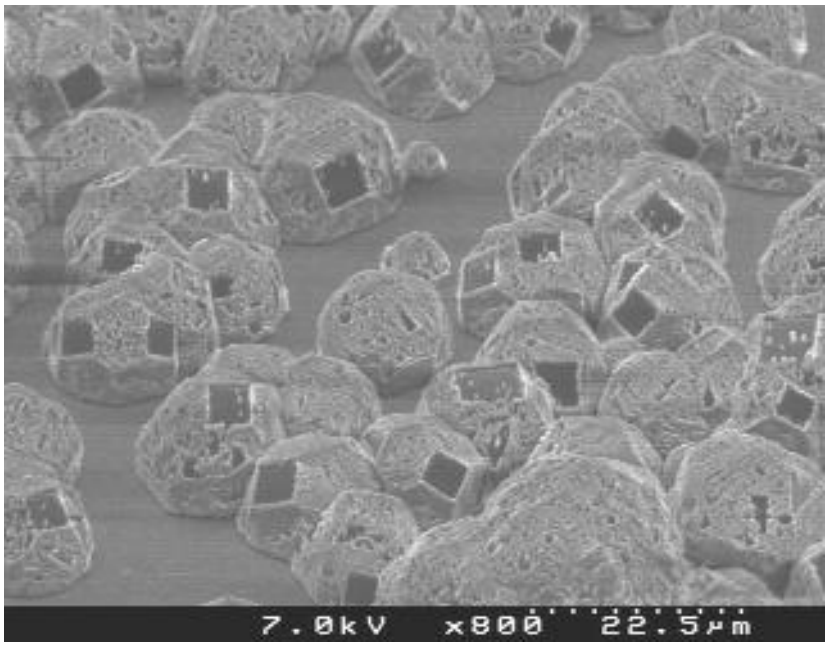

Figure 5.16 SEM of oxygen RIE treated CVD diamond crystallites for 60 min at 100 W, 20 mTorr and 20 sccm.

5.6.5 Atomic Force Microscopy

The effect of the oxygen RIE treatment was examined by contact mode AFM on the surface of (100) highly oriented intrinsic CVD diamond films. The same area on as-grown (100) highly oriented CVD diamond film was examined before and after each subsequent oxygen RIE treatment. The oxygen RIE conditions used for this set of experiments were 100 W RF power, 35 mTorr pressure and 50 ccm gas flow rate. The duration of the treatments was 3 min, 12 min, 15 min and 15 min (45 min total) of oxygen RIE. Figure 5.17 shows AFM topographies from the same area on the (100) highly oriented CVD diamond film acquired a) on the as-grown diamond surface b), c) and d) after 3 min, 15 min and 45 min of oxygen RIE treatment respectively.

No apparent surface morphological changes were observed within the AFM resolution for up to a total of 30 min duration of RIE treatment on the diamond crystallites. Apparently under the present RIE conditions the etch rates are low and the treatment duration was not adequate for morphological changes. Small circular particles appeared on the surface of diamond crystallites after the initial 3 min of RIE treatment.

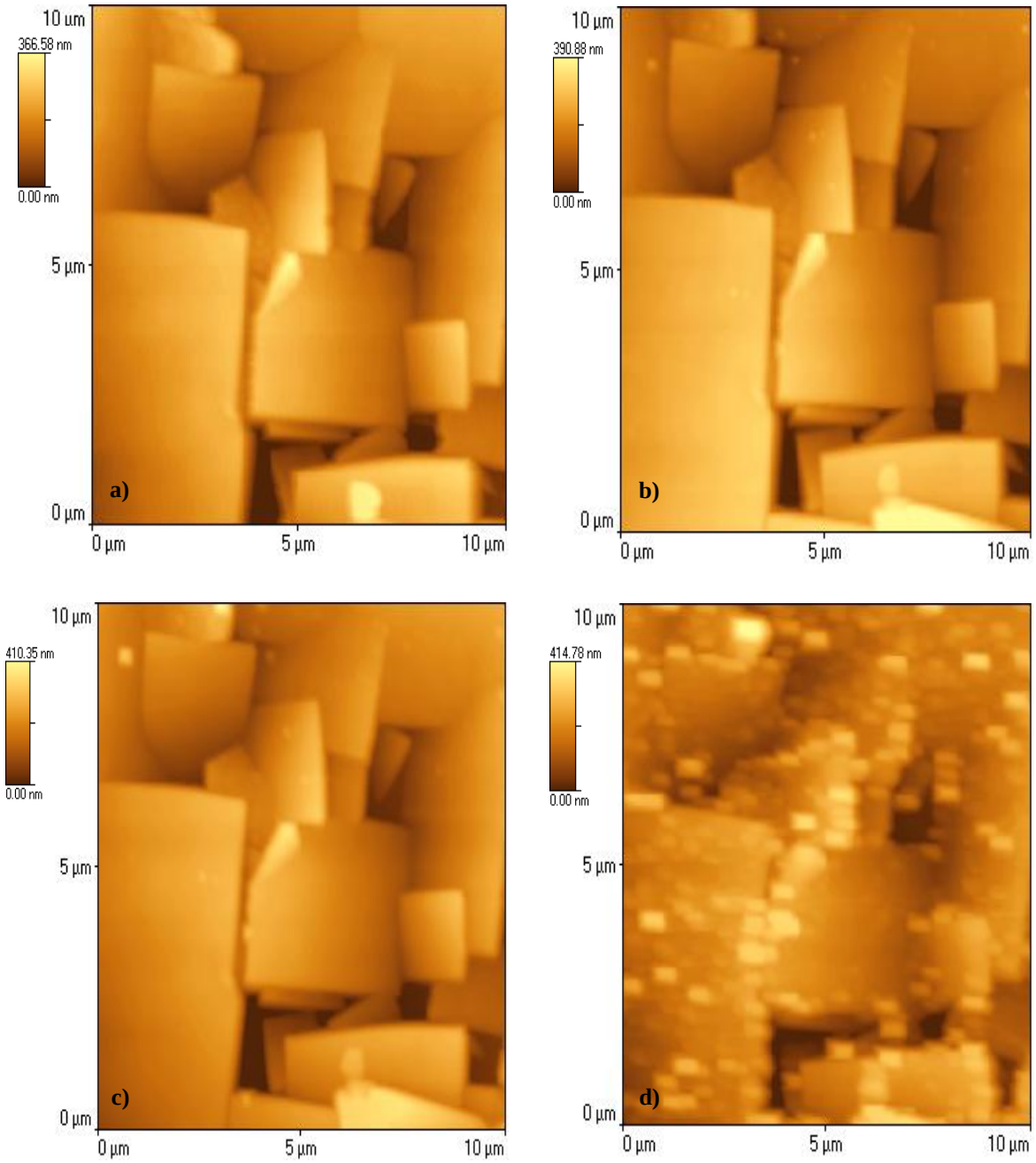

Figure 5.17 Plan AFM topographies of the same area of (100) highly oriented CVD diamond film, a) as-grown and after oxygen RIE treatments at 100W, 35mTorr and 50sccm for b) 3 min, c) 15 min and d) 45 min.

It is believed that they are contamination originating from sample handling during analysis in between the treatments, although subsequent RIE treatments did not remove them from the diamond surfaces.

Interestingly deposition of material was observed during the last 15 minutes of oxygen RIE treatment, Figure 5.17 d). The material was deposited during the RIE treatment and it was distributed uniformly on the diamond crystallites surface. Figure 5.18 shows the AFM topography from the oxygen RIE treated diamond surface after 45min of treatment. The deposited material on the diamond surface was found to exhibit columnar structures with great uniformity and coherence along the grain boundaries of the diamond crystallites.

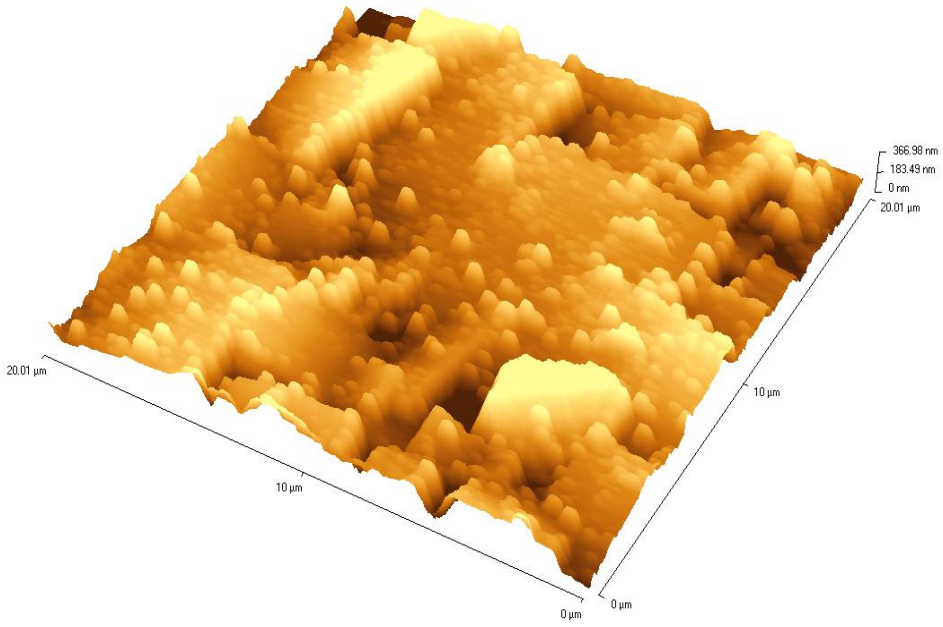

Figure 5.18 Perspective AFM topography of (100) highly oriented CVD diamond film, O_2 RIE treated for 45 min in total at 100 W RF power, 35 mTorr applied pressure and 50 sccm gas flow rate.

Surface roughness was evaluated from averaging over 10 different diamond crystallites on the diamond films. 2D-3 point levelling had been applied to the area under measurement to eliminate errors introduced due to the tilt of the diamond crystallites. The surface roughness was measured for all the subsequent oxygen RIE treatments. As shown in Figure 5.19. the average surface roughness, Ra, was found to increase slightly after the initial oxygen RIE treatment and remained constant up to 30 min of treatment. Surface roughness rapidly increased after 45 min of oxygen RIE as it had been accompanied by the deposition of material.

The effect of the oxygen pressure on the surface roughness of the (100) highly oriented CVD diamond films was examined by AFM. The diamond films had been subjected to oxygen RIE for the duration of 60 min at 200 W RF power and 20 sccm oxygen gas flow for the range of 40-100 mTorr applied oxygen pressure. Applying the same AFM analysis, described above, the surface roughness as measured by AFM decreased monotonically with the applied oxygen pressure as shown in Figure 5.20.

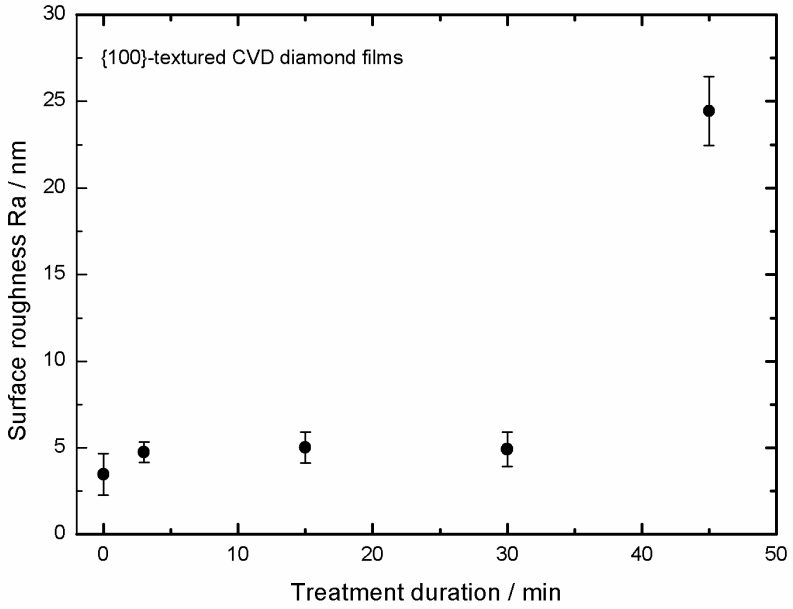

Figure 5.19 Surface roughness of (100) highly oriented CVD diamond films with etching time.

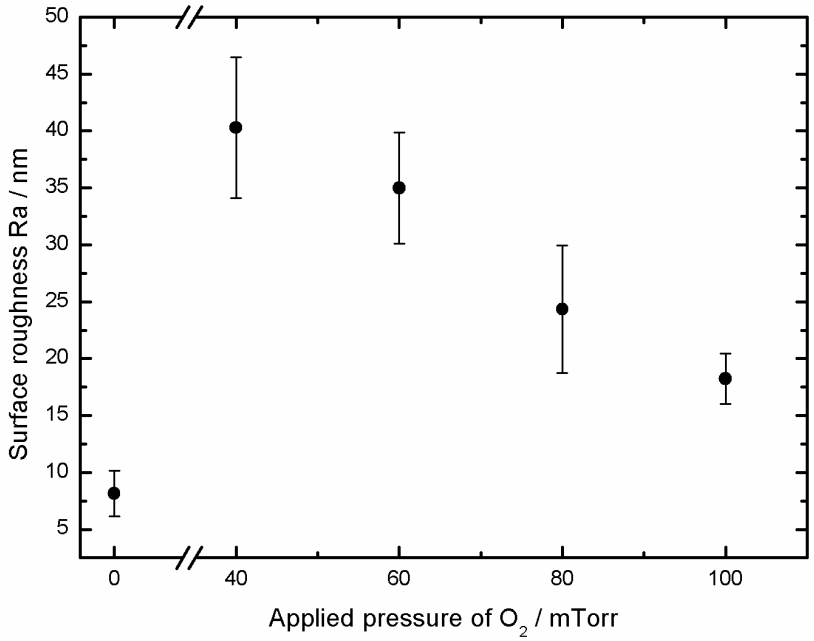

Figure 5.20 Surface roughness of oxygen RIE treated (100) highly oriented CVD diamond films as a function of applied pressure.

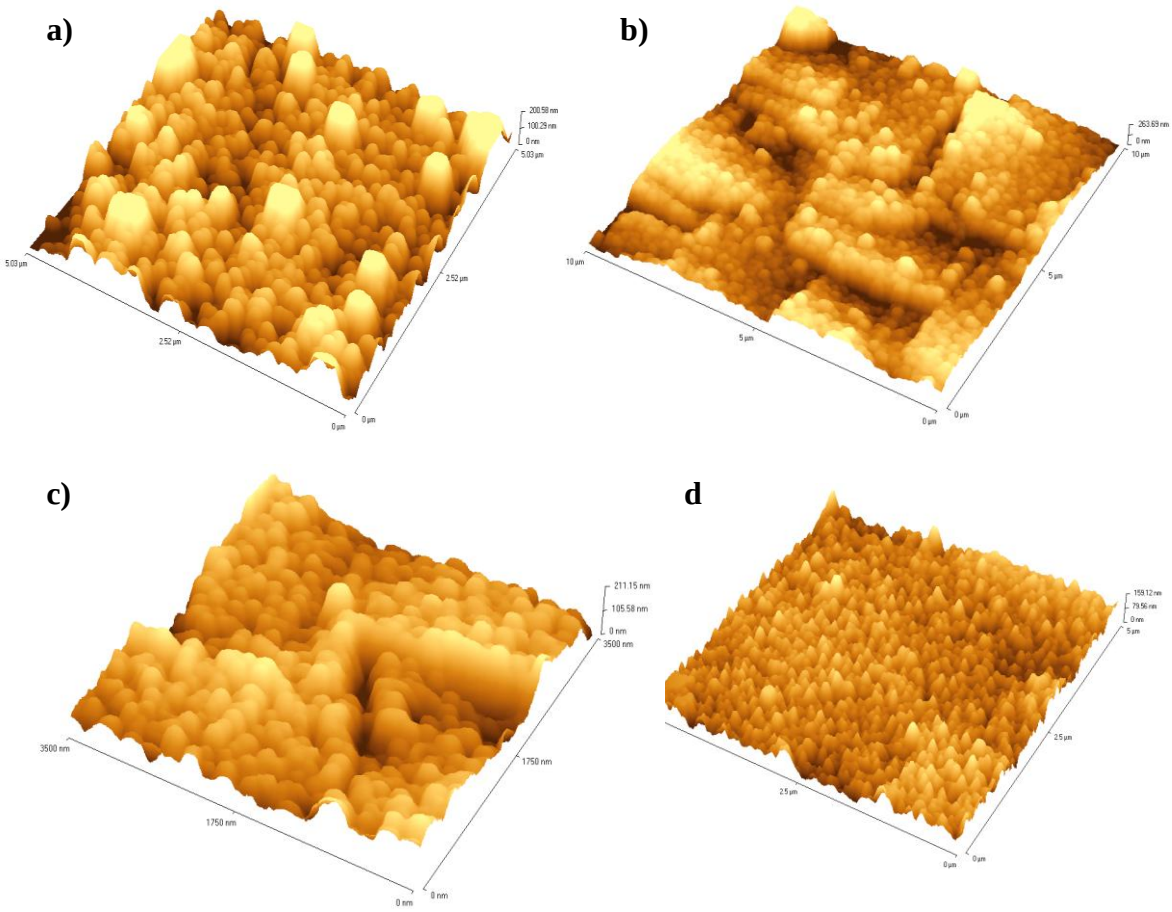

Figure 5.21 AFM topographies of (100) highly oriented CVD diamond films treated for 60 min oxygen RIE at 200 W and 20 sccm, a) 40 mTorr, b) 60 mTorr, c) 80 mTorr and d) 100 mTorr.

Figures 5.21 a) to d) show AFM topographies from a) 40 mTorr, b) 60 mTorr,c) 80 mTorr and d) 100 mTorr applied oxygen pressure. All (100) highly oriented CVD diamond films exhibit strong surface roughening and formation of columnar structures.

The distribution of columnar structures, for applied oxygen pressure of 40mTorr and 60mTorr, was pronounced along the grain boundaries. As applied oxygen pressure increased to 80mTorr and above the formation of columnar structures was on the (100) diamond facets as well as on the inter-granular areas surround them. The decrease of the measured surface roughness values with applied oxygen pressure is attributed to the decrease in the columnar structures height, with applied oxygen pressure.

There are no reports in the literature on the surface roughness depending on applied oxygen pressure, although, Ando *et al* [31] and Leech *et al* [263], reported the increase of the surface roughness of single crystal diamond upon exposure to oxygen RIE treatment. They also saw the formation of columnar structures on the diamond surface after RIE.

5.6.6 X-Ray photoelectron spectroscopy

The wide survey XPS data for a (100) highly oriented CVD diamond film subjected to oxygen RIE treatment (250 W, 20 mTorr, 20 sccm for 60 min) was compared to an 'as-grown' and hydrogen plasma treated (100) highly oriented CVD films, as shown in Figure 5.22. The peaks observed on the XP spectra are denoted on the Figure 5.22 c).

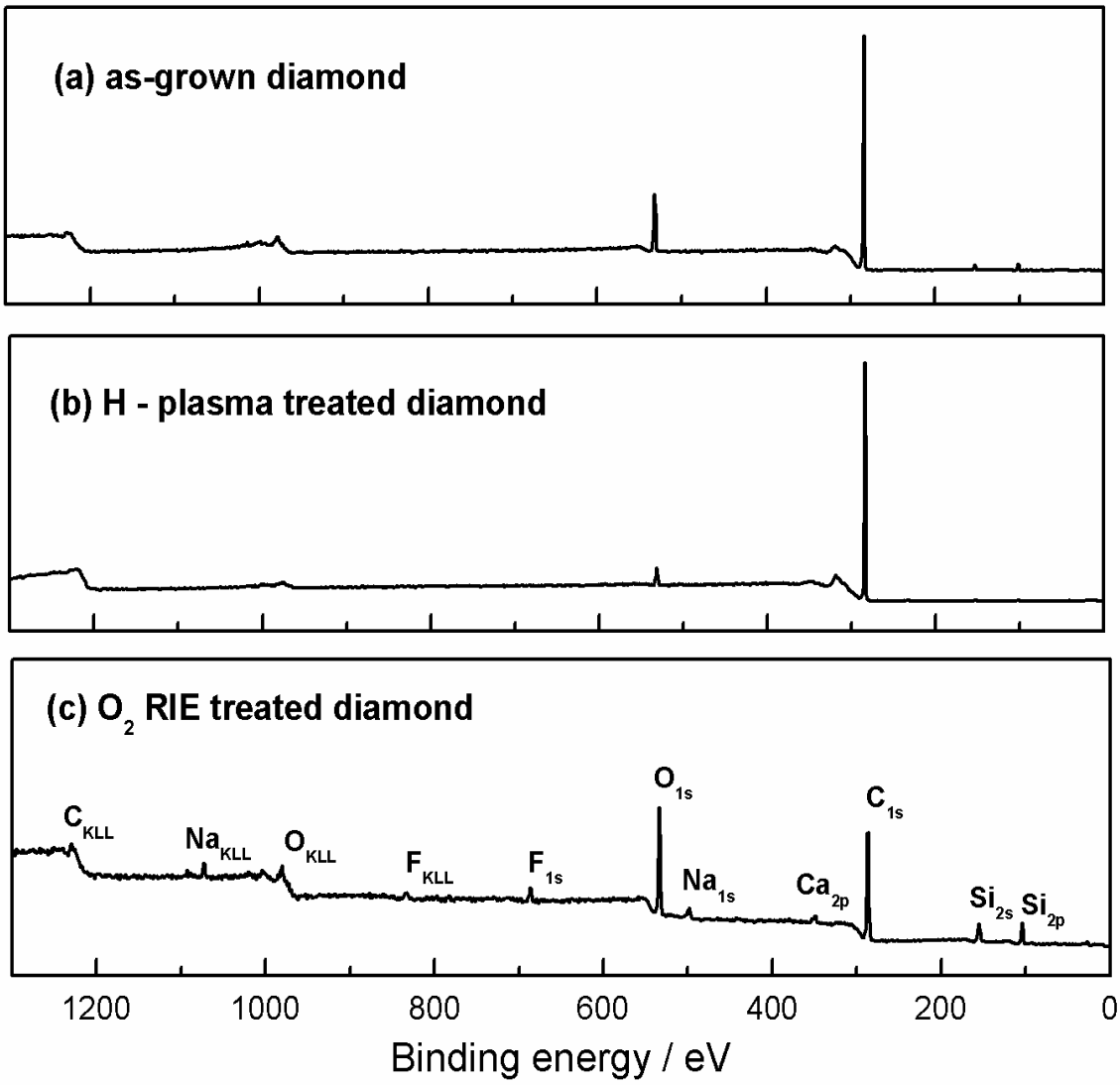

Figure 5.22 Wide scan XP spectra from (a) as-grown, (b) hydrogen–plasma treated (20 hr) and (c) oxygen RIE plasma treated (60 min) (100) highly oriented CVD diamond films.

The C 1s peak is observed at 284.7 eV for all the diamond samples under investigation. The O 1s peak observed at 532 eV for all samples and its intensity was observed to vary with the surface treatment. The silicon Si 2s and Si 2p peaks were observed at 152 eV and 102 eV respectively for the as-grown and oxygen RIE treated diamond films. The intensity of both silicon peaks was found to be higher for the oxygen RIE treated in comparison with the as-grown diamond films.

The present XPS data of the oxygen RIE treated diamond film demonstrated the presence of fluorine F 1s peak at 690 eV and its Auger transition at ~ 830 eV, sodium Na 1s peak at 500 eV and its Auger transition at ~ 1070 eV and calcium Ca 1s peak at 350 eV. The surface of the oxygen RIE treated diamond films was found to be contaminated with those elements which originated from the RIE treatment. Similar surface contamination was observed by XPS analysis on oxygen RIE treated single crystal diamond by Ando *et al* [31] and Dorch *et al* [275].

For a (100) highly oriented CVD diamond sample treated with oxygen RIE at 100W, 50mTorr and 50sccm for 60min, the wide scan spectra (not shown) identified the presence of carbon C 1s and oxygen O 1s peaks and the silicon Si 2s and Si 2p peaks. No other source of contamination was found to be present on the oxygen RIE treated diamond sample.

High resolution XP spectra comprising carbon C 1s, oxygen O 1s, silicon Si 2p were collected from the oxygen RIE treated sample at 100W, 50mTorr and 50sccm for 60 min.

Figure 5.23 compares the high resolution carbon C 1s peak from a hydrogen plasma treated (20 hrs) diamond sample with that of oxygen RIE treated (100 W, 50 mTorr and 50 sccm for 60 min) diamond film.

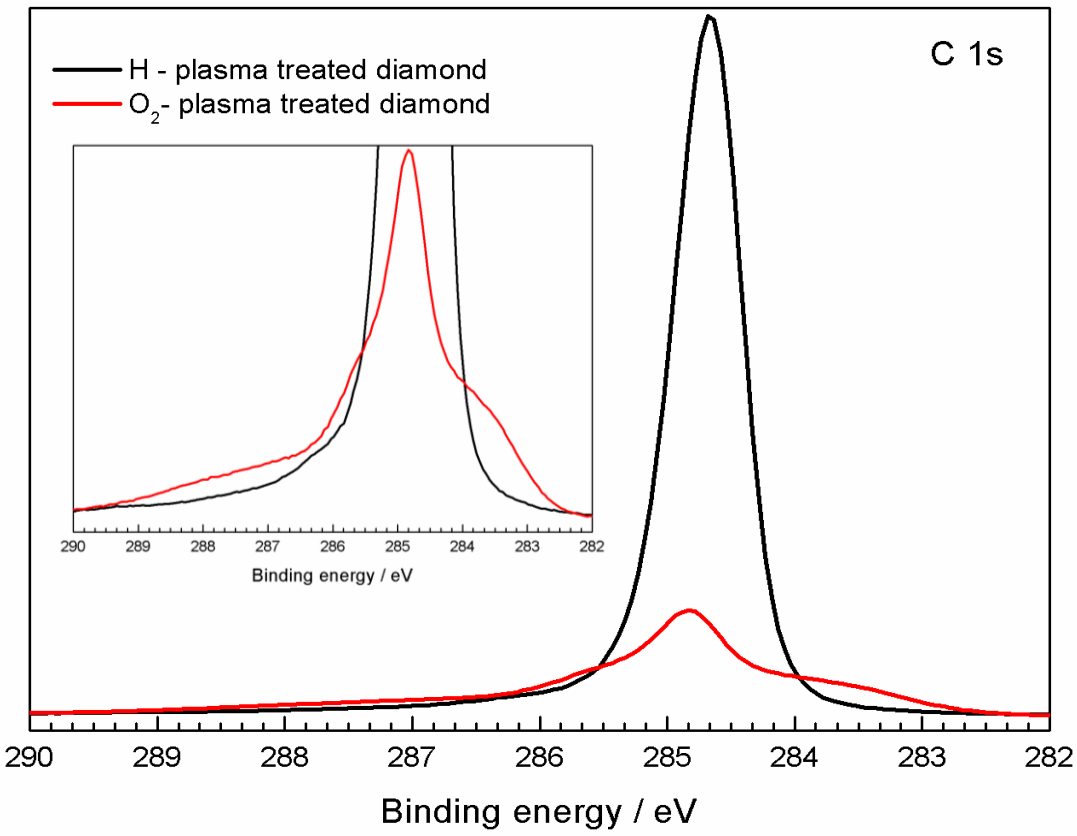

Figure 5.23 High resolution C 1s XP spectra of a hydrogen plasma (20 hrs) and oxygen RIE (100 W, 50 mTorr and 50 sccm for 60 min) treated (100) highly oriented CVD diamond films.

As shown in Figure 5.23 the intensity of the carbon C 1s peak was greatly reduced for the oxygen RIE treated in comparison with that of the hydrogen plasma treated diamond film. This has been observed for all the oxygen RIE treated diamond films investigated by XPS. The reason why there is such a big difference between the intensity of the two peaks is not completely understood. The two carbon C 1s peaks exhibited a pronounced shape difference. The plot has been magnified and presented in the insert to highlight the shape difference between the two carbon C 1s peaks. For the hydrogen plasma treated diamond film the carbon C 1s peak exhibit a symmetric shape, while the carbon C 1s peak for the oxygen RIE treated diamond film displays an asymmetric shape, with a tail on both low and high binding energy regions due to the presence of graphitic and oxygen terminated surfaces.

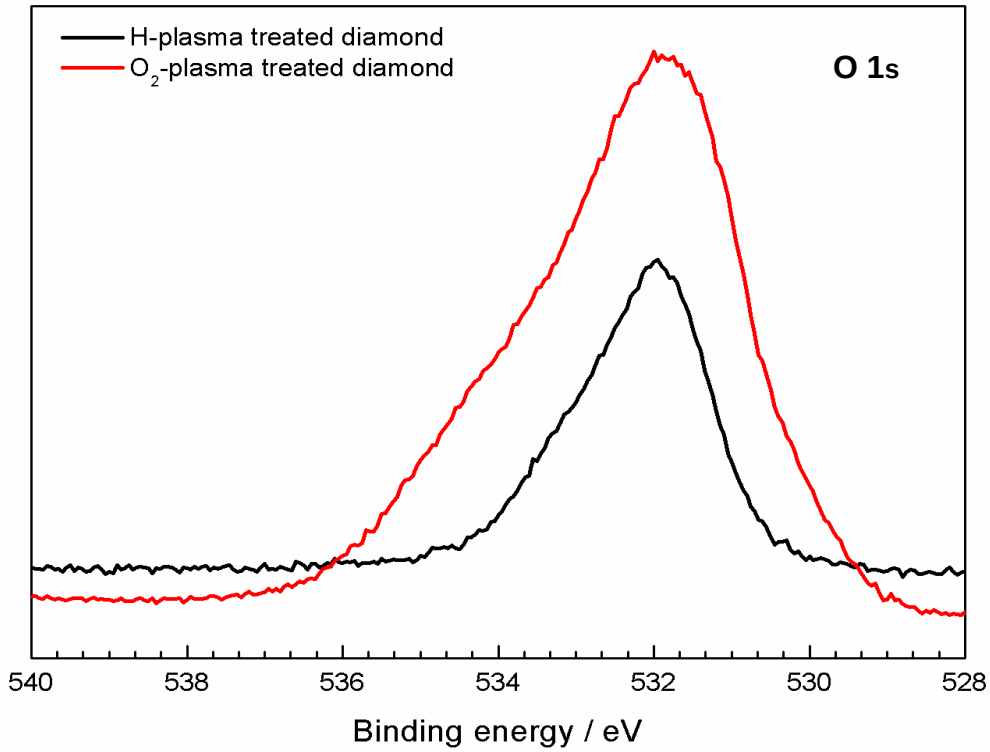

Figure 5.24 High resolution O 1s XP spectra of a hydrogen plasma (20 hrs) treated and oxygen RIE (100 W, 50 mTorr, 50 sccm for 60 min) treated (100) highly oriented CVD diamond films.

The high resolution XP spectra of the oxygen O 1s peak of the oxygen RIE treated (100 W, 50 mTorr, 50 sccm for 60 min) and hydrogen plasma (20 hrs) treated diamond films are compared in Figure 5.24. The shape of the two oxygen O 1s peaks was observed to be similar. The intensity of oxygen O 1s peak of the oxygen RIE treated diamond film was found to be higher as well as it was observed to be a much broader peak than that of the hydrogen plasma treated diamond film.

Deconvolution of the carbon C 1s and oxygen O 1s peaks was carried out by fitting components of Gaussian-Lorentzian mix based on previously published data, as described previously in Chapter 4.

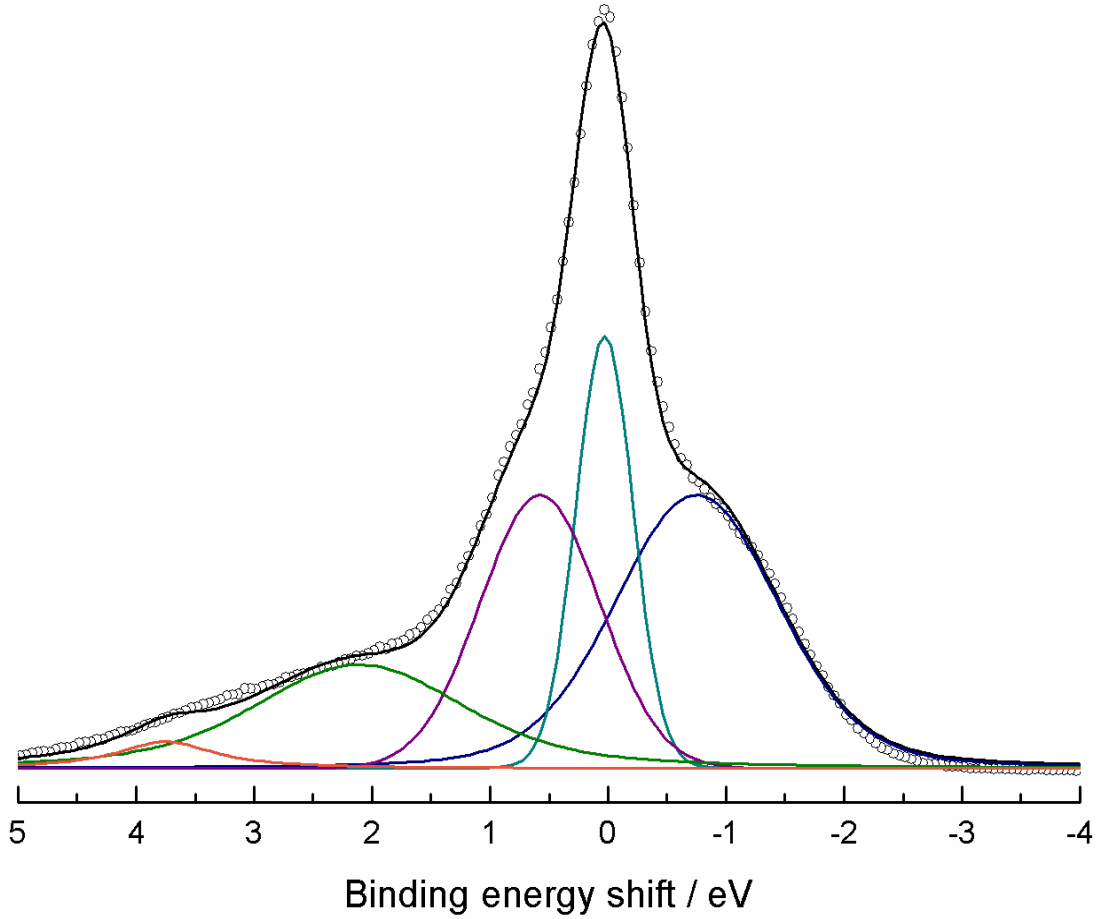

Figure 5.25 Deconvoluted high-resolution XP spectra from the C 1s binding energy peak arising from the oxygen RIE (100 W, 50 mTorr, 50 sccm for 60 min) treated CVD diamond film, showing raw data (black circles) component peaks (coloured lines) and the sum of the peaks (black line). Binding energies are referenced to the main (sp^3) carbon peak at 284.7 eV.

The C 1s peak of the oxygen RIE treated (100 W, 50 mTorr, 50 sccm for 60 min) diamond film has been deconvoluted into five peak components, as shown in Figure 5.25 and listed in Table 5-2. Relative to the main sp^3 component, the peak at -0.7 eV was attributed to graphitic sp^2 carbon [228, 235] and exhibits the highest component peak area of the all the peak components. The peak assigned at +0.5 eV was attributed to the hydrocarbon (CH_x) [202, 203], while the peaks at +2.1 eV and +3.7 eV were assigned to carbonyl (C=O) and carboxyl (O-C=O) groups respectively [228, 233, 235].

Sample	Peak Assignment	BE shift (relative to sp^3 carbon peak)	Peak FWHM / eV	Area/ %
Oxygen RIE Treated	Diamond (sp^3)	0 (by definition)	0.5	18.2
	Graphitic (sp^2)	-0.7	1.6	35.6
	Hydrocarbon (CHx)	+0.5	1.2	23.9
	Carbonyl (C=O)	+2.1	2.1	19.3
	Carboxyl (O-C=O)	+3.7	1.0	2.9

Table 5-2 XPS C 1s peak components position, FWHM and integral area.

There was no requirement to include a deconvolution peak component that could be assigned to ether (O-C-O) as observed in the as-grown diamond films.

The best fit for the deconvolution of the oxygen O 1s peak was achieved by fitting three peak components, as shown in Figure 5.26 and listed in Table 5-3. The deconvoluted peak components could be assigned to ether (O-C-O), carbonyl (C=O) or carboxyl (O-C=O) groups. Both peak components of the carbonyl and carboxyl groups show equivalent contents arising from the oxygen O 1s peak profile whilst the peak at 530.2 eV assigned to the ether grouping show the lowest FWHM and percentage area of all the three peak components.

Sample	Peak Assignment	BE shift (relative to sp^3 carbon peak)	Peak FWHM / eV	Area/ %
Oxygen RIE Treated	Ether (O-C-O)	530.2	1.5	6.0
	Carbonyl (C=O)	531.7	2.0	47.0
	Carboxyl (O-C=O)	533.5	3.2	47.1

Table 5-3 XPS O 1s peak components position, FWHM and integral area.

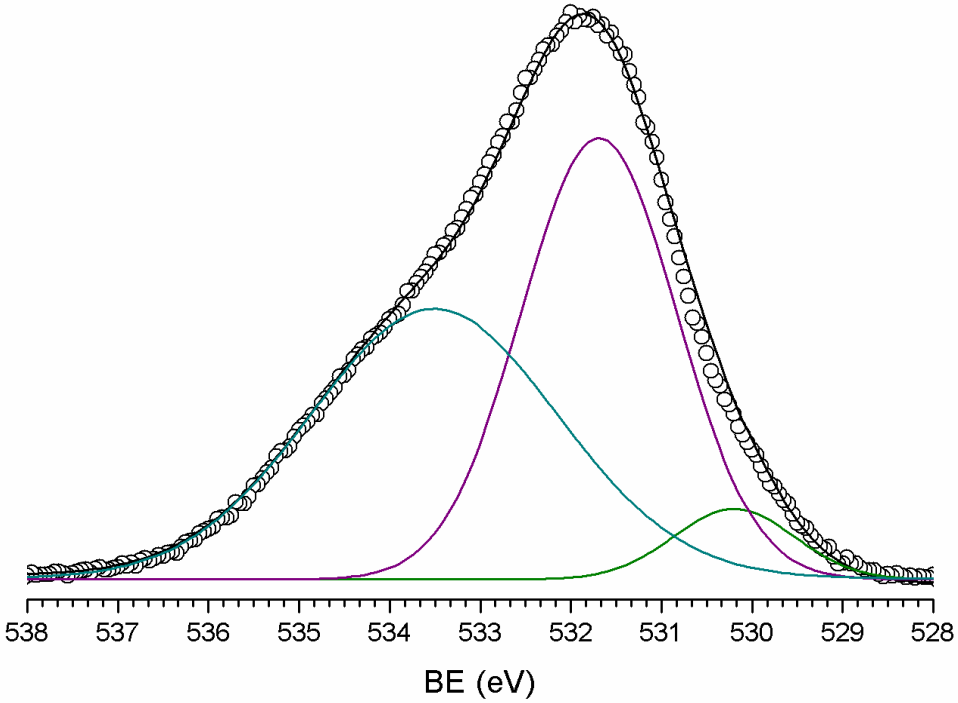

Figure 5.26 Deconvoluted high-resolution XP spectra from the O 1s binding energy band of oxygen RIE (100 W, 50 mTorr, 50 sccm for 60 min) treated (100) highly oriented CVD diamond film, showing raw data (black lines), component peaks (coloured lines) and the sum of the peaks (black lines).

The Si 2p peak of the oxygen RIE treated diamond film was deconvoluted into two peak components, Figure 5.27. The main peak component was located at 101.7 eV while the second one was shifted by + 1.6 eV. Details of the components peak arising from the deconvolution of Si 2p are presented in Table 5-4.

Both peak components exhibits binding energies which are between that of the Si 2p of SiO_2 (104 eV) and that of SiC (100 eV). Similarly with the previous analysis on as-grown diamond film, the peak at 101.7 eV could be assigned to silicon oxycarbide and the latter peak at 103.3 eV to non-stoichiometric silicon oxide SiO_2 ($x<2$) [237].

The presence of silicon oxide on the diamond surface could possibly originate from the silica mask that was used for coating half the diamond surface area during the RIE treatments.

Sample	Peak assignment	BE eV	Peak FWHM / eV	Area / %
O_2 RIE treated	SiO_2	101.7	1.8	65.7
	SiO_x (x<2)	103.3	2.6	34.3

Table 5-4 XPS Si 2p peak components position, full width at half maximum and integral area.

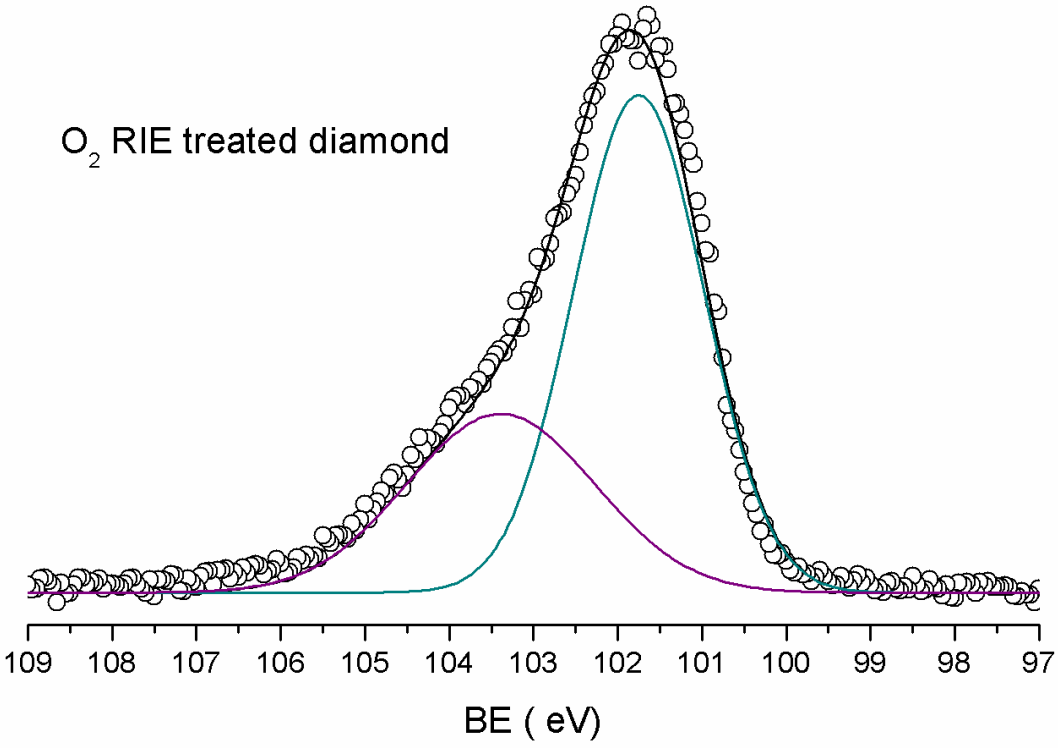

Figure 5.27 Deconvoluted high-resolution XP spectra from the Si 2p binding energy region of oxygen RIE treated CVD diamond film on silicon. Raw data presented here as black circles, component peaks with coloured lines and the sum of the peaks with black line.

XP spectra analysis, (Chapter 4.) on the surface of as-grown (100) highly oriented diamond films, shows the presence of oxygen carbon groups as ether and carbonyl. Exposure of diamond surfaces to hydrogen microwave plasma resulted in the removal of oxygen carbon groups. On the contrary, oxygen RIE treatment on (100) highly oriented diamond surface resulted higher oxidation state groups on the diamond surface. Single bonded oxygen has not been detected on the RIE treated diamond surfaces, while

carbonyl and carboxyl have been detected. However Vivensang *et al* [266] observed by XPS only C-O bonds on the oxygen RIE treated diamond surfaces.

The present results demonstrate that the oxygen RIE treated diamond surface acquired an oxygen-terminated state. As etching of diamond surfaces proceeds by reaction of oxygen radicals leading to the formation of volatile products, the low etch rate as well as the low oxidation rate of diamond under present treatment conditions would allow the formation of oxygen-carbon groups on the diamond surface. The nature of reactive ion etching is complex, as both ions and radicals contribute to etching and to the surface chemistry. Therefore, any effect caused by radicals or ions cannot be treated in isolation.

A relatively small amount of sp^2 carbon was detected on the as-grown (100) diamond films and upon oxygen reactive ion etching the percentage of sp^2 carbon was found to be enhanced. Graphitisation of diamond surface upon exposure to oxygen ions was found to take place for ion energies above 200 eV [259], while etching of single crystal diamond with a number of different oxygen ion-beam techniques demonstrates the graphitisation and the formation of amorphous carbon on the diamond surface [268]. The physical sputtering of reactive ion etching is considered responsible for the graphitisation of the diamond surfaces upon oxygen reactive ion etching.

The presence of silicon oxides has been confirmed for all the oxygen RIE samples examined under XPS. The source of silicon can be attributed to the silica mask used under the present reactive ion etching studies. Silicon can be sputtered by energetic oxygen ions and deposit on the diamond surface during the reactive ion etching treatment. Subsequently, oxidation of the silicon would proceed during the etching process.

5.6.7 EDAX

Energy dispersive X-ray analysis (EDX) measurements were used to determine the qualitative elemental distribution across the samples. The surface of the columnar structures as well as the area surrounded them was examined by EDAX.

Figure 5.28 shows the elemental analysis acquired from the different locations on the oxygen RIE treated diamond films. EDAX spectra acquired from the top of the ridges defining the columnar growth show the presence of significant amount of silicon. The etched diamond surface surrounding the columnar structures showed the presence of insignificant amount of silicon. For both locations on the diamond sample, the presence of oxygen was detected whilst on the diamond area defining the columnar structure fluorine and calcium was also detected.

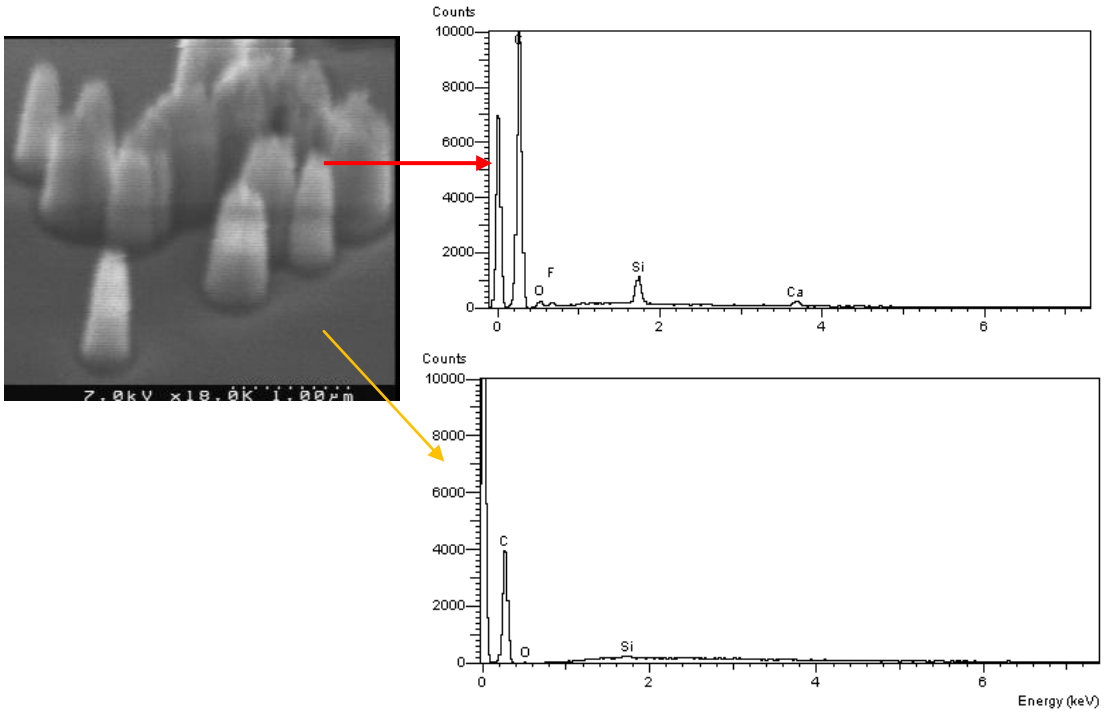

Figure 5.28 EDAX spectra taken a) from the top of the columnar structures and b) from the underlying silicon substrate.

5.7 Discussion

Under the process conditions examined on this project, oxygen reactive ion etching was accompanied with the formation of columnar structures on (100) CVD diamond films. The distribution of columnar structures was found to depend on the applied oxygen pressure. Random distribution of columnar structures was found for high applied oxygen pressure, while preferential formation was observed for lower applied oxygen pressures. Texture of the diamond films affected the distribution and density of columnar structures. It was observed that inter-granular area affect the density of columnar structures. Studies on isolated cubo-octahedrals CVD diamond crystallites show preferentially formation of columnar structures on {111} diamond facets, while the {100} diamond facets were etched producing a smooth surface. Boron doping did not affect the formation of columnar structures. The height of the columnar structures was found to follow the etch rate of the diamond film, therefore it can be postulated that columnar structures were formed at the beginning of the reactive ion etching treatment.

Based on previous published work [31, 207, 214, 260, 261, 275, 279-281]] columnar structure formation on uncoated single crystal and polycrystalline diamond occurs randomly on the diamond surface. In the case of a diamond surface coated, with a layer of silicon oxide or aluminium, formation of columnar structures was found to be preferentially at the grain boundaries, with a much lower density on the diamond crystallites facets.

For these studies the surfaces of the diamond films under investigation were uncoated and a silica mask was used for coating the other half of the sample surface. The presence of silicon oxide was confirmed by XPS and EDAX analysis, with preferential distribution on the columnar structures tip. Micro-masking is been considered as a possible mechanism for the formation of columnar structure upon oxygen RIE on diamond surfaces [23, 31, 204, 207, 210, 211, 214, 260- 263, 271-276, 278-281]. Ion bombardment by highly energetic oxygen ions can cause physical sputtering of the electrode or masking material, which could deposit on the diamond surface. The presence of a micro-masking material with a comparable or lower etch rate than diamond would protect the surface underneath and would lead to preferential etching.

Based on the present experimental evidence, reactions between the sputtered silicon and the diamond surface might lead to a protecting layer which is less susceptible to plasma etching than the underlying diamond. As the height of the columnar structures formed followed the diamond etched depth, it can be assumed that sputtering of the masking material, i.e. silicon, would be uniform across the entire film surface and took place at the beginning of the etching process. According to present studies the reactivities of the sputter material is different on the diamond crystal planes. As grain boundaries were found to be more resistant to oxygen RIE than to the exposed crystal planes, it can be postulated that chemical reactivity of the sputtered material differs.

5.8 Conclusions

Etching of (100) CVD diamond films was achieved with oxygen reactive ion etching. The highest material removal rate was 23 nm min^{-1} at 250W, 20mTorr and 20sccm. Boron doping did not affect the etch rate or textured of the treated diamond films.

Columnar structures have been formed under oxygen reactive ion etching on (100) highly oriented and azimuthally disordered CVD diamond films. The formation of columnar structures was found to predominate at the grain boundaries surrounding the (100) diamond crystallites due to impurity passivation. Grain boundaries and {111} diamond planes were found to be more resistant to oxygen reactive ion etching than {100} diamond facets and it was postulated that chemical reactivity of the sputtered material could differ between different diamond planes.

The surface roughness increased dramatically after RIE treatment, and it was found to be related with the formation of columnar structures on the diamond surface.

High resolution XPS analysis showed the induce graphitisation of the oxygen treated diamond surface and was attributed to oxygen-ion sputtering. The treated diamond surface was found to contain oxygen-carbon groups as carbonyl and carboxyl.

Chapter 6: Thermal oxidation of CVD diamond

6.1 Introduction

The work presented here is focused on the thermal oxidation of the low index planes of CVD cubo-octahedral diamond crystallites. The aim of these studies was to investigate the mechanism of thermal oxidation on the two most common {100} and {111} planes of CVD diamond as they were exposed simultaneously to thermal molecular oxygen. In this way we were able to examine the thermal oxidation on the individual crystal planes and on the individual CVD diamond cubo-octahedral crystallites.

6.2 Oxidation

There are numerous publications reporting on the oxidation of diamond [53, 54, 178, 235, 282-310]. The topic has been the subject of research for a considerable time. Work on oxidation of diamond was first used as a tool for understanding the synthesis of natural diamond [287]. The distribution and occurrence of defects within natural diamonds has been studied by means of oxidation [287, 290, 308] as these defects create preferred reaction sites for oxidation at the crystal surface.

The oxidation of diamond surfaces can be achieved by a number of different methods: chemical [287, 290, 308], electrochemical [51, 234, 299, 313], photochemical [50], plasma or atom beam [235, 294, 296] and thermal processes [18, 53, 178, 234, 235, 285- 289, 291, 292, 294, 299, 301, 302] have demonstrated the richness of diamond oxidation chemistry.

6.2.1 Chemical

The chemical oxidation of diamond surfaces can be achieved with the use of very strong oxidising acids and radical-based chemistry. Molten potassium nitrate [287, 290, 293, 312] and rare earth metals (e.g. cerium) [311-315] have been commonly applied to oxidise and etch diamond surfaces. Occurrence of etch pits on the low-index diamond

surfaces accompanies the oxidation with molten potassium nitrate [287, 288] and it has been suggested that etching proceeds by a step mechanism. Dislocations and surface defects on the diamond surface have been correlated with the formation of surface etch pits. To date, chemical etching is the best method for revealing defects ending on a diamond surface [290, 308].

Boiling solutions of HNO_3/H_2SO_4 and H_2SO_4/H_2O_2 have been applied vigorously as post-treatment *cleaning* of diamond surfaces by the removal of graphitic phases and organic contamination. Surface post-treatment results in an oxidised diamond surface and recently AFM analysis demonstrated the roughening of {111} diamond surfaces upon treatment in boiling HNO_3/H_2SO_4 solutions. Immersion in boiling solutions of H_2SO_4/H_2O_2 produced atomically smooth {111} diamond surfaces [303, 304] and a different reaction mechanism was proposed for the oxidation of diamond surfaces by the latter reagents. The removal of surface hydrogen termination had been demonstrated for the above methods and oxygen functional groups are believed to cover the diamond surfaces. However there is not enough data to identify the oxygen functional groups or the active species involved in the processes.

In contrast, oxygen termination of diamond surfaces by means of radical-based reactions is more controlled and understood [313, 314-316]. The exposure of the diamond surface to gaseous chlorine, activated by UV light, is one of the most common approaches used. The dissociated Cl_2 molecule reacts with the surface terminated hydrogen and removes it from the surface forming HCl, subsequently the surface diamond dangling bonds are terminated by Cl atoms. The resulting chlorinated diamond surface is unstable in a humid environment and oxygen is subsequently introduced into the diamond surface.

6.2.2 Electrochemical

The surface chemical properties of diamond electrodes have been reported to undergo changes upon polarisation treatments. Electrochemical polarisation treatments demonstrated the oxidation of diamond electrodes and the presence of oxygen functional groups such as hydroxyl and carbonyl groups [234, 317]. Although the

oxidation of boron-doped diamond electrodes has attracted great interest the mechanism of the electrochemical oxidation of diamond surfaces is not fully understood to date.

6.2.3 Plasma

Oxygen plasma-based treatments have been used for the patterning of the diamond surfaces. Modification of the diamond surface termination upon plasma treatments has been demonstrated [234, 266, 318, 319]. As discussed in the previous chapter, plasma exposure leading to chemical etching cannot be investigated in isolation as the physical processes of ion bombardment and sputtering take place in parallel. Due to the number of reactions involved in plasma processes and the different plasma systems reported in the literature, the mechanism of the oxidation of diamond surfaces requires further investigation.

6.2.4 Thermal

Thermal oxidation of natural and single crystal CVD diamond has been conducted on well defined crystallographic surfaces [53, 282-289, 295, 297-299, 320,]. Either static or flow vacuum systems have been employed for those investigations. The diamond sample can be heated in either oxygen or in air at sub- and atmospheric pressures which leads to the formation of CO/CO_2 and an oxygenated diamond surface.

Surface morphological changes observed on natural diamond planes triggered the work on the thermal oxidation of diamond. Triangular depressions commonly appeared on the {111} surfaces of natural diamond samples were the subject of a long dispute. Their origin was originally thought to be due to a growth process whilst the work of Frank, Puttick and Wilks proved that they are etch pits formed on the crystal surface [287]. Similarly, square-shape etch pits have been observed on the oxidised single crystal {100} diamond surfaces [284, 287].

The sides of the etch pits on diamond have been observed to be bounded by steps. The relative velocity of those steps was found to be responsible for rotation of the etch pits sides with temperature [284, 286]. Etch pits commonly observed on natural and single

crystal {111} diamond planes [283, 285-288] exhibit a triangular-shape reflecting the crystal three-fold symmetry of this surface shown in Figure 6.1, are referred as trigons or etch pits.

According to Frank *et al* [287] a positive etch pit on the {111} diamond surface would be bounded by vicinal {111+δ} faces with sides parallel to the triad of <110> directions where, δ is an integer. The steps in such a pit have their normal in <$\bar{1}\bar{1}$2> direction, and the atoms of these steps are doubly bonded to the lattice. In contrast a negative etch pit is bounded by vicinal {111-δ} faces while the steps in such a pit have their surface normal in the opposite <11$\bar{2}$> directions and have a three-fold bonding to the surface. The atomic arrangement of the various steps is shown in Figure 6.1.

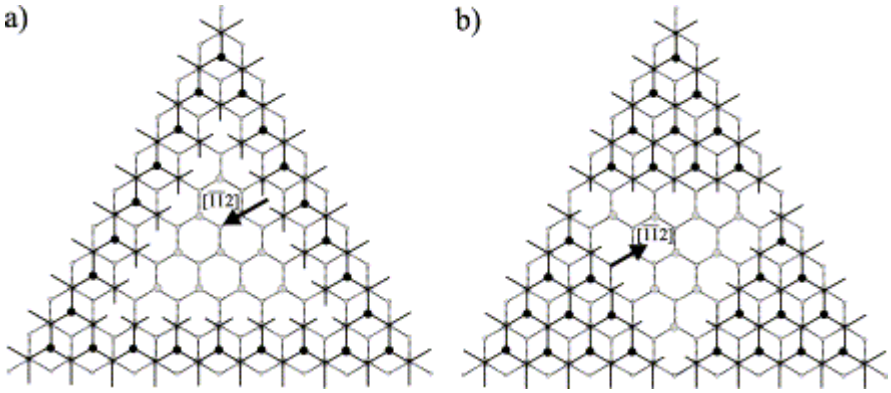

Figure 6.1 Schematic of etch-pits on {111} diamond surface, a) positive etch pit and b) negative etch pit reproduced from reference [287].

Formation of positive etch pits on {111} diamond surfaces has been commonly observed after oxidation in the laboratory [283, 285-287, 305, 308], while negative etch pits were commonly observed on the surface of natural untreated {111} diamond crystals. The rotation by 180^{o} on the etch pits on the {111} diamond surface has been observed upon thermal oxidation at elevated temperatures of ca. 900^{o}C [286].

Etch pits with square symmetry have been observed on the {100} diamond surfaces of natural and single crystals [284, 286]. At thermal oxidation temperatures < 700^{o}C the sides of the etch pits were parallel to the <100> direction, while a 45^{o} rotation of the etch pit sides has been observed as the oxidation temperature was raised above >700^{o}C and the etch pits sides were parallel to <110> [284, 286].

Evans and Sauter [286] observed that for the development of well defined etch pits, the presence of water vapour was necessary in the gas mixture. However, de Theije and co-workers [284, 285] observed the formation of well-defined etch pits despite the absence of water vapour. The formation of well-defined etch pits and the change in etch pit orientation with temperature has been explained by the relative velocities of the different types of steps. It was noted that the outline of the etch pits is determined by the steps with the lowest velocity. Stabilisation of the {100} surface and [$\bar{1}\bar{1}$2] steps on {111} diamond surface by bridging (C-O-C) and carbonyl (>C=O) surface groups, explains etching on the diamond surfaces by a step mechanism [283-286].

Diamond thermal oxidation proceeds faster without the addition of water vapour [284-286]. The removal rate of carbon atoms strongly depends on the O_2 pressure and temperature, the crystallographic orientation of the surface [286], the presence of water vapour or fluorine [282, 321] and the presence of twinning and graphitic or amorphous carbon inclusions [322] in the diamond crystals. Experimental observations of the oxidation rate of single crystal diamond shown that {111} diamond surfaces exhibits the highest rate, followed by {110} whilst the {100} diamond plane displays the lowest oxidation rate [286,323].

Surface chemistry is vital in the understanding of the oxidation mechanism on diamond surfaces. The chemisorption of atomic oxygen on the {100} diamond surface at room temperature has been considered in a number of theoretical studies, whilst the {111} diamond surface has not been studied in the same extent. Two oxygen configurations have been found to exist on the {100} diamond surface; an oxygen atom single bonded to two carbon atoms which is referred to as the bridging configuration and corresponds to the ether structure (COC) and an oxygen atom double bonded on top of a carbon atom which corresponds to carbonyl group (>C=O). Only the former oxygen functional group can exist on the {111} diamond surfaces.

Theoretical studies predict that the two oxygen configurations can coexist due to the small energy difference between them [328, 324]. Theoretical work conducted by Skokov *et al* [324] predicts the bridge configuration to be stable for temperatures below 325^{o}C whilst the on-top configuration is more favourable for temperatures higher than 325^{o}C. IR absorption studies on diamond powders shown that the structures of oxygen

functional groups strongly depend on the oxidation temperature [313]. Oxygen configurations of C-O-C, C=O and C-O-O-C were found to have similar energies on {111} diamond surfaces and they could probably coexist [325]. Figure 6.2 shows the oxygen bridge structure on a (111) diamond surface. When hydrogen is present, either on the diamond surface or in the gas mixture, e.g. water vapour, the formation of –OH group on the diamond surfaces has been found [283-285, 310, 324]. Those oxygen functional groups could exist on the surface terraces, steps and kinks. Reflectance IR studies on oxidised CVD diamond films also show the presence of H_2O adsorption peaks [326].

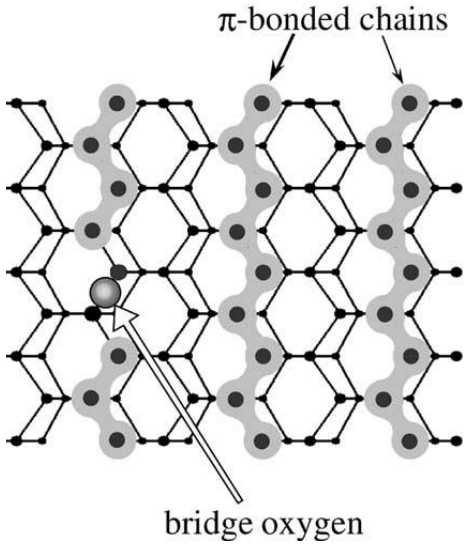

Figure 6.2 Schematic representation of oxygen bridge structure on a (111) diamond surface [327].

Desorption studies of oxygen on the low-index diamond planes, observed the release of CO and CO_2 from the {100} diamond surface [313]. One desorption peak has been observed for the {110} diamond surface, whereas for the {111} diamond surface two desorption peaks have been detected [327]. LEED and AES studies show that O atoms adsorbs on the annealed (111) diamond surface in the form of C-O bonds while maintaining the (2x1) surface reconstruction. Surface reconstruction of the O/C (111)(2x1) surface to (1x1) has been found for exposure to H [328].

6.3 CVD diamond oxidation

The thermal oxidation of CVD diamond films should be identical to that of single crystal diamond although the lower defect densities and improved elemental purity of CVD diamond films could delineate the fundamental processes. Reports so far on the thermal oxidation of CVD diamond films have focused on the etch rates with exposure to high temperatures in air [289, 295, 297, 321-323, 326] Preferential removal of non-diamond carbon has been demonstrated by thermal oxidation [329] and improvement of the diamond quality. A number of possible surface oxygen terminations resulting from various methods of oxidation have been reported by XPS [18, 233, 235].

Data on the thermal oxidation of CVD polycrystalline films has been collected by thermogravimetric analysis (TGA) [289, 295, 321-323, 326] where the kinetics are obtained under non-isothermal conditions. A low oxidation temperature (~ 550^{o}C) has been reported for CVD films in comparison those of natural diamond [323]. Arrhenius-type kinetics have been measured for the etch rate of CVD diamond films and the range of kinetic energies measured are close to those of natural crystals.

Thermal oxidation on polycrystalline CVD diamond films is accompanied with surface morphological changes depending on the crystal plane. Formation of etch pits on {111} diamond planes and selective oxidation at grain boundaries has been observed upon thermal oxidation of polycrystalline diamond films [323], which created a highly porous film [295, 321, 326]. Prolonged thermal oxidation caused the diamond film to collapse "*to a lump of cone-like diamond powder"* [295] while the formation of diamond needles of pyramidal shape has been demonstrated by thermal oxidation of CVD films [297]. Surface morphological changes induced by [295] thermal oxidation affect the optical transmittance, mechanical strength and thermal conductivity of the CVD diamond films [295].

Previous work on the thermal oxidation of CVD diamond films has been conducted at Heriot-Watt University [18, 228, 233, 235, 289]. Surface oxygen termination was found to strongly depended on the applied temperature and humidity of the thermal oxidation process. The formation of carbonyl functional groups on the diamond (100) surface was found to be more favourable at high temperatures and very low humidity. Lower

temperatures and higher levels of humidity promote the formation of ether oxygen functional groups on the diamond (100) surface. Oxidation of (100) diamond films was not observed below ~ 550^{o}C, at which point etching of the diamond surface is first observed. Thermal oxidation of (100)-highly oriented diamond films did not produce pitting or roughening of the surface, suggesting a layer-by-layer mechanism of thermal oxidation [289]. A hydrophilic diamond surface produced by heating in oxygen at 200^{o}C suggesting that oxidation of the diamond surface occurs without removal of oxidised species from the surface. Surface reactions and monolayer oxygen coverage of the diamond surface can be achieved without etching of the surface.

6.4 Experimental details

6.4.1 Thermal oxidation set-up

Thermal oxidation of CVD diamond was carried out in the system shown schematically in Figure 6.3. The thermal oxidation system comprised a stainless steel vacuum chamber which can be pumped by a Pfeiffer-Baltzers turbomolecular and rotary pump combination (TPU 050) down to a base pressure of less than 1 x 10 $^{-6}$ mbar. All seals on the system were made using viton O-rings. The vacuum in the stainless steel chamber was monitored with a Penning gauge (Edwards 8) and for high pressures with a strain gauge based pressure transducer (Bell & Howell 327).

Inside the stainless steel vacuum chamber there is a stainless steel sample holder that can be resistively heated to temperatures up to 620^{o}C. The heating element of the sample holder was controlled by a digital temperature controller (Eurotherm 127) while the heater temperature was continuously monitored with a K-type thermocouple. The Eurotherm temperature controller provided a temperature stability of ± 1^{o}C.

The vacuum chamber has a quartz window on top with a diameter of 120 mm which allowed instrumental and user observation of the sample. During the course of the thermal oxidation experiments the temperature of the diamond samples was continuously and independently monitored with a second thermocouple mounted on the samples surface. A two wavelength (1.17 and 1.25 μm) pyrometer (Micron 3003) was also used during the thermal oxidation experiments to measure the sample temperature.

The vacuum chamber could be filled with Ar and/or oxygen (BOC 99.6 % purity) through a needle valve on the side of the chamber. All gases were passed over a molecular sieve (zeolite A) to dry them before entering the chamber. The levels of oxygen and water in the gas lines were monitored using a BOC Z-ox monitor and MEECO model W electrolytic water analyser respectively.

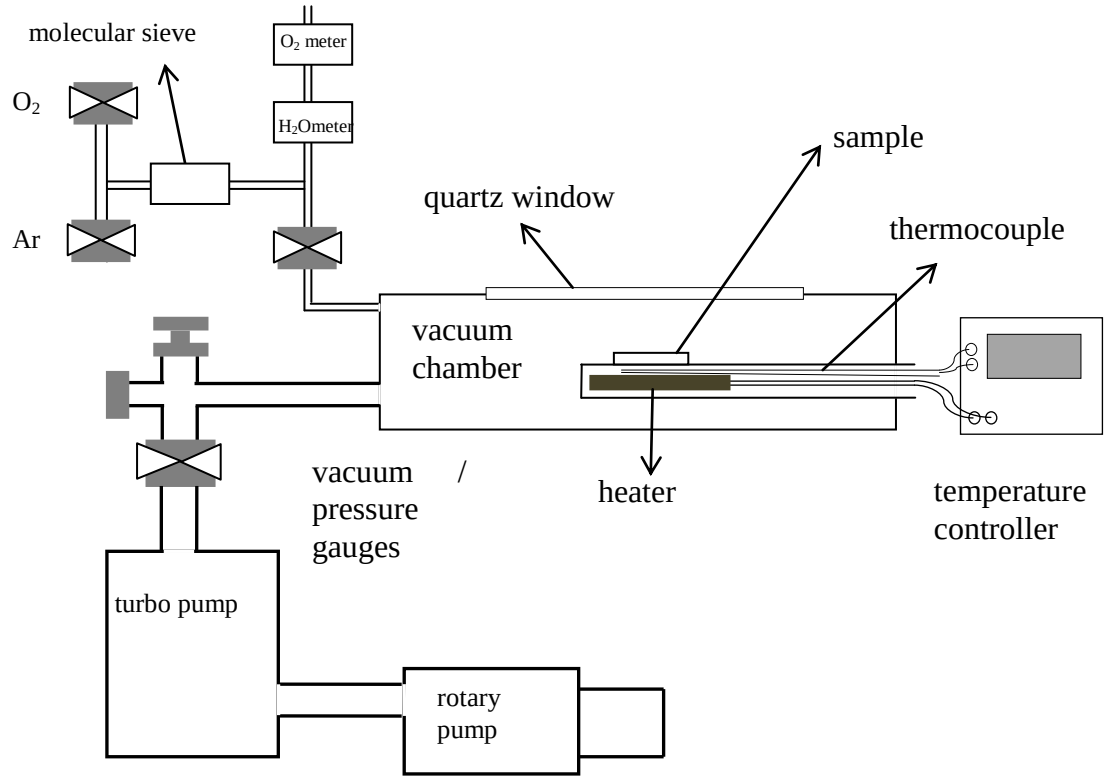

Figure 6.3 schematic representation of the vacuum system used for the thermal oxidation of CVD diamond.

6.4.2 Experimental procedure

Upon inserting the diamond specimens on the vacuum chamber heater/sample holder a thermocouple was placed in contact with the surface. The chamber was sealed from the atmosphere and the chamber was evacuated using the combination of rotary and turbo pumps. When the chamber pressure reached a value of $1x10^{-8}$ mbar, the chamber was isolated from the turbo pumps. Subsequently the chamber was filled with Ar to a certain pressure depending on the experimental conditions.

The heater was turned on and the temperature was increased by increments of 20^{o}C per min until the desired experimental temperature setting was attained. The turbo/rotary pump combination was kept on for the duration of the thermal oxidation experiments, to provide pressure stability in the vacuum chamber. When the chamber pressure and temperature were stabilised, oxygen gas was inserted into the chamber while the rotary/turbo pumps exhausted the Ar/O_2 gas mixture thus keeping the chamber pressure stable at the desired pressure setting.

After the chamber was filled with oxygen, the vacuum cell was isolated from the rotary/turbo pump system and the thermal oxidation treatment was initiated. The duration of each treatment was determined by the temperature and pressure settings chosen. For the whole duration of the thermal oxidation experiments the temperature and chamber pressure were monitored. Any changes occurred in those two settings were compensated manually providing a stable temperature and pressure setting for the whole duration of the thermal oxidation treatments.

When the experimental time had elapsed, the heater was set to cool down with a temperature drop of 20^{o}C per min. To ensure that the diamond samples were cooled in an inert environment, the oxygen gas was replaced with argon.

Once the pyrometer temperature reading reached room temperature the chamber was evacuated using the turbo/molecular pump. After the system was isolated from the vacuum pump system air was allowed inside the chamber up to atmospheric pressure.

6.4.3 Experimental conditions

Thermal oxidation of CVD diamond cubo-octahedral crystallites was carried out in the temperature range 535^{o}C to 600^{o}C, for pressures of dry O_2 in the range 50 torr to 1 atm. The thermal oxidation treatment duration was varied between 60 minutes and 9 hours depending on the process conditions used.

Etching gas	100 % dry O_2
Pressure	50 Torr – 1 atm
Diamond substrate	CVD cubo-octahedral crystallites
Etching temperature	535°C – 600°C
Etching time	60 min – 9 hours

Table 6-1 Thermal oxidation (dry O_2) conditions for CVD cubo-octahedral diamond crystallites.

6.4.4 Sample characterisation

Thermal oxidation experiments, presented in this work, have been carried out on CVD cubo-octahedral diamond crystallites. Those individual diamond crystallites have been grown on the periphery of {100}-highly oriented CVD diamond films, as shown in Figure 6.4. Isolated CVD diamond crystallites on silicon substrates have been selected for the thermal oxidation experiments since they provide both {100} and {111} diamond surfaces. Figure 6.4. shows SEM images of individual as-grown CVD diamond crystallites. The {100} diamond surfaces exhibit the characteristic square shape, while the {111} diamond surfaces have a hexagonal shape.

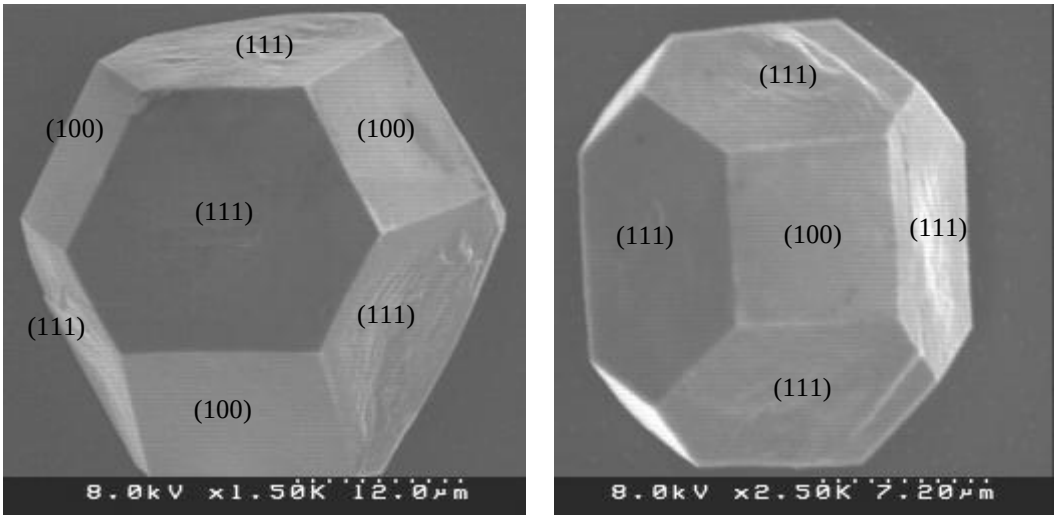

Figure 6.4 SEM images of as-grown CVD cubo-octahedral diamond crystallites.

6.5 Results

6.5.1 Optical profilometry

A Zygo®optical profilometer has been employed to measure the surface height of individual cubo-octahedral CVD diamond crystallites before and after each subsequent thermal oxidation treatment. This enabled the collection of data of height changes caused due to thermal oxidation on the {111} and {100} diamond planes of the crystallites. Using this method the oxidation rates of the {111} and {100} diamond surfaces have been measured as a function of the oxidation temperature and pressure.

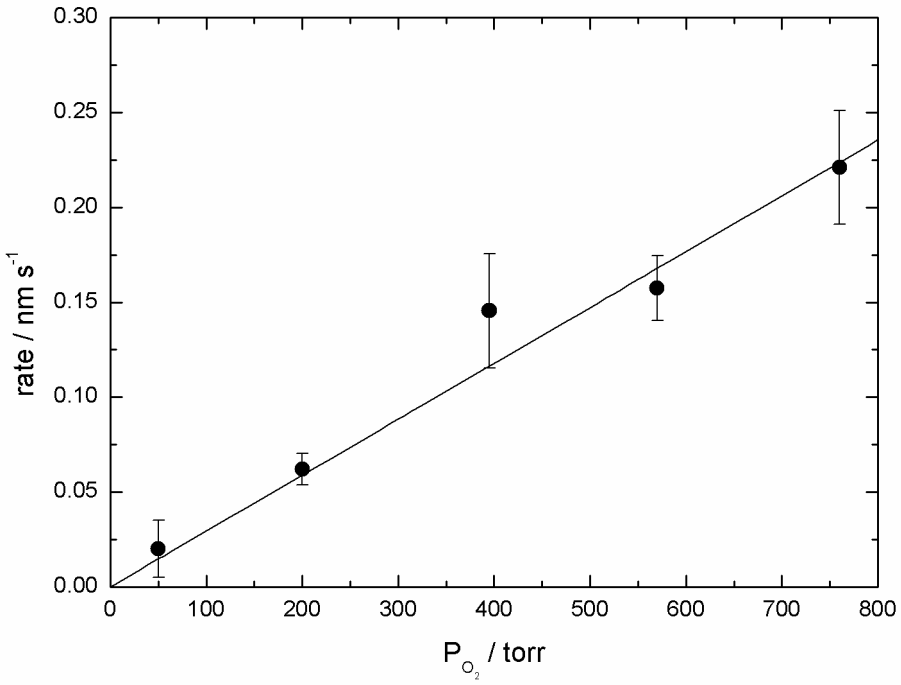

Figure 6.5 The diamond {111} oxidation rate as a function of O_2 partial pressure at 600°C.

The temperature range investigated was 535-600°C at a pressure of 1 atm (760 torr) in dry O_2. The oxidation rates at a temperature of 600°C for the oxygen pressure range of 50-760 torr were used to determine the order of reaction. For both {111} and {100} diamond surfaces, as can be seen in Figure 6.5 and 6.6 the dependence of the oxidation rate of reaction on oxygen pressure is first order and thus follows the equation:

$$\mathbf{rate = k\, P_{O_2}}$$

The solid lines represent the best fits for the data. These observations are in agreement with the first order kinetics previously reported [286, 289] for (100) diamond planes.

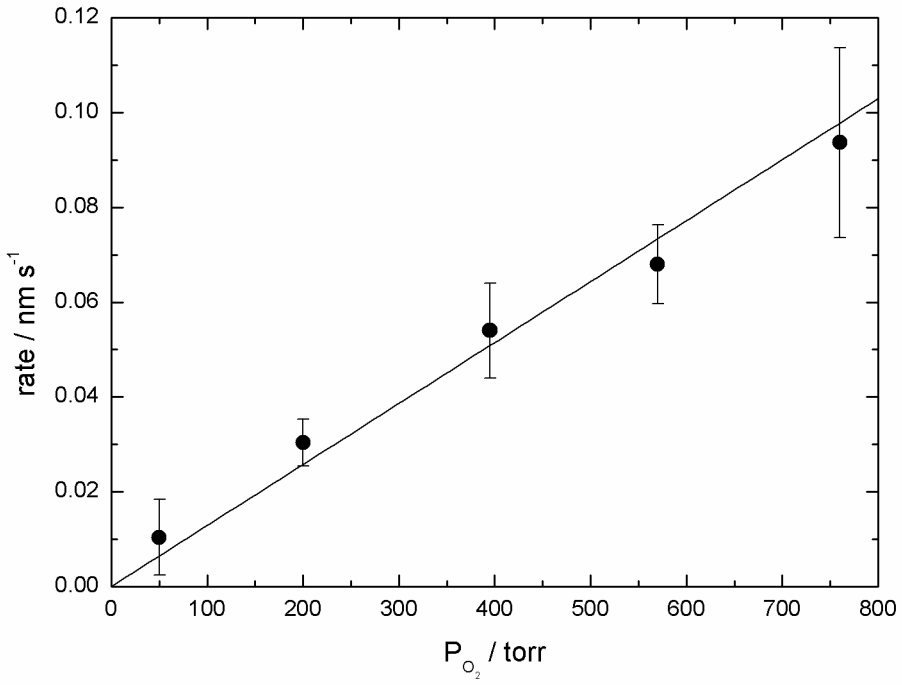

Figure 6.6 The diamond {100} oxidation rate as a function of O_2 partial pressure at 600^{o}C.

The anisotropy between the oxidation rates of the {111} and {100} diamond surface is observed to be high, with the {111} diamond surface exhibiting the highest oxidation rate for all the pressure range investigated. The ratio of the oxidation rates of the two diamond planes is shown in Figure 6.7. It has been observed that the ratio of the two oxidation rates increases slightly with the applied oxygen pressure.

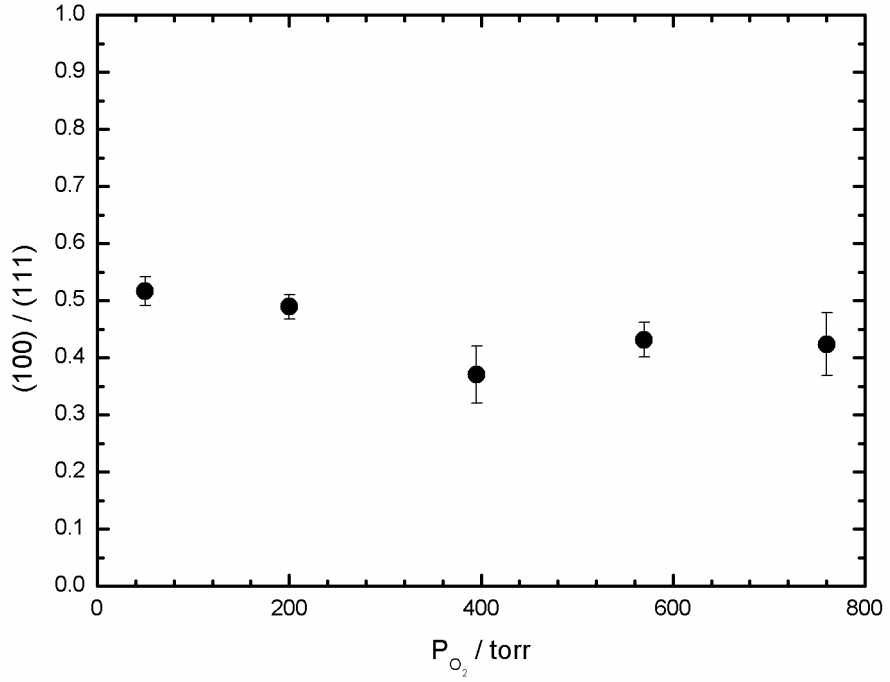

Figure 6.7 Ratio between the oxidation rates of {111} and {100} diamond surfaces as a function of the applied O_2 pressure.

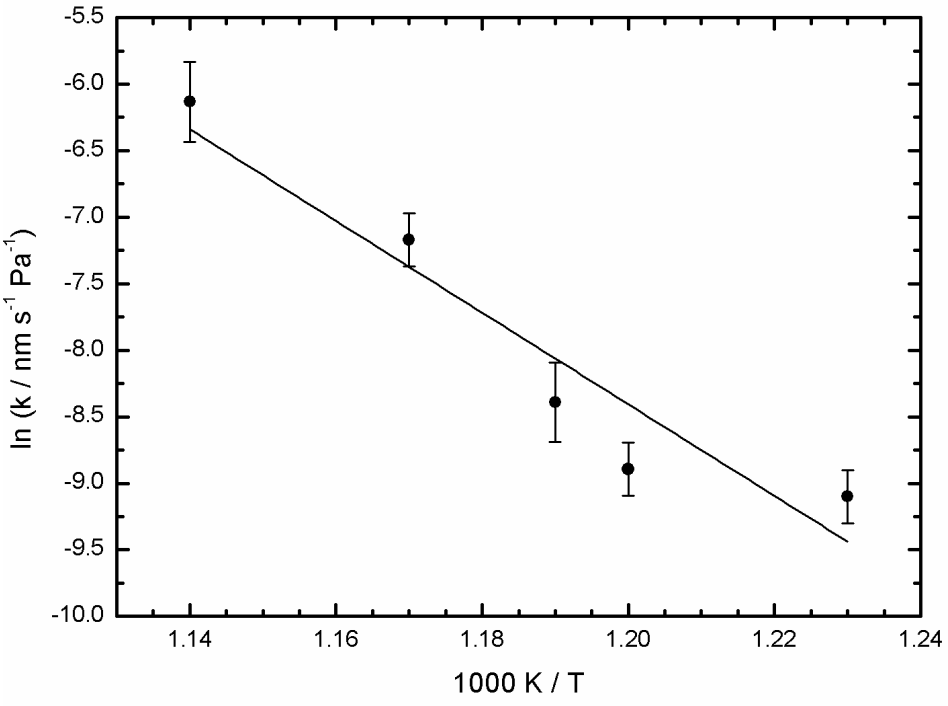

Figure 6.8 Arrhenius plot of the oxidation rate of {111} diamond surface as a function of temperature between 535^{o}C and 600 C. The solid line shows the linear best fit.

For reactions conducted at different temperatures the rate constant, k, was extracted and the temperature dependence of the oxidation rate measured. The Arrhenius plots for {111} and {100} diamond surfaces have been constructed by plotting ln(k) against 1/T as shown in Figure 6.8 and 6.9 respectively, where the solid lines represent the best fit for this data. The activation energy (E_a) and pre-exponential factor (A) of the oxidation reaction was extracted from the Arrhenius plot for each diamond plane:

$$\mathbf{k = Ae^{-(Ea/RT)}}$$

For both diamond planes the slope is constant over the temperature range investigated indicating a temperature independent activation energy for both diamond planes.

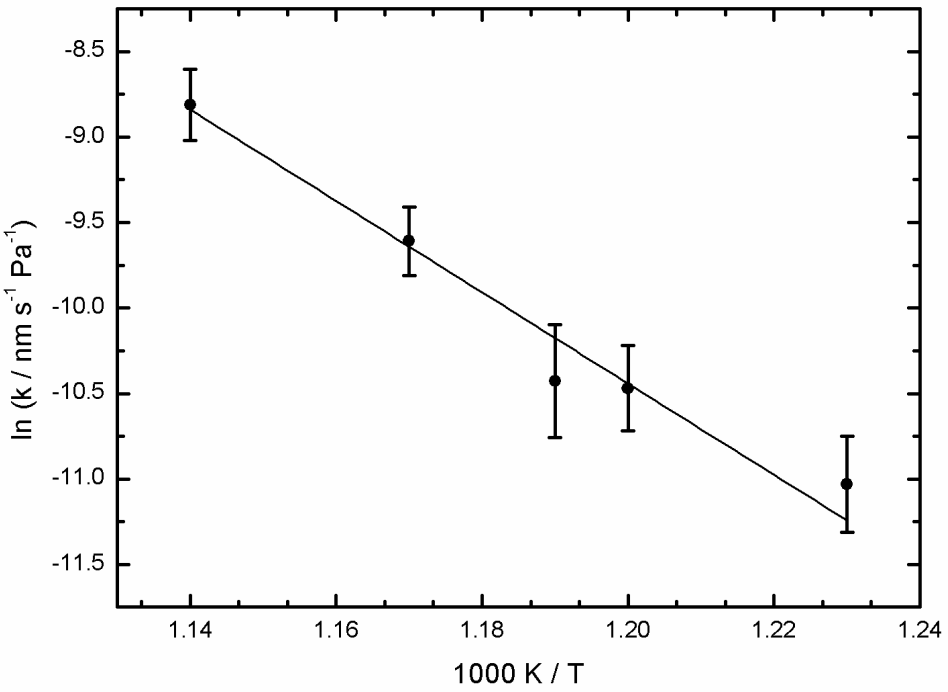

Figure 6.9 Arrhenius plot of the oxidation rate of {100} diamond surface as a function of temperature between 535°C and 600 C. The solid line shows the linear best fit.

For both {111} and {100} diamond surfaces the activation energy was determined from the slope of the best-fit straight line to be 286 ± 29 kJ mol^{-1} for the {111} surface and 221 ± 34 kJ mol^{-1} for the {100} diamond surface.

The Arrhenius pre-exponential factors were determined from the intercept of the slopes to be 1.9 x 10^{14} nm s^{-1} Pa^{-1} and 2.3 x 10^{9} nm s^{-1} Pa^{-1} for the {111} and {100} diamond surface respectively.

For the temperature range of 535°C to 580°C the anisotropy between the oxidation rates of the two diamond surfaces was higher than that at 600°C where the ratio between the two oxidation rates approaches the value of ~ 0.45, as shown in Figure 6.10. The {100} diamond surfaces was found to oxidise more slowly than the {111} surface which have the highest oxidation rate for the temperature range investigated. It is worth mentioning here that ~ 600°C is the temperature reported for the onset of the thermal oxidation of CVD diamond films and is consistent with the present observations.

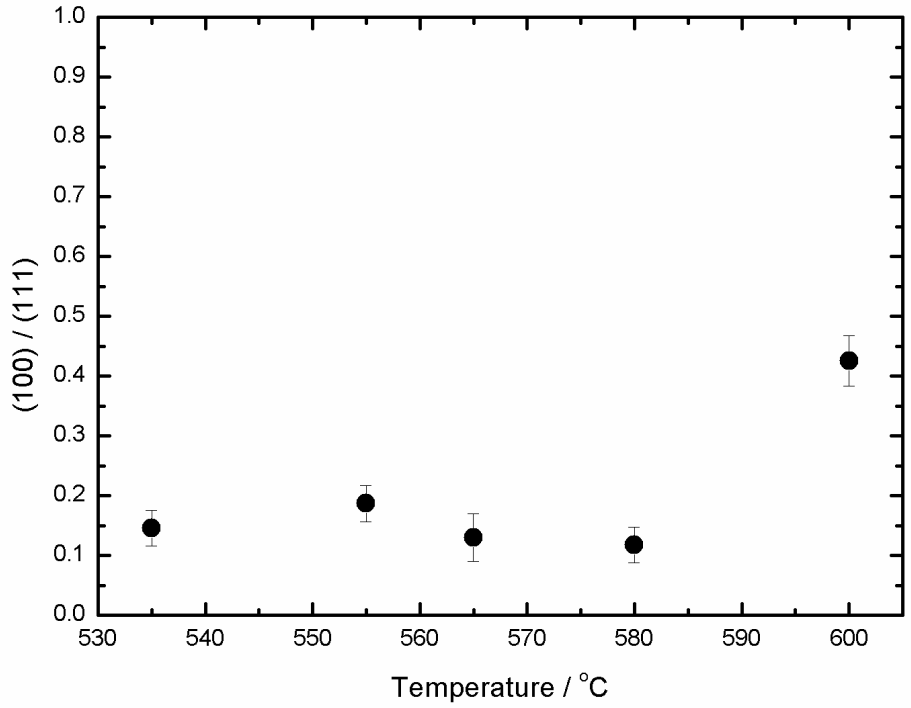

Figure 6.10 Ratio between the oxidation rates of {100} and {111} diamond surfaces as a function of temperature at 1 atm pressure.

6.5.2 Scanning electron microscopy

Scanning electron microscopy SEM was used to examine the surface morphological changes which occurred on thermal oxidation of both {100} and {111} surfaces of diamond CVD crystallites. In this sub-chapter the observations made on the {100} and {111} diamond surfaces are presented individually.

The {100} diamond surface

Oxidation at 535^{o}C and 1 atm pressure using dry O_2 did not cause any morphological changes on the {100} diamond surfaces as observed at SEM resolution. The side edges of the (100) diamond surface have been etched and the sides appeared roughened. The oxidation treatment at 535^{o}C was carried out for 9 hours, and the resulting oxidised (100) surface is shown in Figure 6.11.

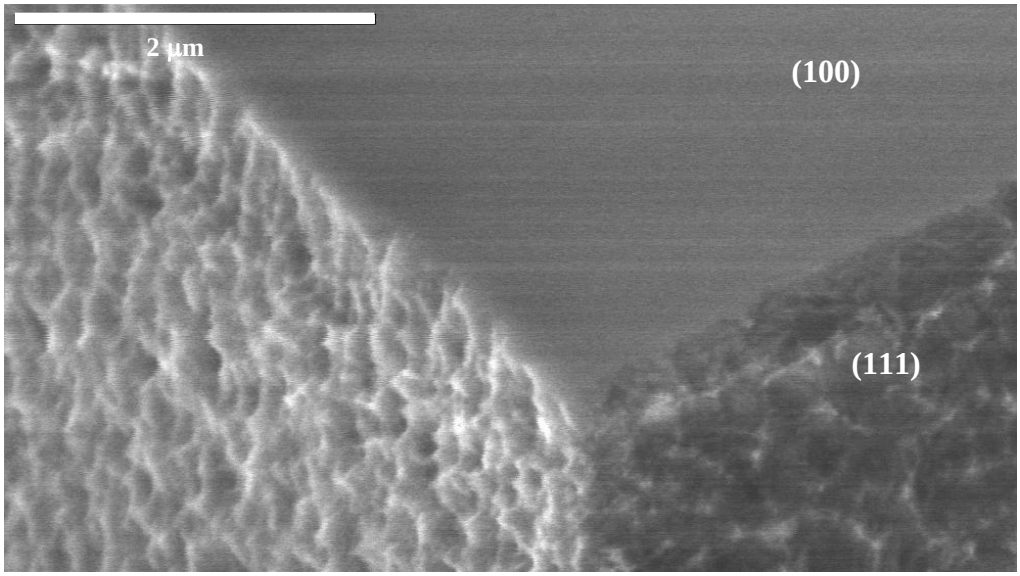

Figure 6.11 SEM image of the (100) and (111) diamond facets of a thermally oxidised CVD cubo-octahedral crystallite at 535^{o}C and 1 atm pressure of dry O_2 for 9 hours.

In contrast, when the thermal oxidation was conducted for the duration of 9 hours at a substrate temperature of 565^{o}C and 1 atm pressure of dry O_2, the {100} diamond surfaces were observed to have been etched preferentially on the edges of the four sides of the surface where the (100) surfaces intersect with four {111} diamond surfaces. The etching process occurred uniformly along the side edges of the {100} diamond facet as shown in Figure 6.12.

When the substrate temperature was raised to 600°C, while keeping 1 atm applied pressure of dry O_2, the thermal oxidation treatment was limited to 60 minutes duration. At the {100} diamond surfaces, as was observed in Figure 6.13, etching of the four intersection edges was more pronounced than that at 565°C. The {100} diamond surfaces remained smooth as evidenced by the SEM images.

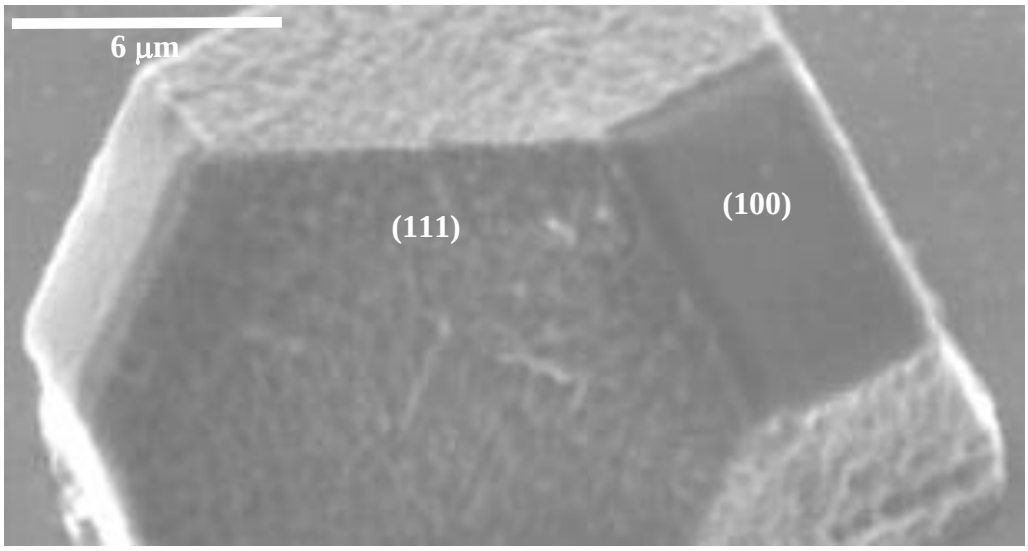

Figure 6.12 SEM image of the (100) and (111) diamond facets of a thermally oxidised CVD cubo-octahedral crystallite at 565°C and 1 atm pressure of dry O_2 for 9 hours.

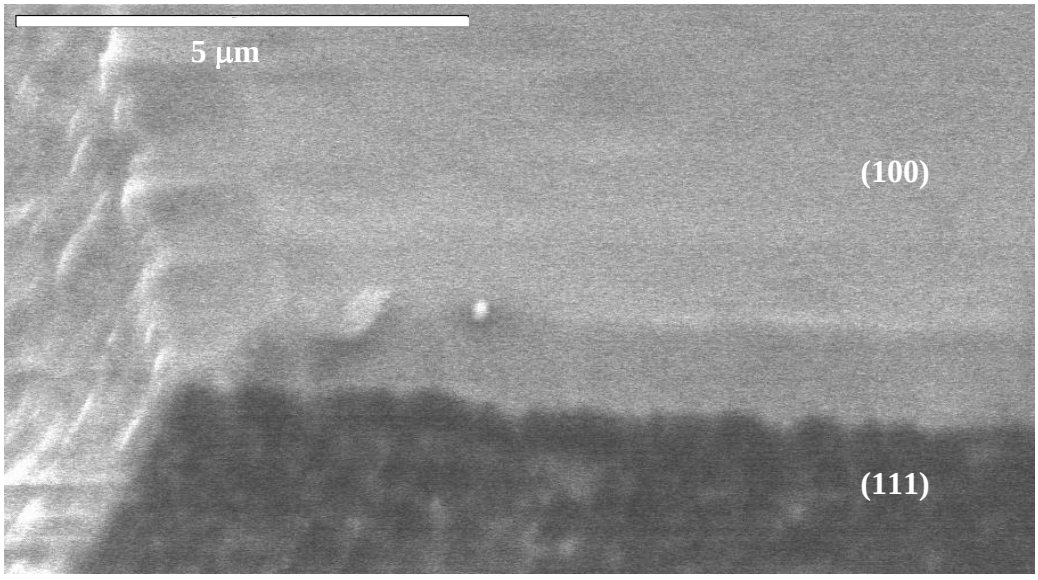

Figure 6.13 SEM image of the cross-section between the (100) and (111) diamond facets of a thermally oxidised CVD cubo-octahedral crystallite at 600°C and 1 atm pressure of dry O_2 for 60 min.

As the duration of the thermal oxidation was increased to 4 hours at 600^{o}C and 1 atm pressure of dry O_2 the more rapid oxidation caused a catastrophic effect on the cubo-octahedral diamond crystallites as shown in Figure 6.14. The {100} diamond surfaces were roughened with a resulting uneven surface morphology.

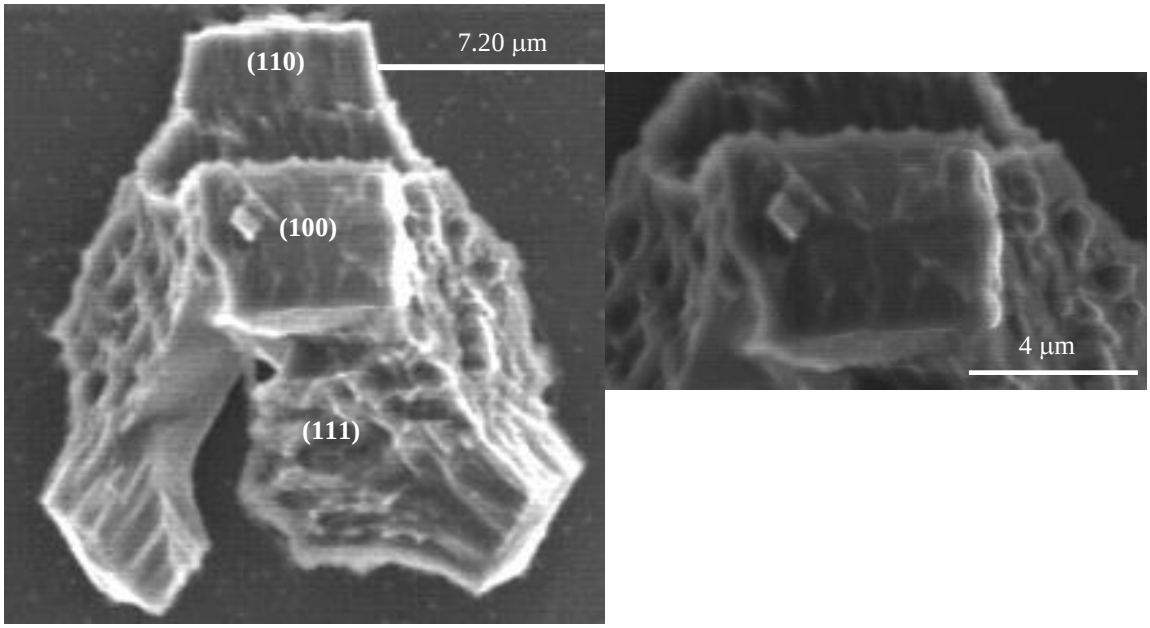

Figure 6.14 SEM image of the thermally oxidised CVD cubo-octahedral crystallite at 600^{o}C and 1 atm pressure of dry O_2 for 4 hours.

The difference between the oxidation rates of {100} and {111} diamond surfaces is high for the present treatment conditions, as a consequence the fast etching of the {111} diamond surface leaves the more stable {100} diamond surfaces. The process is accompanied by the exposure of the {110} diamond surfaces at the intersection of the {100} diamond surfaces, which are more resistant to oxidation than the {111} diamond surfaces.

In order to examine the effect of the pressure of dry O_2 during thermal oxidation on the {100} diamond surface, a series of experiments were conducted at a substrate temperature of 600^{o}C for a range of reduced pressures. The duration of each treatment was adjusted so that the oxidative etching of the cubo-octahedral crystallites was comparable.

Figure 6.15 a) shows the SEM image of a thermally oxidised (100) diamond surface at 395 Torr pressure of dry O_2 for 150 minutes. The emergence of a new plane between the (100) and (111) diamond surfaces was evident under those conditions. Whilst the (100) diamond surface appeared smooth on the SEM images the etched sides of the surface appeared to have developed some surface structural ripples. The shape of the square shape of the (100) diamond surface had changed to a trapezoid due to the oxidation process.

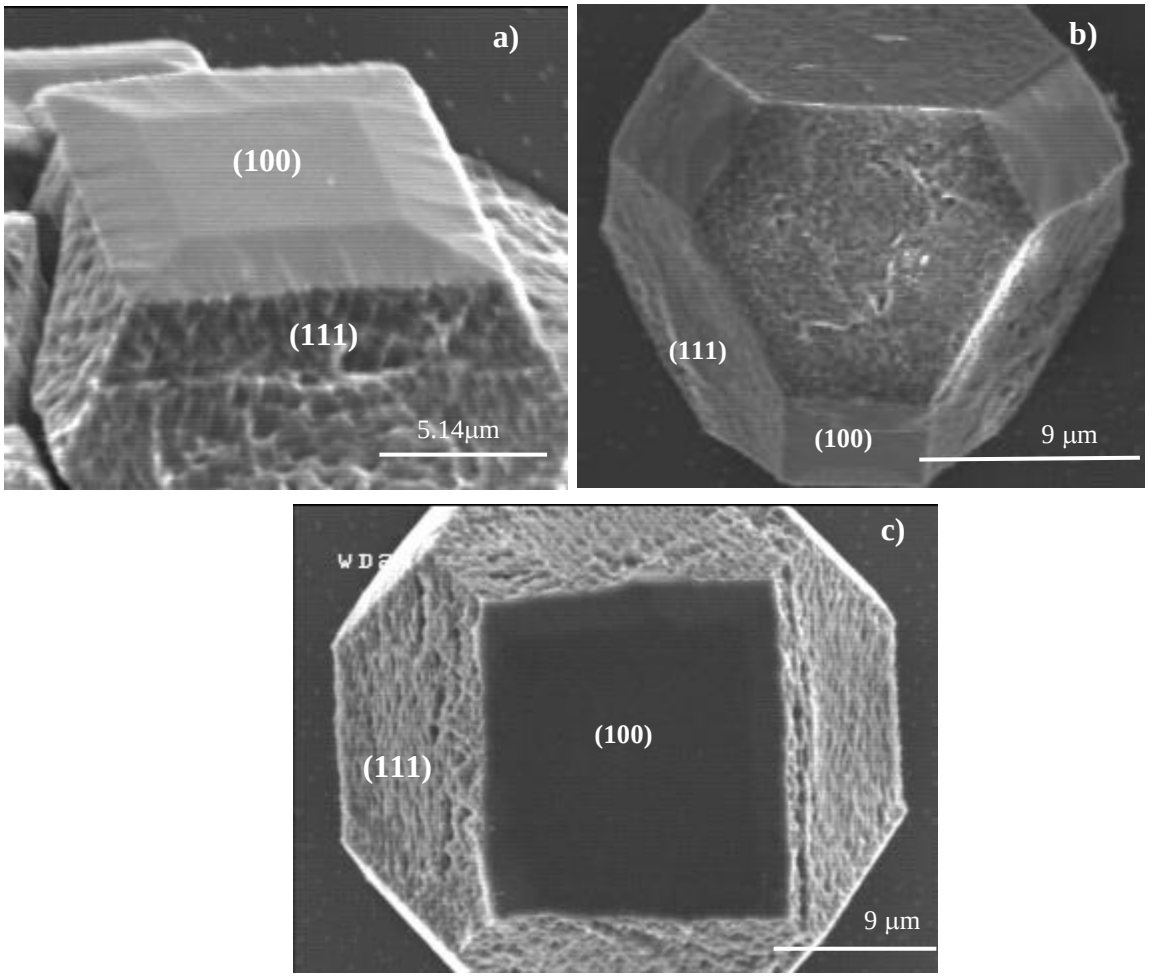

Figure 6.15 SEM images of cubo-octahedral CVD crystallites that have been thermally oxidised at a substrate temperature of 600^{o}C at different pressures of dry O_2 and time durations a) 395 Torr and 150 min, b) 200 Torr and 240 min and c) 50 Torr for 300 min.

The same morphological changes were observed on the (100) diamond facets of the cubo-octahedral CVD crystallites, Figure 6.15 b) and c), at the reduced pressure of 200 Torr and 50 Torr of dry O_2 respectively. The distinctive change of the (100) diamond planar surface to a trapezoid shape has been observed for all the thermal oxidation conditions studied.

The effect of the treatment duration on the surface morphology of {100} diamond surfaces was investigated for a total oxidation duration of 30 hours at 565^{o}C and 1 atm pressure of dry $O_{2.}$ The sample was removed from the vacuum cell for characterisation after 9 hours, 15 hours and 30 hours of subsequent thermal oxidation. Figure 6.16, shows the as-grown (100) diamond surface of a cubo-octahedral CVD diamond crystallite and after it has been subjected to thermal oxidation under the conditions presented in the legend of the Figure.

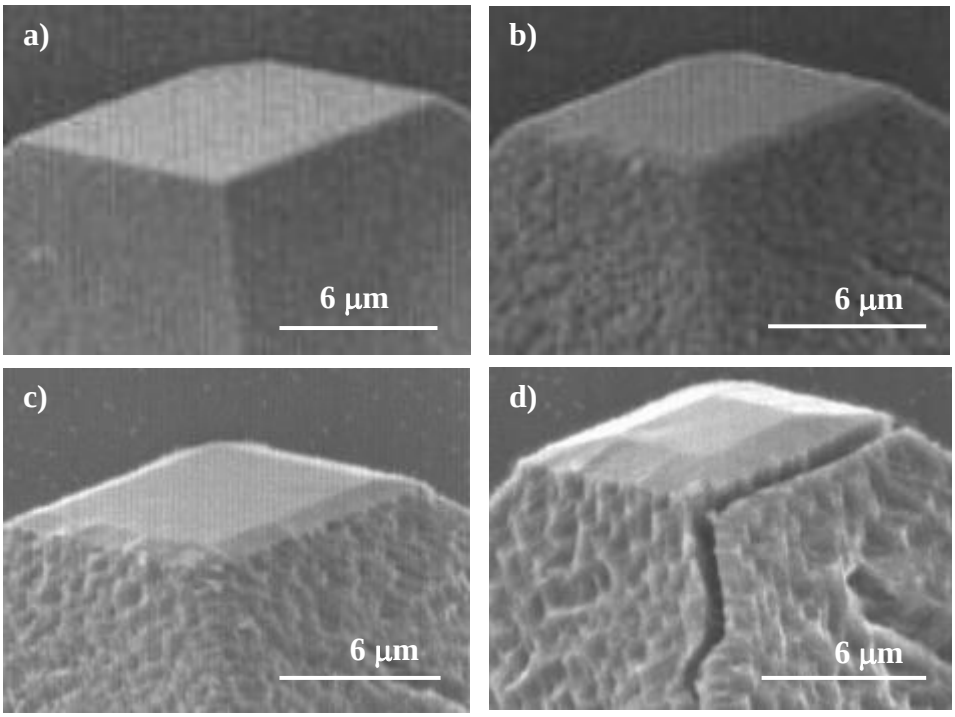

Figure 6.16 SEM images of (100) surface of a CVD cubo-octahedral diamond crystallite a) as grown and after thermally oxidation at 565^{o}C and 1 atm pressure of dry O_2 for b) 9 hours, c) 15 hours and d) 30 hours.

The surface of the (100) diamond facet remained relatively smooth after a total of 30 hours of thermal oxidation. Neither pitting nor formation of etch pits was observed on the (100) diamond facet. Etching of the edges of the sides of the (100) diamond facet increased with the thermal oxidation treatment, causing the (100) diamond facet to adopt a trapezoidal-like shape after 30 hours of treatment, similarly to the (100) diamond facet shown in Figure 6.15 a).

As observed in Figure 6.16 d) a crack developed between the two diamond facets during the final part of the process. Cracks have also been observed to some of the cubo-octahedral CVD diamond crystallites at different stages of the thermal oxidation process but not always between the cross-sections of the two diamond facets. It has been observed that crystal imperfections, such as cracks were preferentially attacked during thermal oxidation.

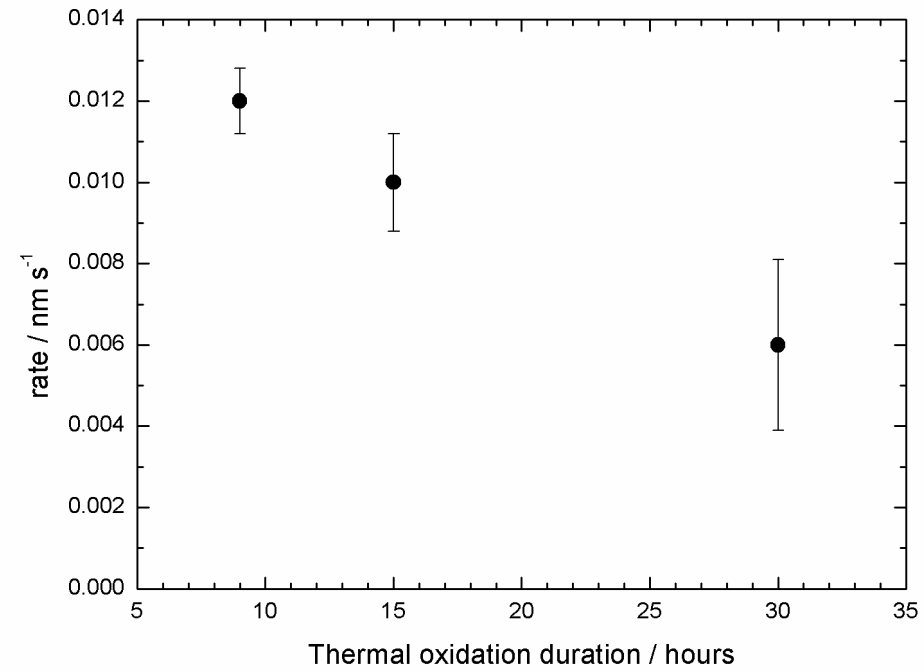

Figure 6.17 Lateral etch rate of {100} diamond surfaces as a function of the duration of thermal oxidation.

It has been observed that the lateral sides of the {100} diamond surfaces of the CVD cub-octahedral diamond crystallites were etched faster than the vertical {100} diamond facets, reducing the lateral dimensions of the {100} diamond surfaces. The SEM images enabled measurements of the lateral etch rate of the {100} diamond facets for the specific process conditions.

Figure 6.17 shows the measured lateral etch rates of the {100} diamond surfaces as a function of the oxidation time. The evaluation of the etch rates was made by measuring the lateral change on ten individual {100} diamond facets for consecutive thermal oxidation treatments.

The measured lateral etch rate of the {100} diamond surfaces was not constant for the whole duration of 30 hours of thermal oxidation. For the first 15 hours of thermal oxidation treatment the lateral etch rate of {100} diamond facet was the same within experimental error. The lateral etch rate decreased during the final 15 hours of thermal oxidation. The etch rate of {100} diamond facets at the same thermal oxidation conditions was measured to be 0.003 ± 0.001 nm sec^{-1}, which is lower than the lateral etch rates measured for the whole duration of the process.

The present results indicate that the reactions on the lateral oxidation of {100} diamond surface were influenced by the duration of thermal oxidation. As the {100} facets were always bonded to four {111} diamond facets, reaction on the {100} diamond surface cannot be treated in isolation. The high oxidation rate of {111} diamond surfaces under the conditions investigated would directly affect the lateral oxidation of {100} diamond plane.

The exposed area of the new crystallographic plane, between the {111} and {100} diamond surfaces, increased with thermal oxidation. SEM images enabled the measurement of the surface area of the new crystallographic plane and an oxidation rate of 0.038 ± 0.006 nm s^{-1} has been found for the new crystallographic plane, under the present experimental condition, as seen in Figure 6.16.

The nature of the exposed plane evident in the SEM micrographs can be determined. Work conducted by Silva *et al* [331, 332] on a geometrical 3D model which governs the homoepitaxial diamond growth on different crystal planes, predicts the coexistence of {100}, {111} and {113} diamond planes. Figure 6.18 shows the illustration of the topographies within the {100}{111}{113} system, taken from reference [331]. Based on this 3D model, the inclusion of {113} diamond planes on the cubo-octahedral crystallite would conserve the cubo-octahedral shape of the crystallites although the {100} diamond facets would be surrounded by stripes corresponding to {113} diamond facets. The percentage surface area of the individual diamond planes on the cubo-octahedral depends on the growth conditions, according to this 3D geometrical model. Theoretical studies conducted by Stekolnikov *et al* [333] showed that the equilibrium diamond crystal shape strongly depends on the absolute surface energies. According to their calculations, the {113} diamond facet can be present on the equilibrium crystal shape, decreasing the surface energy.

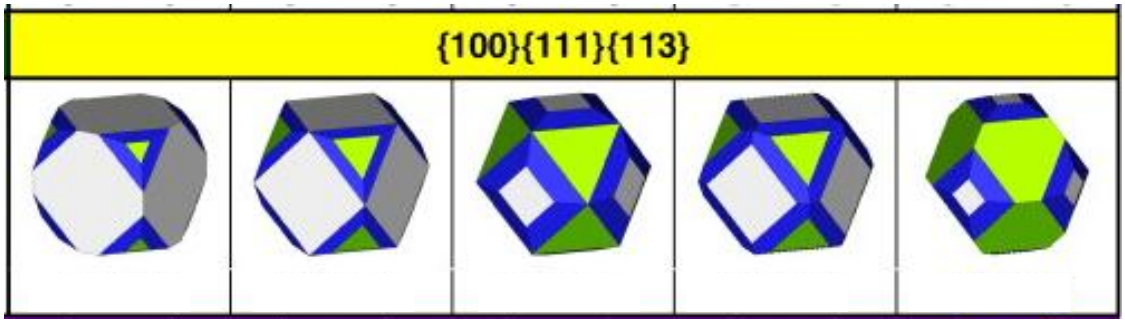

Figure 6.18 Illustration of the topologies within the {100}{111}{113} system, modelled by Silva *et al* [331]. White, blue and green represent the {100}, {113} and {111} diamond planes respectively.

In order to determine the newly exposed facets between the {100} and {111} diamond surfaces were {113} diamond planes, the angles between the {100} diamond surface and the exposed surface were evaluated by optical profilometry. The average measured value for the angle between the two surfaces was calculated to be $26.8^{o} \pm 0.7^{o}$, which is close to 25.24^{o} predicted angle between the {100} and {113} diamond surfaces. The angle between the {100} and {113} diamond planes has been derived using the following equation which defines the angle between two crystal planes:

$$\cos\theta = \frac{(hH + kK + lL)}{\sqrt{(h^2 + k^2 + l^2)(H^2 + K^2 + L^2)}}$$

where (hkl) defines the first crystal plane and (HKL) defines the second crystal plane [334].

According to these results we could suggest that oxidised cubo-octahedral crystallites reveal {113} diamond surfaces which are exposed due to the anisotropy of the oxidation rates of the diamond (100) and (111) planes. Such morphological changes caused by thermal oxidation on the low-index diamond planes have not been reported before.

The oxidation rates of the different diamond planes measured at 565^{o}C and 1 atm pressure of dry O_2, are given in table 6-2. Oxidation rates of {111} and {100} diamond planes were measured by Zygo profilometry, while oxidation rates of {113} and $\{100\}_{\text{Lateral}}$ were evaluated from SEM images. The {113} diamond plane exhibits the

highest oxidation rate followed by {111}, the lateral oxidation rate of {100} and finally the oxidation rate of {100} planes.

Crystal plane	Oxidation rate nm/sec
{113}	0.038 ± 0.009
{111}	0.023 ± 0.003
$\{100\}_{Lateral}$	0.006-0.012 ± 0.0013
{100}	0.003 ± 0.0013

Table 6-2 Oxidation etch rates of diamond planes at substrate temperature of 565^{o}C and 1 atm pressure of dry O_2.

High resolution SEM revealed macro-steps on the {113} diamond planes. Figure 6.19 a) shows the (100) diamond surface after 30 hours of thermal oxidation at 565^{o}C and 1 atm pressure of dry O_2. The oxidised surface had adopted a trapezoidal-like shape and steps were observed parallel to the edges of the surface, such surface steps have their normal to <110>. The average step height measured was 72 ± 5 nm, while the distance between adjacent steps was 163 ± 4 nm.

The steps were observed on the <110> crystal directions while, at the corners of the crystal, rotation on the step direction towards <100> was observed as shown in Figure 6.19 b). The thermally oxidised {100} surface had a different surface morphology compared to the {113} diamond planes, see Figure 6.19 c), indicating a different oxidation mechanism.

The mechanism proposed for the formation of {113} diamond planes due to thermal oxidation will be presented later in this chapter.

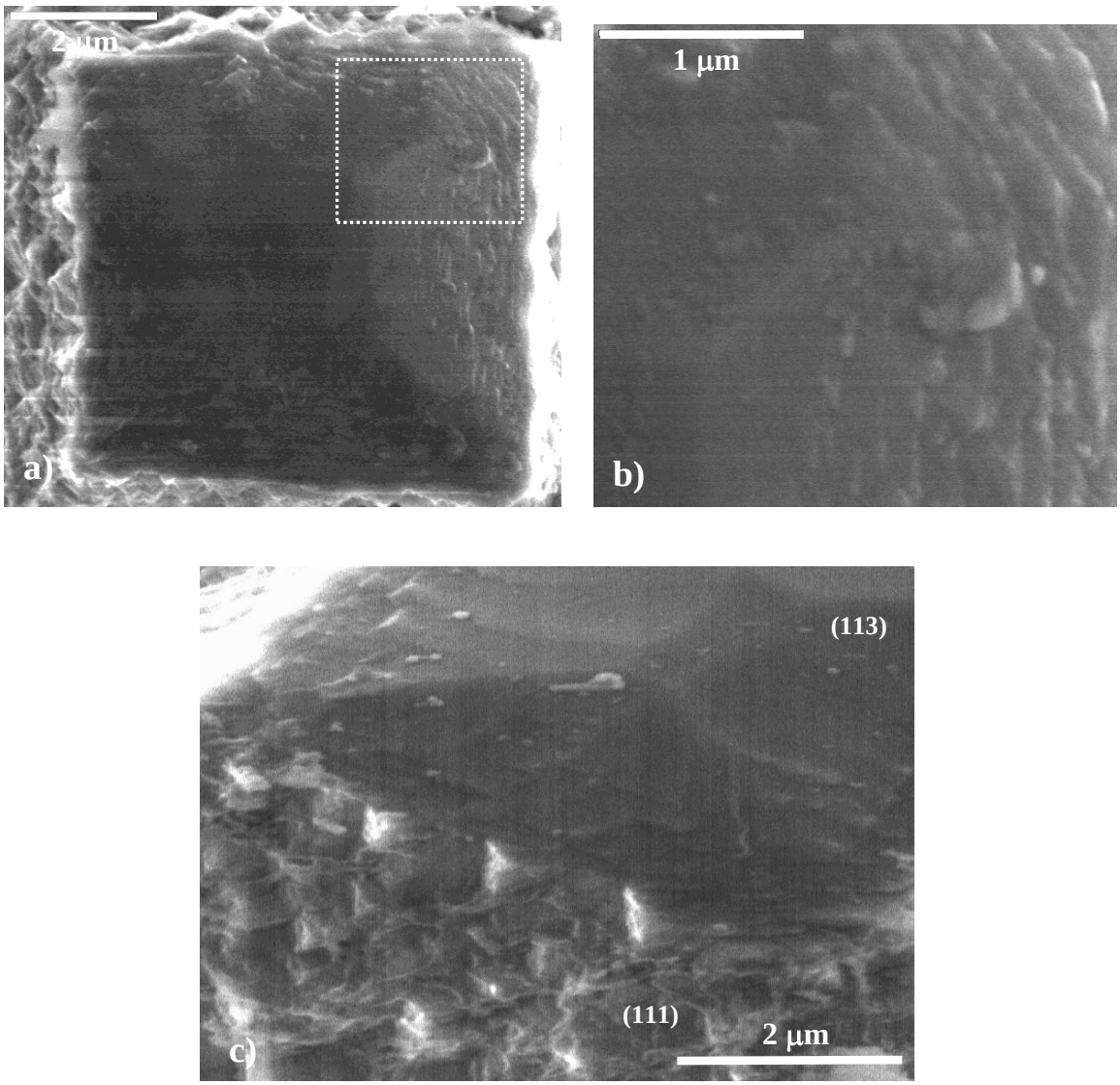

Figure 6.19 SEM images of an oxidised (100) diamond surface a) top view, b) high magnification image of the outlined area of a) and c) side view of the intersection between (113) and (111) diamond planes. Thermal oxidation was conducted at 565^{o}C and 1 atm pressure of dry O_2 for 30 hours.

The {111} diamond surface

Morphological changes have been observed for the {111} diamond surfaces of CVD cubo-octahedral crystallites after thermal oxidation. The {111} diamond surface is not stable upon thermal oxidation at 535^{o}C and 1 atm applied pressure of dry O_2. After 9 hours of thermal oxidation under these conditions, etching of the {111} diamond surface was apparent and it was accompanied by the formation of hollow etch pits distributed along the surface with no preferential orientation, Figure 6.20.

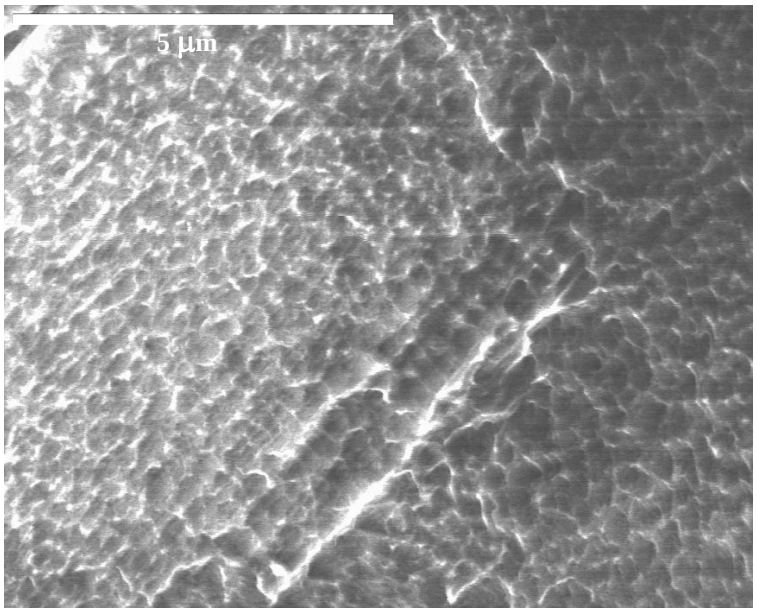

Figure 6.20 SEM image of (111) diamond surface of a CVD cubo-octahedral crystallite after it has been oxidised for 9 hours at 535^{o}C and 1 atm pressure of dry O_2.

No published reports exist on etching and roughening of CVD diamond films at temperatures lower than 550^{o}C. This is the first time that thermal oxidation surface changes have been observed at temperatures as low as 535^{o}C. As the oxidation kinetics at 535^{o}C are slow for the {111} diamond surface a long exposure time is needed in order to observe surface morphological changes by SEM.

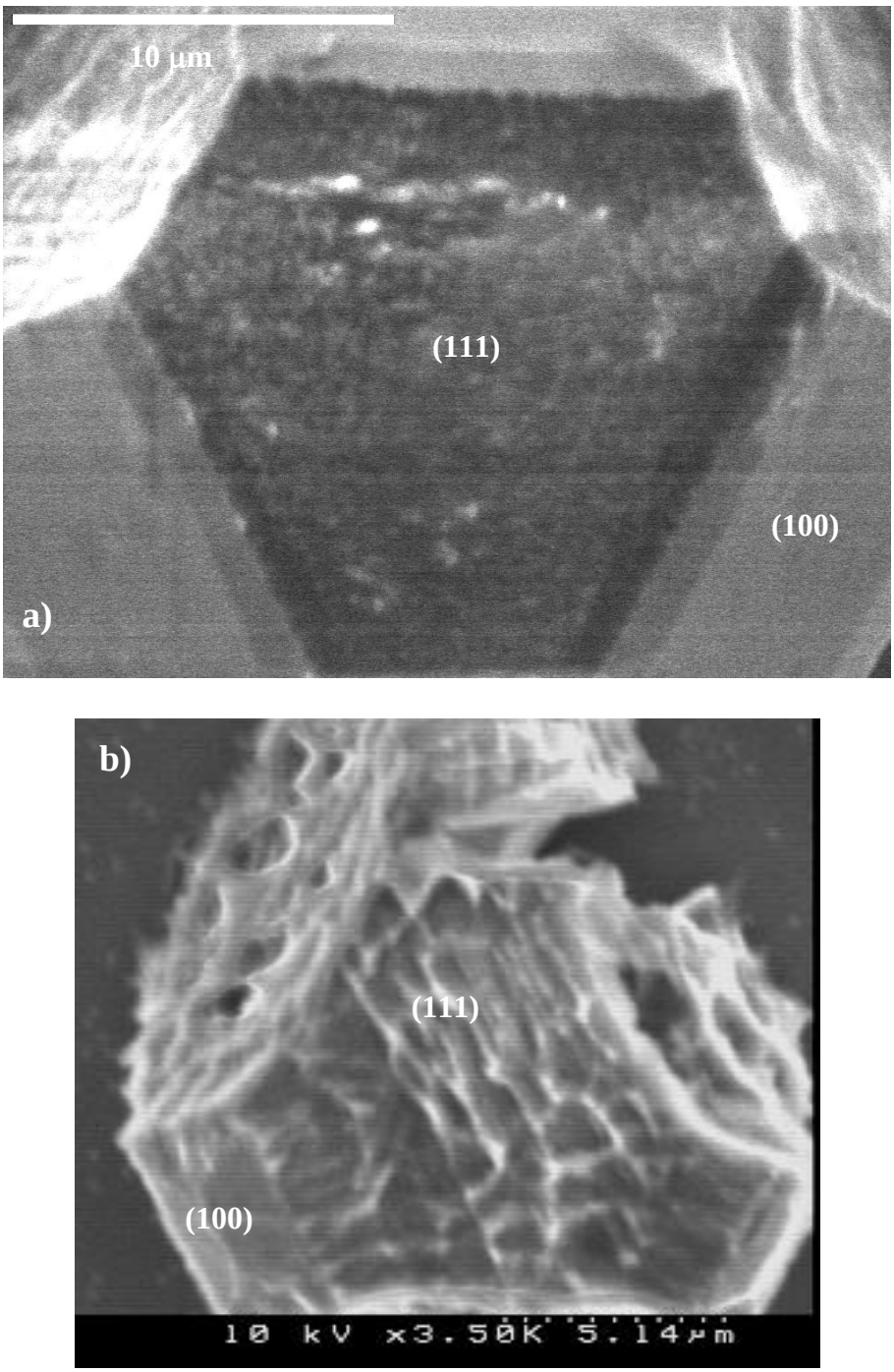

Figure 6.21 SEM image of a CVD cubo-octahedral diamond crystallite thermally oxidised at 600^{o}C and 1 atm pressure of dry O_2 for a) 60 minutes and b) 240 minutes.

When the substrate temperature was raised to 600^{o}C at 1 atm pressure of dry O_2, the duration of the thermal oxidation was limited to 60 minutes due to the high oxidation rate of the {111} diamond surfaces. Under those conditions pitting was observed on the {111} diamond surfaces as shown in Figure 6.21 a). As the kinetics are fast at 600^{o}C,

the etch pits were not well-defined and did not have any specific crystallographic orientation.

The (111) diamond surface turns very rough, with large craters after 240 minutes of oxidation at 600^{o}C, see Figure 6.21 b). The high oxidation rate of the {111} diamond facets caused the collapse of the individual cubo-octahedral diamond crystallites and the exposure new diamond surfaces between the {111} and the {100} diamond surfaces.

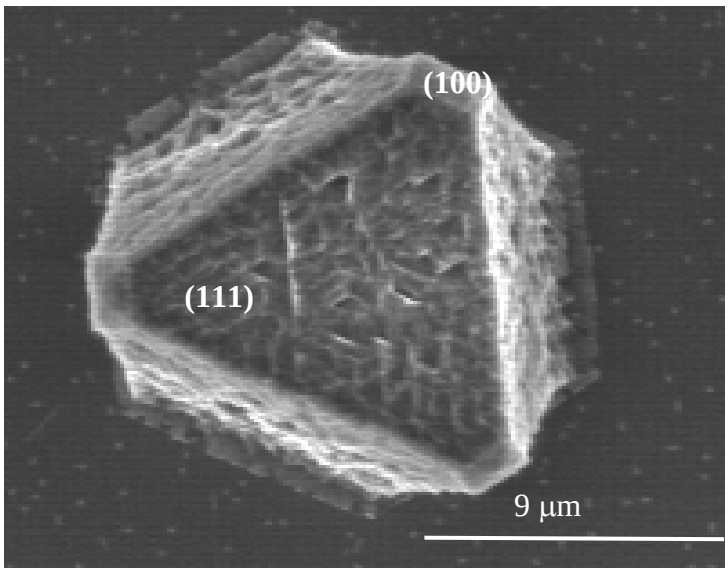

Figure 6.22 SEM image of thermally oxidised CVD cubo-octahedral diamond crystallite at 600^{o}C and 50 Torr of dry O_2 pressure for 5 hours. The {111} diamond surfaces were rough and triangular depressions have been observed with their sides parallel to a triad of <110> directions.

A reduced pressure of dry O_2 at 600^{o}C caused pitting and the formation of triangular depression on the {111} diamond surfaces, as observed in Figure 6.15 a) and b). The triangular depressions formed on the {111} diamond surfaces exhibited sides in the positive direction, according to the etch pit definition given by Frank *et al* [287], as shown in Figure 6.22.

Prolonged thermal oxidation was applied to the same sample for a total duration of 30 hours at 565^{o}C and 1 atm pressure of dry O_2. The sample was removed from the vacuum cell after 9, 15 and 30 hours of treatment for examination. Figure 6.23 a-d) shows the SEM images of the same {111} diamond surfaces at different stages of the thermal oxidation treatment.

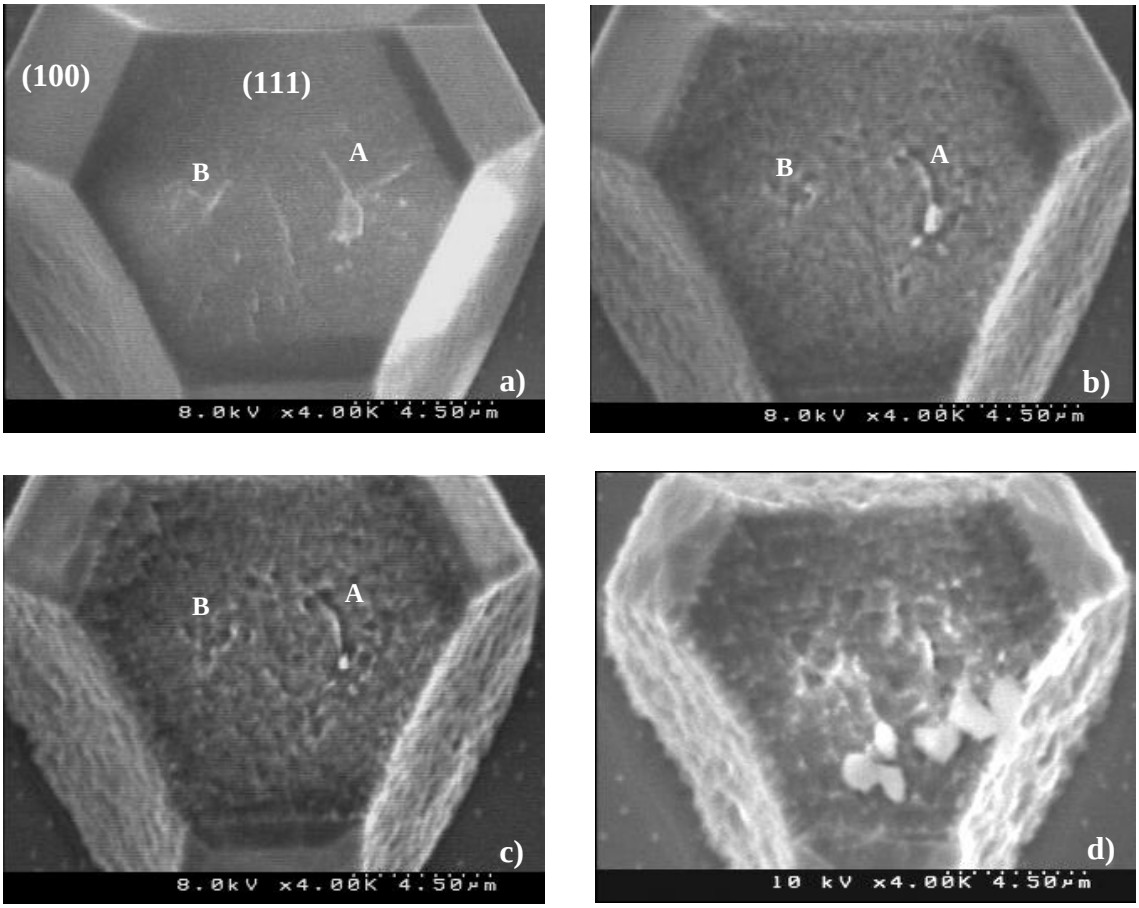

Figure 6.23 SEM images of CVD diamond cubo-octahedral crystallites a) as-grown and after thermal oxidation at 565^{o}C and 1 atm pressure of dry O_2 for a) 9 , b) 15 and 30 hours.

The as-grown {111} diamond surface was not smooth, but comprised surface imperfections such as raised features and hollow structures, as shown in Figure 6.23 a). The {111} diamond surface appears rough after 9 hours of thermal oxidation. Pitting was observed across the entire surface. The raised features have been etched faster than the rest of the surface, creating shallow features on the surface, as highlighted as A and B in Figure 6.23 b). Present results indicate preferential attack on crystal imperfections. As further treatment was applied to the (111) diamond surface, the etch pits became deeper and, after 30 hours of thermal oxidation, resulted in a rugged (111) diamond surface, Figure 6.23 d). The (111) diamond breaks up in a square {100} facets, as seen at the top left hand sector of the facing (111) plane.

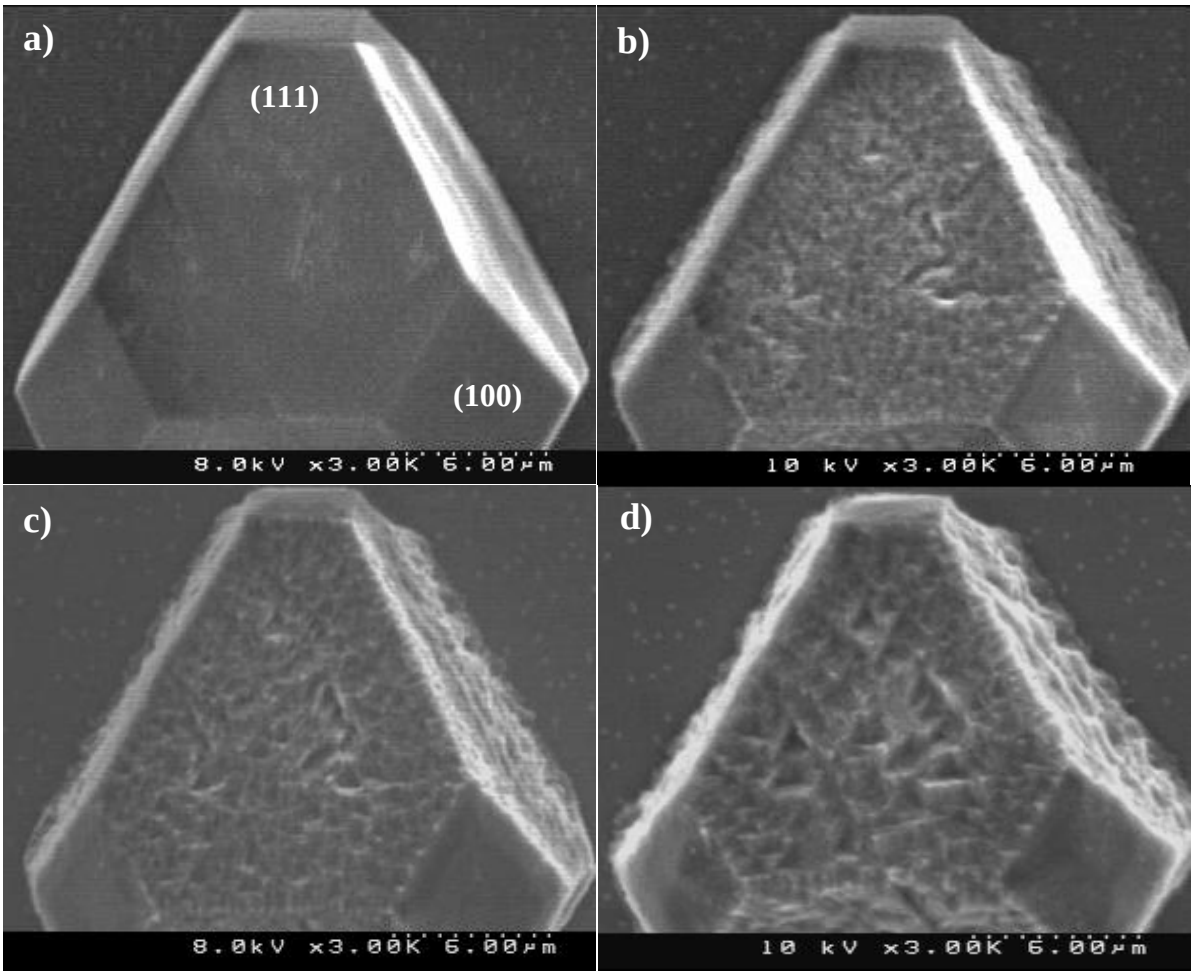

Figure 6.24 SEM images of (111) diamond surface of a CVD diamond cubo-octahedral crystallite a) as-grown and after it has been thermally oxidised at 565^{o}C and 1 atm pressure of dry O_2 for b) 9 hours, c) 15 hours and d) 30 hours.

The cubo-octahedral shape of the individual diamond crystallites changes upon thermal oxidation as curved {111} diamond surfaces are formed, as seen in Figure 6.23 d).

Formation of positive etch pits on the (111) diamond surface has been observed after 9 hours of thermal oxidation at 565^{o}C and 1 atm of pressure of dry O_2. From the distribution of etch pits on the oxidised (111) diamond surface we can assume that they are formed preferentially on surface imperfections, see Figure 6.24 a-d). Further thermal oxidation causes an increase in the depth and lateral dimensions of etch pits on the (111) diamond surfaces.

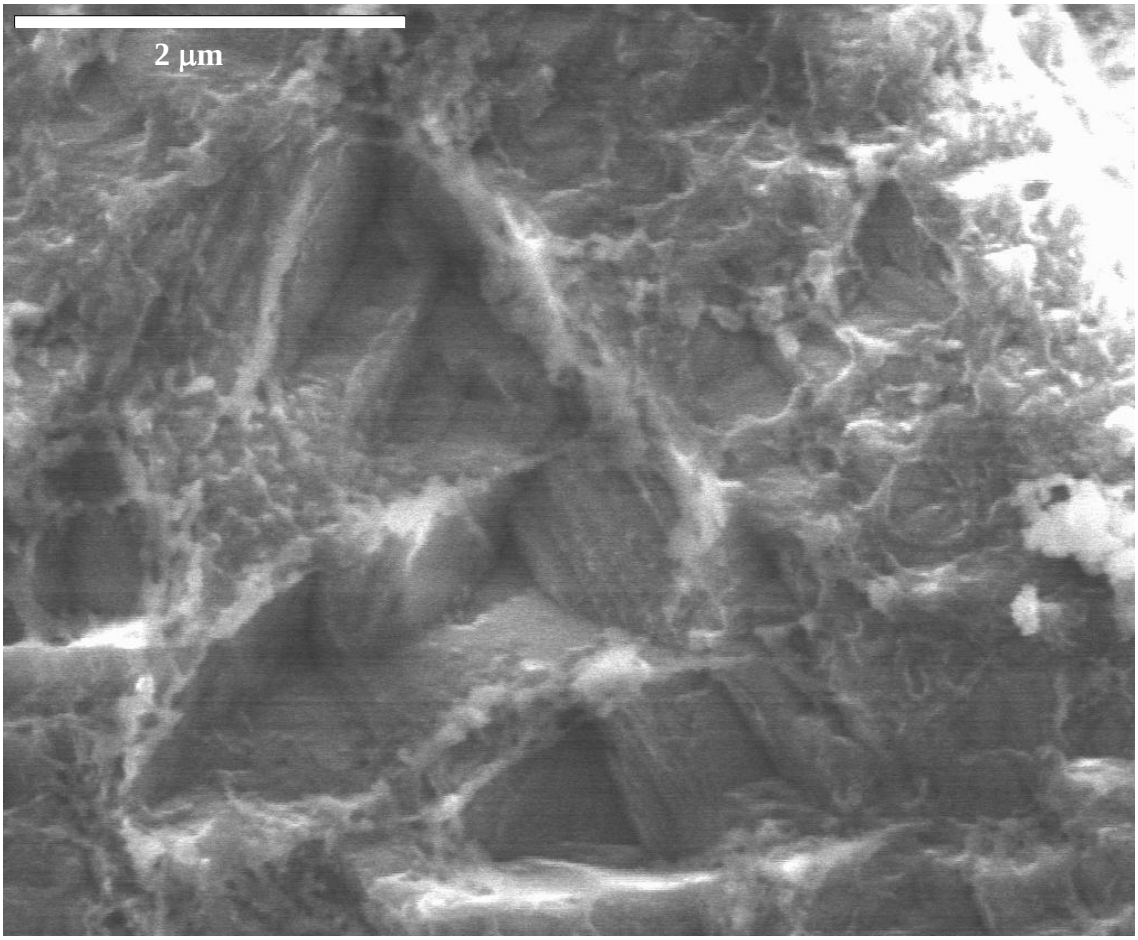

Figure 6.25 Higher magnification SEM of (111) diamond surface from Figure 6.24.

After 30 hours of thermal oxidation, Figure 6.24 d), steep well defined positive trigons were formed on the (111) diamond surfaces. The oxidised surface turned very rough, and square {100} facets were evident on the (111) diamond surfaces.

The triangular depressions formed on {111} diamond planes have been observed with high resolution SEM, as seen in Figure 6.25, to be steep, well defined etch pits with pointed bottoms. The sides of the etched pits comprised surfaces parallel to the triad of <110> directions and, based on the work by Frank *et al* [287] on diamond etch pits; they can be classified as positive trigons.

The area surrounding the well-defined etch pits was found to be rough with almost an amorphous structure. Reported results on the thermal oxidation of {111} diamond planes confirmed that graphitisation occurs upon CO desorption. But most frequently, this phenomenon accompanies thermal oxidation at the much higher temperatures

adopted in the present studies. Although, from the present observations, the induced graphitisation of the oxidised {111} diamond surface cannot be excluded.

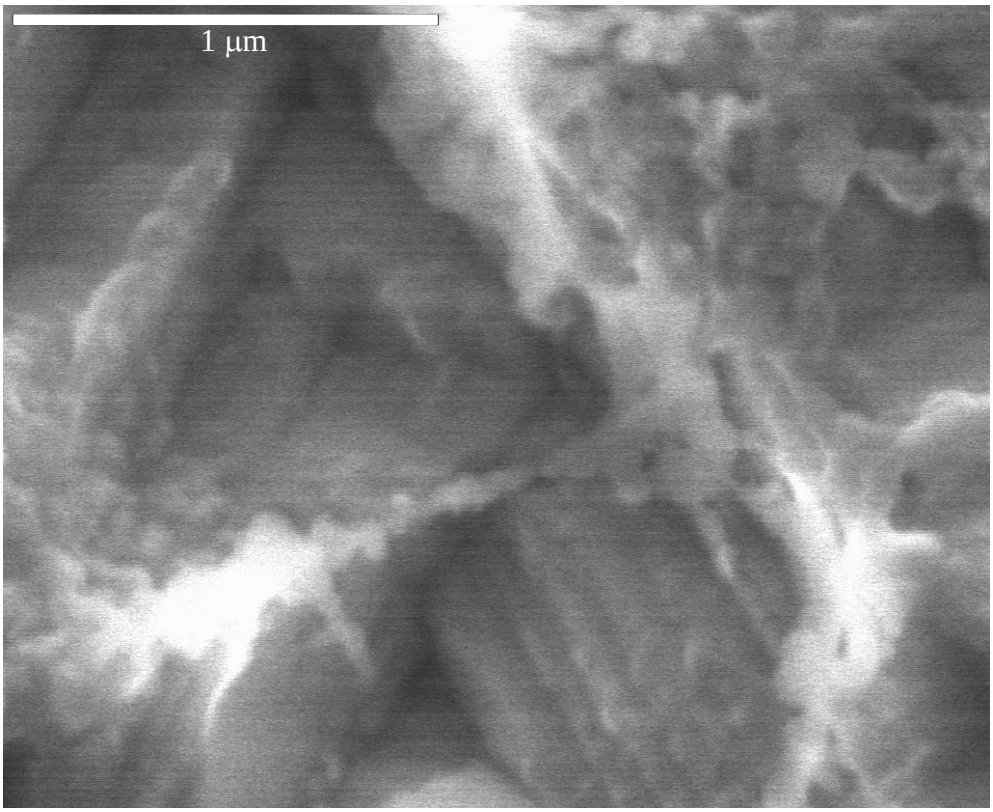

Figure 6.26 High magnification SEM image of positive overlapping etch trigons formed on (111) diamond surfaces.

The sides of the etched trigons comprise steps to their in-plane normals to the [112] directions, highlighted in Figure 6.26. The etch pits appear to overlap as we have observed a large etch trigon to enclose other smaller etched trigons, as shown in Figure 6.26.

This is the first time positive, well-defined etch pits, referred as trigons have been formed due to dry O_2 thermal oxidation of the {111} surfaces of CVD diamond crystallites.

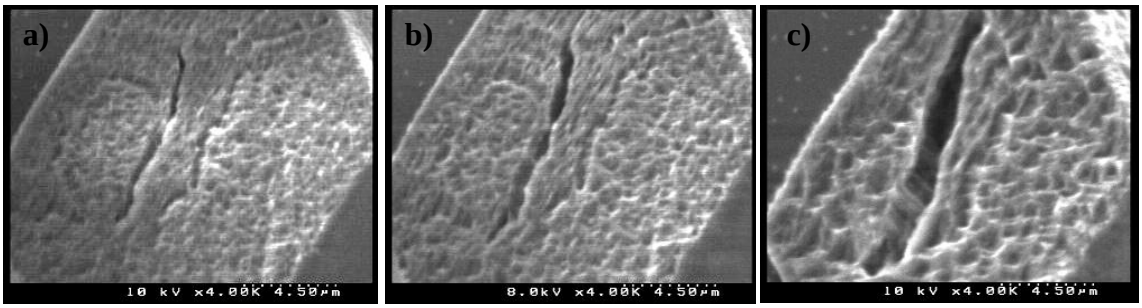

Figure 6.27 SEM images of (111) diamond surface at different stages of thermal oxidation at 565^{o}C and 1 atm pressure of dry O_2, a) 9 hours, b) 15 hours and c) 30 hours.

Upon thermal oxidation imperfections, such as microcracks on the (111) diamond surface, were etched preferentially in comparison with the rest of the surface. Figure 6.27 a-c) shows SEM images of a (111) diamond surface of a CVD cubo-octahedral crystallite thermally oxidised at 565^{o}C at 1 atm pressure of dry O_2 at different oxidation times. Etching of the microcracks resulted in extended pits which have been preferentially etched.

Cubo-octahedral crystallites with fivefold twinning symmetry [335] comprising five {111} diamond planes were examined at different stages of thermal oxidation, at 565^{o}C and 1 atm pressure of dry O_2 as shown in Figure 6.28 a-d).

Similar morphological phenomena, as in the case of {111} diamond surfaces, upon thermal oxidation have been observed for the planes of fivefold twinned crystallites. Hollow structures have been formed on the {111} diamond surfaces while positive etch pits, trigons, were observed. Only after prolonged thermal oxidation have the interfaces between two {111} twinning planes been affected by oxidation, Figure 6.28 c-d).

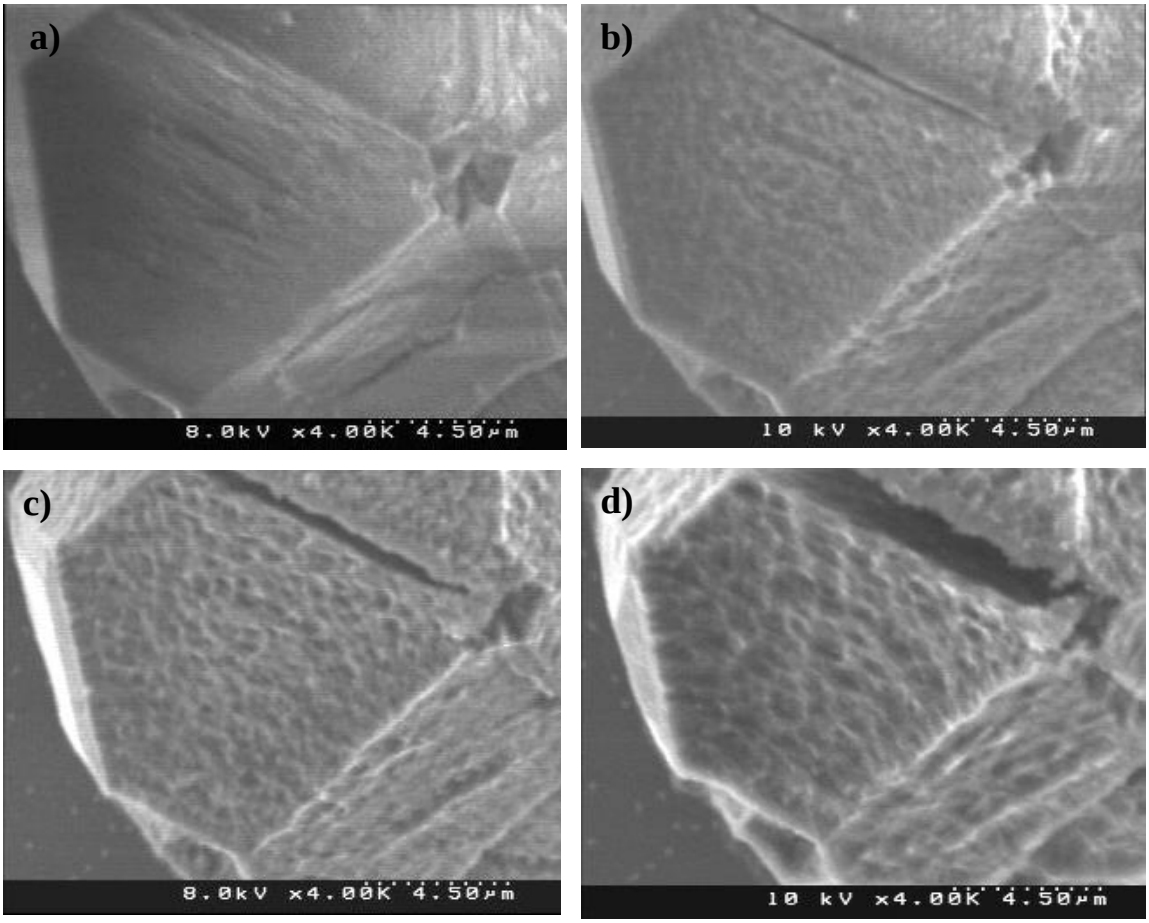

Figure 6.28 SEM images of CVD cubo-octahedral diamond crystallite with fivefold symmetry, a) as-grown and after thermal oxidation at 565^{o}C and 1 atm pressure of dry O_2 for b) 9 hours, c) 15 hours and d) 30 hours. The crystallite reveals five twinned {111} diamond facets.

CVD diamond films

Although the present studies have been focused on thermal oxidation of cubo-octahedral CVD diamond crystallites, a few of the silicon substrates used in these studies included the presence of CVD diamond thin films. Similar surface morphological changes have been observed for thermally oxidised CVD diamond films. Preferential oxidation has been observed on the {111} diamond facets. Roughening of the {111} diamond surface has been induced by oxidation, whilst the formation of hollow structures has been observed after prolonged thermal oxidation, see Figure 6.29 a-d). Triangular depressions, positive etch pits and trigons were not observed within the resolution of SEM.

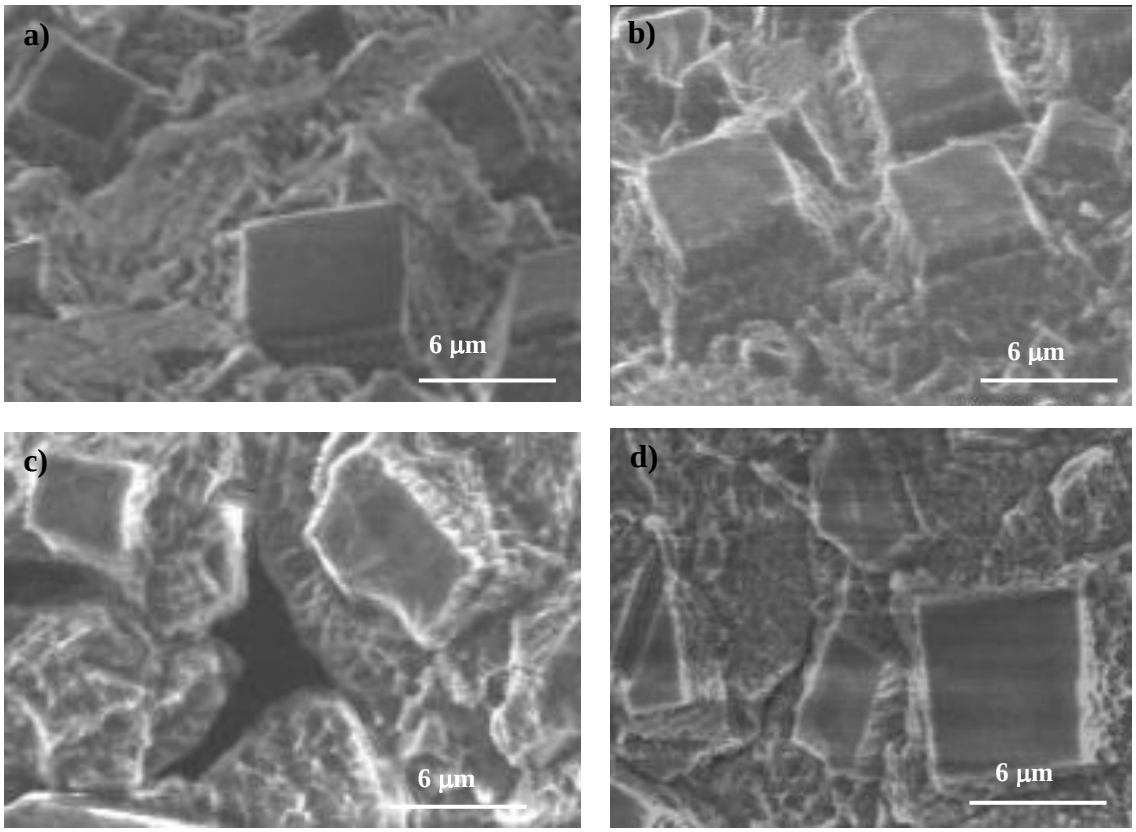

Figure 6.29 SEM images of a thermally oxidised CVD diamond film at 565^{o}C for a) 9 hours (tilted projection, b) 15 hours (tilted projection), c) 30 hours (on-top view) and d) 15 hours (on top view).

The more stable {100} diamond facets of the CVD diamond film have remained intact after 15 hours of thermal oxidation, Figure 6.29 a). After 15 hours of thermal oxidation the {100} diamond facets appeared to have been etched and the surface exhibits craters.

More interestingly the grain boundaries, presumably {111} diamond planes, have been etched much faster causing the exposure of the inter-granular surfaces. For the individual CVD cubo-octahedral crystallites the exposure of {110} diamond planes has been observed after 30 hours of thermal oxidation and to a lesser degree, as previously observed in Figure 6.16 d). After 30 hours of thermal oxidation the surface of {100} facets appears uneven as etching had proceeded at the sides of the crystal facet.

The diamond {111} planes have been etched preferentially and well-defined etch pits have not been observed. The observations made on the CVD diamond films are inconsistent with those made on the isolated CVD cubo-octahedral crystallites. The surface morphological changes appeared to have been more pronounced for the thin films. As oxidation reactions are exothermic, adequate heat conduction is vital for maintaining isothermal conditions. Lee. *et al* [178, 292] show that explosive oxidation can be induced by poor thermal conductivity of diamond powders. It is not clear if that is also true for the present results on CVD diamond films.

From the present results it is apparent that the resistance of CVD diamond films to O_2 at elevated temperatures strongly depends on the surface area of the exposed {111} diamond planes.

6.5.3 Atomic Force Microscopy

Microscopically the {100} and {111} surfaces of the cubo-octahedral CVD diamond crystallites have been examined by contact mode AFM and each low-index plane following thermal oxidation will be presented independently

{100) diamond surface

Figure 6.30 a-c) shows the AFM topography of the as-grown and thermally oxidised (100) diamond surface of a CVD cubo-octahedral crystallite. On the as-grown (100) diamond surface hillocks structures were observed which commonly appeared on the CVD diamond crystallites {100} surfaces.

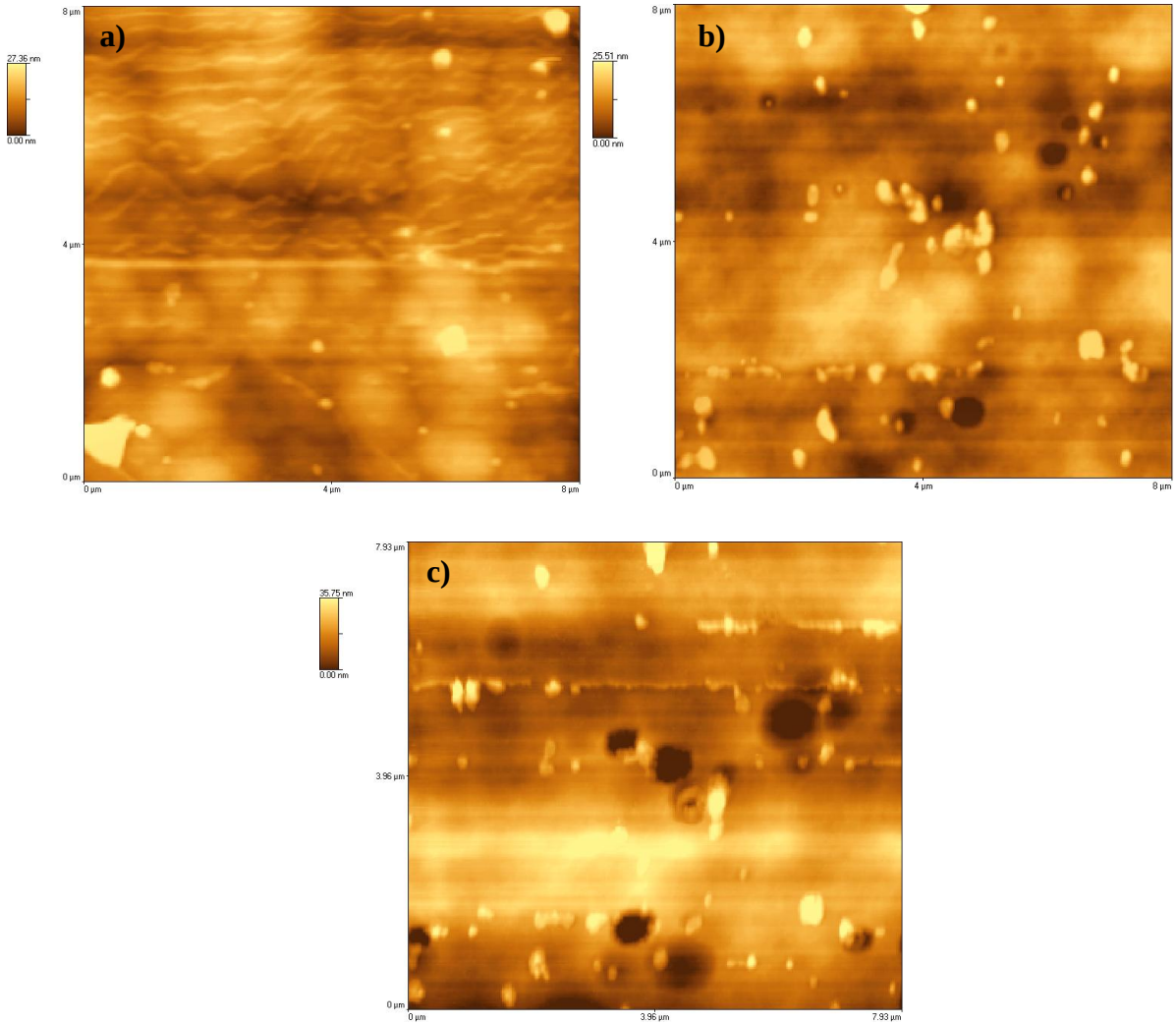

Figure 6.30 AFM micrographs of a) as-grown (100) diamond surface, b) after 60 minutes and c) 120 minutes of thermal oxidation at 555^{o}C and 1 atm pressure of dry O_2.

The sample had been subjected to thermal oxidation at 555^{o}C substrate temperature and 1 atm pressure of dry O_2. After 60 minutes of thermal oxidation shallow hollow etch pits were formed on the surface, as shown in Figure 6.30 b). Hillocks were still present on the diamond surface as well as surface contamination.

Formation of new etch pits has been observed after 120 min of thermal oxidation, while dissolution and enlargment of the existing etch pits has been observed by AFM, see Figure 6.30 c). The increase in the surface roughness of (100) diamond surfaces has been measured as a function of time as shown in Figure 6.31. The formation of etch pits increased the surface roughness values.

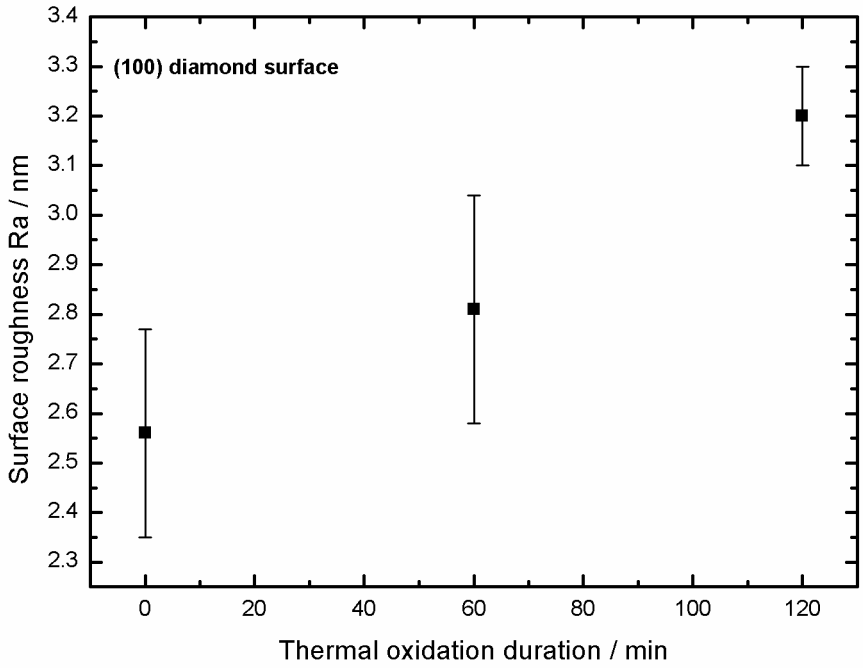

Figure 6.31 Surface roughness of (100) diamond surface with the duration of thermal oxidation.

Figure 6.32 a-b) shows the AFM micrographs of an as-grown and thermally oxidised (100) diamond surface. The oxidation conditions were identical to those presented earlier, as in Figure 6.30, (555^{o}C and 1 atm) whilst the duration was 60 min. Upon thermal oxidation the surface hillocks did not undergo changes, although preferential oxidation attacked the regions between the hillocks. Formation of etch pits was observed in areas between the surface hillocks.

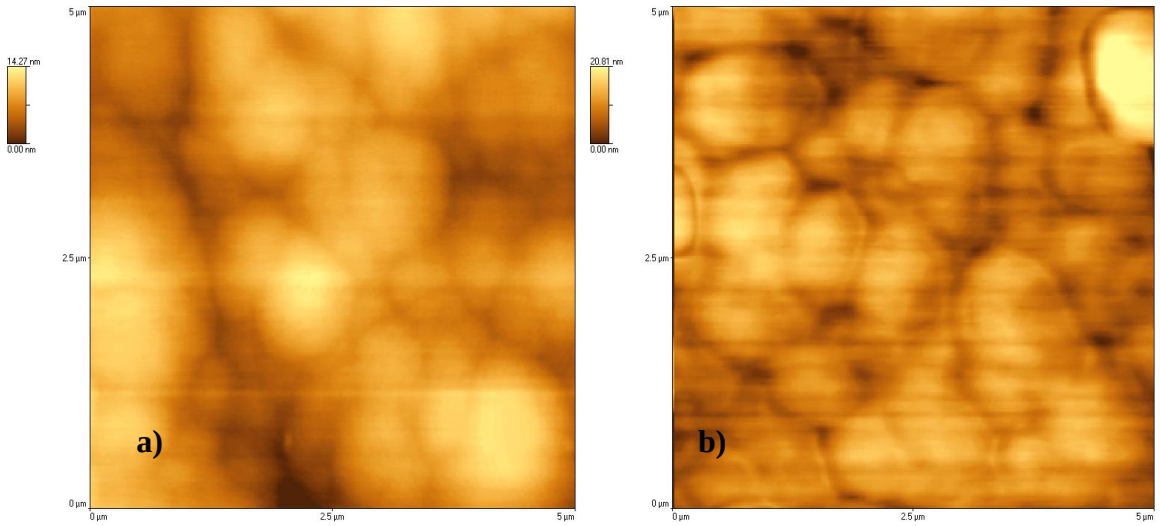

Figure 6.32 AFM micrographs of an a) as-grown (100) diamond surface and b) after thermal oxidation for 60 min at 555°C and 1 atm applied pressure of dry O_2

The (100) diamond surface of a CVD diamond cubo-octahedral crystallite after it has been subjected to thermal oxidation at 565°C and 1 atm pressure of dry O_2 for 30 hours is shown in Figure 6.33.

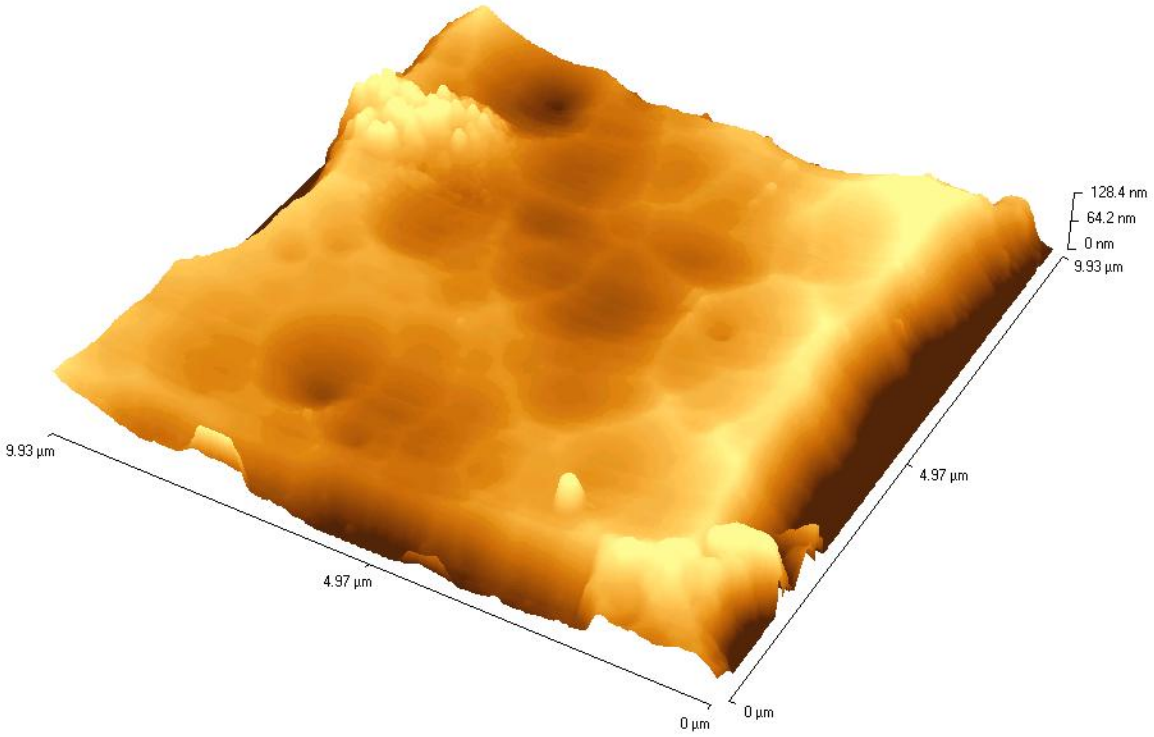

Figure 6.33 AFM image of the (100) surface of a CVD cubo-octahedral crystallite following thermal oxidation at 565°C for 30 hours and 1 atm of dry O_2.

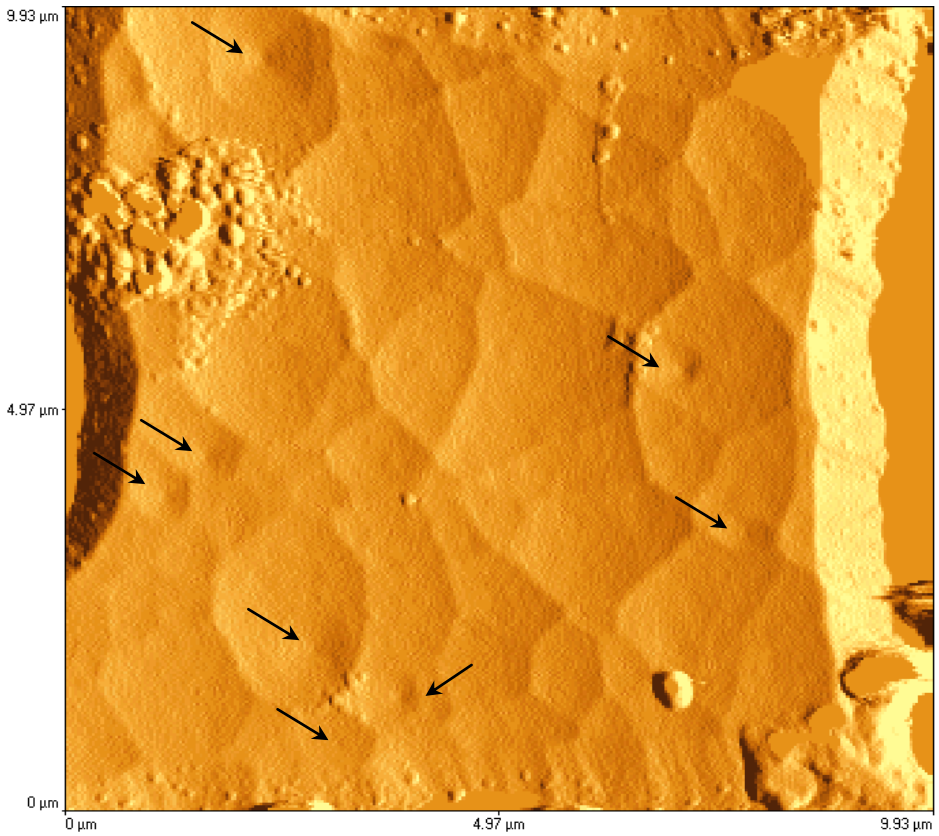

Figure 6.34 AFM image of the (100) surface of a CVD cubo-octahedral crystallite following thermal oxidation at 565^{o}C for 30 hours and 1 atm of dry O_2.

Prolonged thermal oxidation of a (100) diamond surface yielded small craters with a depth and width range of 10 – 90 nm and 1- 2 µm respectively. The small raised features which appearing on the (100) diamond surface are believed to be contamination due to the sample handling during the AFM characterisation.

Etch pits with pointed bottoms have been observed at the centre of the surface crater structures. The sides of the etch pits were found to be along the [110] directions of the surface, which is in agreement with the etch pits observed on natural {100} diamond crystals oxidised at 750^{o}C in dry O_2 [284]. It was not possible to resolve the surface topography at the etch pits due to AFM instabilities in the high resolution scans. The density of the square etch pits was low. Only eight pits were observed in a~ 10 x 10 µm (100) diamond surface area as shown in Figure 6.34. This corresponds to a etch pit density of 8 x 10^{10} cm^{-2} which is close to the reported value of 2 x 10^{10} cm^{-2} for the dislocation density of CVD diamond thin films [336].

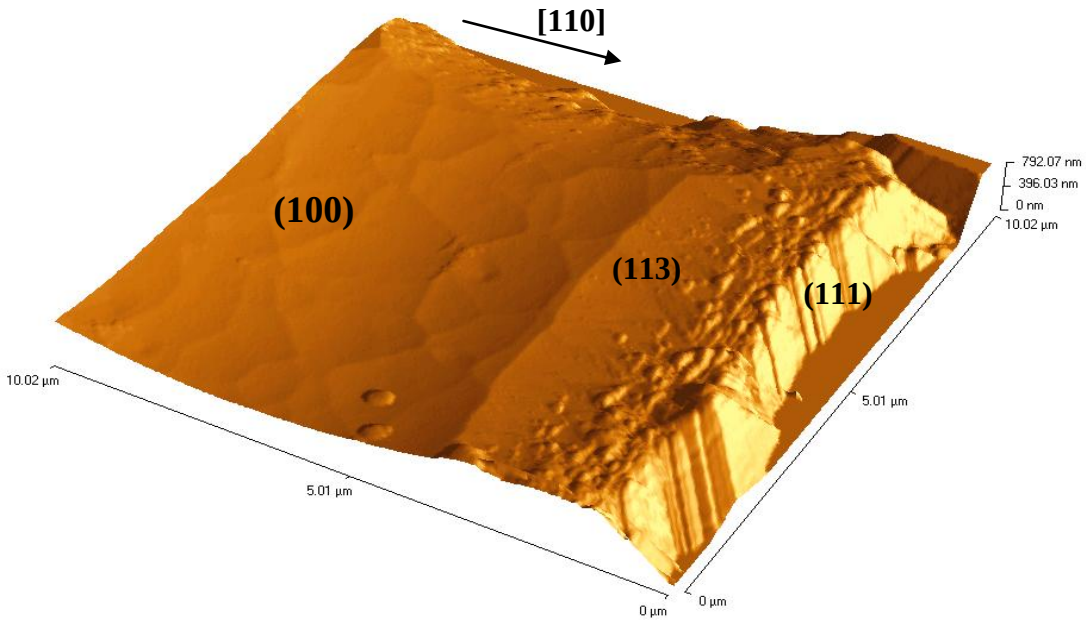

Figure 6.35 AFM topographic images of the corner of the thermally oxidised (100) diamond surface.

The well-formed etch pits exhibit a depth of 25 nm while the depth for the small ones was measured to be around ~ 13 nm. Such a thermally oxidised (100) diamond surface was rough due to the formation of craters and etch pits a surface roughness of Ra = 10.24 nm was measured using the AFM software for the area of the (100) diamond shown in Figure 6.31.

AFM topographies on the {113} diamond planes, Figure 6.35., revealed a different surface morphology compared to a {100} diamond surface, see Figure 6.36. Neither etched craters nor etch pits have been observed on the {113} diamond surface. Instead the surface is covered with raised features with a higher areal density closer to the intersection with the {111} diamond plane. The height of the raised features varied between 6 nm and 16 nm.

Etch pits have also been observed on the (100) diamond surface oxidised for 60 minutes at 600^{o}C and 1 atm pressure of dry O_2. Figure 6.37 a-b) shows the AFM topographies of a thermally oxidised (100) diamond surface. The etch pits exhibit square four-fold symmetry along the <110> directions, while a few etch pits appear to have a hollow shape. Despite the formation of etch pits on the (100) diamond surface the surface roughness measured was Ra = 8.54 nm for the surface area shown in Figure 6.37 b).

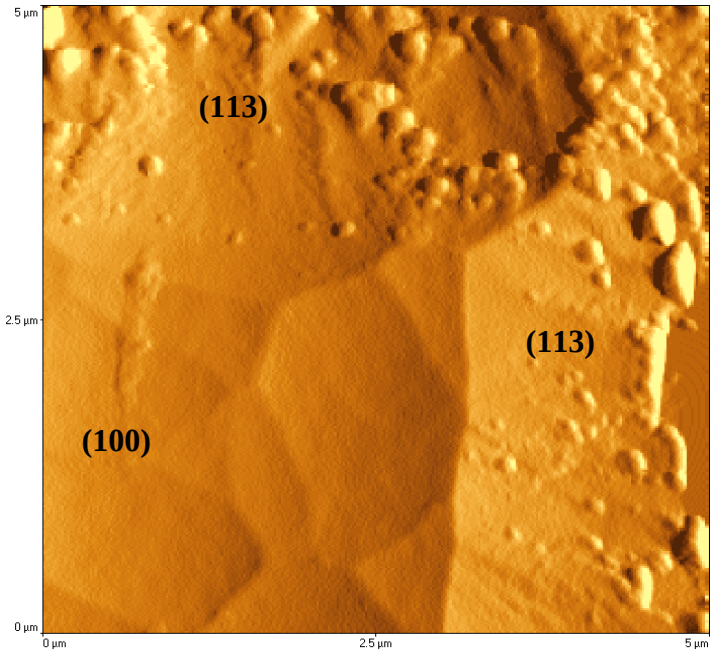

Figure 6.36 AFM topographic images of the intersection of the thermally oxidised (100)/ (113) diamond surfaces.

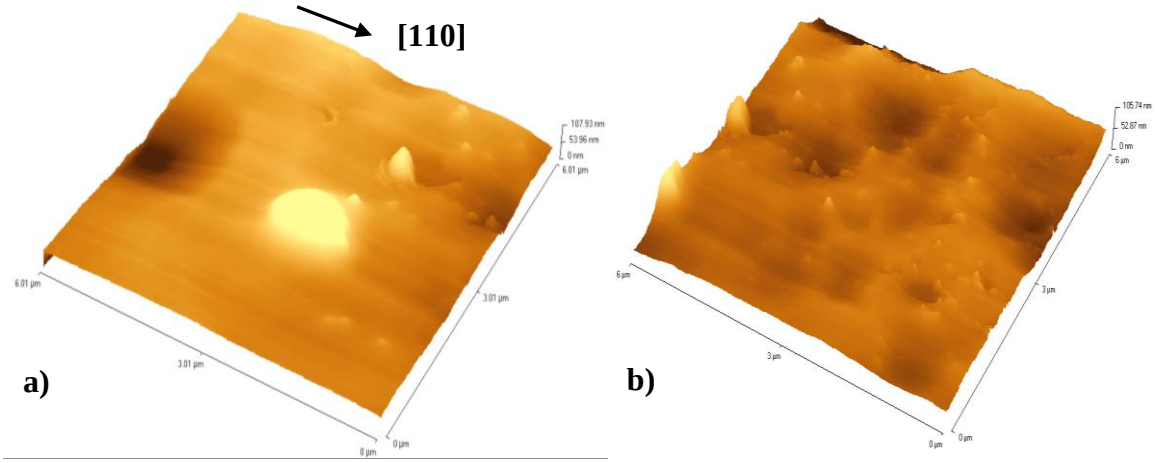

Figure 6.37 AFM topographic images of the (100) diamond surface after thermal oxidation at 600^{o}C and 1 atm pressure of dry O_2 for 60 min.

The (100) diamond surface of the crystallite oxidised at 535^{o}C and 1 atm pressure of dry O_2 for 9 hours appeared to be smooth under SEM analysis. AFM topography revealed that the (100) oxidised surface exhibited small depressions of 1 – 1.5 nm depth and larger ones with greater than 10 nm depth, as shown in Figure 6.38. From SEM analysis it was found that large depressions were present on the as-grown surface, and could be correlated with crystal imperfections. All etch pits exhibited a hollow shape. The surface roughness of the surface area under examination was found to be Ra = 2.55 nm. Square etch pits have not been observed for these oxidation conditions.

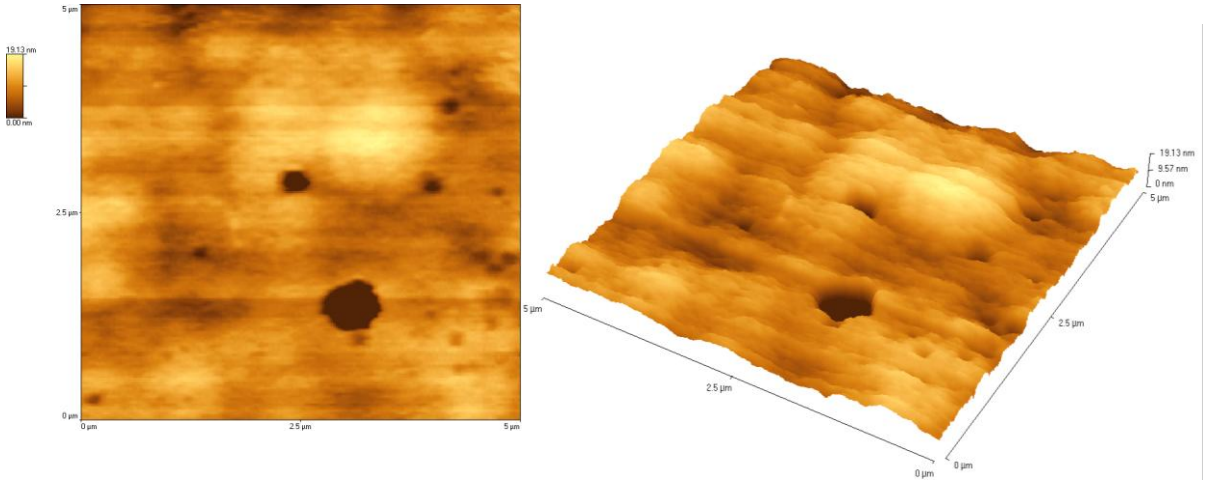

Figure 6.38 The AFM topography of thermally oxidised (100) diamond surface at 535^{o}C and 1 atm pressure of dry O_2 for 9 hours.

The formation of well-defined etch pits on single crystal {100} diamond surfaces without the presence of water vapour has been observed by de Theije and co-workers [283]. This is the first time well defined square etch pits have been observed on CVD {100} diamond surface after thermal oxidation with dry O_2. Discussion on the oxidation mechanism and pit formation of (100) diamond surface will be provided in section 6.6.2.

(111) diamond surface

Figure 6.39 shows the AFM image of an as-grown (111) diamond facet of a CVD cubo-octahedral crystallite. The as-grown (111) facet exhibited a concave shape. Raised features on the (111) plane are possible contamination due to sample handling.

Due to high surface roughness of the thermally oxidised {111} diamond surface the acquisition of AFM surface topographies was not feasible for all the treated samples. For this reason the AFM analysis of {111} diamond surfaces presented in this section is restricted to 60 minutes of subsequent thermal oxidation treatments on the same sample. The conditions of thermal oxidation were chosen to be a substrate temperature of 555^{o}C and 1 atm pressure of dry O_2. AFM micrographs of the as-grown and thermally oxidised (111) diamond facets are shown in Figure 6.40 a-d).

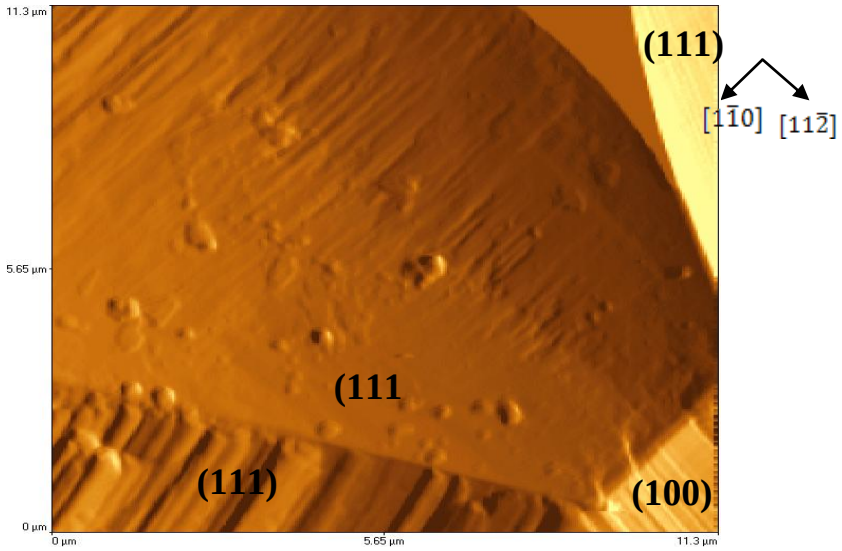

Figure 6.39 AFM micrograph shows the as-grown (111) surface of a CVD cubo-octahedral crystallite image illuminated from the right.

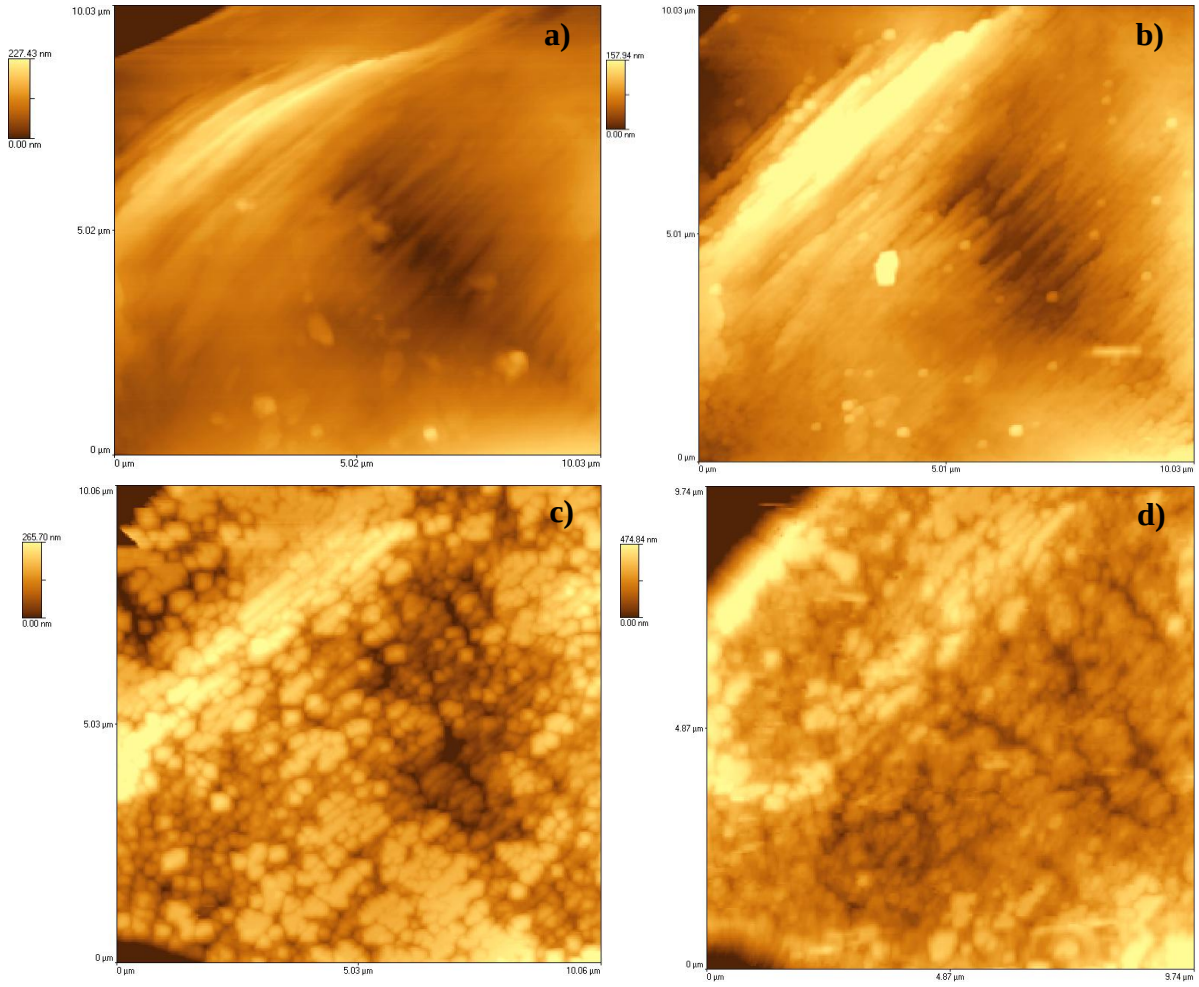

Figure 6.40 AFM topographies of (111) diamond surface a) as grown and after thermal oxidation at 555 ^{o}C substrate temperature and 1 atm pressure of dry O_2 for b) 60 minutes, c) 120 minutes and d) 300 minutes.

After the initial 60 minutes of thermal oxidation, the {111} diamond surface appeared to experience a soft etching treatment. The surface was relatively stable to thermal oxidation. Similar SEM observations were made for the thermal oxidation of {111} diamond surfaces at 565^{o}C and 1 atm pressure for 60 minutes. There was no evidence of surface morphological changes of {111} diamond planes.

A further 60 minutes of thermal oxidation showed that the {111} diamond surface was severely attacked as seen in Figure 6.40 c). The surface broke up as isotropic etching took place and created a rough surface.

After 300 minutes of thermal oxidation it was obvious that the {111} diamond surface was not stable under these conditions. The surface was etched by oxygen by removal of carbon equally on steps and between the terraces. Oxidation was accompanied by the formation of etch pits which can clearly seen, after 300 min of treatment, in Figure 6.40 d).

Prior to, and after, each treatment the surface roughness was evaluated from the AFM data using the software analysis shown in Figure 6.41 along with the surface roughness measured for the intrinsic {100} diamond surface. The measured surface roughness values were consistent with the observed surface morphological changes. The surface roughness of {111} diamond surface increased with thermal oxidation treatment and a very rough surface was formed.

The as-grown (111) diamond plane was examined by AFM, as shown in Figure 6.42 a). The surface was covered with bunched steps along the <110> directions with varied widths, while two types of steps were observed: double steps of depth of 0.5 nm to 1 nm and bunched or macro steps with a varied depth of 1.5 to 20 nm.

Figure 6.42 b) shows that the {111} diamond surface was stable after 60 min of thermal oxidation. The steps had been subjected to etching on the terraces and on the step edges. Oxidation of the surface caused the formation of ball-like shapes along the surface. Etch pits were not observed on the oxidised surface.

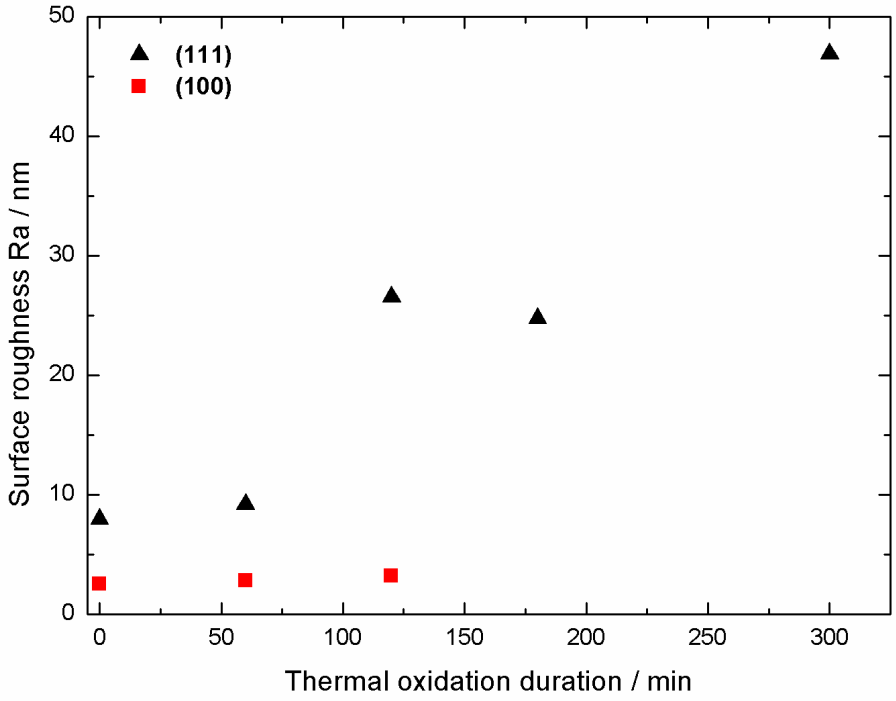

Figure 6.41 Surface roughness, Ra, of diamond surfaces upon thermal oxidation.

The oxidative stability of the {111} diamond surface was lost with a further 60 min of thermal treatment. As can be seen from Figure 6.42 c) the {111} diamond surface was isotropically etched with a further 60 min of thermal oxidation. The surface was etched along the surface and along the edges of the steps. The initial surface morphology was not able to be resolved and the formation of etch pits occurred. Based on these observations neither a layer-by-layer nor step mechanism could be attributed to the thermal oxidation of a {111} diamond surfaces.

After 300 minutes of thermal oxidation the (111) diamond surface became very rough with the formation of etch pits, see Figure 6.42 d). Triangular depressions have not been observed at this stage of thermal oxidation and all the etch pits exhibit a hollow shape. The present AFM topographic images support the chemical roughening of (111) diamond surfaces by thermal oxygen.

As the {111} diamond surface becomes roughened, exposure of new steps and kink atoms along different crystallographic direction occurs. Such a surface would not be expected to be stabilised by oxygen-carbon groups and so roughening would lead to isotropic etching of the surface.

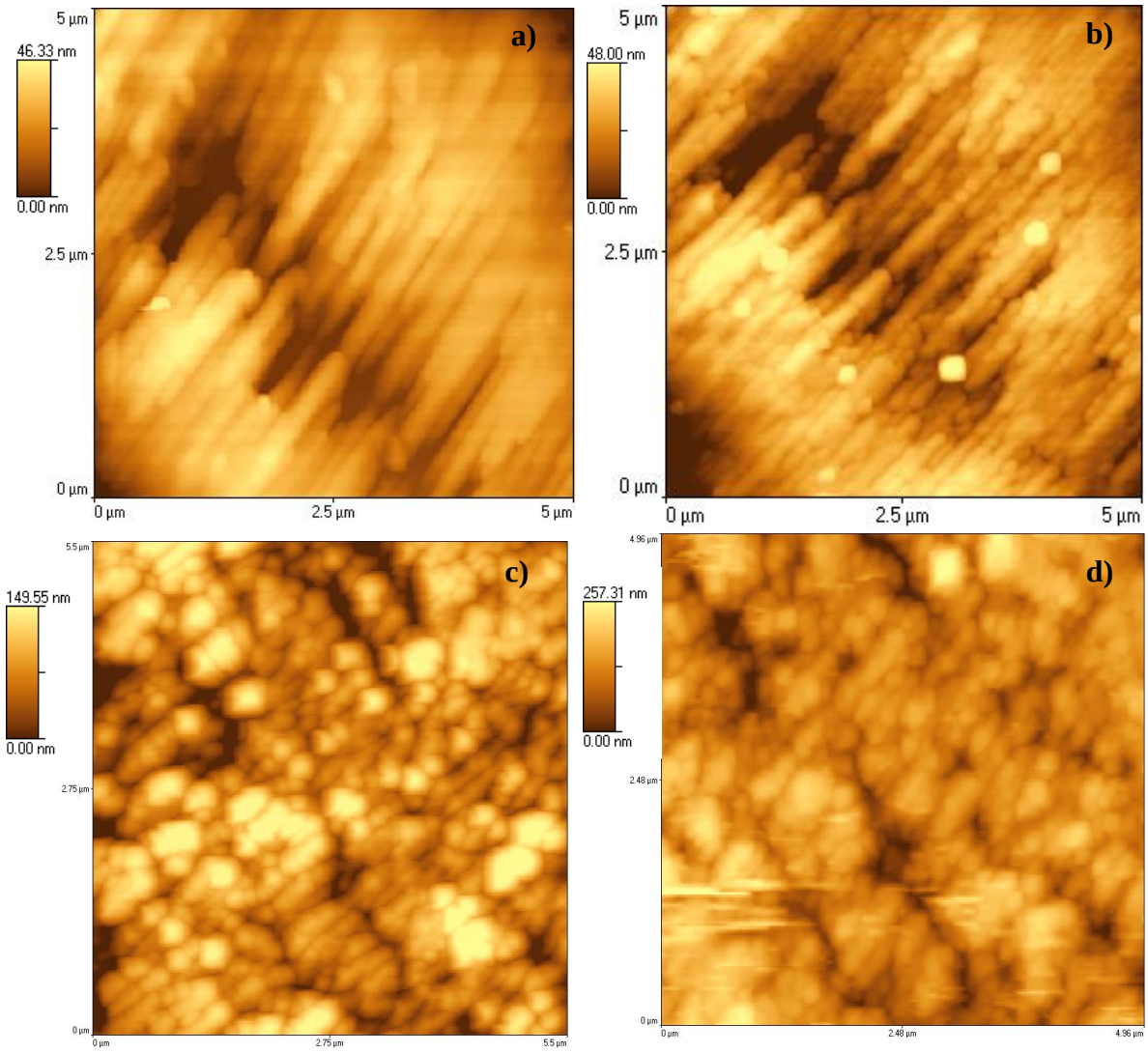

Figure 6.42 AFM topographies of a) an as-grown (111) diamond facet and after thermal oxidation at a substrate temperature of 555^{o}C and 1 atm pressure of dry O_2 for b) 60, c) 120 and d) 300 minutes.

6.6 Discussion

6.6.1 Kinetic analysis

The temperature variation of the oxidation rate of {111} and {100} diamond planes of individual CVD cubo-octahedral crystallites was found to exhibit an Arrhenius-type behaviour, which is in consistent with previous studies [282-284, 289, 295, 322, 323, 327, 328, 337] of natural, CVD single crystal and polycrystalline diamond thin films.

The activation energy for the oxidation of {100} diamond planes of isolated CVD cubo-octahedral crystallites was found to be identical with the value reported for polycrystalline {100}-highly oriented CVD diamond films [289] grown under identical conditions and within the range of values previously reported [284, 295, 321-323] for polycrystalline CVD and natural {100} diamond surfaces.

A summary of the published activation energies for the oxidation of the {100} and {111} diamond surfaces by O_2 is presented in Table 6-3. The use of sensitive optical profilometry to monitor the thermal oxidation of microscopic crystallites enabled the measurement of oxidation rates at lower temperatures than previously reported for both low-index diamond surfaces. This is the first time the activation energy of {111} CVD diamond surfaces has been accurately measured and the value is similar for those measured for natural {111} diamond surfaces [283, 323, 338].

The linearity of the oxidation kinetics shown in Figures 6.5 and 6.6 demonstrates that the activation energy for both diamond planes is constant over the 808-873 K temperature range. The activation energies, evaluated for both {100} and {111} diamond surfaces, are a measure of the rate determining steps leading to the evolution of volatile carbon oxides from the oxygen terminated {100} and {111} surfaces.

Within the temperature and pressure ranges used in these studies the {111} diamond surfaces were found to exhibit higher oxidation rates compared to {100} diamond surfaces. These data are in agreement with those reported for natural and single crystal diamond surfaces [284, 286, 295, 323, 338].

Sample	Crystal plane		$E_{\square}$ / kJ mol^{-1}	Reference
CVD	(100)	Optical profilometry	221 ± 34	This work
	(111)		286 ±29	
CVD	(100)	Interferometry	222 ± 16	
		Thermogravimetric analysis	223 ± 2	
CVD	Polycrystalline		210 ± 10	[295]
CVD	Polycrystalline		213	[321]
Natural	(111)		260	[323]
	(100)		199	
Natural	Polycrystalline		229	
CVD				
Single crystal	(100)	O_2	183±15	[284]
		H_2O	270 ± 5	
		KNO_3	52 ± 15	
Single crystal	(111)	O_2	235 ± 10	[283]
		H_2O	153 ± 12	
		KNO_3	173 ± 16	
Natural	(100)		230	[338]
Single crystal	(100)	CO desorption experimental	188	[330]
		CO desorption theoretical	161	
B-doped	(100)	CO desorption	285	[337]
homoepitaxial				

Table 6-3 Values of the activation energy for diamond oxidation.

6.6.2 Mechanism of diamond oxidation

The {100} diamond surface

Within the combined experimental errors, the activation energy of the oxidation of {100} CVD diamond surfaces is identical to that of natural diamond reported by de Theije *et al* [284]. Formation of shallow square etch pits accompanies the thermal oxidation of natural {100} diamond surfaces and oxidation was suggested to proceed by a step mechanism. The thermal oxidation mechanism, proposed by de Theije and co-corkers [284] supports the stabilisation of dangling bonds on the {100} diamond surfaces with oxygen carbon functional groups. Indeed, even at low temperatures where desoption rates are negligible, the hydrophilic diamond surfaces are decorated with oxygen. In such crystal surfaces the steps are the most reactive sites for dissolution and not the terraces. Oxidative etching therefore would proceed by step propagation and be slower on the carbon terraces.

Crystal defects such as dislocations and stacking faults commonly appear on diamond surfaces. They provide a source of crystal surface stresses where preferential nucleation of monoatonic etch pits occurs. Despite the published work on thermal oxidation on natural {100} diamond surfaces, the nature of nuclei responsible for the formation of etch pits is still unclear. It has been suggested that well defined etch pits can originate from crystal dislocations terminated on the {100} diamond surfaces [284].

The formation of well-defined etch pits with sides along the <110> diamond directions on extensively oxidised {100} CVD diamond surfaces observed in these studies is in agreement with the previously published work at a temperature of 750^{o}C [284]. However in the present studies the AFM resolution was insufficient to image monoatomic steps on the {100} CVD diamond surfaces.

In addition, the formation of shallow hollow-shape etch pits on thermally oxidised {100} CVD diamond surfaces has been observed. Enlargement of the shallow hollow-shape etch pits with thermal oxidation treatment has been observed as well as the complete dissolution of some of the etch pits.

The surface roughness increased linearly with the extent of oxidation due to etch pit formation, indicating the same mechanism of oxidation for the duration of the oxidation period. The nature of the nuclei for the shallow hollow-shape etch pits observed on all the oxidised {100} CVD diamond surfaces is not clear. AFM analysis shows preferential etch pit formation between the surface hillocks. The SEM analysis shows the preferential attack of crystal imperfections. The etched craters on the prolonged oxidised (100) diamond surface indicate that the nuclei responsible for their formation were etched away and lateral etching of steps caused neighbouring pits to overlap and to create large hollow craters.

Surface contamination was evident on the {100} oxidised surfaces which could either reduce the local oxidation rate or promote a catalytic effect of local oxidation. Whilst contamination was experimentally difficult to avoid in highly insulating oxidised samples the nature of the surface contamination has not been determined. In all of the above cases the presence of source nuclei that either increase or decrease the oxidation rate, would cause roughening of the surface. As the etch pit nuclei are removed the surface would undergo kinetic smoothing, although that would only be feasible in a defect free surface.

In contrast the steep well-defined etch pits along the <110> orientation on the oxidised {100} diamond surface show stabilisation of the step sides by oxygen-carbon complexes under the present conditions. Steps along the <110> direction are expected to be stabilised by >C=O bridging or –COC- ether binding. As in the case of shallow hollow-shape etch pits the nature of nuclei responsible for the formation of such etch pits cannot be determined from the current studies. A velocity source which lies at the bottom of the steep square etch pits would be suggested from the present data. Such a type of velocity source can be attributed to crystal dislocations propagating along the crystallite to the surface.

Monolayer coverage of {100} diamond surface, upon thermal oxidation, with oxygen-carbon functional groups has been demonstrated [234] under similar conditions to those described in this thesis for {100}-highly oriented CVD diamond films. High-resolution XPS analysis of thermally oxidised {100}-highly oriented CVD diamond films shows

the presence of carbonyl (>C=O) and ether (COC) species which reside predominantly at the crystallite surfaces.

Due to the small size of the cubo-octahedral CVD diamond crystallites it was not feasible to collect high resolution XP spectra and surface analysis was not carried out on such oxidised samples. Based on the previous studies conducted on {100}-highly oriented CVD diamond films the assumption of full oxygen coverage of the {100} diamond surfaces is a reasonable assumption for the present studies.

Theoretical models suggest that both the ether and carbonyl functional groups stabilise the {100} diamond surfaces [324]. The structure of the oxygen-carbon groups on the {100} diamond surface was found experimentally to depend strongly on the thermal oxidation conditons and the presence of water vapour [228]. At low temperatures the formation of ether type structures was more favorable, while for temperatures above 600^{o}C stabilisation of the (100) diamond surface is achieved by >C=O bridging. As thermal oxidation can occur at temperatures below $\leq$ 600 ^{o}C, ether type structures would be expected to stabilise the steps on the {100} diamond surfaces, although high resolution XPS analysis show the presence of both >C=O and –COC- groups on {100}-highly oriented CVD films .

The features and thus mechanism of the oxidation of diamond surfaces remained unchanged over the oxidation time for the present studies. Therefore it is expected that stabilisation of the {100} diamond surface was the same for the entire oxidation duration within the range of conditions used. The oxygen-carbon groups present on the oxidised {100} and {111} diamond surfaces were not unequivocally established in the work on microscopic crystallites and suggestions can be only made based on previous studies of continuous films.

Step mechanisms were responsible for the morphological changes which occured on the {100} diamond surfaces. Therefore stabilisation of the steps on the <110> directions was achieved using the present oxidation conditions. The rate limiting step for the oxidation of non-stepped {100} diamond surfaces is the adsorption of oxygen onto the C-C partial π-bond.

The {111} diamond surface

The activation energy measured for the {111} CVD diamond surfaces is in accord with the values measured for natural {111} diamond crystals [283, 323] although the appearance of the {111} CVD diamond surfaces after oxidation presents significant differences.

The {111} diamond surfaces were found to be unstable to thermal oxidation; anisotropic etching along steps and terraces created a very rough surface with a high density of etch pits for the whole range of thermal oxidation parameters used in these studies. Upon prolonged exposure to molecular oxygen, the structure breaks up into a rugged surface and {100} diamond facets appeared between the {111} diamond surface. Those observations are in accordance with the work of de Theije *et al* [283] for natural diamond.

The formation of positive etch pits i.e. trigons on the oxidised {111} CVD diamond surfaces has not been observed previously. Prior reports have observed the formation of positive etch pits on natural {111} diamond on the addition of water vapour into the gas mixture [283, 285]. Under these conditions of thermal oxidation a step mechanism was proposed. AFM analysis from the current studies revealed that oxidation of {111} CVD diamond surfaces (with dry O_2) does not proceed via steps or by a layer by layer mechanism.

The present results suggest stabilisation of the {111} diamond surface with oxygen-carbon groups, although an initial H-termination of the as-grown surface would be considered during the final stage of the CVD growth process. Stabilisation of the {111} diamond surface could be achieved with hydroxyl groups. Under such conditions it is known that the surface is stabilised by monovalent –H and –OH groups. In the presence of hydrogen the oxidation would proceed via steps and formation of positive etch pits which was suggested by –C-O-C-O- zigzag chains occuring along the step atoms [283].

Theoretical calculations on the stability of oxygen groups on {111} diamond surfaces, predict the coexistance of stable C-O-C and C-OH groups on the diamond surface [285]. Such a surface would not expected to be stable on removal of CO from the steps, as kinks and terraces would proceed rapidly causing the chemical roughnening of the surface. Present SEM and AFM analysis support the isotropic oxidation of {111} diamond surfaces with dry O_2 and they are in consistent with the reported work [283, 286, 323].

The nuclei for etch pit formation on {111} diamond surfaces have been correlated with surface dislocations on single and natural diamonds [283, 286, 290, 307, 308] and chemical etching is commonly employed to reveal those crystal imperferctions [287, 290, 305, 307]. Thermal oxidation with dry O_2 revealed the formation of positive etch pits preferentially on surface imperfections. As {111} planes exhibit the highest number of surface defects and imperfections in CVD diamond they are therefore expected to have a high etch pit density formation.

The current evidence supports the isotropic etching of {111} diamond surfaces, where etching of carbon atoms proceeds at roughly the same rate from surface steps and terraces, and induce a rough oxidised surface. The formation of well-defined and steep positive etch pits can be attributed to surface dislocations and stabilisation of the steps by –C-O-C- groups.

The {113} diamond surface

The current studies have demonstrated that the {113} diamond planes can be revealed following oxidation from the existing {100} planes by anisotropic etching between {100} and {111} diamond planes. By considering the vertical 2D model of the cross-sections shown in Figure 6.43 and 6.44 and the experimental evidence presented earlier it is apparent that the corner of the {111} and {100} diamond planes intersection would be sensitive to oxidation and gradually expose the {113} planes. The results presented in this thesis illustrate the insight gained when adjoining {111} and {100} diamond planes are both exposed to thermal oxidation. Considering the microscopic view, an explanation is required as to why the outer diamond carbon atoms at the edges of the {100} planes are attacked more rapidly implying a rapid oxidation of {113} surfaces.

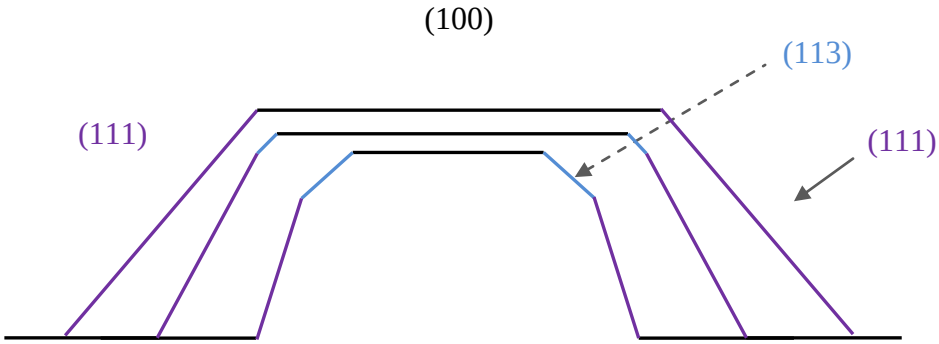

Figure 6.43 Schematic 2D diagram of the cross-section between the {111},{113} and {100} diamond planes with thermal oxidation.

The removal of carbon atoms from the rough {111} diamond planes requires less energy than removal of an atom from the smooth {100} diamond planes. The anisotropy between the etch rates of the {100} and {111} diamond planes, for the conditions examined, was high. The fast removal of the {111} diamond surface would exposed the exterior atoms of the {100} diamond planes at the junction of the planes. Experimental data observation and the large lateral etch rate of {100} diamond surfaces shows that the exposed atoms would oxidise rapidly at these locations.

The stabilisation of the {100} diamond surfaces with oxygen-carbon groups it has been observed and there is evidence that etching proceeds via layer by layer desorption of carbon monoxide from the surface. The oxidation rate on {111} diamond planes is associated with isotropic etching. Based on those observations it can be suggested that

the sides of the {100} diamond surfaces are etched by moving steps created on the {100} sides by the fast etch rate of {111} diamond surface.

A simple two dimensional model of a cubo-octohedral crystallite has been drawn in Figure 6.44 with the intersection of the two major planes. The (100) plane is relatively smooth and etches slowly; the contribution of the vertical etch rate of plane (100) will be ignored in this model. The (111) plane exhibits the greater etch rate and the surface is rougher. Steps sited on {100} diamond surfaces are more active and etching proceeds on those sites, while etching on {111} attacks each individual atom. Removal of atoms from the rough {111} diamond surface will cause the formation of steps at the intersection. If the velocity of those steps is faster than that on the {111} diamond planes, then step movement on {100} surfaces will be achieved. Removal of all steps from the {100} surface would create the initial structure.

The formation and movement of steps creates the faceting of the {100} diamond planes. This model supports the present experimental observations. Bunched-steps have been observed on the exposed {113} diamond with higher density close to the intersection with the {111} diamond surfaces. The orientation of the steps was found to be normal to the sides of the {100} diamond planes, which correspond to the <110> crystal direction. The propagation of those steps was towards the centre of the surface, thus towards the {100} diamond surface.

The generation of steps would depend on, and be close to the etch rate of {111} diamond planes. The angle of the new crystal plane would depend on the ratio of the step height, h, and the step distance, λ, according to:

$$\tan\Theta = \frac{h}{\lambda}$$

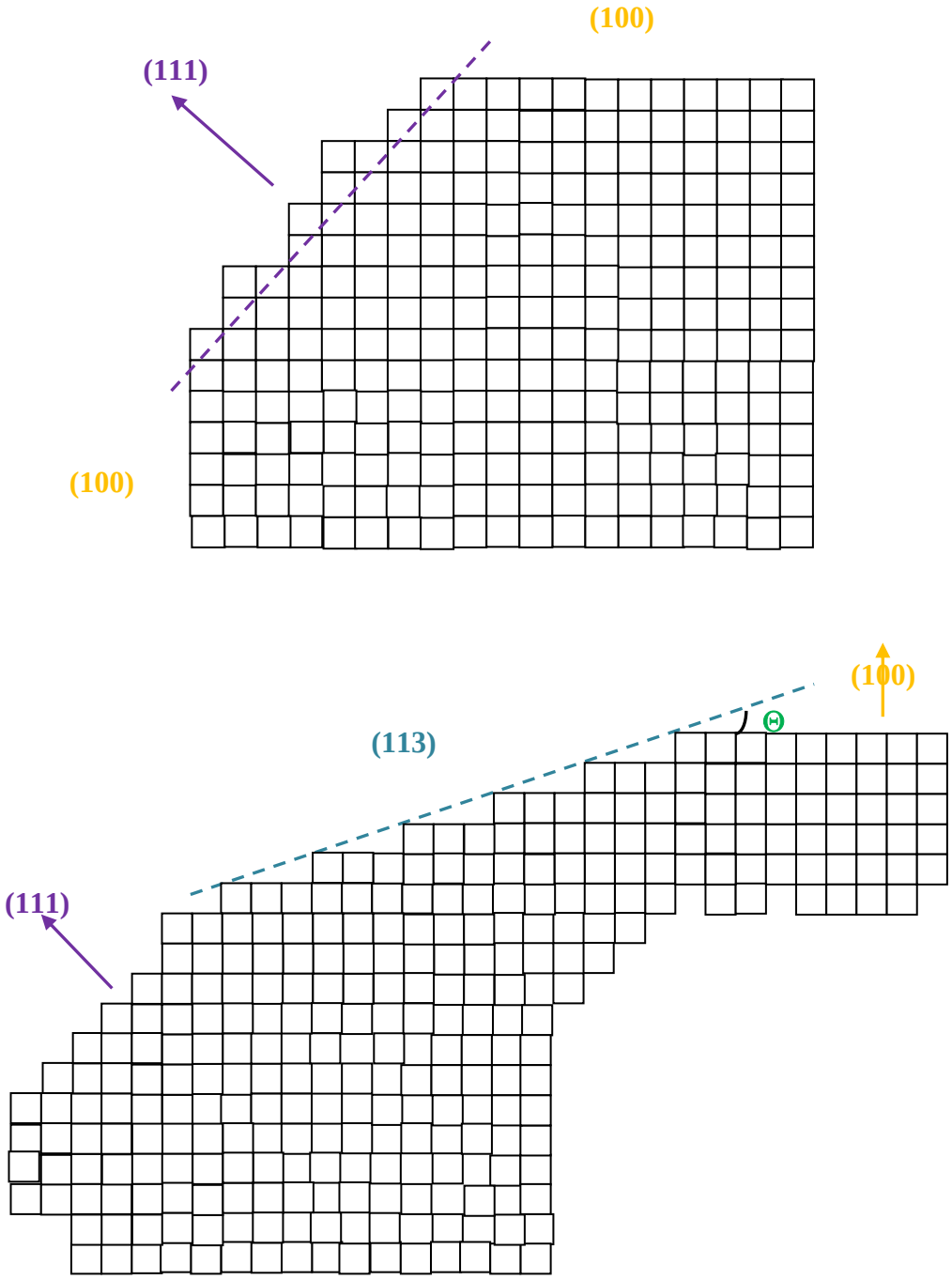

Figure 6.44 Two dimensional schematic of a simple crystal planes produced during etching. Top; The (100) surface is flat and etches slowly while (111) surface etches fast and its rough. Bottom: Anisotropy between etch rates induced by the creation of steps running along the (100) surface.

From SEM observations on the exposed {113} diamond surfaces the step height was measured to have the average value of 72 ± 5 nm and the bunched step separation was measured to 163 ± 4 nm. Using those values in the abovementioned equation the calculated value of the new plane angle was found to be 23.8^{o}. For comparison, the angle between the {100} and the exposed diamond (113) surfaces was measured by optical profilometry to be 26.8 ± 2^{o} for the prolonged oxidised diamond crystallites.

Both measured angle values for the new plane are close to the value predicted by theory of 25. 24^{o} between the {100} and {113} diamond surfaces. Therefore the present results show the exposure of {113} diamond surfaces by the oxidation of carbon at steps on the {100} diamond surfaces induced by the high oxidation rate of {111} diamond surface.

The velocity of the step movement/etching on the {113} diamond surfaces, has been measured to be high. Instability of the surface steps covered with oxygen-carbon groups is low and the oxidation rate is faster than that on {100} diamond surfaces. A slow etching surface would disappear after some time from the crystal and the final crystal facets would only be dominated by fast etching crystallographic planes.

It was mentioned earlier that the generation of steps on {100} diamond planes depends on the oxidation rate of {111} plane and the oxidation anisotropy between the two crystal planes. This statement does not hold true for all the experimental conditions applied here. For example the anisotropy between the etch rates for the{100} and {111} planes is constant between 535^{o}C and 565^{o}C and therefore one would expect the exposure of {113} diamond plane to occur to the same extent for both cases. Experimental observations revealed a different situation; the {113} diamond planes were observed only for oxidation at 565^{o}C after 9 hours of treatment. There was no evidence of the new (113) plane at 535^{o}C. Therefore the exposure of {113} diamond plane is not only effected by the step generation rate along the {100} diamond surface but it is strongly dependent on the reaction kinetics.

The {113} diamond plane has been little explored in the literature as it is one of the diamond planes that rarely survives CVD diamond film growth. Recently Silva and co-workers [345] were able to grow homoepitaxial {113} diamond surfaces through careful selection of growth conditions predicted by a 3-D geometrical model. The {113} diamond faces were stable and slow-growing and it was speculated surface

reconstruction to had taken place during growth. The bulk structure of {113} diamond plane consisted of alternate rows of two-fold coordinated atoms, as in the (100) diamond surface and three-fold coordinated atoms as in (111) surfaces. The structure is presented in Figure 6.43 (top). Possible reconstruction models of the {113} diamond surface have been suggested [339], but, to date, there are no experimental reports of the surface reconstruction of {113} diamond surfaces or the nature of the oxygen-carbon groups on such surfaces.

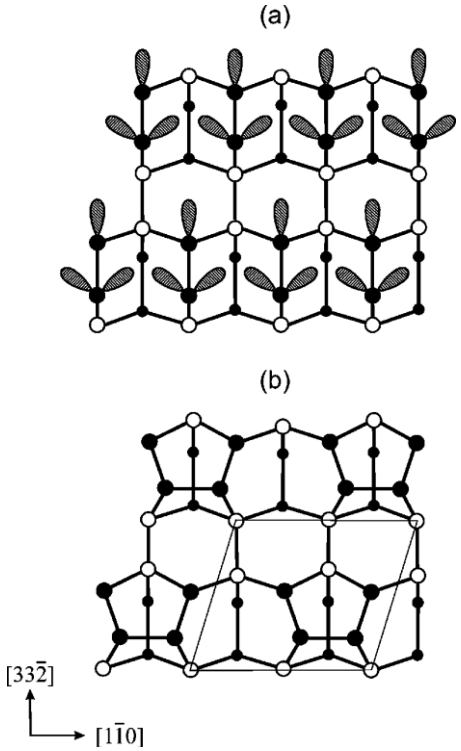

Figure 6.45 a) Schematic plan view of a bulk-terminated (113) diamond surface. The dangling bonds are indicated. b) Top view of a (113) (2x1) surface with symmetric tetramers as reconstruction elements. A possible unit cell is indicated by the thin lines. Filled (open) circles indicate atoms in the top (second) bilayer. Dots represent atoms in the third bilayer [339].

6.7 Conclusions

The rates of dry thermal oxidation of {100} and {111} diamond planes of cubo-octahedral CVD crystallites in O_2 have been measured by optical profilometry for the low temperature regime of 535^{o}C to 600^{o}C. The activation energies of the rate-limited step were determined to be 221 ± 34 kJ mol $^{-1}$ and 286 ± 29 kJ mol $^{-1}$, respectively for the {100} and {111} planes respectively. This is the first report on the reaction order and activation energy of CVD {111} diamond surfaces and complements the data previously reported for {100} surfaces.

Formation of etch pits has been observed on CVD {100} diamond surfaces and oxidation proceed, under these conditions, via a step mechanism. The results presented here are consistent with oxidation mechanism for natural {100} diamond. Isotropic etching of {111} CVD diamond surfaces during oxidation occurs, under the conditions examined, and positive etch pits are preferentially located on surface imperfections. It is the first time well-defined etch pits have been observed on both CVD diamond planes.

The creation of {113} diamond planes has been observed between the two diamond low index planes (100) and (111) upon thermal oxidation. Step propagation along the edges of the {100} diamond surface exposes the {113} diamond plane. It was shown that step generation on the {100} diamond due to high oxidation anisotropy between the {111} and {100} planes is necessary but not directly related to the propagation velocity of the generated steps.

Chapter 7: Conclusions & future work

7.1 Concluding remarks

It has been demonstrated that high quality {100} faceted diamond thin films have been deposited on silicon substrates by microwave plasma chemical vapour deposition. High azimuthal orientated {100} diamond films have been deposited on silicon substrates by applying biased-enhanced nucleation. Atomic force microscopy had shown that on average the as-grown {100} diamond thin film crystallites exhibit a surface roughness of R_a= 3.1 ± 0.1 nm and R_a = 3.3 ± 0.3 nm for the high azimuthal and azimuthally disordered crystallites of the film. The presence of oxygen groups on the as-grown {100} diamond surfaces has been observed by XPS analysis. The surface roughness of the CVD {100} diamond crystallites was reduced upon further exposure to hydrogen microwave plasma, and an average surface roughen of Ra = 0.9 nm has been obtained after 20 hours of hydrogen plasma exposure. Smoothening of the (100} diamond surfaces was not accompanied by surface pitting or etch pit formation. The anisotropy between the etch rate of CVD {100} diamond surfaces and along the <110> directions has both evaluated from AFM topographic analysis. Hydrogen microwave plasma exposure decreases oxygen coverage on the diamond surfaces, and resulted in a oxygen and sp^2 free surface. The electrical conductivity of the {100) diamond films have been found to increase by exposure to hydrogen microwave plasma, subsequently exposure to ambient conditions resulted in a further increase of the surface conductivity.

Etching of {100} diamond films by oxygen reactive ion etching has been demonstrated. Etch rates have been evaluated as a function of oxygen pressure, RF power and gas flow rate. The maximum etch rate measured for {100} highly oriented diamond films was found to be 23 nm min^{-1} at 250W RF power and 20mTorr applied pressure. Etching of diamond films with oxygen reactive ion etching has been accompanied by the formation of columnar structures. Preferential formation of columnar structures has been observed on the intergranular area and {111} diamond facets. Surface roughness of the {100} diamond crystallites increased dramatically due to columnar formation. The reactive ion etched {100} diamond surfaces were found to undergo graphitisation and to contain oxygen groups, as carbonyl and carboxyl. Contamination of the diamond surface with silicon was observed for all the samples etched by oxygen reactive ion etching. The

silicon contamination was found to be preferentially resident on the tip of the columnar structures and to a smaller extent on the surrounding diamond area.

The {111} diamond plane was found to exhibit a higher oxidation rate in respect to the {100} diamond plane for the temperature range of 535^{o}C to 600^{o}C. The activation energies of 221 ± 34 kJ mol $^{-1}$ and 286 ± 29 kJ mol $^{-1}$, have been measured for {100} and {111} diamond planes respectively. Crystal imperfections on both {100} and {111} diamond surfaces were found to be preferentially attacked by thermal oxidation. Etch pit formation accompanied surface morphological changes on both {100} and {111} diamond planes up thermal oxidation exposure. Positive, etch-pits referred as trigons have been observed on oxidised {111} diamond planes. Also the {111} surface undergoes pitting and the surface roughness increased with the duration of thermal oxidation. Two different types of etch pits have been observed on {100} diamond surface, a square-type with sides normal to [110] directions and a hollow-type distributed over the crystallites surface. Although the source of the nuclei for pit formation on {100} diamond surfaces is not clear, lateral step propagation resulted into enlargement of the pits sides and increase of the surface roughness with the duration of thermal oxidation. The diamond {113} plane has been observed to be exposed between the {100} and {111} diamond planes under the present thermal oxidation conditions. Based on experimental observations in has been proposed in these studies that the high anisotropy between the oxidation rates of {100} and {111} diamond planes, induces step propagation on the more oxidation resistant {100} diamond plane. As the step edges would be more reactive than the terraces it was found that step propagation would result in the exposure of the {113} diamond plane.

7.2 Further work

Due to a breakdown on the microwave unit controller of the MPCVD system and insufficient funds to provide a replacement of the vital key components the investigation on hydrogenation and growth of diamond surfaces has stopped.

The production of atomically smooth diamond (100) surfaces which are defect free is a goal which will be required for epitaxial growth of diamond and the utilisation of diamond based devices. In view of the length of time required to attain a roughness commensurate with this aim with a pure hydrogen plasma, it would be worth exploring the possibility of using hydrogen/oxygen plasmas of differing mole ratios and then finally terminating the surface with hydrogen with a pure hydrogen plasma.

The efficiency of the hydrogen and hydrogen/oxygen plasma to remove surface defects from the diamond surfaces can be investigated by employing cathodoluminescence (CL) and photoluminescence (PL) spectroscopies.

One of the major downfalls in the reactive ion etching study of diamond surfaces was the inability to control any residue contamination of the RIE system from previous etching processes. Reduction and control over any residue contamination and induced impurities could be achieved using a RIE system exclusively for etching diamond surfaces or by providing a suitable cleaning procedure of the etching chamber prior to any etching process.

The selective formation of columnar structures on (111) diamond surfaces has been demonstrated to be influenced by the process conditions of the reactive ion etching process. Further investigations are necessary to elucidate the possible mechanism that influence and alters the chemical reactivity between the diamond planes with impurities. Angle resolved XPS spectroscopy would be able to provide information on the surface and in depth distribution of the diamond surfaces upon reactive ion etching. Structural changes upon reactive ion etching could be further investigated by HRTEM as well as the crystal structure of the columnar structures.

Electrical characterisation *in vacuo* and at room conditions would be able to provide crucial information for the possibility of applying the columnar structures for diamond electron emitters and diamond electrodes.

Progress has been made, especially from the analysis of the oxidation of cubo-octahedral crystallites, on the relative thermal oxidation rates of low index planes of diamond. However, further work will be needed to image the respective planes by scanning tunnelling microscopy to observe the formation of atomic steps. In this thesis, studies were made on intrinsic diamond. With the increasing popularity of boron doped diamond as electrodes, it would be informative to study the effect of dopants such as Boron or Nitrogen on the oxidation rates of well characterised planes of diamond. In all these samples, additional work would be required to study the effect of water vapour on the kinetic parameters since previous work on natural single crystal diamond has indicated a change in the mechanism due to the presence of water.

Finally, there remains considerable uncertainty as to the microscopic mechanism of the oxidation of the (111) surface of diamond. The etching proceeds with considerable roughening of the surface even at the earliest stages of oxidation. Techniques would need to be developed to study monolayer oxidation of the (111) surface to be able to observe the movement of the atoms and interaction with molecular oxygen. Investigation of thermal oxidation on an atomically smooth (111) diamond surface by employing scanning tunnelling microscopy would enable to retrieve important information for the oxidation mechanism down to microscopic level.

There are still a large amount of information to be extracted from the (113) diamond surface using STM and other characterisation techniques. Further work on the (113) diamond surface will investigate the surface reconstruction and stability upon oxygen or hydrogen termination, and a clean carbon surface. Growth on (113) diamond surfaces is a possibility, which may open the route to explore new surface phenomena.

References

[1] Balmer, R.S. et al., *Chemical vapour deposition synthetic diamond: materials, technology and applications.* Journal of Physics: Condensed Matter, 2009. **21**(36): p. 364221.

[2] Porro, S., et al., *Nanocrystalline diamond coating of fusion plasma facing components.* Diamond and Related Materials, 2009. **18**(5-8): p. 740-744.

[3] Porro, S., et al., *Effects in CVD diamond exposed to fusion plasmas.* physica status solidi (a), 2009. **206**(9): p. 2028-2032.

[4] Bergonzo, P., et al., *CVD diamond for radiation detection devices.* Diamond and Related Materials, 2001. **10**(3-7): p. 631-638.

[5] Wang, L., et al., *Infrared optical properties of diamond films and electrical properties of CVD diamond detectors.* J. Phys. D: Appl. Phys, 2003. **36**: p. 2548.

[6] Makino, T., et al., *Electrical and optical characterizations of (001)-oriented homoepitaxial diamond p-n junction.* Diamond and Related Materials, 2006. **15**(4-8): p. 513-516.

[7[Spaziani, F., et al., *Optimized spectral collection efficiency obtained in diamond-based ultraviolet detectors using a three-electrode structure.* Applied Physics Letters, 2003. **82**(21): p. 3785-3787.

['8] Teraji, T., et al., *Highly sensitive UV photodetectors fabricated using high-quality single-crystalline CVD diamond films.* Diamond and Related Materials. **13**(4-8): p. 858-862.

[9] Almaviva, S., et al., *Extreme UV photodetectors based on CVD single crystal diamond in a p-type/intrinsic/metal configuration.* Diamond and Related Materials, 2009. **18**(1): p. 101-105.

[10] Borst, T.H., et al, *High-temperature diamond p-n junction: B-doped homoepitaxial layer on N-doped substrate.* Applied Physics Letters, 1995. **67**(18): p. 2651-2653.

[11] Ito, T., et al., *Electron emissions from CVD diamond surfaces.* Diamond and Related Materials, 2003. **12**(3-7): p. 434-441.

[12] Ito, T., et al, *Highly efficient electron emission from diode-type plane emitters using chemical-vapor-deposited single-crystalline diamond.* Applied Physics Letters, 1998. **73**(25): p. 3739-3741.

[13] Wu, E., et al., *Room temperature triggered single-photon source in the near infrared* New Journal of Physics, 2007. **9**: p. 434.

[14] Compton, R.G., et al, *Electroanalysis at Diamond-Like and Doped-Diamond Electrodes.* Electroanalysis, 2003. **15**(17): p. 1349-1363.

[15] Tang, L., et al., *Biocompatibility of chemical-vapour-deposited diamond.* Biomaterials, 1995. **16**(6): p. 483-488.

[16] Fujishima, A., et al, *New directions in structuring and electrochemicalapplications of boron-doped diamond thin films.* Diamond and Related Materials, 2001. **10**(9-10): p. 1799-1803.

[17] Park, J., et al., *Fabrication, characterization, and application of a diamond microelectrode for electrochemical measurement of norepinephrine release from the sympathetic nervous system.* Diamond and Related Materials, 2006. **15**(4-8): p. 761-772.

[18] Troupe, C.E., et al., *Diamond-based glucose sensors.* Diamond and Related Materials, 1998. **7**(2-5): p. 575-580.

[19] Achard, J., et al., *The control of growth parameters in the synthesis of high-quality single crystalline diamond by CVD.* Journal of Crystal Growth, 2005. **284**(3-4): p. 396-405.

[20] Tallaire, A., et al., *Origin of growth defects in CVD diamond epitaxial films.* Diamond and Related Materials, 2008. **17**(1): p. 60-65.

[21] Achard, J., et al., *Identification of etch-pit crystallographic faces induced on diamond surface by H_2/O_2 etching plasma treatment.* physica status solidi (a), 2009. **206**(9): p. 1949-1954.

[22] Tran, D.T., et al., *Microwave plasma-assisted etching of diamond.* Diamond and Related Materials, 2008. **17**(4-5): p. 717-721.

[23] Sirineni, G.M.R., et al., *Reactive ion etching of diamond as a means of enhancing chemically-assisted mechanical polishing efficiency.* Diamond and Related Materials, 1997. **6**(8): p. 952-958.

[24] Cheng, C.Y., et al., *An oxidation enhanced mechanical polishing technique for CVD diamond films.* Diamond and Related Materials, 2005. **14**(3-7): p. 622-625.

[25] Buchkremer-Hermanns, H., et al., *ECR plasma polishing of CVD diamond films.* Diamond and Related Materials, 1996. **5**(6-8): p. 845-849.

[26] Koslowski, B., et al., *Ion polishing of a diamond (100) surface artificially roughened on the nanoscale.* Diamond and Related Materials, 2000. **9**(3-6): p. 1159-1163.

[27] Rawles, R.E., et al., *Mechanism of surface smoothing of diamond by a hydrogen plasma.* Diamond and Related Materials, 1997. **6**(5-7): p. 791-795.

[28] Zheng, X., et al., *Investigation on the etching of thick diamond film and etching as a pretreatment for mechanical polishing.* Diamond and Related Materials, 2007. **16**(8): p. 1500-1509.

[29] Ilias, S., et al., *Planarization of diamond thin film surfaces by ion beam etching at grazing incidence angle.* Diamond and Related Materials, 1996. **5**(6-8): p. 835-839.

[30] Ri, S.-G., et al., *Hydrogen plasma etching mechanism on (0 0 1) diamond.* Journal of Crystal Growth, 2006. **293**(2): p. 311-317.

[31] Ando, Y., et al., *Smooth and high-rate reactive ion etching of diamond.* Diamond and Related Materials. **11**(3-6): p. 824-827.

[32] Silva, F., et al., *3D crystal growth model for understanding the role of plasma pre-treatment on CVD diamond crystal shape.* physica status solidi (a), 2006. **203**(12): p. 3049-3055.

[33] Silva, F., et al., *High quality, large surface area, homoepitaxial MPACVD diamond growth.* Diamond and Related Materials. **18**(5-8): p. 683-697.

[34] Bogdan, G., et al., *Freestanding (100) homoepitaxial CVD diamond.* Diamond and Related Materials, 2006. **15**(4-8): p. 508-512.

[35] Tallaire, A., et al., *Oxygen plasma pre-treatments for high quality homoepitaxial CVD diamond deposition.* physica status solidi (a), 2004. **201**(11): p. 2419-2424.

[36] Rezek, B. et al, *Electronic properties of plasma hydrogenated diamond surfaces: A microscopic study.* Diamond and Related Materials, 2006. **15**(9): p. 1374-1377.

[37] Ostrovskaya, L., et al., *Wettability and surface energy of oxidized and hydrogen plasma-treated diamond films.* Diamond and Related Materials, 2002. **11**(3-6): p. 845-850.

[38] Pietzka, C., et al., *Electronic surface barrier properties of boron-doped diamond oxidized by plasma treatment.* Diamond and Related Materials, 2010. **19**(2-3): p. 213-216.

[39] Salvadori, M.C., et al., *Termination of diamond surfaces with hydrogen, oxygen and fluorine using a small, simple plasma gun.* Diamond and Related Materials. **19**(4): p. 324-328.

[40] Landstrass, M.I. et al., *Resistivity of chemical vapor deposited diamond films.* Applied Physics Letters, 1989. **55**(10): p. 975-977.

[41] Baumann, P.K. et al., *Negative electron affinity effects on H plasma exposed diamond (100) surfaces.* Diamond and Related Materials, 1995. **4**(5-6): p. 802-805.

[42] Nebel, C.E., et al., *Low temperature properties of the p-type surface conductivity of diamond.* Diamond and Related Materials, 2002. **11**(3-6): p. 351-354.

[43] Ristein, J., et al., *Diamond surface conductivity experiments and photoelectron spectroscopy.* Diamond and Related Materials, 2001. **10**(3-7): p. 416-422.

[44] Maier, F., et al., *Origin of Surface Conductivity in Diamond.* Physical Review Letters, 2000. **85**(16): p. 3472.

[45] Foord, J.S., et al, *An investigation of the surface reactivity of diamond photocathodes with molecular and atomic oxygen species.* Diamond and Related Materials, 2001. **10**(3-7): p. 710-714.

[46] Shirafuji, J. et al, *Electrical properties of diamond surfaces.* Diamond and Related Materials, 1996. **5**(6-8): p. 706-713.

[47] Foord, J.S., et al., *Influence of the environment on the surface conductivity of chemical vapor deposition diamond.* Diamond and Related Materials, 2002. **11**(3-6): p. 856-860.

[48] Yamada, T., et al, *Electron emission from hydrogenated and oxidized heteroepitaxial diamond doped with boron.* Diamond and Related Materials, 2002. **11**(3-6): p. 780-783.

[49] Saby, C. et al, *Photoelectron spectroscopy of boron-doped homoepitaxial diamond (100) surfaces with several terminations and related Schottky barriers.* Diamond and Related Materials. **11**(3-6): p. 851-855.

[50] Boukherroub, R., et al., *Photochemical oxidation of hydrogenated boron-doped diamond surfaces.* Electrochemistry Communications, 2005. **7**(9): p. 937-940.

[51] Notsu, H., et al., *Introduction of Oxygen-Containing Functional Groups onto Diamond Electrode Surfaces by Oxygen Plasma and Anodic Polarization.* Electrochemical and Solid-State Letters, 1999. **2**(10): p. 522-524.

[52] Yagi, I., et al., *Electrochemical selectivity for redox systems at oxygen-terminated diamond electrodes.* Journal of Electroanalytical Chemistry, 1999. **473**(1-2): p. 173-178.

[53] Pehrsson, P.E. et al, *Oxidation of the hydrogenated diamond (100) surface.* Surface Science, 2000. **460**(1-3): p. 49-66.

[54] Ando, T., et al., *Vapour-phase oxidation of diamond surfaces in O_2 studied by diffuse reflectance Fourier-transform infrared and temperture-programmed desorption spectroscopy.* J. Chem. Soc., Faraday Trans., 1993. **89**: p. 3635 - 3640,.

[55] Goeting, C.H., et al., *Electrochemically induced surface modifications of boron-doped diamond electrodes: an X-ray photoelectron spectroscopy study.* Diamond and Related Materials, 2000. **9**(3-6): p. 390-396.

[56] Notsu, H., et al., *Hydroxyl Groups on Boron-Doped Diamond Electrodes and Their Modification with a Silane Coupling Agent.* Electrochemical and Solid-State Letters, 2001. **4**(3): p. H1-H3.

[57] Kanazawa, H., et al., *Effect of iodide ions on the hydrogen-terminated and partially oxygen-terminated diamond surface.* Diamond and Related Materials, 2003. **12**(3-7): p. 618-622.

[58] Riedel, M., et al, *The impact of ozone on the surface conductivity of single crystal diamond.* Diamond and Related Materials, 2004. **13**(4-8): p. 746-750.

[59] Greenwood N.N., *Chemistry of the Elements Second Edittion*. 1997.

[60] Pierson, H.O., *Handbook of Carbon, Graphite, Diamond and Fullerenes.* 1993.

[61] Wolf, E.I., *Nanophysics and Nannotechnology: An introduction to Modern Concepts in Nanoscience, Second Ediition.* 2006.

[62] Spear, K.E. et al., *Synthetic diamond :emerging CVD science and technology.* 1994.

[63] Pierson, H.O., *Handbook of Chemical Vapor Deposition, Technology and Applications*. 2nd Edition ed. Materials Science and Process Technology. 2000, New York: William Andrew Publishing.

[64] Bundy, F., *The P, T Phase and Reaction Diagram for Elemental Carbon.* J. Geophys. Res., 1980. **85**(B12): p. 6930-6936.

[65] Liander, H. et al., *Artificial diamonds.* ASEA journal, 1955. **28**: p. 97.

[66] Bundy, F.P. et al., *Man-made diamonds,* Nature. 1955. 176: p. 51.

[67] Choudhary, D. et al., *Manufacture of gem quality diamonds: a review.* Ceramics International, 2000. **26**(1): p. 73-85.

[68] Field, J.D., *The properties of natural and synthetic diamond.* 1992.

[69] Eversole, W.G., *US Pat.* 3 030 187 and 3 030 188, 1958.

[70] Derjaguin, B.V., et al., *Filamentary diamond crystals.* Journal of Crystal Growth, 1968. **2**(6): p. 380-384.

[71] Angus, J.C., et al., *Growth of Diamond Seed Crystals by Vapor Deposition.* Journal of Applied Physics, 1968. **39**(6): p. 2915-2922.

[72] Poferl, D.J., et al., *Growth of boron-doped diamond seed crystals by vapor deposition.* Journal of Applied Physics, 1973. **44**(4): p. 1428-1434.

[73] Spitsyn, B.V.,et al., *Vapor growth of diamond on diamond and other surfaces.* Journal of Crystal Growth, 1981. **52**(Part 1): p. 219-226.

[74] Matsumoto, S., et al., *Growth of diamond particles from methane-hydrogen gas.* Journal of Materials Science, 1982. **17**(11): p. 3106-3112.

[75] Kamo, M., et al., *Diamond synthesis from gas phase in microwave plasma.* Journal of Crystal Growth, 1983. **62**(3): p. 642-644.

[76] Matsumoto, S., et al., *Vapor Deposition of Diamond Particles from Methane.* Jpn. J. Appl. Phys., 1982. **21**: p. L183.

[77] Li, D.M., et al., *Diamond deposition by coiled and grid filaments using high methane concentrations.* Diamond and Related Materials, 1996. **5**(3-5): p. 350-353.

[78] Griesser, M., et al., *Characterization of tantalum impurities in hot-filament diamond layers.* Diamond and Related Materials, 1994. **3**(4-6): p. 638-644.

[79] Kurihara, K., et al., *High rate synthesis of diamond by dc plasma jet chemical vapor deposition.* Applied Physics Letters, 1988. **52**(6): p. 437-438.

[80] Hsu, W.L., *Gas-phase kinetics during microwave plasma-assisted diamond deposition: Is the hydrocarbon product distribution dictated by neutral-neutral interactions?* Journal of Applied Physics, 1992. **72**(7): p. 3102-3109.

[81] Funer, M., et al., *Novel microwave plasma reactor for diamond synthesis.* Applied Physics Letters, 1998. **72**(10): p. 1149-1151.

[82] Bachmann, P.K., et al., *Post-depositional diamond etching.* Diamond and Related Materials, 1993. **2**(5-7): p. 683-693.

[83] Liang, Q., et al., *Recent advances in high-growth rate single-crystal CVD diamond.* Diamond and Related Materials, 2009. **18**(5-8):p. 698-703.

[84] Goodwin , D.G. et al. *Theory of Diamond Chemical Vapour Deposition*, in *Handbook of Industrial Diamonds and Diamond Films,*, G.P. in: M.A. Prelas, L.K. Bigelow (Eds.),, Editor. 1998, Marcel Dekker,: New York. p. 527-581.

[85] McMaster, M.C., et al., *Dependence of the gas composition in a microwave plasma-assisted diamond chemical vapor deposition reactor on the inlet carbon source: CH_4 versus C_2H_2.* Diamond and Related Materials, 1995. **4**(7): p. 1000-1008.

[86] Ma, J., et al., *Quantum cascade laser investigations of CH_4 and C_2H_2 interconversion in hydrocarbon/H_2 gas mixtures during microwave plasma enhanced chemical vapor deposition of diamond.* Journal of Applied Physics, 2009. **106**(3): p. 033305.

[87] Rego, C.A., et al., *In-situ mass spectrometric study of the gas-phase species involved in CVD of diamond as a function of filament temperature.* Diamond and Related Materials, 1995. **4**(5-6): p. 770-774.

[88] Leeds, S.M., et al., *Molecular beam mass spectrometry studies of the gas-phase chemistry occurring during microwave plasma assisted chemical vapour deposition of diamond.* Diamond and Related Materials, 1999. **8**(8-9): p. 1377-1382.

[89] Tang, C.J., et al., *Effect of nitrogen and oxygen addition on morphology and texture of diamond films (from polycrystalline to nanocrystalline).* Diamond and Related Materials, 2008. **17**(1): p. 72-78.

[90] Tang, C.J., et al., *Study the effect of O_2 addition on hydrogen incorporation in CVD diamond.* Diamond and Related Materials, 2004. **13**(1): p. 203-208.

[91] Chein, T.-H., et al., *Synthesis of diamond in high power-density microwave methane/hydrogen/oxygen plasmas at elevated substrate temperatures.* Diamond and Related Materials, 1999. **8**(8-9): p. 1686-1696.

[92] Mollart, T.P. et al., *Optical-quality diamond growth from CO_2-containing gas chemistries.* Diamond and Related Materials, 1999. **8**(2-5): p. 236-241.

[93] Ruan, J., et al., *Effect of oxygen on boron doping in chemical vapor deposition of diamond as deduced from cathodoluminescence studies.* Applied Physics Letters, 1992. **60**(15): p. 1884-1886.

[94] Bachmann , P.K., *Microwave chemical vapour of diamond,* in *Handbook of Industrial Diamond,* M.P.e. al, Editor. 1997. p. 821-850.

[95] Hong, F.C.-N., et al., *Low-temperature deposition of diamond using chloromethane in a hot-filament chemical vapor deposition reactor.* Diamond and Related Materials, 1993. **2**(2-4): p. 365-372.

[96] Silva, V.A., et al., *Influence of CF_4 addition for HFCVD diamond growth on silicon nitride substrates.* Diamond and Related Materials, 2001. **10**(11): p. 2002-2009.

[97] Schmidt, I. et al , *Using fluorine and chlorine in the diamond CVD process.* Diamond and Related Materials, 1999. **8**(2-5): p. 231-235.

[98] Liu, Z.-J., et al., *Effects of fluorine addition on driving force for CVD diamond growth.* Thin Solid Films, 2000. **368**(2): p. 208-210.

[99] Muller-Sebert, W., et al., *Nitrogen induced increase of growth rate in chemical vapor deposition of diamond.* Applied Physics Letters, 1996. **68**(6): p. 759-760.

[100] Cao, G.Z., et al., *Growth of {100} textured diamond films by the addition of nitrogen.* Journal of Applied Physics, 1996. **79**(3): p. 1357-1364.

[101] Asmussen, J., et al., *The effect of nitrogen on the growth, morphology, and crystalline quality of MPACVD diamond films.* Diamond and Related Materials, 1999. **8**(2-5): p. 220-225.

[102] Jackson, K., et al, *Donor levels and impurity-atom relaxation in nitrogen- and phosphorus-doped diamond.* Physical Review B, 1990. **41**(18): p. 12641.

[103] Koizumi, S., et al., *Growth and characterization of phosphorous doped {111} homoepitaxial diamond thin films.* Applied Physics Letters, 1997. **71**(8): p. 1065-1067.

[104] Flemish, J.R., et al., *Growth and characterization of phosphorus doped diamond films.* Diamond and Related Materials, 1994. **3**(4-6): p. 672-676.

[105] Kato, H., et al., *N-type doping on (001)-oriented diamond.* Diamond and Related Materials, 2006. **15**(4-8): p. 548-553.

[106] Locher, R., et al., *Optical and electrical characterization of boron-doped diamond films.* Diamond and Related Materials, 1995. **4**(5-6): p. 678-683.

[107] Lee, B.-J., et al., *Variations of morphology and electrical property of diamond with doping using diborane in a methane-hydrogen gas mixture.* Diamond and Related Materials, 1999. **8**(2-5): p. 251-256.

[108] Tsubota, T., et al., *Surface morphology and electrical properties of boron-doped diamond films synthesized by microwave-assisted chemical vapor deposition using trimethylboron on diamond (100) substrate.* Diamond and Related Materials, 2000. **9**(7): p. 1362-1368.

[109] Maeda, H., et al., *Growth behavior of boron-doped diamond in microwave plasma-assisted chemical vapor deposition using trimethylboron as the dopant source.* Diamond and Related Materials, 1998. **7**(1): p. 88-95.

[110] Fontaine, F., et al., *Boron implantation/in situ annealing procedure for optimal p -type properties of diamond.* Applied Physics Letters, 1996. **68**(16): p. 2264-2266.

[111] Kalish, R., et al., *Doping of polycrystalline diamond by boron ion implantation.* Applied Physics Letters, 1994. **64**(19): p. 2532-2534.

[112] Butler, J.E., et al., *Thin Film Diamond Growth Mechanisms [and Comment]*. Philosophical Transactions of the Royal Society of London. Series A: Physical and Engineering Sciences, 1993. **342**(1664): p. 209-224.

[113] Sque, S.J., *A First-Principles Study on Bulk and Transfer Doping of Diamond*. 2005, PhD Thesis, University of Exeter: Exeter.

[114] Hamza, A.V., et al., *Hydrogen chemisorption and the structure of the diamond C(100)-(2 × 1) surface.* Surface Science, 1990. **237**(1-3): p. 35-52.

[115] Tsuno, T., et al., *Epitaxially Grown Diamond (001) 2x1/1x2 Surface Investigated by Scanning Tunneling Microscopy in Air.* Jpn. J. Appl. Phys., 1991. **30**(1).

[116] Kawarada, H., et al, *Scanning-tunneling-microscope observation of the homoepitaxial diamond (001) 2 x 1 reconstruction observed under atmospheric pressure.* Physical Review B, 1995. **52**(15): p. 11351.

[117] Stallcup II, R.E., et al. *Atomic structure of the diamond (100) surface studied using scanning tunneling microscopy*. 1996: AVS.

[118] Mehandru, S.P. et al, *Adsorption of H, CH_3, CH_2 and C_2H_2 on 2×1 restructured diamond (100): Theoretical study of structures, bonding, and migration.* Surface Science, 1991. **248**(3): p. 369-381.

[119] Yang, S.H., et al, *Ab initio study of diamond C(100) surfaces.* Physical Review B, 1993. **48**(8): p. 5261.

[120] Yu, Y., et al., *Ab initio structural characterization of a hydrogen-covered diamond (001) surface.* Physical Review B, 2004. **70**(12): p. 125423.

[121] Thoms, B.D. et al, *HREELS and LEED of H/C(100): the 2 × 1 monohydride dimer row reconstruction.* Surface Science, 1995. **328**(3): p. 291-301.

[122] Butler, J.E. et al., *Understanding the chemical vapor deposition of diamond: recent progress.* Journal of Physics: Condensed Matter, 2009. **21**(36): p. 364201.

[123] Hukka, T.I.,et al., *Chemisorption of Hydrogen on the Diamond (100)2 .times. 1 Surface: An ab Initio Study.* The Journal of Physical Chemistry, 1994. **98**(47): p. 12420-12430.

[124] Furthmüller, J., et al., *Structural and Electronic Properties of Clean and Hydrogenated Diamond (100) Surfaces* Europhysics Letters, 1994. **28**(9): p. 659.

[125] Battaile, C.C., et al., *Atomic-scale simulations of chemical vapor deposition onflat and vicinal diamond substrates.* Journal of Crystal Growth, 1998. **194**(3-4): p. 353-368.

[126]. Davidson, B.N. et al., *Tight-binding study of hydrogen on the C(111), C(100), and C(110) diamond surfaces.* Physical Review B, 1994. **49**(16): p. 11253.

[127] Horner, D.A., et al., *A theoretical study of the energetics of insertion of dicarbon (C_2) and vinylidene into methane C---H bonds.* Chemical Physics Letters, 1995. **233**(3): p. 243-248.

[128] Pandey, K.C., *New dimerized-chain model for the reconstruction of the diamond (111)-(2 x 1) surface.* Physical Review B, 1982. **25**(6): p. 4338.

[129] Chin, R.P., et al., *Interaction of atomic hydrogen with the diamond C(111) surface studied by infrared-visible sum-frequency-generation spectroscopy.* Physical Review B, 1995. **52**(8): p. 5985.

[130] Cheng, C.-L., et al., *The absolute absorption strength and vibrational coupling of CH stretching on diamond C(111).* The Journal of Chemical Physics, 1997. **106**(17): p. 7411-7421.

[131] Butler, J.E. et al., *A mechanism for crystal twinning in the growth of diamond by chemical vapour deposition.* Philosophical Transactions of the Royal Society A: Mathematical, Physical and Engineering Sciences, 2008. **366**(1863): p. 295-311.

[132] Harris, S.J., *Mechanism for diamond growth from methyl radicals.* Applied Physics Letters, 1990. **56**(23): p. 2298-2300.

[133] Frenklach, M. et al., E, *Growth mechanism of vapor deposited diamond.* J. Mater. Res, 1988. **3**: p. 133.

[134] Belton, D.N.et al., *A mechanism for growth on diamond (110) from acetylene.* The Journal of Chemical Physics, 1992. **96**(3): p. 2371-2377.

[135] Harris, S.J. et al., *Methyl versus acetylene as diamond growth species.* J. Mater. Res., 1991. **5**: p. 2313.

[136] Frenklach, M. et al, *Detailed surface and gas-phase chemical kinetics of diamond deposition.* Physical Review B, 1991. **43**(2): p. 1520.

[137] Garrison, B., et al., *Molecular dynamics simulations of dimer opening on a diamond (001) (2x1) surface.* Science, 1992. **255**: p. 835-838.

[138] Cheesman, A., et al., *Studies of Carbon Incorporation on the Diamond {100} Surface during Chemical Vapor Deposition using Density Functional Theory.* The Journal of Physical Chemistry A, 2008. **112**(45): p. 11436-11448.

[139] Battaile, C.C., et al., *A kinetic Monte Carlo method for the atomic-scale simulation of chemical vapor deposition: Application to diamond.* Journal of Applied Physics, 1997. **82**(12): p. 6293-6300.

[140] Harris, S.J. et al., *Growth on the reconstructed diamond (100) surface.* The Journal of Physical Chemistry, 1993. **97**(1): p. 23-28.

[141] Frenklach, M. et al., *Surface Migration in Diamond Growth.* The Journal of Physical Chemistry B, 1997. **101**(16): p. 3025-3036.

[142] Netto, A.et al., *Kinetic Monte Carlo simulations of CVD diamond growth--Interlay among growth, etching, and migration.* Diamond and Related Materials, 2005. **14**(10): p. 1630-1646.

[143] Lee, N. et al., *Effect of misorientation angles on the surface morphologies of (001) homoepitaxial diamond thin films.* Applied Physics Letters, 1995. **66**(17): p. 2203-2205.

[144] May, P.W., et al., *Simplified Monte Carlo simulations of chemical vapour deposition diamond growth.* Journal of Physics Condensed Matter, 2009. **21**: p. 364203.

[145] Skokov, S., et al., *Elementary Reaction Mechanism for Growth of Diamond (100) Surfaces from Methyl Radicals.* The Journal of Physical Chemistry, 1994. **98**(28): p. 7073-7082.

[146] Battaile, C.C., et al., *Etching effects during the chemical vapor deposition of (100) diamond.* The Journal of Chemical Physics, 1999. **111**(9): p. 4291-4299.

[147] Skokov, S., et al., *Chemistry of Acetylene on Diamond (100) Surfaces.* The Journal of Physical Chemistry, 1995. **99**(15): p. 5616-5625.

[148] May, P.W., et al., *Simulations of polycrystalline CVD diamond film growth using a simplified Monte Carlo model.* Diamond and Related Materials, 2010. **19**(5-6): p. 389-396.

[149] Mankelevich, Y.A. et al., *New insights into the mechanism of CVD diamond growth: Single crystal diamond in MW PECVD reactors.* Diamond and Related Materials, 2008. **17**(7-10): p. 1021-1028.

[150] May, P.W., et al., *Microcrystalline, nanocrystalline, and ultrananocrystalline diamond chemical vapor deposition: Experiment and modeling of the factors controlling growth rate, nucleation, and crystal size.* Journal of Applied Physics, 2007. **101**(5): p. 053115.

[151] May, P.W. et al., *From Ultrananocrystalline Diamond to Single Crystal Diamond Growth in Hot Filament and Microwave Plasma-Enhanced CVD Reactors: a Unified Model for Growth Rates and Grain Sizes.* The Journal of Physical Chemistry C, 2008. **112**(32): p. 12432-12441.

[152] Tsuda, M., et al., *Epitaxial growth mechanism of diamond crystal in methane-hydrogen plasma.* Journal of the American Chemical Society, 1986. **108**(19): p. 5780-5783.

[153] Huang, D.et al., *Potential energy calculations of diamond growth by methyl radicals.* The Journal of Physical Chemistry, 1991. **95**(9): p. 3692-3695.

[154] Larsson, K. et al., *Incorporation of C into Growth Steps of Diamond (111).* physica status solidi (a), 2001. **186**(2): p. 319-330.

[155] Larsson, K.,et al., *Adsorption of hydrocarbon species on a stepped diamond (111) surface.* Physical Review B, 1997. **56**(23): p. 15452.

[156] Battaile, C.C., et al., *Morphologies of diamond films from atomic-scale simulations of chemical vapor deposition.* Diamond and Related Materials, 1997. **6**(9): p. 1198-1206.

[157] Dischler, B. et al., *Low-pressure synthetic diamond: Manufacturing and applications*. 1998: Springer.

[158] Van der Drift.A, Phillips Res. Rep, 1967. **22**: p. 267.

[159] Wild, C., et al., *Oriented CVD diamond films: twin formation, structure and morphology.* Diamond and Related Materials, 1994. **3**(4-6): p. 373-381.

[160] Wild, C., et al., *Chemical vapour deposition and characterization of smooth {100}-faceted diamond films.* Diamond and Related Materials, 1993. **2**(2-4): p. 158-168.

[161] Popovici, G.et al, *Nucleation and Selective Deposition of Diamond Thin Films.* physica status solidi (a), 1992. **132**(2): p. 233-252.

[162] Sawabe, A. et al., *Growth of diamond thin films by electron-assisted chemical vapour deposition and their characterization.* Thin Solid Films, 1986. **137**(1): p. 89-99.

[163] Stoner, B.R., et al., *Highly oriented, textured diamond films on silicon via bias-enhanced nucleation and textured growth.* J. Mater. Res., 1993. **8**(6): p. 1334 1340.

[164] John, P., et al., *The growth of (100) orientated diamond films.* Diamond and Related Materials, 1994. **3**(4-6): p. 388-392.

[165] John, P., et al., *An FTIR study of the heteroepitaxy of diamond on silicon.* Diamond and Related Materials, 1996. **5**(3-5): p. 256-260.

[166] Kulisch, W., et al., *On the Mechanisms of Bias Enhanced Nucleation of Diamond.* physica status solidi (a), 1996. **154**(1): p. 155-174.

[167] Jiang, X.et al. *Recent Developments in Heteroepitaxial Nucleation and Growth of Diamond on Silicon.* physica status solidi (a), 1996. **154**(1): p. 175-183.

[168] Jubber, M.G., et al., *Design of a UHV reactor for microwave plasma deposition of diamond films.* Vacuum, 1994. **45**(5): p. 499-506.

[169] Schreck, M., et al., *Structural characterization of diamond films grown epitaxially on silicon.* Diamond and Related Materials, 1994. **3**(4-6): p. 510-514.

[170] Potts, P.J., *A Handbook of Silicate Rock Analysis*. 1987: Blackee.

[171] Dore, P., et al., *Infrared Properties of Chemical-Vapor Deposition Polycrystalline Diamond Windows.* Appl. Opt., 1998. **37**(24): p. 5731-5736.

[172] Anzai, T., et al., *Vibrational sum-frequency generation spectroscopy of a homoepitaxially-grown diamond C(100) surface.* Journal of Molecular Structure, 1995. **352-353**: p. 455-463.

[173] Chin, R.P. and et al., *Anharmonicity and Lifetime of the CH Stretch Mode on Diamond H/C(111)-(1 Ã— 1).* EPL (Europhysics Letters), 1995. **30**(7): p. 399.

[174] Dischler, B., et al., *Hydrogen in polycrystalline diamond: An infrared analysis.* Physica B: Condensed Matter, 1993. **185**(1-4): p. 217-221.

[175] McNamara, K.M., et al., *Identification of defects and impurities in chemical-vapor-deposited diamond through infrared spectroscopy.* Journal of Applied Physics, 1994. **76**(4): p. 2466-2472.

[176] Titus, E., et al., *Quantitative analysis of hydrogen in chemical vapor deposited diamond films.* Diamond and Related Materials. **14**(3-7): p. 476-481.

[177] Bachmann, P.K., et al., *Influence of surface modifications on the electronic properties of CVD diamond films.* Diamond and Related Materials, 1996. **5**(11): p. 1378-1383.

[178] Lee, J.-K., et al., *Oxidation of CVD diamond powders.* Diamond and Related Materials. **13**(4-8): p. 1070-1074.

[179] Okushi, H., et al., *Device-grade homoepitaxial diamond film growth.* Journal of Crystal Growth, 2002. **237-239**(Part 2): p. 1269-1276.

[180] Vouagner, D., et al., *Photoemission properties and hydrogen surface coverage of CVD diamond films.* Diamond and Related Materials. **13**(4-8): p. 969-974.

[181] Takeuchi D., et al., *Recovery of negative electron affinity by annealing on (111) oxidized diamond surfaces*, Diamond and Related Materials, 18 (2-3) :p 206-209

[182] Banno, T., et al., *Fabrication of diamond single-hole transistors using AFM anodization process.* Diamond and Related Materials. **11**(3-6): p. 387-391.

[183] Tachiki, M., et al., *Fabrication of single-hole transistors on hydrogenated diamond surface using atomic force microscope.* Applied Physics Letters, 2002. **81**(15): p. 2854-2856.

[184] Rezek, B. et al., *Hydrogenated diamond surfaces studied by atomic and Kelvin force microscopy*. Diamond and Related Materials, 2004. **13**(4-8): p. 740-745.

[185] Hayashi, K., et al., *Atomic force microscopy study of atomically flat (001) diamond surfaces treated with hydrogen plasma.* Applied Surface Science, 1998. **125**(1): p. 120-124.

[186] Wang, Y.M., et al., *Surface structure of C(100)-(2x1)-H studied by a quantitative LEED analysis.* Physical Review B, 1999. **59**(15): p. 10347.

[187] Thoms, B.D., et al., *Production and characterization of smooth, hydrogen-terminated diamond C(100).* Applied Physics Letters, 1994. **65**(23): p. 2957-2959.

[188] Nützenadel, C., et al., *STM investigations with atomic resolution on the (2 × 1) monohydride natural doped diamond (100) surface.* Surface Science, 1996. **369**(1-3): p. L111-L116.

[189] Küttel, O.M., et al., *The preparation and characterization of low surface roughness (111) and (100) natural diamonds by hydrogen plasma.* Surface Science, 1995. **337**(1-2): p. L812-L818.

[190]. Koslowski, B., et al., *On the roughness of hydrogen-plasma treated diamond(100) surfaces.* Diamond and Related Materials, 1998. **7**(2-5): p. 322-326.

[191] Koslowski, B., et al., *Roughness transitions of diamond(100) induced by hydrogen-plasma treatment.* Applied Physics A: Materials Science & Processing, 1998. **66**(0): p. 1159-1163.

[192] Lee, N. et al., *A study on surface morphologies of (001) homoepitaxial diamond films.* Diamond and Related Materials, 1997. **6**(1): p. 130-145.

[193] Yamazaki, Y., et al., *Structural change in diamond by hydrogen plasma treatment at room temperature.* Diamond and Related Materials, 2005. **14**(11-12): p. 1939-1942.

[194] Bobrov, K., et al., *Atomic-scale desorption of hydrogen from hydrogenated diamond surfaces using the STM.* Surface Science, 2003. **528**(1-3): p. 138-143.

[195] Fitzgerald, A.G., et al., *Characterization of the surface morphology and electronic properties of microwave enhanced chemical vapor deposited diamond films.* Journal of Vacuum Science & Technology B: Microelectronics and Nanometer Structures, 2000. **18**(6): p. 2714-2721.

[196] Cheng, C.L., et al., *Direct Observation of Hydrogen Etching Anisotropy on Diamond Single Crystal Surfaces.* Physical Review Letters, 1997. **78**(19): p. 3713.

[197] Stallcup, R.E. et al., *Scanning Tunneling Microscopy Studies of Temperature-Dependent Etching of Diamond (100) by Atomic Hydrogen.* Physical Review Letters, 2001. **86**(15): p. 3368.

[198] Stallcup Ii, R.E., et al., *Formation of nanometer-size high-density pits on epitaxial diamond (100) films.* Diamond and Related Materials, 2007. **16**(9): p. 1727-1731.

[199] Uchida, N., et al., *Hydrogen post-etching effect on CVD diamond films.* Journal of Materials Science Letters 1990. **9**: p. 251-252.

[200] Mercer, T.W., et al., *The effect of a hydrogen plasma on the diamond (110) surface.* Surface Science, 1997. **392**(1-3): p. L21-L26.

[201] Oleinik, I.I., et al., *Theoretical study of chemical reactions on CVD diamond surfaces.* Diamond and Related Materials, 2000. **9**(3-6): p. 241-245.

[202] Bobrov, K., et al., *Atomic-scale visualization and surface electronic structure of the hydrogenated diamond C(100)-(2x1):H surface.* Physical Review B, 2003. **68**(19): p. 195416.

[203] Graupner, R., et al., *High-resolution surface-sensitive C 1s core-level spectra of clean and hydrogen-terminated diamond (100) and (111) surfaces.* Physical Review B, 1998. **57**(19): p. 12397.

[204] Sandhu, G.S. et al., *Reactive ion etching of diamond.* Applied Physics Letters, 1989. **55**(5): p. 437-438.

[205] Kanai, C., et al., *Ab initio calculations on etching of graphite and diamond surfaces by atomic hydrogen.* Physical Review B, 2001. **63**(23): p. 235311.

[206] Lafosse, A., et al., *Surface defects induced by in-situ annealing of hydrogenated polycrystalline diamond studied by high resolution electron energy loss spectroscopy.* Diamond and Related Materials, 2008. **17**(6): p. 949-953.

[207] Bello, I., et al., *Effects at reactive ion etching of CVD diamond.* Thin Solid Films, 2000. **368**(2): p. 222-226.

[208] Zhang, W.J., et al., *Bias-assisted etching of polycrystalline diamond films in hydrogen, oxygen, and argon microwave plasmas.* Journal of Vacuum Science & Technology A: Vacuum, Surfaces, and Films, 1999. **17**(3): p. 763-767.

[209] Stoner, B.R., et al., *Bias assisted etching of diamond in a conventional chemical vapor deposition reactor.* Applied Physics Letters, 1993. **62**(15): p. 1803-1805.

[210] Zhang, W.J., et al., *Structuring single- and nano-crystalline diamond cones.* Diamond and Related Materials, 2004. **13**(4-8): p. 1037-1043.

[211] Zhang, W.J., et al., *Structuring nanodiamond cone arrays for improved field emission.* Applied Physics Letters, 2003. **83**(16): p. 3365-3367.

[212] Jiang, X., et al., *Effects of ion bombardment on the nucleation and growth of diamond films.* Physical Review B, 1998. **58**(11): p. 7064.

[213] Kobashi, K., et al., *Formation of fibrous structures on diamond by hydrogen plasma treatment under DC bias.* Diamond and Related Materials, 2001. **10**(11): p. 2039-2043.

[214] Ando, Y., et al, *Nano-rods' of single crystalline diamond.* Diamond and Related Materials. **13**(4-8): p. 633-637.

[215] Jiang, X. et al., *Defect examination of diamond crystals by surface hydrogen-plasma etching.* Applied Physics Letters, 1999. **75**(25): p. 3935-3937.

[216] Albin, S. et al., *Electrical properties of hydrogenated diamond.* Applied Physics Letters, 1990. **56**(15): p. 1454-1456.

[217] Hayashi, K., et al., *Investigation of the effect of hydrogen on electrical and optical properties in chemical vapor deposited on homoepitaxial diamond films.* Journal of Applied Physics, 1997. **81**(2): p. 744-753.

[218] Tsugawa, K., et al., *High-preformance diamond surface-channel field-effect transistors and their operation mechanism.* Diamond and Related Materials, 1999. **8**(2-5): p. 927-933.

[219] Denisenko, A., et al., *Hypothesis on the conductivity mechanism in hydrogen terminated diamond films.* Diamond and Related Materials, 2000. **9**(3-6): p. 1138-1142.

[220] Hellner, L., et al., *Hydrogenated diamond crystal C(100) conductivity studied by STM.* Diamond and Related Materials, 2005. **14**(9): p. 1529-1534.

[221] Andriotis, A.N., et al., *Surface Conductivity of Hydrogenated Diamond Films.* Physical Review Letters, 2008. **100**(10): p. 106801.

[222] Kulesza, S., et al., *Spontaneous decrease of high surface electrical conductivity in diamond exposed to atmospheric air.* Chemical Physics Letters, 2004. **391**(1-3): p. 56-59.

[223] Szameitat, M., et al., *Influence of adsorbates on the surface conductivity of chemical vapor deposition diamond.* Applied Physics Letters, 2000. **77**(10): p. 1554-1556.

[224] Piantanida, G., et al., *Effect of moderate heating on the negative electron affinity and photoyield of air-exposed hydrogen-terminated chemical vapor deposited diamond.* Journal of Applied Physics, 2001. **89**(12): p. 8259-8264.

[225] Ristein, J., *Surface transfer doping of diamond.* Journal of Physics D: Applied Physics, 2006. **39**(4): p. R71.

[226] John, P., et al., *Fundamental limits to growth rates in a methane-hydrogen microwave plasma.* Diamond and Related Materials, 1994. **3**(1-2): p. 56-60.

[227] Celii, F.G. et al, *Diamond Chemical Vapor Deposition.* Annual Review of Physical Chemistry, 1991. **42**(1): p. 643-684.

[228] Troupe, C.E., *Glucose sensors utilising CVD diamond* 1998, PhD Thesis, Heriot-Watt University: Edinburgh.

[229] Dkaki, M., et al., *Infrared spectroscopy and transmission electron microscopy of polycrystalline silicon carbide.* Materials Science in Semiconductor Processing, 2001. **4**(1-3): p. 201-204.

[230] Tang, C.J., et al., *Simultaneous formation of silicon carbide and diamond on Si substrates by microwave plasma assisted chemical vapor deposition.* New Carbon Materials, 2008. **23**(3): p. 250-258.

[231] Sun, Z., et al., *Epitaxially grown β-SiC on Si in the CH_4---H_2 system by hot filament chemical vapour deposition.* Materials Science and Engineering B, 1995. **34**(2-3): p. L13-L16.

[232] Michaelson, S. et al., *Ambient contamination of poly-crystalline diamond surfaces studied by high-resolution electron energy loss spectroscopy and X-ray photoelectron spectroscopy.* Diamond and Related Materials, 2008. **17**(6): p. 920-924.

[233] Polwart, N., *Modification of diamond (100) surfaces*. 2003, PhD Thesis, Heriot-Watt University: Edinburgh, UK.

[234] Ferro, S. et al, *Chemical surface characterization of electrochemically and thermally oxidized boron-doped diamond film electrodes.* Carbon, 2005. **43**(6): p. 1191-1203.

[235] Wilson, J.I.B., et al., *Analysis of chemical vapour deposited diamond films by X-ray photoelectron spectroscopy.* Journal of Electron Spectroscopy and Related Phenomena, 2001. **121**(1-3): p. 183-201.

[236] Ando, T., et al., *Diffuse reflectance infrared Fourier-transform study of the plasma hydrogenation of diamond surfaces.* J. Chem. Soc., Faraday Trans., 1993. **89**: p. 1383-1386.

[237] Haq, S., et al., *An X-ray photoelectron spectroscopy study of the surface layers between diamond crystallites and silicon substrate deposited by microwave-plasma-assisted chemical vapour deposition.* Diamond and Related Materials, 1993. **2**(2-4): p. 558-561.

[238] Schroder, D.K., *Semiconductor material and device characterisation*. 2006, Wiley-Blackwell.

[239] Li, Y.L., et al., *Effect of grain boundary on local surface conductivity of diamond film.* Journal of Applied Physics, 2009. **105**(1): p. 013706.

[240] Theije, F.d., *Diamond Surfaces - Growth and Etching Mechanisms*. 2001, Katholieke Universiteit Nijmegen: Nijmegen.

[241] Wang, X.D., et al., *Precise patterning of diamond films for MEMS application.* Journal of Materials Processing Technology, 2002. **127**(2): p. 230-233.

[242] Ramesham, R., *Fabrication of diamond microstructures for microelectromechanical systems (MEMS) by a surface micromachining process.* Thin Solid Films, 1999. **340**(1-2): p. 1-6.

[243] Fox, N.A., et al., *Properties of electron field emitters prepared by selected area deposition of CVD diamond carbon films.* Diamond and Related Materials, 2000. **9**(3-6): p. 1263-1269.

[244] Ha, S.C., et al., *Fabrication of gated diamond field emitter array using a selective diamond growth process.* Thin Solid Films, 1999. **341**(1-2): p. 216-220.

[245] Björkman, H., et al., *Diamond microstructures for optical micro electromechanical systems.* Sensors and Actuators A: Physical, 1999. **78**(1): p. 41-47.

[246] Fu, Y., et al., *Patterning of diamond microstructures on Si substrate by bulk and surface micromachining.* Journal of Materials Processing Technology, 2003. **132**(1-3): p. 73-81.

[247] Narayan, J. et al., *Laser patterning of diamond films.* Journal of Applied Physics, 1992. **71**(8): p. 3795-3801.

[248] Chan, S.S.M. et al., *The effect of excimer laser etching on thin film diamond.* Semiconductor Science and Technology, 2003. **18**(3): p. S47.

[249] Geis, M.W.E. et al., *Diamond cold cathode.* Electron Device Letters, IEEE 1991. **12**(8): p. 456 - 459.

[250] Grot, S.A.G., et al, *Diamond thin-film recessed gate field-effect transistors fabricated by electron cyclotron resonance plasma etching.* Electron Device Letters, IEEE 1992. **13**(9): p. 462 - 464.

[251] Shiomi, H.N., et al; *Pulse-doped diamond p-channel metal semiconductor field-effect transistor.* Electron Device Letters, IEEE, 1995. **16**(1): p. 36 - 38.

[252] Kohn, E., et al., *Diamond MEMS -- a new emerging technology.* Diamond and Related Materials, 1999. **8**(2-5): p. 934-940.

[253] Karlsson, M.K.H., et al., *Transfer of continuous-relief diffractive structures into diamond by use of inductively coupled plasma dry etching.* Optics Letters, 2001. **26**(22): p. 1752 - 1754.

[254] Otterbach, R. et al., *Reactive ion etching of CVD-diamond for piezoresistive pressure sensors.* Diamond and Related Materials, 2002. **11**(3-6): p. 841-844.

[255] Banno, T., et al., *Fabrication of diamond in-plane-gated field effect transistors using oxygen plasma etching.* Diamond and Related Materials, 2003. **12**(3-7): p. 408-412.

[256] Lee, C.L., et al., *Etching and micro-optics fabrication in diamond using chlorine-based inductively-coupled plasma.* Diamond and Related Materials, 2009. **17**(7-10): p. 1292-1296.

[257] Lister, K.A., et al., *Pattern transfer of a 23 nm-period grating and sub-15 nm dots into CVD diamond.* Microelectronic Engineering, 2004. **73-74**: p. 319-322.

[258] Rossnagel, S.M., et al, *Handbook of plasma processing technology:Fundamentals, etching, deposition and surface interactions, 1989, Noyes Publications, New Jersey*

[259] Beerling, T.E. et al., *Direct observation of the etching of damaged surface layers from natural diamond by low-energy oxygen ion bombardment.* Applied Physics Letters, 1994. **64**(3): p. 288-290.

[260] Ding, G., et al., *Patterning of diamond films by RIE and its MEMS applications.* In Micromachining and Microfabrication Process Technology VI, Proc. SPIE, 2000. **4174**: p. 451-461.

[261] Ding, G.F., et al., *Micromachining of CVD diamond by RIE for MEMS applications.* Diamond and Related Materials, 2005. **14**(9): p. 1543-1548.

[262] Li, C.Y. et al, *Nanowhiskers formation by radio frequency Ar/O2 plasma etching of aluminum coated diamond films.* Thin Solid Films, 2007. **515**(9): p. 4172-4176.

[263] Leech P. W. et al., *Reactive ion etching of diamond in CF_4, O_2, O_2 and Ar-based mixtures* Journal of Materials Science, 2001. **36**(14): p. 3453-3459.

[264] Shiomi, H., *Reactive Ion Etching of Diamond in O_2 and CF_4 Plasma, and Fabrication of Porous Diamond for Field Emitter Cathodes.* Jpn. J. Appl. Phys., 1997. **36**: p. 7745-7748.

[265] Silva, F., et al., *Reactive ion etching of diamond using microwave assisted plasmas.* Diamond and Related Materials, 2003. **12**(3-7): p. 369-373.

[266] Vivensang, C., et al., *Reactive ion etching of diamond and diamond-like carbon films.* Diamond and Related Materials, 1994. **3**(4-6): p. 645-649.

[267] Kobayashi, K., et al.,, *Surface properties of diamond and diamond-like hydrogenated amorphous carbon films resulting from r.f. plasma etching.* Thin Solid Films, 1991. **200**(1): p. 139-145.

[268] Kawabata, Y., et al., *XPS studies on damage evaluation of single-crystal diamond chips processed with ion beam etching and reactive ion beam assisted chemical etching.* Diamond and Related Materials, 2004. **13**(1): p. 93-98.

[269] Yamada, T., et al., *Cycle of two-step etching process using ICP for diamond MEMS applications.* Diamond and Related Materials, 2007. **16**(4-7): p. 996-999.

[270] Vivensang, C., et al., *Surface smoothing of diamond membranes by reactive ion etching process.* Diamond and Related Materials, 1996. **5**(6-8): p. 840-844.

[271] Li, C.Y. et al., *Preparation of diamond whiskers using Ar/O_2 plasma etching.* Diamond and Related Materials, 2005. **14**(11-12): p. 1780-1783.

[272] Li, C.Y. et al., *Function of aluminum coating on fabrication of nanowhiskers by radio frequency plasma etching.* Diamond and Related Materials, 2006. **15**(4-8): p. 1122-1125.

[273] Zou, Y.S., et al., *Fabrication of diamond nanocones and nanowhiskers by bias-assisted plasma etching.* Diamond and Related Materials, 2007. **16**(4-7): p. 1208-1212.

[274] Wang, Q., et al., *The growth and characterization of diamond cone arrays formed by plasma etching.* Diamond and Related Materials, 2006. **15**(4-8): p. 866-869.

[275] Dorsch, O., et al., *Dry etching of undoped and boron doped polycrystalline diamond films.* Diamond and Related Materials, 1995. **4**(4): p. 456-459.

[276] Kiyohara ,S.Y.Y.,et al. *Plasma etching of CVD diamond films using an ECR-type oxygen source* Nanotechnology 1999. **10**(4): p. 385-388.

[277] Vescan, A., et al., *Electrical characterisation of diamond resistors etched by RIE.* Diamond and Related Materials, 1996. **5**(6-8): p. 747-751.

[278] Uetsuka, H., T. et al., *ICP etching of polycrystalline diamonds: Fabrication of diamond nano-tips for AFM cantilevers.* Diamond and Related Materials, 2008. **17**(4-5): p. 728-731.

[279] Yoshikawa, H., et al., *Smooth Surface Dry Etching of Diamond by Very High Frequency Inductively Coupled Plasma.* New Diamond and Frontier Carbon Technology, 2006. **16**(2): p. 97.

[280] Baik, E.S., et al., *Fabrication of diamond nano-whiskers.* Thin Solid Films, 2000. **377-378**: p. 295-298.

[281] Baik, E.S., et al., *Diamond tip fabrication by air-plasma etching of diamond with an oxide mask.* Diamond and Related Materials, 1999. **8**(12): p. 2169-2171.

[282] Chu, C.J., et al., *F_2, H_2O, and O_2 etching rates of diamond and the effects of F_2, HF and H_2O on the molecular O_2 etching of (110) diamond.* Diamond and Related Materials, 1995. **4**(12): p. 1317-1324.

[283] Theije de, F.K., et al., *Atomic structure of diamond {111} surfaces etched in oxygen water vapor.* Physical Review B, 2001. **64**(8): p. 085403.

[284] Theije de, F.K., et al., *Oxidative etching of diamond.* Diamond and Related Materials. **9**(3-6): p. 929-934.

[285] Theije de, F.K., et al., *Oxidative etching of cleaved synthetic diamond {1 1 1} surfaces.* Surface Science, 2001. **492**(1-2): p. 91-105.

[286] Evans, T.et al., *Etching of diamond surfaces with gases.* Philosophical Magazine, 1961. **6**(63): p. 429 - 440.

[287] Frank, F.C., et al, *Etch pits and trigons on diamond: I.* Philosophical Magazine, 1958. **3**(35): p. 1262 - 1272.

[288] Howe, J.Y., et al., *The evolution of microstructure of CVD diamond by oxidation.* Carbon, 2000. **38**(6): p. 931-934.

[289] John, P., et al., *The oxidation of (100) textured diamond.* Diamond and Related Materials. **11**(3-6): p. 861-866.

[290] Khokhryakov, A.F. et al., *Revealing of dislocations in diamond crystals by the selective etching method.* Journal of Crystal Growth, 2006. **293**(2): p. 469-474.

[291] Klauser, F., et al., *Comparison of different oxidation techniques on single-crystal and nanocrystalline diamond surfaces.* Diamond and Related Materials, 2010. **19**(5-6):p. 474-478.

[292] Lee, J.-K., et al., *Explosive oxidation of HPHT diamond particles.* Diamond and Related Materials, 2006. **15**(9): p. 1206-1209.

[293] Li, J., et al., *Erosion resistance of polycrystalline diamond films to atomic oxygen.* Carbon, 2003. **41**(9): p. 1847-1850.

[294] Loh, K.P., et al., *Surface oxygenation studies on (1 0 0)-oriented diamond using an atom beam source and local anodic oxidation.* Surface Science, 2002. **505**: p. 93-114.

[295] Lu, F.X., et al., *Oxidation behaviour of high quality freestanding diamond films by high power arcjet operating at gas recycling mode.* Diamond and Related Materials, 2004. **13**(3): p. 533-538.

[296] Notsu, H., et al., *Surface carbonyl groups on oxidized diamond electrodes.* Journal of Electroanalytical Chemistry, 2000. **492**(1): p. 31-37.

[297] Obraztsov, A.N., et al., *Production of single crystal diamond needles by a combination of CVD growth and thermal oxidation.* Diamond and Related Materials, 2009. **18**(10): p. 1289-1293.

[298] Pehrsson, P.E. et al., *Oxidation of heated diamond C(100):H surfaces.* Surface Science, 2000. **460**(1-3): p. 74-90.

[299] Pehrsson, P.E., et al., *Thermal oxidation of the hydrogenated diamond (1 0 0) surface.* Surface Science, 2002. **497**(1-3): p. 13-28.

[300] Pipkin, N.J., *Etch features on synthetic diamond crystals oxidized in fused salts.* Journal of Materials Science, 1980. **15**(7): p. 1755-1764.

[301] Pu, J.-C., et al., *High-temperature oxidation behavior of nanocrystalline diamond films.* Journal of Alloys and Compounds. **489**(2): p. 638-644.

[302] Pu, J.-C., et al., *High-temperature oxidation behaviors of CVD diamond films.* Applied Surface Science, 2009. **256**(3): p. 668-673.

[303] Tokuda, N., et al., *Flattening of oxidized diamond (111) surfaces with H_2SO_4/H_2O_2 solutions.* Diamond and Related Materials. **18**(2-3): p. 213-215.

[304] Tokuda, N., et al., *Roughening of atomically flat diamond (111) surfaces by a hot HNO_3/H_2SO_4 solution.* Diamond and Related Materials. **17**(4-5): p. 486-488.

[305] Tolansky, S., et al., *Changes in orientation of etch pits produced on the cubic faces of diamond.* Philosophical Magazine, 1972. **26**(6): p. 1275 - 1280.

[306] Wang, M., et al., *Comparison of the chemical composition of boron-doped diamond surfaces upon different oxidation processes.* Electrochimica Acta, 2009. **54**(24): p. 5818-5824.

[307] Khokhryakov, A.F.et al., *Revealing of planar defects and partial dislocations in large synthetic diamond crystals by the selective etching.* Journal of Crystal Growth, 2007. **306**(2): p. 458-464.

[308] Patel, A.R., et al., *Optical and interferometric studies on the cleavages of synthetic diamonds and their etch patterns.* British Journal of Applied Physics, 1963. **14**(5): p. 284-286.

[309] Larsson, K., et al., *Role of water and oxygen in wet and dry oxidation of diamond.* Journal of Applied Physics, 2001. **90**(2): p. 1026-1034.

[310] Nakamura, J. et al., *Oxidization process of CVD diamond (1 0 0):H 2 × 1 surfaces.* Applied Surface Science, 2005. **244**(1-4): p. 301-304.

[311] Jin, S., et al., *Thermal conductivity in molten-metal-etched diamond films.* Applied Physics Letters, 1993. **63**(5): p. 622-624.

[312] Jin, S., et al., *Anisotropy in diamond etching with molten cerium.* Applied Physics Letters, 1994. **65**(21): p. 2675-2677.

[313] Ando, T., et al., *Chemical modification of diamond surfaces using a chlorinated surface as an intermediate state.* Diamond and Related Materials, 1996. **5**(10): p. 1136-1142.

[314] Nakamura, T., er al., *Photochemical modification and functionalization of carbon surfaces with fluorine moieties.* Diamond and Related Materials, 2004. **13**(4-8):p. 1084-1087.

[315] Miller, J.B. et al., *Properties of photochemically modified diamond films.* Diamond and Related Materials, 1995. **4**(4): p. 435-440.

[316] Coffinier, Y., et al., *Covalent linking of peptides onto oxygen-terminated boron-doped diamond surfaces.* Diamond and Related Materials. **16**(4-7): p. 892-898.

[317] Girard, H., et al., *Effect of anodic and cathodic treatments on the charge transfer of boron doped diamond electrodes.* Diamond and Related Materials, 2007. **16**(2): p. 316-325.

[318] Bernard, M., et al., *Electron cyclotron resonance oxygen plasma etching of diamond.* Diamond and Related Materials, 2004. **13**(2): p. 287-291.

[319] Ramesham, R., et al., *Plasma etching and patterning of CVD diamond at <100°C for microelectronics applications.* Thin Solid Films, 1997. **304**(1-2): p. 245-251.

[320] Ando, T. et al., *Thermal hydrogenation of diamond surfaces studied by diffuse reflectance Fourier-transform infrared, temperature-programmed desorption and laser Raman spectroscopy.* J. Chem. Soc., Faraday Trans., 1993. **89**: p. 1783-1789.

[321] Johnson, C.E., et al., *Thermogravimetric analysis of the oxidation of CVD diamond films.* J. Mater. Res, 1990. **5**(11): p. 2320-2325.

[322] Nimmagadda. R.R, et al., *Role of microstructure on the oxidation behavior of microwave plasma synthesized diamond and diamond-like carbon films.* J.Mater. Res., 1990. **5**(11): p. 2445-2450.

[323] Sun, Q., et al., *Relative Oxidation Behavior of Chemical Vapor Deposited and Type IIa Natural Diamonds.* Journal of The Electrochemical Society, 1992. **139**(3): p. 933-936.

[324] Skokov, S., et al., *Theoretical study of oxygenated (100) diamond surfaces in the presence of hydrogen.* Physical Review B, 1997. **55**(3): p. 1895. Skokov, S., et al., *Molecular-dynamics study of oxygenated (100) diamond surfaces.* Physical Review B, 1994. **49**(16): p. 11374.

[325] Zheng, X.M., et al., *The stable configurations for oxygen chemisorption on the diamond (100) and (111) surfaces.* Surface Science, 1992. **262**(1-2): p. 219-234.

[326] Tankala, K., et al., *Oxidation of diamond films synthesized by hot filament assisted chemical vapor deposition.* J. Mater. Res, 1990. **5**(11): p. 2483-2489.

[327] Bobrov, K., et al., *Molecular oxygen adsorption and desorption from single crystal diamond (1 1 1) and (1 1 0) surfaces.* Applied Surface Science, 2002. **196**(1-4): p. 173-180.

[328] Klauser, R., et al., *The interaction of oxygen and hydrogen on a diamond C(111) surface: a synchrotron radiation photoemission, LEED and AES study.* Surface Science, 1996. **356**(1-3): p. L410-L416.

[329] Uchida, N., et al., *Thermochemical etching effect on CVD diamond film in an oxygen atmosphere.* J. Mater. Sc. Lett, 1990. **9**: p. 249-250.

[330] Frenklach, M., et al., *Activation energy and mechanism of CO desorption from (100) diamond surface.* Applied Physics Letters, 1993. **63**(22): p. 3090-3092.

[331] Silva, F., et al., *Geometric modeling of homoepitaxial CVD diamond growth: I. The {1 0 0}{1 1 1}{1 1 0}{1 1 3} system.* Journal of Crystal Growth, 2008. **310**(1): p. 187-203.

[332] Silva, F., et al., *Single crystal CVD diamond growth strategy by the use of a 3D geometrical model: Growth on (113) oriented substrates.* Diamond and Related Materials. **17**(7-10): p. 1067-1075.

[333] Stekolnikov, A.A., et al., *Shape of free and constrained group-IV crystallites: Influence of surface energies.* Physical Review B, 2005. **72**(12): p. 125326.

[334] Runyan, W.A. and T.J.S. Shaffner, *Semiconductor Measurements and Instrumentation*. Second Edition ed.

[335] Sawada, H., et al., *Atomic structure of fivefold twin center in diamond film.* Diamond and Related Materials, 2005. **14**(1): p. 109-112.

[336] Steeds, J.W., et al., *On the nature of grain boundary defects in high quality CVD diamond films and their influence on physical properties.* Diamond and Related Materials, 1999. **8**(6): p. 996-1005.

[337] Hossain, M.Z., et al., *Chemisorbed states of atomic oxygen and its replacement by atomic hydrogen on the diamond (100)-(2×1) surface.* Surface Science, 1999. **436**(1-3): p. 63-71.

[338] Evans, T., et al., Proc.of the 5th Biennial conference on Carbon, 1962, **1**:p. 147

[339] Stekolnikov, A.A., et al., *Tetramers on diamond, Si, and Ge(113) surfaces: Ab initio studies.* Physical Review B, 2003. **68**(20): p. 205306.